The Ancient Rocky Surfaces of Mars:

Analysis of Spacecraft Data and the Development of Laboratory Instrumentation

by

Christopher Edwards

A Dissertation Presented in Partial Fulfillment
of the Requirements for the Degree
Doctor of Philosophy

Approved August 2012 by the
Graduate Supervisory Committee:

Philip Christensen, Chair
James Bell
Amanda Clarke
Thomas Sharp
Everett Shock

ARIZONA STATE UNIVERSITY

December 2012

ABSTRACT

Early spacecraft missions to Mars, including the Marnier and Viking orbiters and landers revealed a morphologically and compositionally diverse landscape that reshaped widely held views of Mars. More recent spacecraft including Mars Global Surveyor, Mars Odyssey, Mars Express, Mars Reconnaissance Orbiter, and the Mars Exploration Rovers have further refined, enhanced, and diversified our understanding of Mars. In this dissertation, I take a multiple-path approach to planetary and Mars science including data analysis and instrument development.

First, I present several tools necessary to effectively use new, complex datasets by highlighting unique and innovative data processing techniques that allow for the regional to global scale comparison of multiple datasets.

Second, I present three studies that characterize several processes on early Mars, where I identify a regional, compositionally distinct, *in situ,* stratigraphically significant layer in Ganges and Eos Chasmata that formed early in martian history. This layer represents a unique period in martian history where primitive mantle materials were emplaced over large sections of the martian surface. While I originally characterized this layer as an effusive lava flow, based on the newly identified regional or global extent of this layer, I find the only likely scenario for its emplacement is the ejecta deposit of the Borealis Basin forming impact event. I also re-examine high thermal inertia, flat-floored craters identified in Viking data and conclude they are typically more mafic than the surrounding plains and were likely infilled by primitive volcanic materials during,

or shortly after the Late Heavy Bombardment. Furthermore, the only plausible source for these magmas is directly related to the impact process, where mantle decompression melting occurs as result of the removal of overlying material by the impactor.

Finally, I developed a new laboratory microscopic emission and reflectance spectrometer designed to help improve the interpretation of current remote sensing or *in situ* data from planetary bodies. I present the design, implementation, calibration, system performance, and preliminary results of this instrument. This instrument is a strong candidate for the next generation *in situ* rover instruments designed to definitively assess sample mineralogy and petrology while preserving geologic context.

DEDICATION

To my wife for all her patience

and discussions of other worlds

ACKNOWLEDGEMENTS

The completion of my graduate work would not have been possible without the help of several people. First, I would like to thank Philip Christensen for taking a chance on an economics undergraduate major that he did not know. This chance given to me fundamentally changed the course of my life and I am grateful for it. Secondly, all of my graduate student peers and collaborators for helpful discussions and support along the way including Sylvain Piqueux, Joshua Bandfield, Deanne Rogers, Timothy Glotch, Alicia Rutledge and Michael Veto, among many others who work at the Mars Space Flight Facility that made things easier on me. I would also like to thank my parents for unwavering support and love. And most of all, I would like to thank my wife Laurie who has always been there for me in good times and bad, who read countless papers on Mars, and supported me through my academic career; on to our next adventure!

TABLE OF CONTENTS

Page

CHAPTER Page

CHAPTER Page

CHAPTER Page

CHAPTER Page

LIST OF TABLES

LIST OF FIGURES

Figure Page

Figure Page

Figure Page

CHAPTER 1

INTRODUCTION

Early planetary missions to Mars made fundamental observations of the planet's surface morphology, composition, and physical properties that re-characterized Mars from widely held views formed in the early telescopic era [e.g. *Lowell*, 1896]. Early spacecraft included the Mariner 6, 7 and 9 [e.g. *Chase et al.*, 1970; *Neugebauer et al.*, 1971; *Sagan et al.*, 1973], and Viking orbiters [*Klaasen et al.*, 1977], and landers which carried a wide range of instruments including the Visual Imaging subsystem [*Klaasen et al.*, 1977] and the Infrared Thermal Mapper (IRTM) [*Kieffer et al.*, 1977].

Beginning with Mars Global Surveyor carrying the Mars Orbiter Camera (MOC) [*Malin et al.*, 1998] wide angle and narrow angle instruments, the Thermal Emission Spectrometer (TES) [*Christensen et al.*, 2001], and the Mars Orbiter Laser Altimeter (MOLA) [*Smith et al.*, 2001] instruments, new views of the planet's surface revolutionized the manner and detail in which Mars was studied. Detailed topographic models [*Smith et al.*, 2001], mineralogy maps [e.g. *Bandfield*, 2002], and high resolution fine-scale morphology played an important role in again re-characterizing Mars as a geologically interesting and diverse world.

Spacecraft including the 2001 Mars Odyssey, Mars Express, and the Mars Reconnaissance Orbiter have sent an unprecedented suite of instruments into orbit around Mars. A sampling of these instruments includes the Thermal Emission Imaging Systems (THEMIS) [*Christensen et al.*, 2003b; *Christensen et al.*, 2004a]

visual and infrared imagers, the High-Resolution Stereo Camera (HRSC) [*Neukum et al.*, 2004; *Jaumann et al.*, 2007] visible imager, Observatoire pour la Minéralogie, l'Eau, les Glaces, et l'Activité (OMEGA) [*Bibring et al.*, 2005], High Resolution Imaging Science Experiment (HiRISE) [*McEwen et al.*, 2007], Context Imager (CTX) [*Malin et al.*, 2007], and the Compact Reconnaissance Imaging Spectrometer for Mars (CRISM) [*Murchie et al.*, 2007] and the Gamma Ray Spectrometer (GRS) instrument suite [*Boynton et al.*, 2002; *Feldman et al.*, 2002; *Mitrofanov et al.*, 2002; *Boynton et al.*, 2007] which have all provided new and unique views of the planet.

Landed spacecraft, including the Viking landers, the Mars Exploration Rovers, and the Phoenix Lander have all provided additional views of several regions of the martian surface, including near polar regions [e.g. *Smith et al.*, 2009] and environments that were clearly formed or modified by water related processes (e.g. Gusev Crater, Meridiani Planum, etc. [e.g. *Squyres et al.*, 2004b; *Squyres et al.*, 2004a; *McLennan et al.*, 2005; *Squyres and Knoll*, 2005; *Squyres et al.*, 2006]). The instruments available on these landed spacecraft are extensive and include a variety of *in situ* and remote sensing techniques, such as the Alpha-Particle X-ray Spectrometer (APXS) [*Gellert et al.*, 2006], Mössbauer [*Morris et al.*, 2004], Microscopic Imager (MI) [*Herkenhoff et al.*, 2003], Mini-Thermal Emission Spectrometer (Mini-TES) [*Christensen et al.*, 2003a], and Panoramic Camera (PanCam) [*Bell et al.*, 2006]. The combination of *in situ* (e.g. MI, APXS, Mössbauer) and remote sensing (e.g. PanCam, Mini-TES) instruments have proved to be especially successful in both identifying potential targets at a

distance and characterizing those targets in detail [*Gellert et al.*, 2004; *Klingelhöfer et al.*, 2004; *McLennan et al.*, 2005; *Golombek et al.*, 2006; *Ruff et al.*, 2006; *Squyres et al.*, 2007; *Lewis et al.*, 2008; *Rogers and Aharonson*, 2008; *Squyres et al.*, 2008; *Ruff et al.*, 2011].

In the coming months, the Mars Science Laboratory (MSL) will further the *in situ* investigations of the martian surface with the most sophisticated and complicated suite of instruments sent to the martian surface to date. These instruments include the Mast Camera (MastCam), a Laser Induced Breakdown Spectrometer (LIBS) for remote elemental composition (ChemCam), a microscopic imager (MAHLI), an Alpha-particle X-ray spectrometer (APXS), chemistry and mineralogy by powder X-ray diffraction and X-ray fluorescence (CheMin), as well as a quadrupole mass spectrometer, a gas chromatograph, and a tunable laser spectrometer (SAM). While martian landers characterize specific small sections of the surface in great detail, no landed spacecraft will likely explore vast areas of martian surface in the coming decades, due to the high cost of landed spacecraft and significant diversity of landscapes present on the martian surface. Complementary techniques from orbit and at lander scales are paramount for the extrapolation of the findings from landers to the rest of the planetary surface due to the extremely detailed, but overall limited scope of data that landers provide.

Spectroscopic observations of the martian surface provide fundamental understandings of surface mineralogy and composition and are completed from orbit and landed spacecraft. These data have significantly evolved our

understanding of the martian surface in the past decade from a global view [e.g. *Mustard and Sunshine*, 1995; *Bandfield et al.*, 2000a; *Christensen et al.*, 2000a; *Bandfield*, 2002; *Ruff and Christensen*, 2002; *Bibring et al.*, 2005; *Mustard et al.*, 2005; *Poulet et al.*, 2005; *Rogers et al.*, 2007; *Rogers and Christensen*, 2007; *Koeppen and Hamilton*, 2008; *Osterloo et al.*, 2008; *Ehlmann et al.*, 2011a] to regional and local studies [e.g. *Hoefen et al.*, 2003; *Hamilton and Christensen*, 2005; *Rogers et al.*, 2005; *Mustard et al.*, 2007; *Edwards et al.*, 2008; *Ehlmann et al.*, 2008; *Tornabene et al.*, 2008; *Ehlmann et al.*, 2009; *Mustard et al.*, 2009; *Rogers et al.*, 2009; *Rogers and Fergason*, 2011; *Wray et al.*, 2011] to outcrop scale observations where landed spacecraft have been sent [e.g. *Gellert et al.*, 2004; *Klingelhöfer et al.*, 2004; *McLennan et al.*, 2005; *Golombek et al.*, 2006; *Ruff et al.*, 2006; *Squyres et al.*, 2007; *Lewis et al.*, 2008; *Rogers and Aharonson*, 2008; *Squyres et al.*, 2008; *Ruff et al.*, 2011].

A large body of work regarding the aqueous alteration of the martian surface exists using spectroscopic methods, primarily derived from visible and near-infrared spectrometers (CRISM and OMEGA). While Mars shows significant mineralogical variably associated with aqueous alteration, it commonly occurs at a small scale and covers a minor area of the surface [*Poulet et al.*, 2005; *Ehlmann et al.*, 2008; *Squyres et al.*, 2008]. Mars is primarily a volcanic planet that is dominated basaltic lava flows [*McEwen et al.*, 1999; *Christensen et al.*, 2000a] and volcaniclastic deposits [*Robbins et al.*, 2011] which is the focus of this dissertation.

A primary challenge of constraining the geologic history of Mars from remotely sensed data is the ability to discriminate between *in situ* materials and those that have been transported, altered, and/or weathered. While spectroscopic data can help constrain the alteration history of geologic materials, constraining the particle size of the material in question is largely completed using orbital thermal inertia data [e.g. *Presley and Christensen*, 1997b; c; *Mellon et al.*, 2000; *Putzig et al.*, 2005; *Fergason et al.*, 2006a; *Edwards et al.*, 2009; *Piqueux and Christensen*, 2009; *Piqueux and Christensen*, 2011] where microscopic imager data is not available [e.g. *Herkenhoff et al.*, 2003].

The rockiest areas on Mars are likely in-place, geologically significant materials. The most common agents of erosion on Mars are aeolian and impact related processes along with volcanism, tectonism and fluvial activity occurring primarily earlier in Mars history [*Edwards et al.*, 2009]. Aeolian action is generally not capable of moving or eroding bedrock and large boulders [*Greeley et al.*, 1980; *Greeley et al.*, 1992] and impact events would generally distribute these materials in an observable pattern. Therefore, if I find materials that are consistent with in-place bedrock I can be confident that they have not been transported significant distances or significantly disturbed by impact or other erosional processes on Mars.

The primary goal of this dissertation is to constrain several aspects of the early history of Mars using ancient *in situ* rocky materials [*Edwards et al.*, 2009]. Significant fractions of martian landscape are ancient, including the heavily cratered terrain of the southern highlands from the late heavy bombardment

(LHB) and the relatively smooth northern lowlands modified subsequent to the LHB. Fast crustal recycling, abundant water, widespread volcanism, and gradational processes associated with plate tectonics have largely erased the most ancient materials from the geologic record on Earth. While many of the same processes occur on Mars, a large proportion of the surface is ancient (Noachian or early Hesperian) and represents a portion of geologic time that has been largely erased from Earth's geologic record.

In **Chapter 2** of this dissertation I provide an investigation and description of some of the advanced techniques developed for the processing and mosaicking of THEMIS infrared multispectral data [*Edwards et al.*, 2011b]. With the abundance of data returned from Mars, it is necessary to develop advanced techniques for mosaicking the data together, as well as processing data to remove systematic instrument artifacts or noise. Furthermore, significant data processing challenges emerge as multiple datasets are required and utilized to solve geologic problems. While the techniques discussed for THEMIS are somewhat specific, the mosaicking and stretching algorithms presented are novel and have enabled the creation of both quantitative and qualitative global data products of Mars. These mosaicking techniques are generic enough and can be applied to other planetary and Earth based datasets.

In the following chapters I present several detailed studies of the martian surface using multiple datasets from orbit (**Chapter 3 through Chapter 5**), and the development of a new microscopic emission spectrometer (**Chapter 6**) for *in situ* lander based measurements of the martian surface.

In **Chapter 3**, I present work that identified an *in situ*, olivine-enriched stratigraphic layer near the bottom of Valles Marineris in Ganges and Eos Chasmata, which extends laterally over a distance of >1,100 km and has a minimum volume of ~9.9×10^4 km^3 [*Edwards et al.*, 2008]. This layer was characterized and identified utilizing TES spectral data and THEMIS multi-spectral images, along with THEMIS nighttime temperature data to determine the thermophysical properties of the outcrops. Furthermore the strike and dip of this layer was characterized using MOLA elevation data and was found to be essentially flat-lying.

Building on this work, in **Chapter 4,** I examined the surrounding locations to Ganges and Eos Chasmata and found that this layer extends significantly further (>4000 km laterally) and has a significantly larger volume (1.5×10^6 km^3 to $>5 \times 10^6$ km^3) than previously estimated. A detailed survey of all related locations was conducted and I propose this layer is at least regional and possibly global in extent. After the characterization of this layer, I present several hypotheses for the formation of this ancient and extensive geologically significant unit on Mars.

Chapter 5 examines another unique and likely widespread process on early Mars, where the removal of crustal material by impact events in the LHB caused widespread magmatism as a result of decompression melting of the martian mantle. In order to assess this process, I examine the distribution, thermophysical, and compositional characteristics of high thermal inertia flat floored craters on Mars which were originally identified by *Arvidson* [1974] and *Christensen* [1983] and were further characterized as containing bedrock outcrops

by *Edwards et al.* [2009]. These craters have a degraded morphology, flat floors, no central peak and the highest thermal inertia materials are associated with the crater floor and not the crater walls. The detailed compositional and thermophysical investigation of these craters, combined with age dates for >100 crater floors, allows us to definitively constrain the formation mechanism for a significant majority of crater fill material on Mars

While the analysis of currently available martian data is a critical part of understanding martian history, rigorous laboratory investigations are required for instrument calibration and refinement of data interpretation. In **Chapter 6,** I present the instrument description, calibration, and design of a laboratory microscopic emission and reflectance spectrometer designed to improve the interpretation of current remote sensing or *in situ* data from planetary bodies. This instrument is able to examine analog materials in detail and is also a strong candidate for the next generation of *in situ* instruments designed to definitively assess sample mineralogy and petrology while preserving geologic context. In this chapter, I discuss the instrument capabilities, signal and noise, and overall system performance. Furthermore, I evaluate the ability of this instrument to quantitatively discriminate and determine sample mineralogy, including bulk mineral abundances, and make the case for this instrument as a candidate for the next generation of *in situ* instruments that should be sent to the martian surface.

Chapter 7 summarizes the main results and findings presented throughout this dissertation.

CHAPTER 2

MOSAICKING OF GLOBAL PLANETARY IMAGE DATASETS: TECHNIQUES AND DATA PROCESSING FOR THEMIS MULTI-SPECTRAL DATA

Edwards, C. S., K. J. Nowicki, P. R. Christensen, J. Hill, N. Gorelick, and K. Murray (2011), Mosaicking of global planetary image datasets: 1. Techniques and data processing for Thermal Emission Imaging System (THEMIS) multi-spectral data, *J. Geophys. Res.*, *116*(E10), E10008, doi:10010.11029/12010JE003755.

The mosaicking of global planetary datasets allows for the examination of local, regional, and global scale processes on all planetary bodies. Processing techniques that allow us and other users to crate mosaics of tens of thousands of images are documented along with the associated errors introduced by each image-processing algorithm. These techniques (e.g. non-uniformity correction, running contrast stretches, line and row correlated noise removal, and random noise removal) were originally developed for the 2001 Mars Odyssey Thermal Emission Imaging System (THEMIS) infrared multispectral imager data but can be adapted and applied to other datasets by the alteration of input parameters. The techniques for mosaicking planetary image datasets (e.g. image registration, blending, and normalization) are also presented along with the generation of qualitative and quantitative products. These techniques are then applied to

generate THEMIS daytime and nighttime infrared, Viking, Context Imager (CTX), and Mars Orbiter Camera (MOC) visible mosaics using a variety of input and output types at a variety of scales. By creating mosaics of the same area using different datasets such as those that illustrate compositional diversity, thermophysical properties, or small-scale morphology, it is possible to view the surface of the planet and geologic problems through many different perspectives. In addition to the techniques used to create large-scale seamless mosaics, I also present the THEMIS daytime and nighttime relative temperature global mosaics, which are the highest resolution (100 m/pixel) global scale datasets available for Mars to date.

2.1 Introduction

Images of other planetary bodies in our solar system are some of the most widely utilized data products available to the planetary science community. Mars has a wealth of these data, which have been acquired from the beginning of NASA's exploration of the solar system to the present day. Imaging cameras and spectrometers such as the Viking Orbiter Visual Imaging Subsystems (VIS) [*Klaasen et al.*, 1977], the Mars Orbiter Camera (MOC) [*Malin et al.*, 1998] wide angle and narrow angle instruments, the Thermal Emission Imaging Systems (THEMIS) [*Christensen et al.*, 2003b; *Christensen et al.*, 2004a] visual and infrared imagers, the High-Resolution Stereo Camera (HRSC) [*Neukum et al.*, 2004; *Jaumann et al.*, 2007] visible imager, and the Mars Reconnaissance Orbiter's High Resolution Imaging Science Experiment (HiRISE) [*McEwen et al.*, 2007], Context Imager (CTX) [*Malin et al.*, 2007], and the Compact

Reconnaissance Imaging Spectrometer for Mars (CRISM) [*Murchie et al.*, 2007] have all provided new and unique views of the planet that have revolutionized the manner and detail in which Mars is studied. While many of these instruments do not provide global scale coverage in a single image (in fact many instruments only provide meter to kilometer scale snapshots of the surface), the combination of hundreds to tens of thousands of these individual observations provides a remarkably powerful tool for scientific investigations.

The construction and use of global datasets has vastly increased the present understanding of many aspects of Mars, including its crustal and regolith composition, thermophysical character, magnetic field anomalies, active processes, climate, and geologic history. Here I will document the processes that are used to create large-scale regional and global mosaics of thousands of individual Thermal Emission Imaging System (THEMIS) images and demonstrate the versatility of these tools by applying them to other planetary image datasets including Viking VIS, MOC, and CTX. The companion paper to this publication, *Edwards et al.* [*2011a*], Mosaicking of Global Planetary Image Datasets, Part 2: Application to Wind Streaks Observed in THEMIS Daytime and Nighttime Infrared Data, hereinafter referred to as Paper 2, uses the THEMIS daytime and nighttime infrared mosaics as reconnaissance tools and presents unique scientific results made possible by the creation of the mosaic.

THEMIS provides excellent means to address many local and regional scale geologic problems, with its high spatial sampling and its ability to discriminate between geologic materials of different compositions. These

compositional data have allowed for the investigation of a variety of areas in detail, including the Nili Fossae [*Hamilton and Christensen*, 2005], Ganges and Eos Chasmata [*Edwards et al.*, 2008], Ares Vallis [*Rogers et al.*, 2005], Mare Serpentis [*Rogers et al.*, 2009], and a variety of other locations. The majority of these studies utilized THEMIS data in conjunction with Thermal Emission Spectrometer (TES) [*Christensen et al.*, 2000a; *Christensen et al.*, 2001], CRISM [*Murchie et al.*, 2007; *Pelkey et al.*, 2007] and Observatoire pour la Minéralogie, l'Eau, les Glaces, et l'Activité (OMEGA) [*Bibring et al.*, 2005; *Mustard et al.*, 2005] data to better constrain the compositions highlighted by THEMIS data. These compositional data have also been used in conjunction with THEMIS thermophysical data [*Fergason et al.*, 2006a; *Bandfield*, 2008; *Bandfield and Rogers*, 2008; *Edwards et al.*, 2008] to constrain the nature of the material (e.g. unconsolidated sand or dust). Additionally, these data have allowed for the investigation of *in situ* bedrock or rocky materials [*Edwards et al.*, 2009] and primarily aeolian deposits in Arabia Terra [*Fergason and Christensen*, 2008], where likely the most primitive unmodified crustal and the most homogenized materials, respectively, are observed on the planet.

In this paper, I present the highest resolution global datasets of Mars to date with a spatial sampling of 100 m/pixel or ~592 pixels per degree (ppd) at the equator. Both nighttime temperature and daytime temperature qualitative global datasets have been produced at this scale. While these data do not provide quantitative thermophysical or compositional information about the surface, they are extremely useful as reconnaissance tools. This is especially true for areas with

materials that exhibit a range of thermophysical characteristics, which can be readily identified. In addition, the daytime data can be used for morphologic studies, crater counting, and as indicators of thermophysical properties or compositional variations. The construction of qualitative data products is the initial step required for subsequent work to construct global thermal inertia, multi-band decorrelation stretch, 10-band emissivity, and surface kinetic temperature mosaics at the same 100 m/pixel scale.

2.2 Data Processing Tools

The construction of these datasets necessitates the use of advanced image processing techniques that were originally developed for use with THEMIS image data products but can be adapted to a variety of other datasets through the alteration of input parameters. These techniques are used to create well-calibrated high quality quantitative data from which additional products can be derived, as well as large-scale qualitative image products, which are equally useful and provide regional morphologic and relative thermophysical context. Often, the size of the region of interest will require the concatenation of many hundreds to thousands of images (or tens of thousands as is the case for the THEMIS daytime and nighttime global mosaics).

Here I present the generic techniques and tools which can be used to create mosaics from any images projected by the Integrated Software for Imagers and Spectrometers (ISIS; http://isis.astrogeology.usgs.gov/) package provided by the United States Geological Survey (USGS) [e.g. *Torson and Becker*, 1997; *Anderson et al.*, 2004]. ISIS provides many useful processing tools (projection

and other geometric processing of images with high precision, based on rigorous camera models, precise radiometric calibration for many instruments, and a large but certainly not complete set of other cartographic and image processing functions such as map transformations and spatial filtering), but is not provided to the end user as a development platform for new algorithms. It supports predetermined processing steps used to manipulate data in a standard and established manner.

Other than map projecting data to a planet's surface, all data processing and mosaicking was completed using an open source software package entitled DaVinci, which is maintained by the Mars Space Flight Facility at Arizona State University (http://davinci.asu.edu) in partnership with other institutions. DaVinci is a generic array-processing tool that allows for symbolic and mathematical manipulation of hyper-spectral planetary image data and provides support for importing and exporting current ISIS data formats. DaVinci allows the end user to develop image-processing algorithms with an interactive scripting interface. Its plotting and image display capabilities let the user visualize the effect of data processing in real-time. Processing algorithms developed in DaVinci can be easily integrated with ISIS to provide a flexible compliment to the established ISIS routines.

ISIS currently supports Linux and MacOS X installations and requires up to 70 Gigabytes of storage for the application and mission data. DaVinci supports Linux, MacOS X, and Windows installations and only requires 100 Megabytes of storage for the entire application. Both applications have detailed documentation,

tutorials, and additional information that can be found at their respective websites.

A combination of ISIS and DaVinci was used to create mosaics for several different datasets including the Viking VIS [e.g. *Klaasen et al.*, 1977], MOC wide-angle camera [e.g. *Malin et al.*, 1998], CTX [e.g. *Malin et al.*, 2007] and THEMIS infrared and visible imagers [*Christensen et al.*, 2003b; *Christensen et al.*, 2004a]. In addition, I demonstrate the efficacy of the aforementioned techniques and software to create regional multi-band mosaics using decorrelation stretch [*Gillespie et al.*, 1986] THEMIS images that vividly illustrate the compositional diversity of the Martian crust.

2.3 THEMIS Specific Data Processing

2.3.1 Dataset/Instrument Description

The THEMIS instrument includes two separate cameras: a thermal infrared pushbroom line scanner consisting of a 9 spectral channel, 320 by 240 element uncooled microbolometer array that covers a wavelength range of 6.7 to 14.8 μm and a visible 1024 by 1024 framelet imager split into 5 spectral channels in ~50nm bands centered from 0.42 to 0.86 μm [*Christensen et al.*, 2004a]. The infrared imager has 100 m/pixel spatial sampling and the visible imager has ~18m/pixel spatial sampling from the ~420 km altitude orbit of the 2001 Mars Odyssey spacecraft. The infrared imager acquires extremely long (typically > 6000 lines, covering > 600 km), narrow (320 samples, covering only 32 km) images. Several issues commonly exist with line scanner instruments like

THEMIS including: 1) variations in detector readout voltage that can cause enhanced line-to-line noise, 2) the delay between the acquisition of each band that necessitates the use of map projection software to align each band to the surface before the multispectral data are utilized, and 3) calibration errors as these instruments will often acquire data for long periods of time covering large distances on the surface.

Candidate images are first selected using parameters in a database (available through a DaVinci Simple Query Language (SQL) interface or http://viewer.mars.asu.edu) and are chosen according to the desired use of the mosaic. For example, it is possible to select images based on surface temperature, atmospheric opacities, thermal inertia, TES albedo, incidence angle, solar longitude, and a variety of other acquisition and observational parameters [e.g. *Christensen et al.*, 2007]. Additional quality control constraints are useful to eliminate noisy, poorly calibrated data. Data with the following parameters are preferred: 1) the time difference between the end of the image and the acquisition of the calibration image should be limited to <150 seconds to minimize the potential changes in instrumental conditions, 2) images with a small number of saturated or under-saturated pixels, 3) images with low percentages of data dropouts, and 4) images that do not have enhanced line-to-line noise.

Prior to mosaicking, visual examination of every image is often included as an additional step. Data that are often excluded include images containing elevated line-to-line or white noise and excessive repeated dropouts, which render the blending of several images difficult, and images collected during periods of

high atmospheric dust where the overall contrast of the image is reduced. The highest quality images correspond to data with the warmest surfaces and lowest atmospheric opacity, although for qualitative, single-band mosaics, data with lower surface kinetic or brightness temperatures are often acceptable. Other instruments (both line scanner and frame imagers) have a similar set of numeric and visual selection criteria that will be applied to arrive at a high-quality image set for mosaicking.

2.3.2 THEMIS Global Mosaic Data Selection

Perhaps the most important aspect of the entire mosaicking process is the selection of high quality, well-calibrated data. During the THEMIS mapping mission, images were both systematically and priority targeted, potentially covering the same area on the planet many times over. Data were initially selected following the guidelines in section 2.3.1; however, when an area was imaged multiple times, the data with the highest visual quality were selected and other lower quality data were removed, reducing the probability of blending poorly registered data.

Equatorial and mid-latitude data from -60˚ N to 60˚ N were limited by a solar incidence angle < 85˚ for daytime and >95˚ for nighttime, ensuring that the sun was at least 5˚ above or below the horizon respectively. Additionally, only full-resolution (unsummed) data were used. Images where the time between the end of image acquisition and the collection of calibration data exceeds 150 seconds were omitted as a quality control measure, helping to ensure the usage of well-calibrated data. Longer times between the data collection and calibration

image acquisition translate into larger uncertainties due to focal plane temperature drift. Images with any oversaturated or undersaturated pixels identified in the initial image calibration (these pixels have DN values at the minimum or maximum of the 12-bit THEMIS instrument and are logged as the fraction of saturated pixels to the total number of pixels in the image) were also rejected as these pixels can introduce undesirable image artifacts, negatively influencing the overall image quality and visual appearance in the final mosaic product.

Only the daytime mosaic was constructed for latitudes poleward of 60˚ as nighttime surface temperatures are exceedingly low (e.g. <160 K) and instrument signal-to-noise is low at these temperatures. As the THEMIS global mosaics are designed to maximize coverage and not minimize seasonal effects, no restriction on season was placed on daytime images poleward of 60˚ latitude. Seasonal effects in daytime data could cause significant temperature variations between images; however, these variations are most obvious in nighttime temperatures. Constructing a daytime mosaic that incorporates all seasons is a reasonable task for the mid- to upper-latitudes [e.g. *Bandfield*, 2007; *Bandfield and Feldman*, 2008]. Near the Martian poles, the presence or absence of seasonal ice and clouds is another issue that must be addressed [e.g. *Kieffer et al.*, 2000; *Kieffer and Titus*, 2001; *Piqueux et al.*, 2003; *Piqueux et al.*, 2008]. Polar features are highly variable and can change on a daily basis. No attempt, other than removing images with large areas of seasonal CO_2 ice, has been made to eliminate seasonal variations; therefore polar regions (as with the rest of the global mosaics) are a combination of data from a variety of seasons and conditions. Without the use of

the image processing techniques discussed in this paper, I would be unable to create seamless global-scale mosaics composed of tens of thousands of images, which are acquired at different seasons and times of day.

2.3.3 Standard THEMIS Processing

THEMIS data are provided as Reduced Data Records (RDR) through the Planetary Data System (PDS, http://pds.nasa.gov), which are radiometrically calibrated radiance data derived from the THEMIS Experimental Data Record (EDR) [*Christensen*, 2002, THEMIS calibration report, available at http://themis-data.mars.asu.edu/pds/calib/calib.pdf; *Christensen et al.*, 2004a]. Through the completion of the mosaicking process, images remain consistent to the PDS RDR calibrated radiance form, retaining all spectral bands, processing history, and data precision, as it provides the most flexibility to convert the data to other products (e.g. emissivity, stretched single- and multi-band images, surface temperature etc.) and quantitative data retained until the very last step where the mosaic is scaled for viewing. Some processes require pixel-to-pixel registration (e.g. band-dependent line- and row-correlated noise removal and random noise removal) provided by the THEMIS camera model using the ISIS software and all data products after an ISIS processing step are consistent with the ISIS format, again retaining all spectral bands, processing history, and data precision.

In order to display the data for viewing, several different methods must be taken to scale the data and maximize the desired features. These techniques range from single band histogram and linear stretches to multiple band principal component analysis and decorrelation stretches [e.g. *Gillespie et al.*, 1986].

Decorrelation stretches are the predominant technique that is utilized in this paper. In THEMIS data, decorrelation stretches maximize the compositional/spectral variation (which is related to the second and third principal components), while retaining much of the morphologic/temperature context (which is captured primarily in the first principal component). This type of stretch was chosen because it is extremely good at highlighting second and third order spectral variations, which is the main focus of the THEMIS data processing presented in this paper. Additionally, decorrelation stretches are used throughout this paper to provide a consistent means of viewing the effects of the different algorithms.

A flow chart illustrating the order, input, output, and changes to the data are shown in Figure 2.1. This figure also includes corresponding section numbers and information about the mosaicking procedure described below, as well as specific function names for both DaVinci and ISIS. Unless otherwise stated, all of the following algorithms and processes have been completed using the DaVinci software package.

The RDR data are first corrected for time-dependent focal plane temperature variations in the detector array which causes a ±1DN offset at scales of ~50-200 line in the image [*Bandfield et al.*, 2004b]. Additionally, the image is corrected for lower frequency temperature drift (±10 DN on the dayside and ±5 DN on the night side), which is related to the constantly changing position of the instrument relative to the Sun and the temperature of the observed target. These offsets are determined using the THEMIS atmospheric channel (band 10), with

the assumption that the atmosphere does not have high frequency temperature variations [*Bandfield et al.*, 2004b].

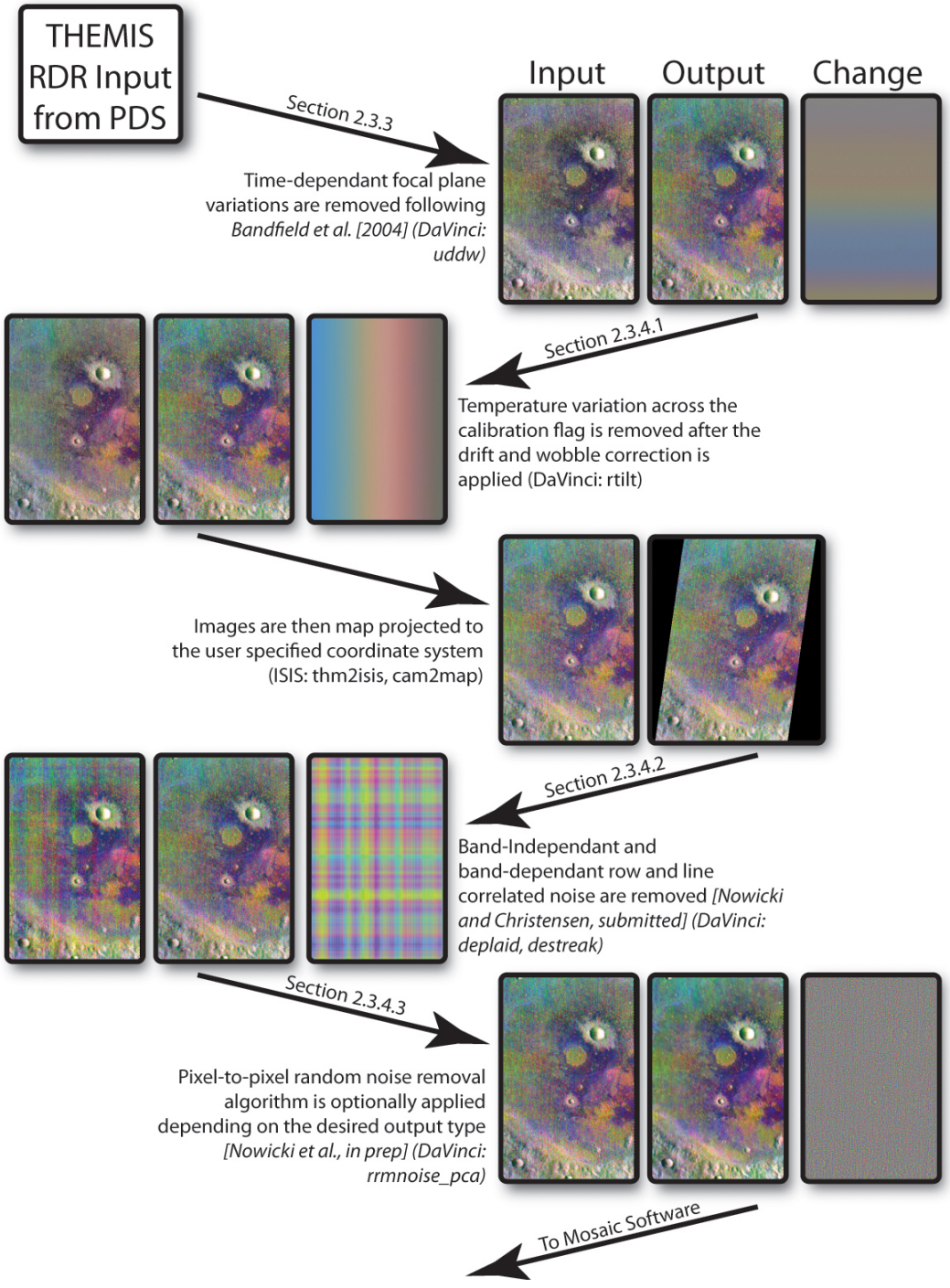

Figure 2.1. This set of flow charts details the processing steps that are taken to process both THEMIS data and qualitative/quantitative mosaics.

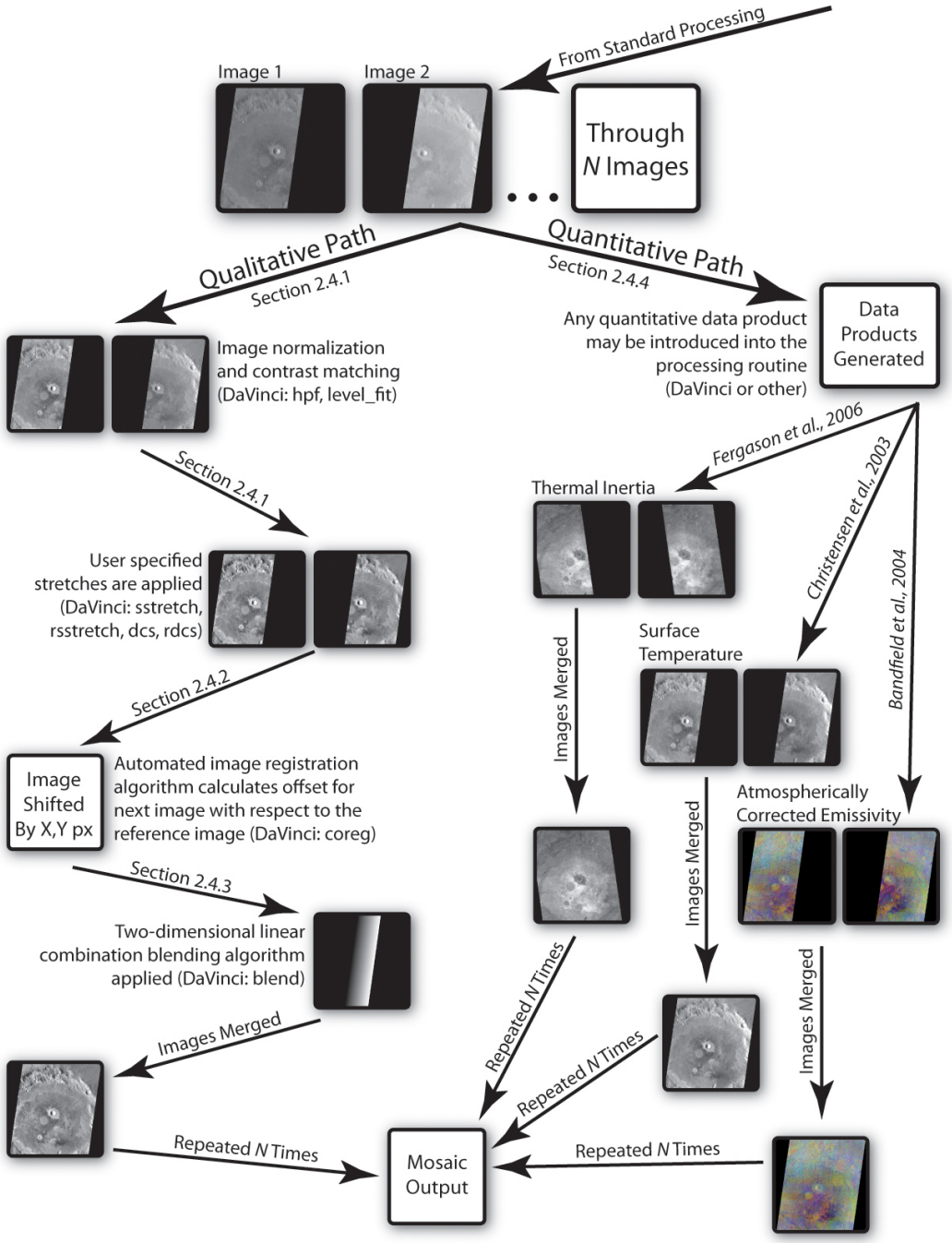

Figure 2.1. continued For each processing step a reference to the corresponding section in the text is provided on the arrow, as well as a short description of the step, the software package used (DaVinci or ISIS) and the function name that completes the task adjacent to the image set. **A)** THEMIS standard processing

Figure 2.1. continued

flow chart illustrating the typical steps used to process THEMIS data into the form commonly used to mosaic these data. THEMIS data are ingested at the RDR state from the Planetary Data System (PDS) archive and then follow the arrows in the diagram through the various processing stages. Each of these stages (except for the map projection) is optional and may be excluded depending on the final processing state required. Three images are shown where the leftmost is the input image, the center is the output data from the algorithm, and the rightmost image is the difference between the two. Each set of three images has been stretched using a decorrelation stretch with the same statistics so a direct comparison can be made between the image set. **B)** The standard mosaic processing flow chart illustrates the two-path (qualitative and quantitative) nature of the software. If the desired end result is qualitative then processing steps that disrupt the calibration of the data are taken to provide a visually appealing mosaic. However, if the desired end result is quantitative, then no normalization steps are taken, preserving the nature of the input data. Three sample data types (Thermal Inertia, Emissivity, and Surface Temperature) are shown along with the associated papers [*Christensen et al.*, 2003b; *Bandfield et al.*, 2004b; *Fergason et al.*, 2006a] that describe the techniques required to process the input data to these stages. Any number of additional data types may be created here and will follow the same path as the quantitative products.

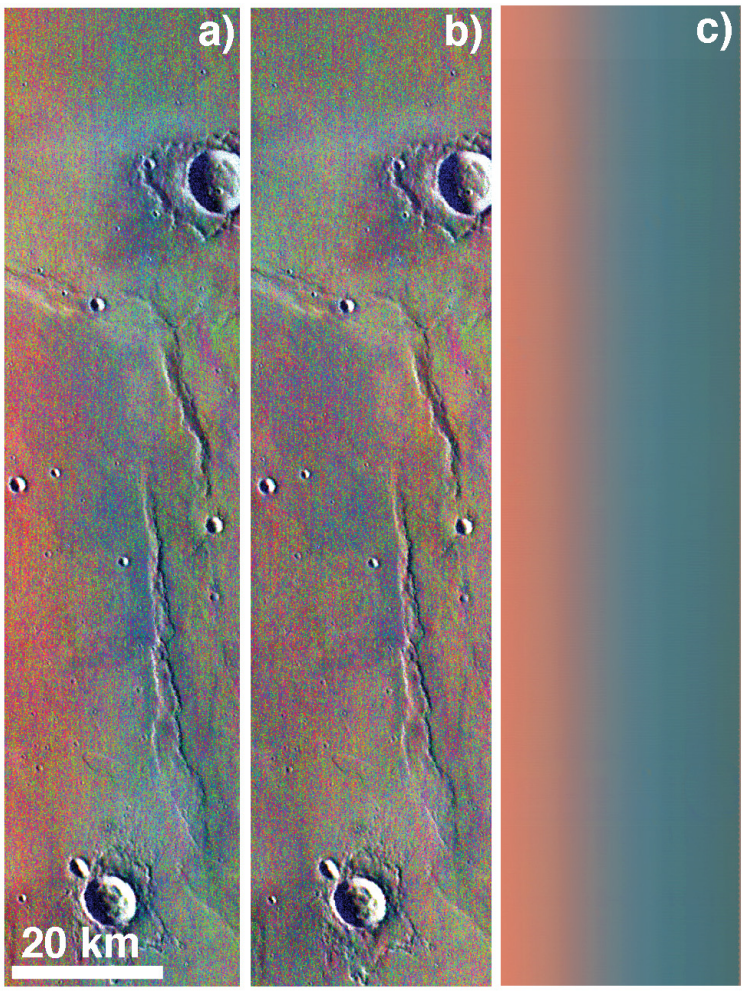

Figure 2.2. These images are decorrelation stretches of the same THEMIS image (I26686040, bands 9, 6, and 4) **A)** The original THEMIS image before the tilt removal algorithm has been applied. Tilt is manifested as a red to blue to green shift (from left to right) in this case. **B)** The same image that has undergone the tilt removal process, which has removed the left to right color variation. **C)** The difference of the radiance between the images from Figure 2.2a, b where the data have been decorrelation stretched using the same stretch as the image in Figure 2.2b. This illustrates what has been removed from the uncorrected data to produce the corrected data.

2.3.4 Advanced THEMIS Data Processing

2.3.4.1 Temperature Variation Across the Calibration Flag Correction

Following the removal of time-dependent focal plane temperature variations and the low frequency temperature drift, a temperature variation across the calibration flag is removed. This effect creates an apparent cross-track slope in the temperature image. The amplitude of slope is typically small (<1 K), but can cause difficulty in making seamless mosaics; the temperature gradient across the image results in artificially bright regions in one image being abutted to artificially dark regions in its neighbor. As is nearly always the case, the temperature variation across the calibration flag is consistent in its slope (e.g. always negative, or left to right in an image). A calibration flag is the primary means by which THEMIS data are converted from raw data numbers to calibrated radiance. The calibration flag is a known temperature that is imaged by the microbolometer array after every image acquisition and provides a single point to relate back to the THEMIS instrument response function lookup table. The temperature variation across the calibration flag is variable, but not independent for each band, as the bands are not acquired simultaneously while observing the same position on the planet (or in this case calibration flag). The variation is also visible in decorrelation stretch images where it shows up as a color variation (e.g. red to blue tones, green to blue tones) from the left side of the image to the right side of the image (Figure 2.2a, 2.2c) depending on the selection of bands. Figure 2.3 illustrates the absolute temperature difference for two bands before and after

the calibration flag temperature variation removal algorithm is applied. The observed difference in slope between bands 4 and 9 is the cause of the color variation observed in the decorrelation stretch images in Figure 2.2.

In addition to varying across the image, the temperature variation is not constant throughout the duration of the image, implying that some residual time-dependent parameter is not being completely removed and may be related to another instrument component. In order to correct for these variations, I average all the columns of the image in 4000 line segments and convolve this average with a filter comparable to the width of the image (e.g. 320 samples), which is then subtracted with the overall average value of the section added back. I allow for 2000 lines of overlap between sections to ensure that the time-dependent parameter is removed and then perform a linear ramp over the overlapping region to ensure that a smooth transition from section to section is achieved. This processes is called a "running" or windowed process, as it operates upon independent but multiply redundant sections of the image simultaneously and linearly combines overlapping pieces with fractions of the data ranging from 0 to 1 (depending on their position) and relative contributions to create the final output. In this case, the algorithm is only applied in one direction (along track), but for other processes the running algorithm may be applied in two or three dimensions with differing amounts of overlap.

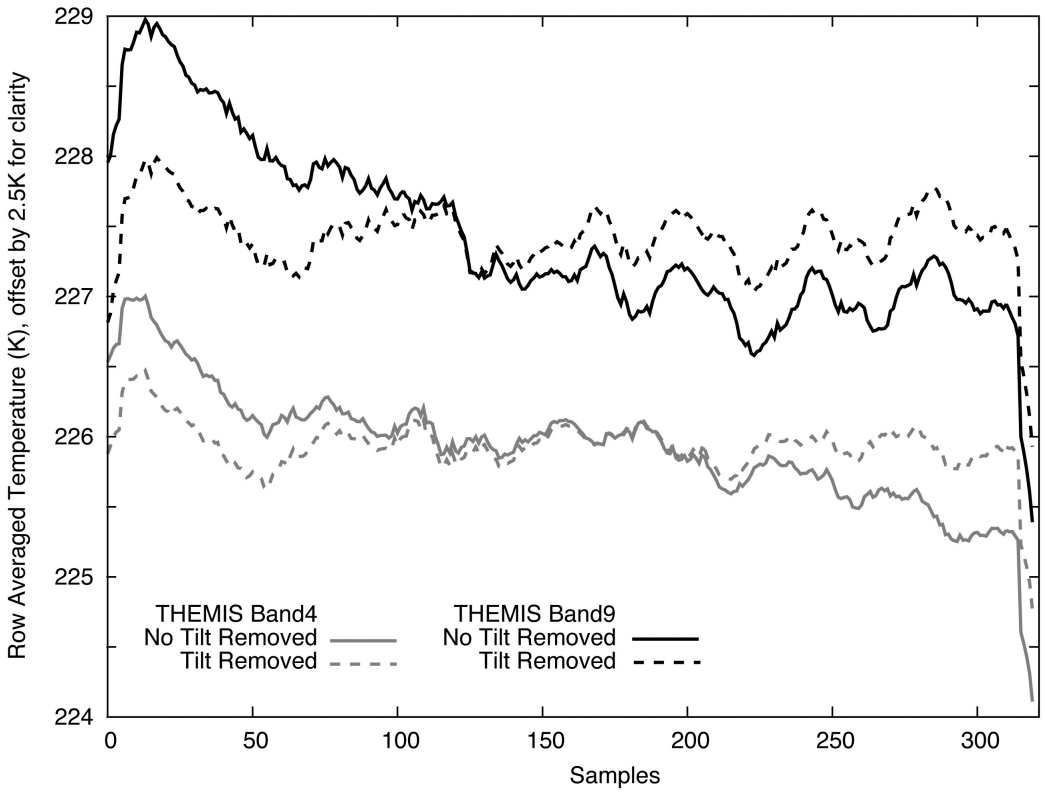

Figure 2.3. Row averaged temperature plotted for a relatively long THEMIS image (I26686040, >10000 lines) illustrates the effect of tilt. The solid lines are the original data and the dashed lines have had the tilt removal algorithm applied. At most the temperature difference between the solid and dashed lines is ~±1 K and the tilt is interpreted to be the slope from left to right (in this specific instance). The dashed line has been normalized for this slope, while retaining the spatial information. The offset between bands 4 and 9 is artificial, for clarity; however, the difference in slopes between the bands is real.

2.3.4.2 Band-Independent and Band-Dependent Row and Line Correlated Noise Removal

The corrected data are then map projected using the ISIS software, which utilizes a camera model to accurately describe the mapping of detector pixels to the surface of Mars. Once the bands are spatially registered, a form of row- and column-correlated band-independent noise, also known as "plaid", is apparent in decorrelation stretch and single band nighttime images. This form of row- and column-correlated noise is primarily a spectral contribution (e.g. varying for each band) and is identified by abnormally high or low row- or column-average values in one spectral band but not any of the other spectral bands. This effect was first noted by Bandfield *et al.* [2004b] and the correction algorithm and cause of the plaid is described in detail by *Nowicki and Christensen* [in prep]. The row-correlated component of plaid is residual electronic noise that is mapped into the RDR during the read-out of the array and consequent transfer to the spacecraft memory buffer. The column-correlated component of the plaid is caused by variations across the detector that are not adequately removed by the instrument response function. These artifacts are typically at the level of ± 1 DN and are only evident in decorrelation stretch images or other extreme processing approaches such as image ratioing or principal components analysis that emphasize small differences between spectral bands. However similar artifacts may become increasingly evident with lower signal to noise (SNR) data, as is the case with a significant portion of nighttime infrared images and in instruments with a lower SNR than THEMIS.

2.3.4.3 Random Noise Removal

In decorrelation stretch images, pixel-to-pixel white noise can be significant, obfuscating surface features and the interpretation of false color images. Spectral differences between adjacent pixels are maximized by the decorrelation stretch and can often account for a large fraction of the spectral variability in a scene (Figure 2.4a and 2.4c). I use a white noise removal algorithm to reduce the random pixel-to-pixel noise and accentuate the underlying surface spectral variation in the component images of mosaics (Figure 2.4b and 2.4d).

In this algorithm, each band of THEMIS radiance is converted into a percentage of the total signal. The total signal is the integral of all of the radiances in all of the surface sensitive bands. To convert each band into a percentage of the total signal, I divide the radiance of each band by the total signal, yielding a fractional contribution image with values ranging from 0 to 1. Each band of the fractional contribution image is then typically convolved with a 7x7 pixel boxcar filter and then multiplied by the total signal image to regain original radiance units. The assumption behind the algorithm is that no two adjacent pixels in any band should contribute a significantly large difference in the percentage of the total signal. This assumption breaks down at bright and dark (or hot and cold) boundaries where artificially high or low radiance values are imparted in the data by the convolution. The difference between the original radiance and the newly filtered radiance is largely composed of random noise, plus the artificially elevated or lowered boundary data. The difference image is

then converted to a principle component image, of which the first principle component is the correlated boundary data. The first principle component is removed and the image is converted back into radiance units, resulting in an image with only randomly distributed noise. The randomly distributed noise is subtracted from the original radiance image to obtain the noise-free radiance data. To obtain high correlation values in the principle component image, this entire operation is calculated for every 1001 by 1001 pixel segment of an image in the same manner as the running stretches described in section 2.4.1.

Figure 2.5 illustrates the absolute radiance difference between the corrected and uncorrected data for several THEMIS bands. The maximum correction in this case corresponds to ~$1x10^{-5}$ W cm^{-2} μm^{-1} sr^{-1} with an average correction of -$1.6x10^{-12}$ ±$1.4x10^{-6}$ W cm^{-2} μm^{-1} sr^{-1}. Outside the case of decorrelation stretches, the alterations to the data from this algorithm are undetectable and functionally insignificant. For a more detailed discussion of this algorithm and the errors associated with its use, see *Nowicki et al.* [in prep].

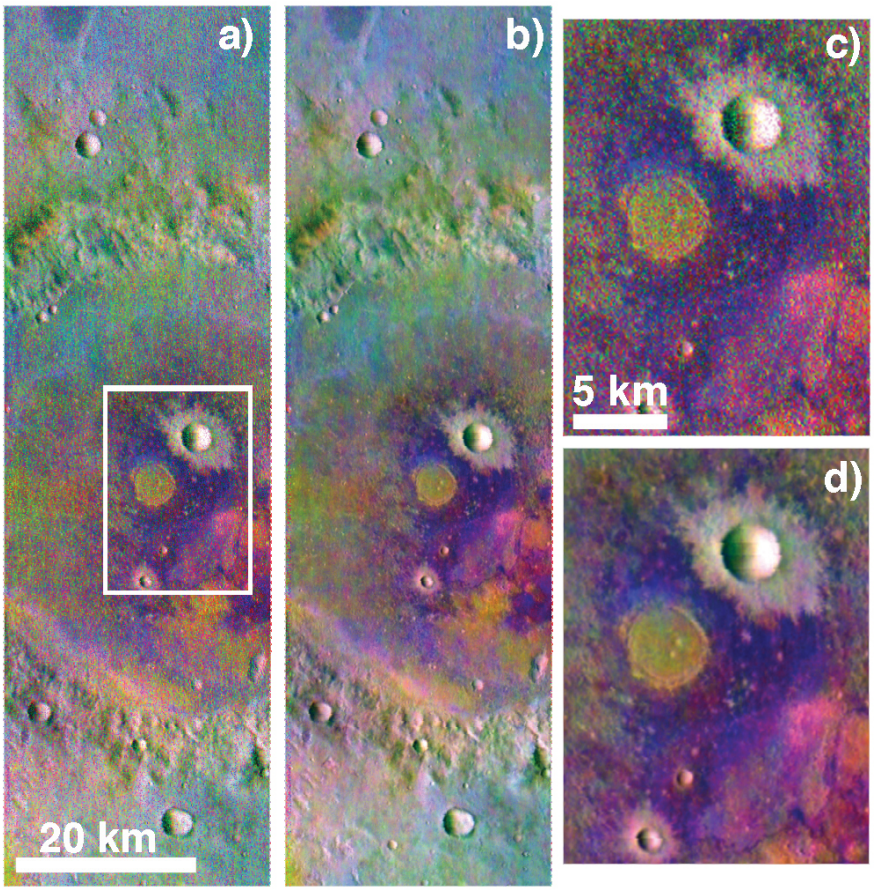

Figure 2.4. A) The original THEMIS data (I25647004) decorrelation stretched with THEMIS bands 8, 7, and 5 illustrates the white noise that is the focus of this example. The white noise in this data is characterized by multicolored speckles distributed randomly throughout the image. **B)** The same image data with the white noise removal algorithm applied exhibits much less of the speckled texture that was observed in the companion image. Additionally, features that are not visible in the original data are easily observed in this new image, as the amount of random or white noise has been significantly reduced. **C)** A subsection of the image in a) illustrating the level of the white noise **D)** A subsection of the image in b) illustrating the effect of the noise removal algorithm.

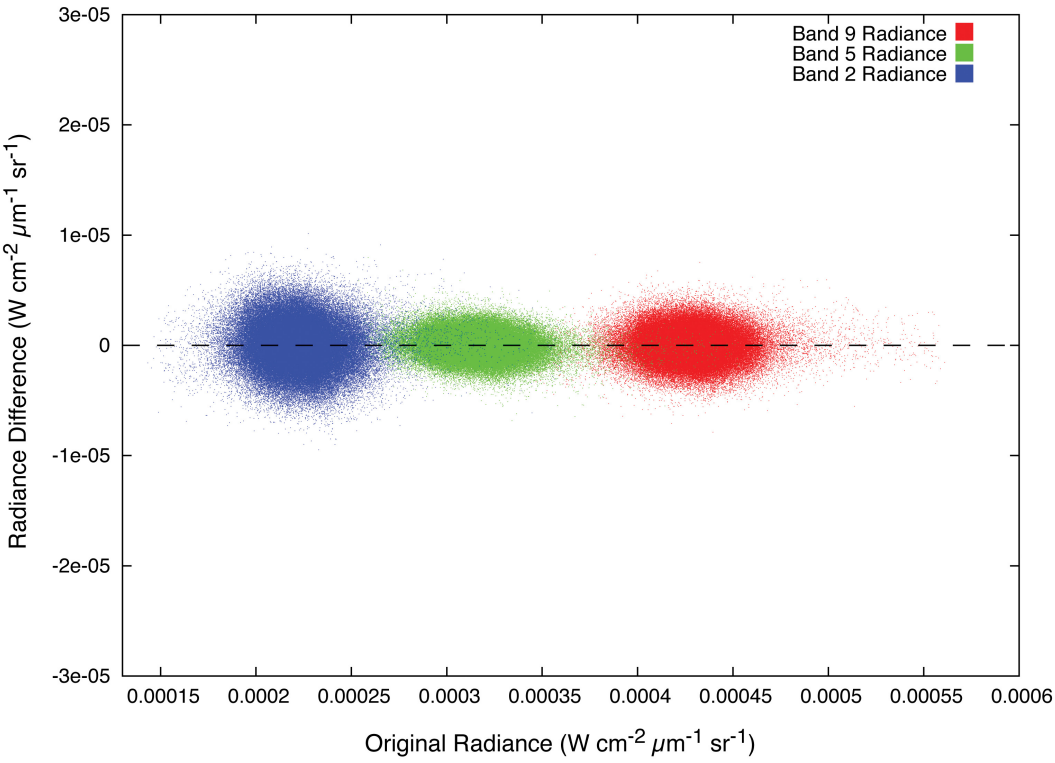

Figure 2.5. THEMIS image (I25647004) band 2 (blue), 5 (green), and 9 (red) uncorrected radiance plotted versus the difference between white noise corrected and uncorrected radiance for the corresponding bands. In this case, every pixel in a THEMIS image with the white noise removal algorithm applied is subtracted from the corresponding pixel in the original data. This allows for a direct comparison of the effectiveness and scale of the correction. If no correction was applied, the data would follow the horizontal axis. The spread in the data is roughly the same for each band with the maximum correction corresponding to ~ $\pm 1 \times 10^{-5}$ W cm^{-2} μm^{-1} sr^{-1} and an average correction of $-1.6 \times 10^{-12} \pm 1.4 \times 10^{-6}$ W cm^{-2} μm^{-1} sr^{-1}.

2.4 Mosaicking Algorithms and Procedure

The DaVinci software package provides the ability to load ISIS data cubes (among a variety of other file formats) into a manageable format and extract the required information for mosaicking, including mapping parameters such as the coordinate system, the line and sample projection offset, resolution/map scale, image width and height, etc. as well as quantitative spectral and temperature data. If a single band mosaic is desired, then a single band is extracted from the ISIS data cube. At the wavelengths covered by THEMIS band 9, surface emissivity is high (~0.90), atmospheric opacity is low, and the surface-atmosphere temperature contrast is high, making this the most common THEMIS band utilized in the mosaicking process as it has the highest signal to noise ratio for both daytime and nighttime data.

Once the data are ingested and the bounds for the mosaic have been set, either by the maximum extent of the images used or a user defined latitude/longitude range, the appropriate line projection offset and sample projection offset are used to place the data into the context of the mosaic region for the given projection. Figure 2.1b illustrates the typical order and results of the mosaicking algorithms described below. Two paths are shown, where one is the path taken for a qualitative product while the other path is taken for a quantitative end result. The algorithms used to create the quantitative data products are not discussed here in detail as they vary significantly between the data being derived and the science objectives [e.g. *Christensen et al.*, 2003b; *Bandfield et al.*, 2004b; *Fergason et al.*, 2006a].

2.4.1 Running Stretches

After the initial image position in the mosaic region has been determined, several additional processing steps occur to ensure that the final mosaic is seamless. As THEMIS infrared images are commonly 10 to 20 times longer than they are wide and the 2001 Mars Odyssey is in polar orbit, images cover large ranges of latitude (often > 15˚), where surface temperatures may vary significantly. Several processes are performed on the data to normalize for the temperature difference.

First, a large (often > 1001 by 1001 pixels) high pass filter can be applied to the data to remove the low frequency change in surface temperature, caused by the differences in acquisition latitude. Additionally, similar to the temperature variation across the calibration flag correction algorithm, a running histogram or decorrelation stretch can also be preformed to maximize the local variation in the scene. For THEMIS, these stretches are typically done on ~1000 by 1000 line sections in two dimensions with 50% overlap of each section as this provides the best image-to-image normalization for long images. An example of the small-scale detail that is enhanced with this method is shown in Figure 2.6 where running histogram stretch was applied to the data. In cases where the final product is not intended to preserve a physical quantity such as temperature, the data are stretched prior to being inserted into the final mosaic region, yielding better contrast-matched mosaics.

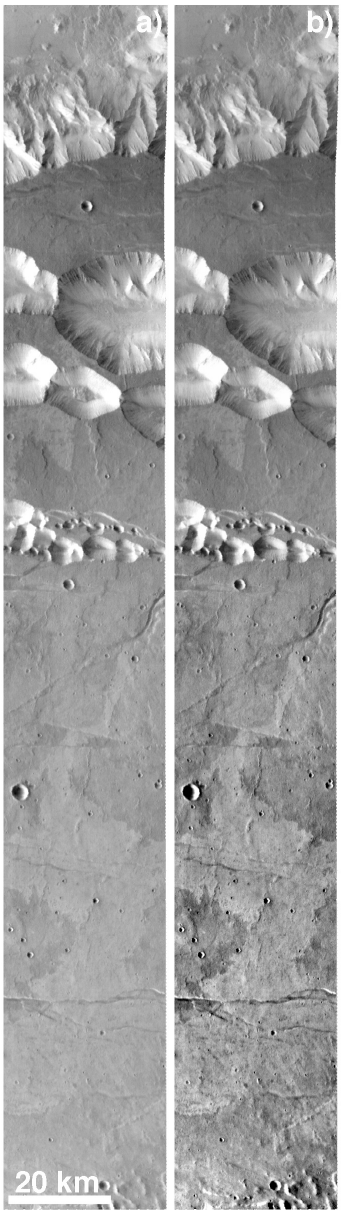

Figure 2.6. Two different stretches of the same THEMIS image (106568023, band 9 radiance) presented side by side, illustrating the advantage of a running histogram stretch. An image of Valles Marineris was chosen to highlight the strengths of the running histogram stretch. Similar advantages are observed with running decorrelation stretches. **B)** A standard histogram stretch of a THEMIS image, where some saturated and undersaturated locations are present in the

Figure 2.6. continued

canyon and craters walls. Additionally, the plains have low contrast, as the statistics for the entire scene are being dominated by warm and cold locations in the canyon walls. **B)** A running histogram stretch of the same image. In this case, the canyon walls are less saturated than in the standard case. However, the most significant differences are observed in the plains, where details that were not visible previously are now easily observed. However, the data values associated with this stretch are relative to one another over the window size of the algorithm, whereas in the standard histogram stretch case all the values in the entire image are relative to each other. For example, the stretched values of pixels containing the same calibrated radiance values may not be mapped to the same stretched value, or pixels with significantly different radiance values may end up with similar stretched values.

2.4.2 Automated Image Registration

An automated image registration algorithm can applied to correct for potential location inaccuracies due to uncertainties in the timing of the start of the image or spacecraft pointing. In THEMIS data this uncertainty results in a ±2 pixel (200 m) error in absolute position on the surface of Mars in the along track direction. There may also be absolute errors in cross-track position, which for THEMIS are typically <1 pixel (100 m) that is related to the inaccuracies in the derived spacecraft position and pointing. In the case of THEMIS data, only one offset is stored for each image and individual bands of an image are not shifted independently, as the THEMIS camera model in ISIS aligns the individual bands to <0.1 pixel.

Spacecraft pointing errors are typically small for THEMIS infrared and visible data; however, for older datasets where the position and pointing of the spacecraft was not as well known, (e.g. Viking), the offsets due to pointing errors can be significant, often greater than several kilometers (e.g. 100s of pixels). For this algorithm to be applied, a reference image or image location must be chosen, from which to base all subsequent positioning of images. For consistency, the images are typically sorted from west to east, but may also be sorted by maximum overlap. The auto-registration algorithm is a two-dimensional difference minimization technique, where a random sampling of pixels in the original overlapping image pairs are taken and a search radius of R number of pixels are compared to the sum of the difference of the values of the two images. The process is repeated until the algorithm arrives at the local minimum value of the

solution space. Implementation of a random sampling technique and the auto registration algorithm is applied twice to ensure that the minimum reached ensuring that the first solution is in fact the true minimum and not a local minimum. It is possible to perform an exhaustive search of the overlapping region, where every pixel is compared to every other pixel in the search radius, but these operations are computationally costly, especially when this process must be completed for each overlapping image (up to several thousand times). Experience has shown that the random technique produces a comparable result to an exhaustive search.

2.4.3 Image to Image Blending

As a final step the data are blended using a two dimensional linear combination ramp of the overlapping regions to insert the new image into the mosaic and is stretched as the last step just prior to insertion into the final region. This blending algorithm does not blend all images at once; rather each subsequent image is blended into the final output image and the resultant image can be the average of many images. However, this algorithm will favor the most recently added image, as the overlapping sections are only a weighted average of what exists in the destination image (which could be many previously averaged images) and the newly inserted image. In summary, for qualitative data products, the best results are typically achieved when a large high pass filter is applied to remove the low frequency change in surface temperature, followed by the stretching of individual images (either by a running or standard stretch type), and

then a multi-directional blend of adjacent images, which are inserted into the final mosaic scene.

2.4.4 Quantitative Mosaics

Data normalization steps such as non-linear stretches and running stretches (Section 2.4.1), high-pass filters (Section 2.4.1), and random noise removal (Section 2.3.4.3) remove the quantitative aspect of data and should be excluded in the creation of quantitative mosaics (Figure 2.1b). However, other empirical data corrections such as the removal of the temperature variation across the calibration flag (Section 2.3.4.1) and the removal of band-dependent and band-independent line- and row-correlated noise (Section 2.3.4.2) result in data that have values that more closely represent actual conditions and are less effected by instrumental artifacts, making them desirable corrections to produce accurate and well calibrated data. When creating a quantitative mosaic, the use of additional algorithms to compute the desired value (e.g. thermal inertia [*Fergason et al.*, 2006a] or emissivity [*Christensen et al.*, 2003b]) commonly have the effect of normalizing data in a quantitative manner. When these types of processes can be applied, they are preferred over the less well-characterized data normalization algorithms presented in this work. Figure 2.1b illustrates the two-path approach (qualitative on the left and quantitative on the right) that is taken by the mosaic software where three sample data types (emissivity [*Christensen et al.*, 2003b], surface temperature [*Bandfield et al.*, 2004b], and thermal inertia [*Fergason et al.*, 2006a]) are shown. While these three data examples are specific to THEMIS, it is possible to derive any desired data products such as mineral maps or albedo by

following the same procedures, creating a high quality quantitative regional or global data product.

2.5 Effects of Image Manipulation Algorithms

Documenting the effects of image manipulation algorithms on quantitative data (i.e. THEMIS radiance data) is an important aspect of algorithm development. In order to assess the validity of the techniques described above, the potential error and corrections they introduce into the final data must be addressed. In this manuscript, I do not attempt to provide an exhaustive error analysis for each of the techniques described previously, but rather I attempt to incorporate reasonable errors and contributions for each technique and view them through the perspective of the mosaic process. Additionally, for nearly all the algorithms discussed in this manuscript a detailed error analysis has been reported in other technical publications that document the algorithms and their effects in detail [e.g. *Bandfield et al.*, 2004b; *Christensen et al.*, 2004a; *Nowicki and Christensen*, in prep; *Nowicki et al.*, in prep].

2.5.1 Temperature Variation across the Calibration Flag Correction

As the temperature variation across the calibration flag correction is purely empirical and the subtraction from the image is related solely to image derived parameters that have no corresponding physical measurements, this process should typically only be performed on data where the end product will not be used for spectral analysis. However, this technique further reduces instrument noise, making qualitative spectral variation in decorrelation stretch images significantly

more apparent. The temperature differences removed by this technique (e.g. 1-2 K, Figure 2.3) are small enough that it can be safely used if the goal is only derived brightness temperature and not emissivity. The temperature differences are within the predicted temperature error associated with THEMIS images [*Christensen et al.*, 2004a]. Subsequently, the atmospheric correction [*Bandfield et al.*, 2004b] applies a similar technique (e.g. removing a temperature difference based on image derived parameters); however, this atmospheric correction is rooted in the assumption that THEMIS atmospheric band (~14.88 μm) is not correlated with the surface and the temperature differences calculated from that band are then applied to every other band of the image. This is not the case with the temperature variation across the calibration flag correction algorithm, which is why an extremely large filter (4000 lines) is used to correct the data for each band. If a semi-linear feature is present running parallel to the direction of image acquisition (e.g. a large scarp), it is possible that this technique could induce artifacts (in the form of brightness smearing) into the original data. The likelihood of this is extremely small and occurs infrequently (<<0.1% of all images); the potential for artifacts to occur is largely outweighed by the benefits associated with the algorithm.

2.5.2 Random Noise Removal

The details of the white noise removal algorithm have been documented by *Nowicki et al.* [in prep] and show that the effect of this algorithm on the order of < ±1 DN for an individual pixel, though this varies from image to image. Additionally the difference in radiance between any one pixel in the original data

and data that have had the white noise removal algorithm applied is typically << $5x10^{-6}$ W cm^{-2} μm^{-1} sr^{-1} (Figure 2.5) though in the most extreme cases can be as much as $1x10^{-5}$ W cm^{-2} μm^{-1} sr^{-1}. In this maximum case, this radiance corresponds to a temperature uncertainty of ~1.1 K at typical daytime temperatures of 275K. For the former case, the temperature uncertainty is much less, corresponding to ~0.01K at 275 K. The largest of these value differences are always associated with pixels constituting strong thermal boundaries and are easily located and ignored in qualitative and quantitative analyses. From a perspective of a global or regional mosaic product, the final contributions of this algorithm are minimal, as mosaics are typically made from a single band and are displayed as grayscale and not as multi-band decorrelation stretch mosaics, where white noise is most evident. Additionally, if overlap between images is present, white noise is further reduced as data are averaged (often several times) in the overlapping regions.

2.5.3 Image Registration and Image Geometry

Image registration is the process that locates images from one dataset to other images from the same dataset and to additional datasets. Several methods exist for generating well-controlled mosaics and are referred to as controlled (externally referenced mosaics, e.g. through bundle adjustment) and semi-controlled (internally referenced mosaics, e.g. through pixel shifting one image to match another). Completely uncontrolled mosaics result from only a priori information about the camera and spacecraft position, pointing, and camera model.

The absolute accuracy of the camera pointing for THEMIS data is sufficient (less than ±2 pixels or 200 m) to allow for the creation of high quality uncontrolled products. There are two main sources of image registration error associated with THEMIS: 1) the uncertainty in the timing of the detector readout as compared to the spacecraft clock count that is recorded for each image, and 2) inaccuracies in the spacecraft pointing/orbital position. Errors related to the timing of the detector readout occur only in the along-track direction and are responsible for approximately ±2 pixels of error. The error is assumed to be Gaussian, meaning that most errors will occur at the sub-pixel to one pixel level, and will thus be un-recognizable in the final mosaic. Errors related to the inaccuracy in the spacecraft pointing/orbital position occur in both the along-track and cross-track directions and are responsible for approximately ±1 pixel error. Since these errors are at the one pixel level, most misregistered images are difficult to identify.

The automatic registration algorithm described above is based off of a single reference image and is characterized as a semi-controlled method; its use can result in systematic offsets, causing the mosaic to be either larger or smaller than predicted. This method is considered semi-controlled because it results in images that are well registered to each other but no attempt has been made to register the data to another dataset; in a worst case, a ~1000 km THEMIS mosaic may be >4 km (0.4%) larger or smaller than the unregistered mosaic. This size difference results from small inaccuracies in the model that describes the instrument or camera and how images are mapped to the planet. These products

are generally well registered to themselves but not necessarily to the surface of the planet. The probability of a single image being misregistered to a large (>1000 images) scene is small (~1-2%) and in this case nearly all misregistrations are at the 1 to 2 pixel level, though it is often difficult to determine registration at a single pixel level by eye.

Controlled mosaics have the highest level of absolute pixel accuracy on the planet's surface that can be achieved. The procedure for generating a controlled mosaic is difficult and I make no attempt to generate these types of data products using DaVinci; however, ISIS has some methods by which these types of data products can be generated. An established technique and one that ISIS supports is called bundle adjustment [*Triggs et al.*, 2000; *Kirk et al.*, 2006]. In this type of process, images are tied via reference points to both each other and other datasets such as Mars Orbiter Laser Altimeter (MOLA) [*Smith et al.*, 2001]. This process requires the generation of control tie points that represent the same physical place on the planet in both the unreferenced image and the reference dataset such as MOLA. Once these locations are established through careful hand examination, the bundle adjustment is performed to generate new camera and spacecraft pointing and positional information. This updated information is used in the map projection step to accurately locate the image to the planet's surface, requiring no further image adjustment or warping after the initial projection.

2.5.4 THEMIS Global Mosaic Registration

For the construction of the THEMIS daytime and nighttime global mosaics, I have elected to forego the use of any image registration algorithm and

the mosaics should be considered geographically uncontrolled products. The only information used to project the images on the planet comes from the spacecraft and planet position during image acquisition and the THEMIS camera model. For this study, the data have been dead reckoned, meaning that no offset or warping has been applied to the data other than what is predicted by the initial map projection. By choosing to dead reckon these data, I have foregone the difficult task of tie pointing, relating mosaics to reference locations on the surface, and a bundle adjustment of all images. This task is difficult with THEMIS data for several reasons including: 1) the narrow width and large length of the images, 2) difficulty in automatically identifying suitable tie pointing features, and 3) the number of images required to construct the mosaics (> 20,000 individual images for the daytime mosaic, and 18,000 individual images for the nighttime mosaic).

These mosaics are not cartographically controlled but are likely accurate to less than ±2 100 m THEMIS pixels on the surface of Mars. This error results from the uncertainty in the timing of the detector readout as compared to the spacecraft clock and inaccuracies in the spacecraft pointing/orbital position. No attempt to correct for these errors has been made and the only information placing the image at the surface location is derived from the spacecraft pointing relative to the planet and the THEMIS camera model. However, poorly registered data or data that reduced the overall quality of the mosaic were removed to produce a high quality product. In practice, very few images (< 200 in each global mosaic) were removed due to the above mentioned errors, indicating that these types of errors occur infrequently at levels >1 pixel. Images were removed by visual

inspection only when they affected the overall quality of the mosaic, with an end result of high quality mosaics with few and minor registration errors.

2.5.5 Running Stretches

Classifying the observable effects of running stretches qualitatively is straightforward and functionally results in increased local contrast and detail as compared to standard stretches. Figure 2.6 illustrates differences associated with a running histogram stretch and a standard histogram stretch. The overall contrast of the image in Figure 2.6 is no longer controlled by the large bright and dark areas in the scene associated with the valley walls. The difference associated with a running stretch in low contrast areas are often times >15% different from the original stretched values. However, the stretch applied is now not only scene dependent but also dependent on the scale of the features in the scene as related to the box size associated with the running stretch. It is most evident in Figure 2.6 where ~500 pixels from the edge of the canyon the contrast of the plains is still relatively low as compared to a scene with just the plains observed. This is a result of the bright and dark areas of the canyon walls dominating the stretch until they are not present in the scene being stretched. This artifact is important to note as it could possibly lead to the misinterpretation of geologic features in a given scene. As running stretches serve to normalize the scene locally, they also prove to be useful in creating large-scale mosaics. If the scene is not locally stretched and long images are included, features just outside of one image, but not another may result in badly mismatched stretches, making mosaicking and blending more difficult.

2.6 Results

2.6.1 Large Scale Seamless Mosaics

One of the main goals of the advanced THEMIS data processing is the ability to create large-scale (i.e. global) mosaics where no seams or individual images are visible. Processing tens of thousands of infrared images acquired at different local times, seasons, and years proves to be a difficult challenge as each of these parameters changes the characteristics of the acquired data. The algorithms described in the previous section, including such techniques as tilt and plaid removal, in addition to the use of running stretches allows the effect of these parameters to be minimized and provide the ability for contrast matching without intensive post-processing and contrast adjustment of the images subsequent to stretching.

In addition to creating large-scale seamless mosaics, this software provides the ability to selectively mosaic images of specified interests. An example of this has been illustrated by *Piqueux et al.* [2008], where a quantitative temperature mosaic of the south polar cap was constructed to map the composition of exposed ices (e.g. CO_2 and H_2O). In this case, images were limited by season and surface temperature in order to avoid times when the seasonal CO_2 cap was present.

2.6.2 Mosaicking Processes on Global-Scale THEMIS Data

The THEMIS daytime and nighttime infrared 100 m/pixel global mosaics (Figures 2.7a and 2.7b) are publicly available through the THEMIS website

(http://themis.asu.edu), as well as the Java Mission-planning and Analysis for Remote Sensing (JMARS) software package (http://jmars.asu.edu), and will be released to the Planetary Data System (PDS) as a value added product from the 2001 Mars Odyssey mission.

The mosaicking procedure described in this paper was also employed to create the THEMIS global mosaics, where the same algorithms were utilized following the same steps to process the THEMIS data into a visually appealing, qualitative mosaic. The main differences between the mosaicking of THEMIS global data and the generic procedure is the set of criteria that were used to create the THEMIS daytime and nighttime 100m/pixel global mosaics (Section 3.2). Additionally, every image was hand examined to ensure that it was artifact-free and that the location on the planet was relatively accurate (Section 2.5.4). This procedure, while eliminating potentially valid data, resulted in a mosaic with significantly higher overall quality than if poorly registered images or low quality data were left in the final product.

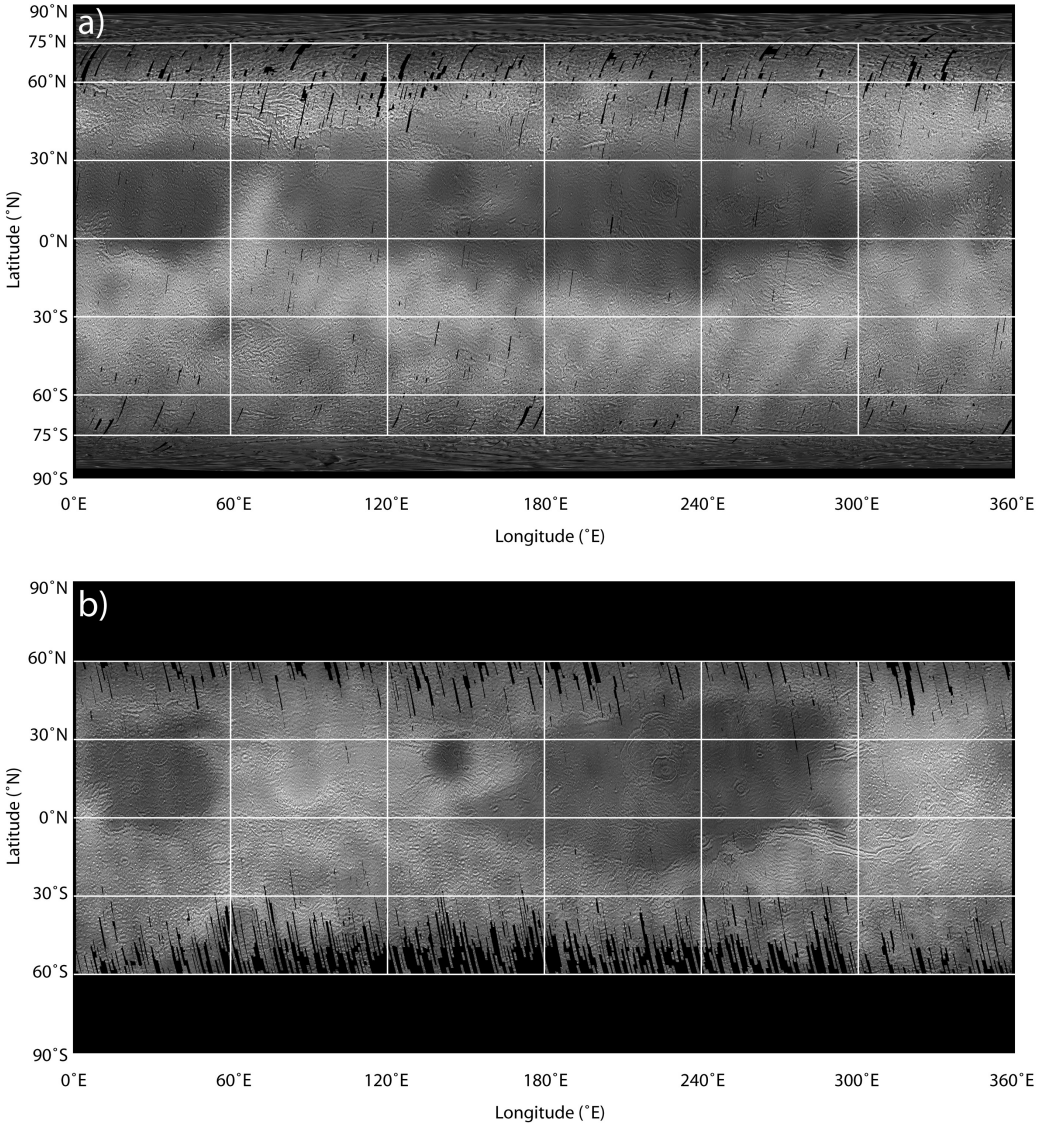

Figure 2.7. The THEMIS global **A)** daytime and **B)** nighttime mosaics shown in this figure are the combination of the high-frequency information (small-scale) and low-frequency information (large-scale) for viewing at this low-resolution in a simple cylindrical projection. Each box in this figure represents a tile that was individually processed for the construction of the THEMIS daytime and nighttime global mosaic. The equatorial tiles (60˚ N-60˚ S) are 30˚ latitude by 60˚ longitude

Figure 2.7. continued

with a 2˚ padding around each tile for blending purposes. The near-polar tiles (60˚ N-75˚ N and 60˚ S-75˚ S), which were only constructed for daytime data are 15˚ latitude by 60˚ longitude with a 2˚ padding as well. The two polar regions (poleward of 75˚), which were also only constructed for the daytime mosaics are 15˚ latitude by 360˚ longitude with 2˚ padding on the anti-poleward edge. These regions were constructed in a polar stereographic projection and have been re-projected to a simple cylindrical projection for this figure.

While registration errors may cause blurriness and reduce the overall visual appeal of the final product, they are not the only causes of blurriness. Seasonal variations at high latitudes (e.g. poleward of 60˚) must also be considered. Several studies [e.g. *Bandfield*, 2007; *Bandfield and Feldman*, 2008; *Kreslavsky et al.*, 2008; *Smith et al.*, 2009] indicate that high latitudes likely have large amounts of near surface water ice, which may cause both visual and thermophysical changes in the observed landscape. For instance, *Bandfield* [2007] illustrates through the use of two THEMIS images obtained at different solar longitudes, it is possible to measure and model temperature differences that are a direct result of sub-surface water ice. Dataset observation restrictions, image processing, and mosaicking techniques described in this paper help to minimize this temperature difference; however, temperature variations may occur at different rates throughout the scene depending on the proximity of the ice to the surface [e.g. *Bandfield*, 2007; *Bandfield and Feldman*, 2008] resulting in images that have differing physical properties being abutted directly next to one another.

Polar processes may also responsible for large observed changes. Many studies have focused on observed changes associated with the polar regions of Mars, both seasonally [e.g. *Leighton and Murray*, 1966; *Kieffer et al.*, 2000; *Kieffer and Titus*, 2001; *Bibring et al.*, 2005] and perennially [e.g. *Malin et al.*, 2001; *Byrne and Ingersoll*, 2003; *Thomas et al.*, 2005]. In these studies, seasonal changes where the polar cap extends and recedes throughout the year are clearly observed in the temperature data. In this dataset, I have minimized these effects through visual inspection to obtain high quality data of the surface and minimize

the amount of seasonal CO_2 ice present in the mosaic. Changes in the perennial cap have been interpreted through the observations of recession and growth of the various pitted terrain present (e.g. Swiss cheese terrain) [e.g. *Malin et al.*, 2001; *Byrne and Ingersoll*, 2003]. However, other examples where the polar cap has apparently grown over tens of years are given from differences observed in Mariner 9 to Viking data [*James et al.*, 1979] and in THEMIS data [*Piqueux and Christensen*, 2008]. These changes are typically small (often < 1 pixel) or occur over longer periods of time and are thus insignificant in the final mosaicked product.

Another consideration of these mosaicking techniques is the possibility that non-polar surface features may change. In general, two scales of change are typically observed from orbit, fine scale (meters to 10s of meters) where new deposits, new craters, and modified dunes are typically observed, [e.g. *Malin et al.*, 2006; *Bourke et al.*, 2008] and global scale changes (10s to 100s of kilometers), [e.g. *Christensen*, 1988; *Smith*, 2004; *Fenton et al.*, 2007] which are commonly observed as differences in albedo and thermal inertia. However, changes on the scale of hundreds of meters to kilometers are have not yet been observed. The daytime and nighttime THEMIS global mosaics provide excellent means to investigate the possibility of these changes. While this is not the specific goal of these data products, change may be observed as a blurry feature in the mosaics, where there is a difference in the surface observed in two overlapping images that were taken at different times. In many cases, overlapping areas may be separated by several (e.g. > 2) Mars years. A key to

recognizing this type of change is to distinguish it from poorly registered data. If an image is simply poorly registered, the entire overlapping area should be blurry as a result of the blending algorithm, but if surface features have changed over time, only a small region of the overlapping areas should be blurry. While change effects in mosaics are generally considered artifacts, the techniques described in this paper to normalize and register overlapping images of different times may be used to compare images prior to mosaicking and could be powerful way to search for surface feature changes.

A good application of detecting change would be to search for wind streak changes, where there might be growth or change in direction of the deposit or removal area. At this time I have not yet conclusively identified areas where change has been observed; this remains as a future research opportunity.

2.6.3 Mosaics from Other Instruments and Additional Datasets

This software has the ability to ingest and mosaic additional datasets including MOC Wide Angle, CTX, and Viking visible imager data, taking advantage of the advanced data processing techniques originally intended for THEMIS data. Additionally these techniques can be applied to other planetary datasets including the Advanced Spaceborne Thermal Emission and Reflection Radiometer (ASTER) [e.g. *Yamaguchi et al.*, 1998].

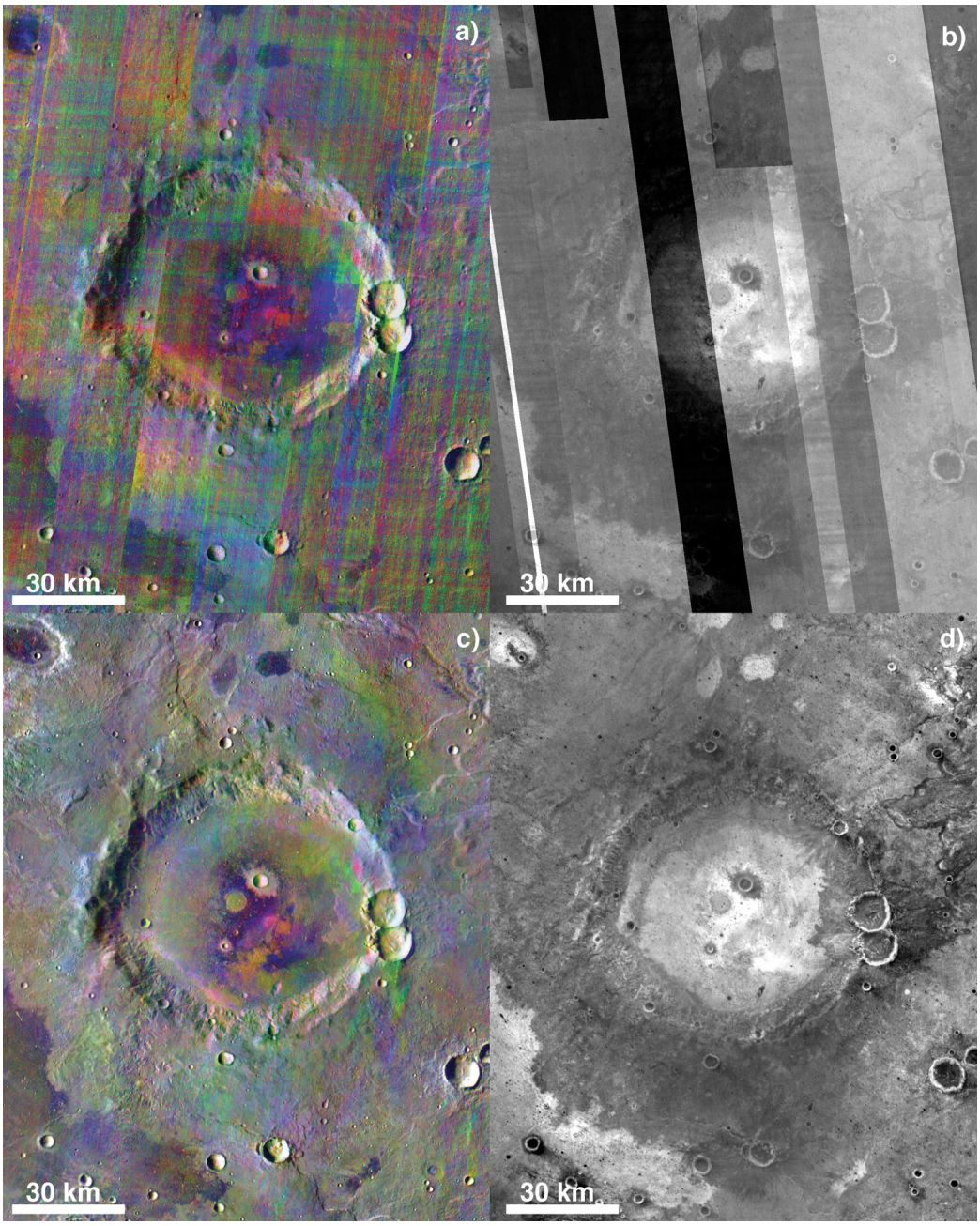

Figure 2.8. Before and after images illustrating the effects of algorithms and processing detailed in this paper. **A)** THEMIS decorrelation stretch mosaic of bands 8, 7, and 5 (centered at 53.25˚ E, 21.6˚ S) illustrating the compositional variation as viewed by THEMIS (15 images, 100 m/pixel, 1186 x 1482 pixels, ~1 minute execution time excluding image map projection). This band combination

Figure 2.8. continued

was chosen to highlight the presence of olivine, as there is an olivine absorption in THEMIS band 7. In this case, olivine-bearing materials are concentrated in the floor of the crater. **B)** THEMIS unprocessed nighttime temperature mosaic of the same area. **C)** THEMIS decorrelation stretch mosaic of the same area. The images in this mosaic have had many of the processes described in this paper applied. **D)** THEMIS nighttime temperature mosaic where the images have had many of the processes described in this paper applied. The combination of these two figures illustrates not only the compositional diversity of the area but also the nature of that material. For example, in this case the most olivine enriched materials correlate with the highest thermal inertia values (or warmest nighttime temperatures).

The area chosen is representative of a high thermal inertia crater floor [*Edwards et al.*, 2009], where material with a thermal inertia of >1200 J m^{-2} K^{-2} $s^{-1/2}$ was identified and has been interpreted as in-place bedrock. Additionally, the decorrelation stretch mosaic of this area demonstrates that this material exhibits the characteristic absorptions associated with olivine-bearing basalts. The use of these two datasets in combination provides the ability to not only establish the composition of the material in question, but also the physical characteristics of the material (e.g. sand sized particles or *in situ* rock). The use of these two types of data in combination can help reconstruct the geologic history of a region. For example, *Rogers et al.* [2005; 2009] have utilized this method to characterize the geologic history of several regions on Mars including Ares Vallis [*Rogers et al.*, 2005] and Mare Serpentis [*Rogers et al.*, 2009]. In these instances, compositional as well as thermophysical THEMIS data have been utilized extensively, and indicate that materials with the highest thermal inertia typically correspond to olivine enriched materials. Additional authors have also identified this trend [e.g. *Hamilton and Christensen*, 2005; *Bandfield and Rogers*, 2008; *Tornabene et al.*, 2008] observed not only in THEMIS but CRISM and OMEGA data as well.

2.6.3.1 THEMIS Decorrelation Stretch Mosaics

Here I demonstrate the use of this mosaic and processing software on several different datasets. In order to best demonstrate the techniques described for processing THEMIS data, two mosaics using a running decorrelation stretch radiance mosaic (Figures 2.8a and 2.8c) and a single band nighttime temperature mosaic (Figures 2.8b and 2.8d) were created. These two mosaics utilize every

algorithm described in the methods section. In addition to the fully processed data (Figures 2.8c and 2.8d), Figures 2.8a and 2.8b are mosaics of the same area and same data, where none of the algorithms described in this paper were applied.

2.6.3.2 MOC Wide Angle Global Data

MOC acquired a complete image of the planet nearly every Mars day (12 Mars Global Surveyor orbits). This data record extends for nearly 5 Mars years. Additionally, Mars Color Imager (MARCI) [*Malin et al.*, 2008] can be mosaicked in a similar manner, providing long term near continuous coverage of the entire surface of Mars. These data provide a unique view of the surface of Mars and can be used to examine active processes on Mars, such as cloud distributions, (e.g. orographic clouds surrounding volcanoes, low lying clouds filling Hellas basin and Valles Marineris and their respective timings), dust storm activity (e.g. views of the initiation location of dust storms), and additional parameters such as albedo changes related to the re-distribution of dust on the surface. This data complements other global data sets such as Thermal Emission Spectrometer (TES) [*Christensen et al.*, 1998; *Christensen et al.*, 2001] global albedo [e.g. *Smith et al.*, 2002; *Fenton and Mellon*, 2006] and thermal inertia maps [*Mellon et al.*, 2000; *Putzig et al.*, 2005; *Putzig and Mellon*, 2007]. Figure 2.9 is an example of a global MOC wide-angle map processed with the mosaic software. An empirical correction for the opposition photometric surge has been applied, though residual effects can still be observed as light toned streaks following the orbit track of Mars Global Surveyor. The photometric opposition surge described above has been observed in Viking data [e.g. *Thorpe*, 1978; *Thorpe*, 1979] and

has been modeled with physical parameters [e.g. *Hapke*, 1986; *Helfenstein and Shepard*, 1999; *Hapke*, 2002], though these models are complex and the application of these models to imagery often does not completely remove the effect [e.g. *Helfenstein et al.*, 1997; *Hapke et al.*, 1998]. This effect is often most easily corrected by an empirical flat field approach for non-quantitative products.

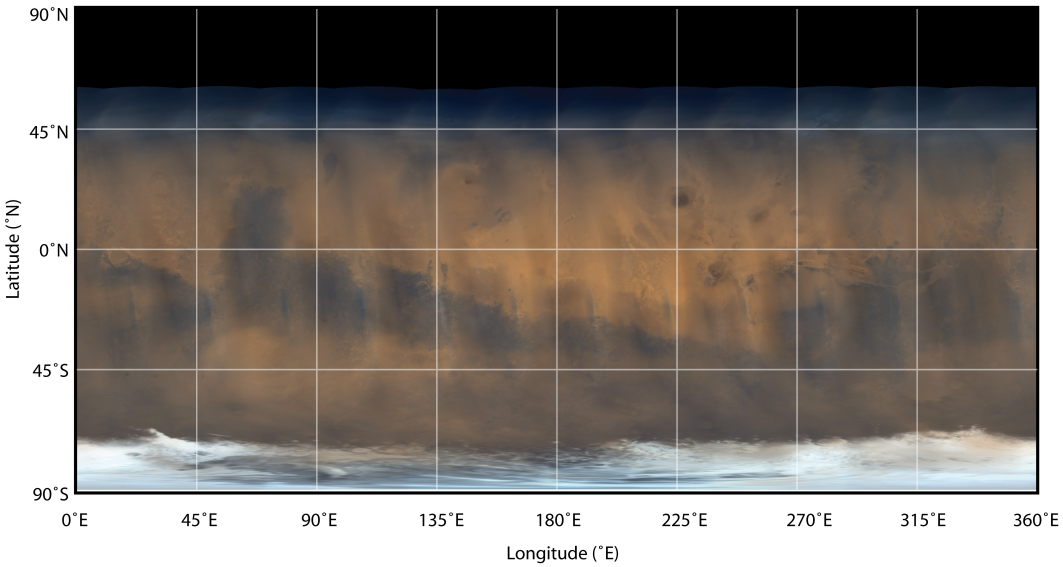

Figure 2.9. By using all the images from a 12 orbit time period (34 images, 6 km/pixel, 3556 x 1779 pixels, ~30 execution time excluding image map projection) a MOC Wide Angle color image of nearly the entire Martian surface can be created. This mosaic was constructed from orbits 3012 to 3024 of the Mars Global Surveyor spacecraft. These data have been empirically corrected for the opposition phase inversion.

2.6.3.3 Viking Visible Data

Several mosaics of the summit of Apollinaris Patera utilizing a variety of datasets including Viking (Figure 2.10), THEMIS daytime and nighttime infrared (Figure 2.11), and CTX (Figure 2.12) were created to illustrate the versatility of the mosaicking techniques presented. These mosaics were created in the same projection but at different scales to illustrate the ability of these algorithms to process, register, and mosaic a wide range of datasets.

The Viking visible imager mosaic was created using seven of the highest resolution data available of the Apollinaris Patera region. These data were projected to 200m/pixel at the latitude of scale (in this case latitude 0˚ N). The pre-processing steps for these data were performed using the ISIS software package, including image calibration. Once these images are ingested into the mosaic software, contrast matching, blending, and advanced stretching algorithms were applied to create a seamless normalized mosaic. The spacecraft pointing data for these images is quite poor, resulting in image warping and absolute position errors of >100 pixels. This makes auto-registration relatively difficult, though by manually adjusting these data to relatively close locations (e.g. <50 pixels) the auto-registration software was able to find a best match, which corresponded to the best-aligned data. Subsequently, individual images were stretched with a histogram stretch to highlight the regional variations in reflectivity observable in the data, rather than the small-scale variations that would be highlighted with a running histogram stretch.

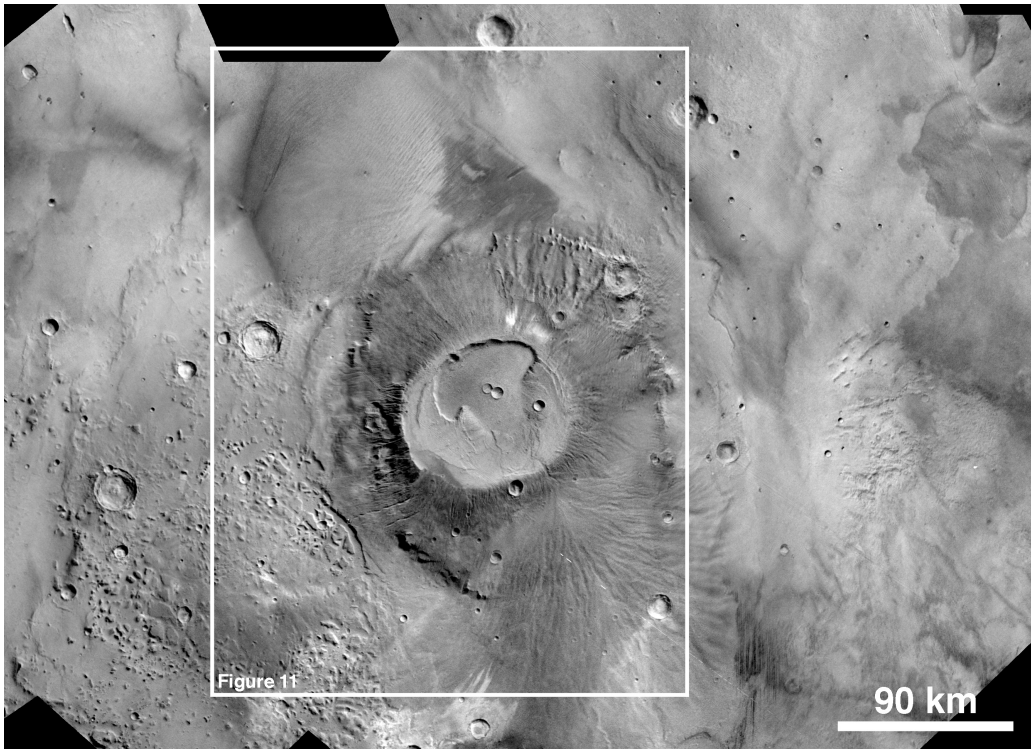

Figure 2.10. An automated mosaic of Viking visual images (7 images, 200 m/pixel, 2665x2393 pixels, ~30 minute execution time excluding image map projection) centered on Apollinaris Patera (174˚ E, 8˚ S). This example data begins to illustrate the usefulness of combining many different datasets to characterize an area. The white box highlights the location of Figure 2.11 to provide context.

2.6.3.4 THEMIS Daytime and Nighttime Infrared Data

Colorizing nighttime temperature data and superposing it on daytime temperature data provides insight into the morphologic features from the daytime data associated with thermophysical properties contributed by the nighttime data. Figure 2.11 is an illustration of this type of data, where nearly 200 images each were used to create the daytime and nighttime mosaics. As this region is relatively small and close to the landing site of the Mars Exploration Rover Spirit [e.g. *Squyres et al.*, 2004a], the coverage of this area with THEMIS data is high and thus many images have been averaged to create these mosaics. In this case (Figure 2.11), as is the case with most examples of this combination, the material with the warmest nighttime temperatures, and thus highest thermal inertia values, are concentrated where the steepest slopes are observed (e.g. cliffs, walls of craters). However, in this case warmer material is also observed on the flanks of Apollinaris Patera. This may indicate that more rocky material is exposed lower on the slopes of the large volcano. Additionally, relatively rocky material is also visible in the caldera of the volcano. These higher thermal inertia surfaces correspond to fractured and layered regions exposed in the caldera. It is possible that these may be linked to past lava flows which are rockier than the surrounding material.

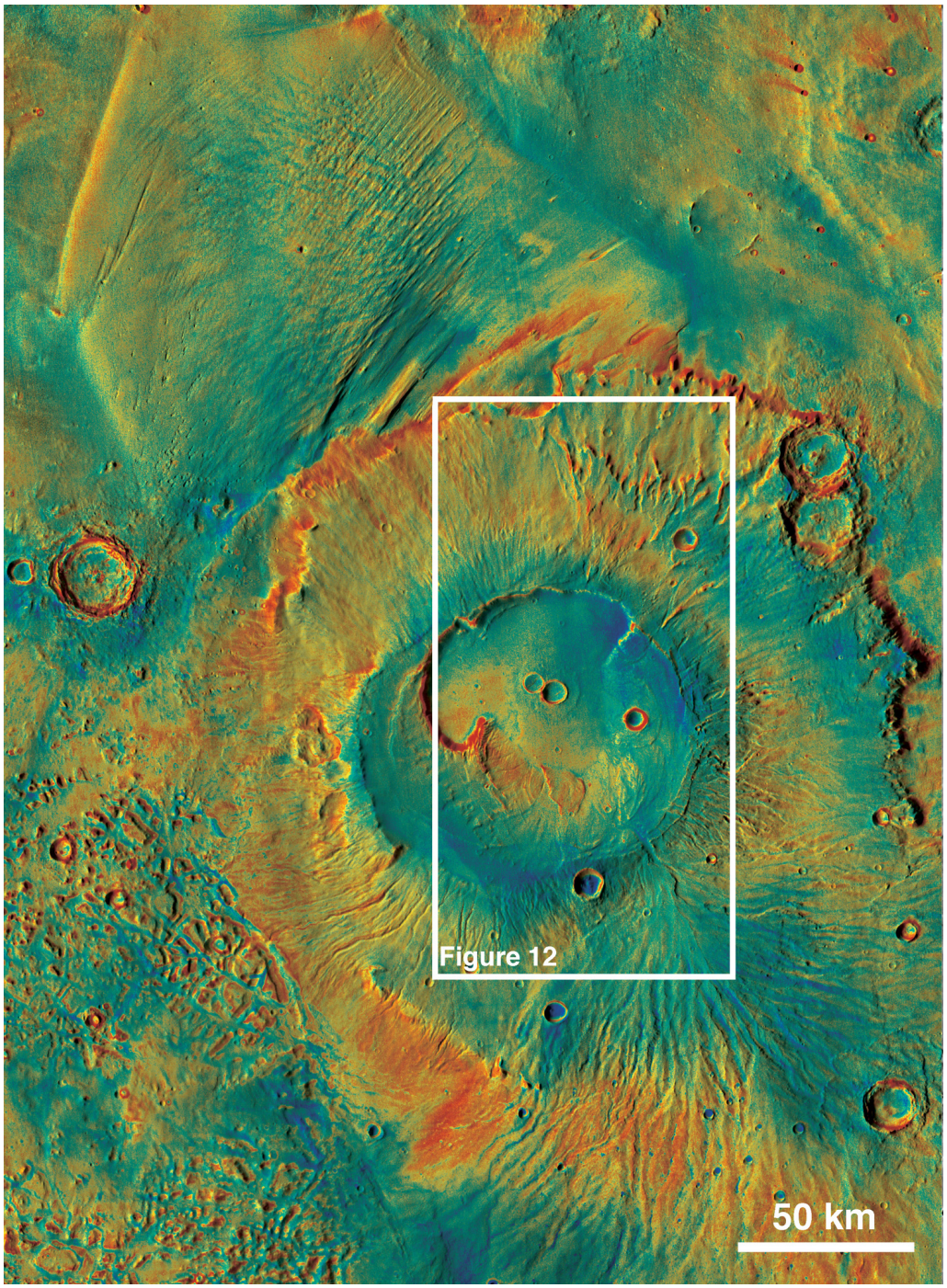

Figure 2.11. Colorized THEMIS nighttime temperature data (301 images, 100 m/pixel, 5336 x 4743 pixels, ~12 minute execution time excluding image map) overlain on a THEMIS daytime temperature mosaic (259 images, 100 m/pixel, 5336 x 4743 pixels, ~10 minute execution time excluding image map projection)

Figure 2.11. continued

centered on Apollinaris Patera (174˚ E, 8˚ S). Blue tones correspond to dustier material while red tones correspond to rockier material. This technique of overlaying a colorized nighttime temperature map on a daytime temperature mosaic provides the morphologic context for the thermophysical (nighttime infrared) data. The white box highlights the location of Figure 2.12 to provide context for the higher-resolution data in Figure 2.12.

2.6.3.5 CTX Visible Data

CTX data of the same area provides high-resolution (~6 m/pixel) imagery that illustrates the small-scale morphology associated with the Apollinaris Patera caldera. Figure 2.12 is a mosaic of four CTX images processed through the standard mosaicking techniques described above. Figure 2.12a shows the overview of the region where the four CTX images were mosaicked together. Figures 2.12b and c are subsequently closer views of this mosaic. In these closer views, more detail regarding the nature of the material is observed. For instance, areas with the highest thermal inertia values (red and yellow tones in Figure 2.11) correspond to the roughest appearance material in Figure 2.12. These surfaces have a knobby and bumpy appearance. Small craters are abundant and likely contribute to the elevated thermal inertia values, as the walls of these craters are expected to be composed of less mantled, rockier materials.

The use of these three datasets to provide the overall context, large-scale morphology, thermophysical properties, and small-scale morphology, enables a more complete investigation of the area in question linking large-scale trends with small-scale observations. While the three coincident datasets shown in this example were all qualitative products, the possibility for creating quantitative products exists and may be used to further classify (e.g. linking quantitative compositional THEMIS deconvolution results [e.g. *Bandfield*, 2008] to quantitative thermal inertia values [e.g. *Fergason et al.*, 2006a; *Edwards et al.*, 2008]).

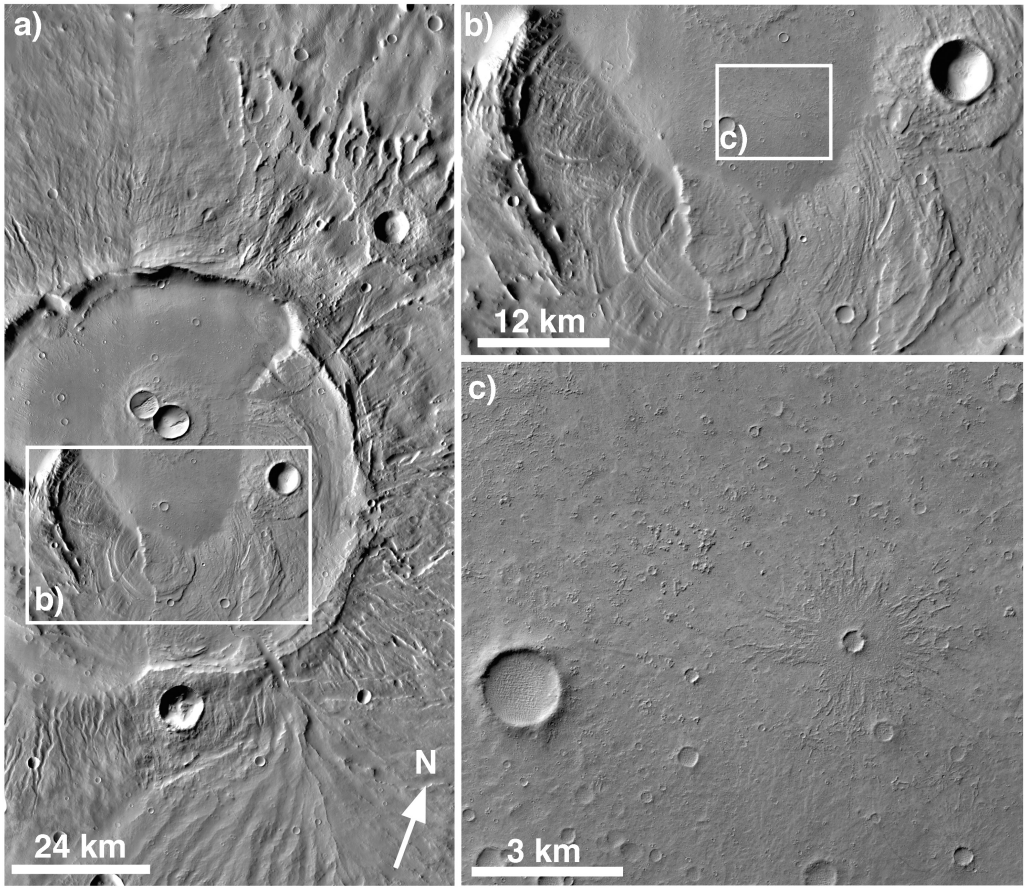

Figure 2.12. An automated mosaic of CTX high-resolution (4 images, 6 m/pixel, 20576 x 59705 pixels, ~2 hour execution time excluding image projection) visible images was also created centered on Apollinaris Patera (174˚ E, 8˚ S). **A)** This is the overview of the mosaic region. Even at this scale, additional details not observed in Figures 2.10 and 2.11 can be observed. For example, small radial channels originating at the rim of Apollinaris patera encircle nearly the entire caldera. **B)** This illustrates the nature of the layered terrain as discussed in reference to Figure 2.11. This material typically has an elevated thermal inertia and a fractured appearance. **C)** Additionally, other unique features such as the crater with well-defined ejecta is easily observed at the full resolution of CTX

Figure 2.12. continued

data but not in either of the previous datasets. Of additional interest are the small-scale textures associated with the surfaces that have elevated thermal inertia values. These surfaces are typically pitted, have abundant small craters and often have a knobby texture.

2.7 Conclusions

I have shown the utility of several advanced image processing techniques as applied to THEMIS and other datasets. However, the possibility of applying these techniques, such as the temperature variation across the THEMIS calibration flag correction, random noise removal, and running stretches, is not limited to the datasets presented in this work and may be applied to past, current, and future data. Though the use of these techniques must be carefully validated for each dataset to quantify the effects that may be introduced to the data.

The construction of the mosaics presented and others like them using the techniques described in this paper, provide the ability to view the surface of Mars and geologic problems through many different perspectives. For example, one can obtain high-resolution visible imagery of an area, which may help illuminate compositional and thermophysical data, providing a more complete view of geologic processes on Mars. The mosaicking techniques presented in this work are not limited to the datasets presented here, but may be applied to any dataset which can be projected using the USGS ISIS tools.

Additionally, this allows the mosaicking of global planetary data from Mars and other planetary bodies such as new data from the Moon and other outer planets missions. This mosaicking ability provides an unprecedented amount of flexibility to the end user to produce both quantitative and qualitative large-scale seamless products. These products can be constructed relatively easily and scientific investigations are not limited to the extent of a single image; rather, they

can be combinations of tens to several thousands of images as is the case with the THEMIS global mosaics.

The data selection, mosaicking procedure, quality control measures, and the registration considerations for the THEMIS daytime and nighttime relative temperature global mosaics are presented here. These mosaics are the highest resolution (100m/pixel) global scale datasets available for Mars to date.

2.8 Future Work

Several additional steps may be taken to further improve the THEMIS global mosaic datasets presented here. One major step is to align every THEMIS image on the planet using tie points and a bundle adjustment to Mars Orbiter Laser Altimeter (MOLA) data [*Smith et al.*, 2001]. By using common geographical features (e.g. impact craters) in both THEMIS mosaics and MOLA georeferenced data it is possible to force the THEMIS data to match MOLA through a bundle adjustment, creating a cartographically controlled product that is as geographically accurate as the lower resolution MOLA data allows. Quantitative THEMIS data products could also be created, as the software described does not discriminate between qualitative and quantitative products. The software has the ability to work with numerically meaningful data as well as stretched image values. Possible data products include thermal inertia and 10-band emissivity data mosaics. The difficulty in creating these data products does not lie in the mosaic software but in the initial image processing and calibration. As data processing and calibration techniques improve, more sophisticated THEMIS data products will likely emerge.

CHAPTER 3

EVIDENCE FOR EXTENSIVE OLIVINE-RICH BASALT BEDROCK OUTCROPS IN GANGES AND EOS CHASMAS, MARS

Edwards, C. S., P. R. Christensen, and V. E. Hamilton (2008), Evidence for extensive olivine-rich basalt bedrock outcrops in Ganges and Eos chasmas, Mars, *J. Geophys. Res*, *113*(E11003), doi:10.1029/2008JE003091.

Several localized outcrops of olivine-enriched bedrock have been previously identified in the Ganges and Eos Chasmata area on the eastern end of Valles Marineris with the Thermal Emission Imaging System multi-spectral images. These outcrops form a layer in the walls of Ganges Chasma, and appear to be the remnants of a once-continuous unit, which was mapped over ~100 km. In this study I further characterize the composition (~Fo_{68}), olivine abundance (10 to >15%), thermal inertia (>600 J K^{-1} m^{-2} $s^{-1/2}$, consistent with in-place rocky material), vertical dimension (~60 m to ~220 m), extent (>1,100 km laterally), volume (~$9.9x10^4$ km^3), dip (~0.013˚ NE), and continuity of this layer utilizing Thermal Emission Spectrometer hyper-spectral, Thermal Emission Imaging System multi-spectral, and Mars Orbiter Laser Altimeter elevation data. Morphologic data from high-resolution imagery display a relatively unmantled, rough and pitted surface associated with the olivine-enriched material, consistent with thermal inertia data. Four possibilities for the origin of the olivine-enriched unit are 1) volcanism associated with tectonic rifting of the Valles Marineris

system, 2) a volcaniclastic flow deposit, 3) an intrusive mafic sill, or 4) a discrete episode in martian history during which flood lavas were erupted onto the surface. The most likely origin is an eruptive event consisting of compositionally uniform flood lavas originating from a primitive mantle source region, possibly associated with the initiation of Tharsis volcanism. This unit is one of the largest continuous compositional units found on Mars and is strikingly similar to other olivine-enriched deposits identified in previous studies where compositional, morphologic, and thermophysical similarities are observed. These similarities may indicate that there was a period in early martian history, where compositionally uniform and extensive olivine-enriched flood basalts were erupted on the martian surface.

3.1 Introduction

Mars is a planet whose surface is dominated by basalt in the southern highlands, and basaltic-andesite or weathered basalt in the northern lowlands [e.g. *Bandfield et al.*, 2000a; *Wyatt and McSween*, 2002], which have been further characterized into four primary sub-components [*Rogers and Christensen*, 2007]. However on a the local scale, the martian surface displays a wide range of volcanic compositions including olivine-enriched basalt [*Christensen et al.*, 2003b; *Hamilton et al.*, 2003; *Hoefen et al.*, 2003; *Hamilton and Christensen*, 2005; *Mustard et al.*, 2005; *Rogers et al.*, 2005; *McSween et al.*, 2006; *Tornabene et al.*, 2008] and more felsic materials such as dacite observed in the Syrtis Major caldera [*Christensen et al.*, 2005]. Although many areas have been characterized by their compositional data and physical nature, the detailed distribution of

differing volcanic rock units discovered to date, has not been fully investigated. Of particular interest is the occurrence and distribution of olivine-enriched basalts in space and time. Olivine-enriched units have been identified globally and in situ [*Mustard et al.*, 2005; *McSween et al.*, 2006; *Rogers and Christensen*, 2007; *Koeppen and Hamilton*, 2008; *Tornabene et al.*, 2008] but their spatial and temporal relationships remain uncertain.

Several localized outcrops of olivine-enriched bedrock have been previously identified in the Ganges and Eos Chasmata area on the eastern end of Valles Marineris with the Thermal Emission Imaging System (THEMIS) onboard the 2001 Mars Odyssey Spacecraft [*Christensen et al.*, 2003b; *Hamilton et al.*, 2003; *Hamilton and Christensen*, 2004]. These outcrops form a ~50 m thick layer exposed in the walls of Ganges Chasma, and appear to be the remnants of a once-continuous unit that was mapped over a ~100 km distance using THEMIS multi-spectral images [*Christensen et al.*, 2003b]. Thermal Emission Spectrometer (TES) spectra show this unit to be an olivine-enriched basalt with 10-15% olivine abundance with a composition of Fo68 [*Christensen et al.*, 2003b].

Several questions have arisen since the initial identification of these olivine-enriched basalt outcrops. Has olivine rich material formed continuously throughout martian history, was it an episodic event, or was it emplaced in a limited time range or locality? Also, is the Ganges unit continuous and if so, what is its extent? How does this unit relate to other olivine-enriched locations on Mars? THEMIS infrared multi-spectral data provide excellent means to address several of these issues due to the high spatial resolution, the nearly global

coverage, and their strong ability to discriminate olivine-bearing materials. When THEMIS data are used in conjunction with other datasets (e.g. TES and Mars Orbiter laser Altimeter (MOLA) data), constraints on the lateral extent, the stratigraphic distribution, olivine abundance, and composition can be made. However, the full extent of this unit may be unmappable with this technique in areas of high dust cover (as dust easily obscures the underlying bedrock composition at thermal infrared wavelengths [*Ruff and Christensen*, 2002]) to the north and west of Ganges Chasma where exposures are lacking.

3.2 Method

In order to assess the spatial distribution of the Ganges and Eos Chasmata olivine-enriched deposits, I created a false-color mosaic of THEMIS multi-spectral daytime infrared data at 100 meter per pixel spatial sampling, using bands 8, 7, and 5 (11.79, 11.04 and 9.35 μm respectively). I chose these bands to emphasize the strong absorption in band 7 due to olivine [e.g. *Christensen et al.*, 2003b] that is lacking in the surrounding basalt units. A decorrelation stretch [*Gillespie et al.*, 1986] was performed on the multi-band mosaic to emphasize spectral differences; using the 8, 7, and 5 band combination, the olivine-enriched unit appears purple. I extended the mosaic in all directions until the olivine-bearing unit could no longer be identified, with the mosaic eventually covering an area of approximately 1.2 x 10^6 km^2 (Figure 3.1).

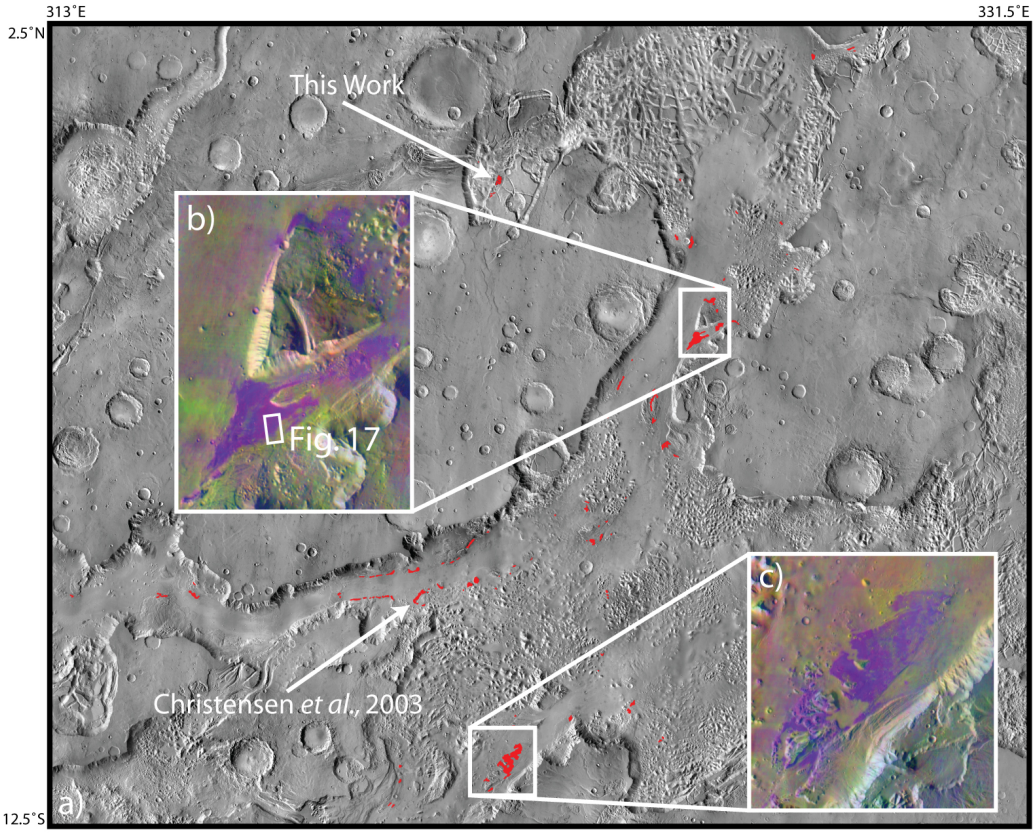

Figure 3.1. A) THEMIS daytime infrared temperature mosaic (background) of the study area (2.5˚ N-12.5˚ S and 313˚ E-331.5˚ E) constructed from a large-scale decorrelation stretch mosaic. Red features are the identified olivine-enriched basalt outcrops. The locations of the example TES spectral ratios (Figure 3.4) are identified by white arrows for both this study and the *Christensen et al.* [2003b] study. **B)** An example decorrelation stretch radiance mosaic of THEMIS bands 8, 7, and 5. Purple tones indicate the presence of olivine. This example was chosen to illustrate the bench forming nature of the outcrops, as the outcrop in question is the largest observed outcrop in the canyon with an area of ~800 km^2. C**)** Another example of a decorrelation stretch radiance mosaic of THEMIS bands 8, 7, and 5, where purple tones again indicate the presence of olivine. The outline of MOC

Figure 3.1. continued

image R0802721 (Figure 3.5) can be seen crossing the contact between the olivine-enriched unit and the surrounding canyon floor.

THEMIS data up to Mars Odyssey orbit ~25,000 were used in this study, as there were no significant dust storm events up to this time during the Mars Odyssey mission and atmospheric dust content remained low and relatively uniform. The variations in atmospheric dust content in the data used for this study are small enough that they can be ignored and no atmospheric correction needs to be performed on the THEMIS data. Also, because this olivine-enriched unit typically occurs within ~200 m of the relatively flat canyon floor, the atmospheric path lengths of this unit and the surrounding floor material vary by less than ~10%. This is important for determining the composition of the outcrops, as I assume that the only difference between the olivine-bearing unit and the surrounding material is the presence or absence of olivine. This assumption can only hold true if the atmospheric path lengths are similar; as the path length increases more atmospheric signal is included in the spectrum making direct comparisons difficult. In this study, comparisons have only been made where path lengths are relatively similar (typically <200 m difference), precluding comparisons between the floor of Valles Marineris and the surrounding plateau.

Nighttime temperature is a good proxy for thermal inertia where warm (e.g. 200 K) material corresponding to high thermal inertia material (e.g. >600 J $K^{-1} m^{-2} s^{-1/2}$) is more consolidated and/or rockier than colder material (e.g. 185 K, 200 J $K^{-1} m^{-2} s^{-1/2}$), such as dust or sand deposits [e.g. *Palluconi and Kieffer*, 1981]. I calculated thermal inertia for individual THEMIS images following the method described by *Fergason et al.* [2006a], which uses the KRC thermal model [*Kieffer*, submitted], for several of the outcrops under investigation. I created a

100 meter per pixel nighttime temperature mosaic (Figure 3.2), which allowed for another method to help identify rockier locations commonly associated with olivine-enriched outcrops. These rockier outcrops are likely indicative of *in situ*, stratigraphically significant materials, which are the focus of this study. Although these large-scale mosaics were useful for identifying potential outcrop locations, I manually validated the location of outcrops using both individual daytime and nighttime THEMIS images. This was necessary as these mosaics are composed of individually stretched images and not the actual radiance and thermal inertia data respectively. Additionally, this hand validation allowed for the calibration (e.g. low time duration between the shutter closing calibration image and data acquisition, low atmospheric dust opacities) and data quality (e.g. high signal to noise, warm images) to be assessed.

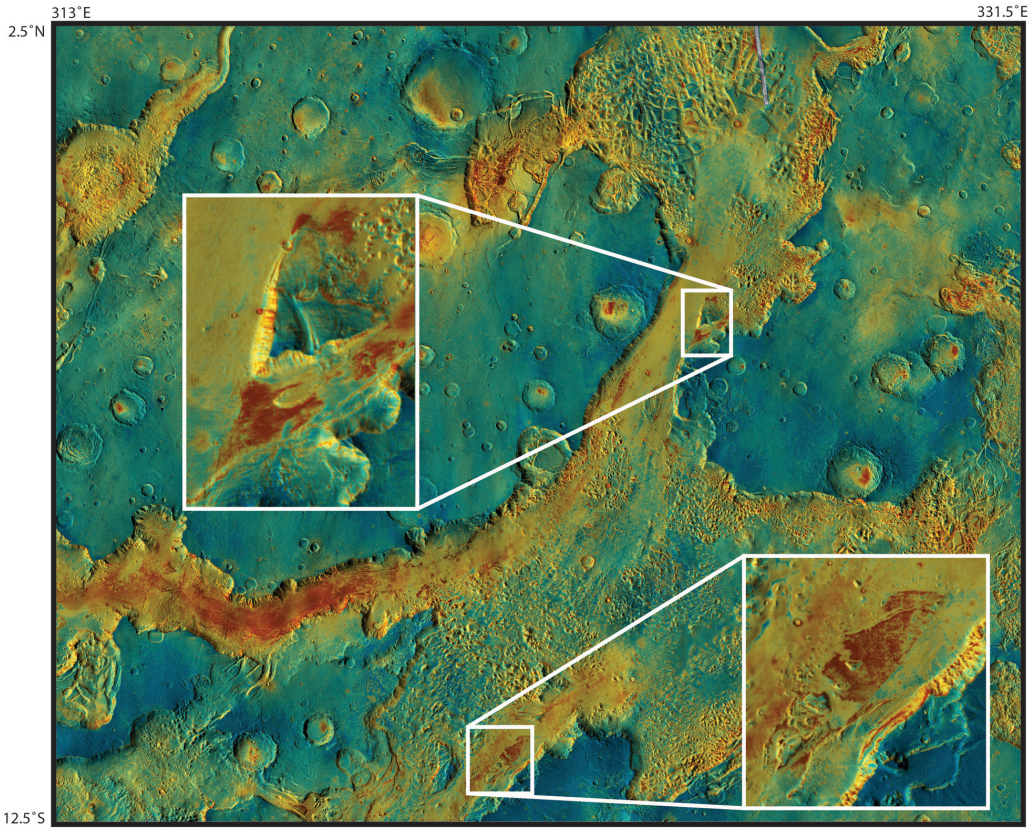

Figure 3.2. THEMIS linearly colorized nighttime temperature mosaic overlain on a THEMIS daytime temperature mosaic (2.5° N-12.5° S and 313° E-331.5° E) illustrating the elevated nighttime temperature (and thus thermal inertia) associated with the olivine-enriched outcrops. In this image blue tones are colder nighttime temperatures (lower thermal inertia) while red tones are hotter nighttime temperatures (higher thermal inertia). The highest thermal inertias (>600 J K^{-1} m^{-2} $s^{-1/2}$, with extremes of >1200 J K^{-1} m^{-2} $s^{-1/2}$) in this region are associated with the olivine-enriched outcrops, indicating that they are rockier, in place material. Two close up views of the same outcrops illustrated in Figures 3.1b and 1c also show elevated thermal inertia values associated with the olivine-enriched outcrops.

I am able to identify the olivine-enriched unit locally based on its thermal inertia, with a typical range of ~400 to ~600 J K^{-1} m^{-2} $s^{-1/2}$ and greater. Many of the unit's outcrops have much higher thermal inertia than the surrounding floor material and can also have an extremely high thermal inertia (>1200 J K^{-1} m^{-2} $s^{-1/2}$). Several of these outcrops have been classified as a high inertia surface by *Edwards et al.* [2005], indicating that this material is consistent with in place rock. Materials with high thermal inertia have more significant implications for the geologic history of the area than if the thermal inertia were that of unconsolidated mobile sediments. However, all high thermal inertia materials may not be comprised of olivine-enriched basalt, requiring the consideration of multi- and hyper-spectral data to accurately identify the composition of these outcrops. I mapped out the locations of olivine-bearing outcrops on a background daytime infrared mosaic after they were identified on the original multi-spectral mosaic, nighttime temperature mosaic and subsequently confirmed through the analysis of individual images. Two examples of smaller decorrelation stretch mosaics are shown in Figures 3.1b-c.

The composition of the olivine in some of these units was constrained by *Christensen et al.* [2003b] and *Hamilton et al.* [2003] using two different approaches. *Christensen et al.* [2003b] ratioed a TES spectrum from a prominent olivine-enriched outcrop to a spectrum of the nearby canyon floor and showed that the resulting spectral shape is a good match to Fo_{68} olivine. They concluded that this unit is an olivine-enriched basalt with 10-15% olivine. *Hamilton et al.* [2003] used martian meteorite spectra and TES-derived martian surface spectra to

model TES spectra of Mars and identified these areas as basaltic with components (concentrations up to 20%) that are matched by the martian meteorites Chassigny and ALH 77005, both of which contain large amounts of Fo_{68} olivine. In this paper, I took an approach similar to that of *Christensen et al.* [2003b] and have examined several outcrops (5 locations with the best data coverage, where TES footprints covered a large fraction (>60%) of the location in question and highest data quality, where the warmest (250-300 K), lowest atmospheric opacity (both dust and ice), nadir looking spectra were used to study the composition of this unit over its full extent.

After I identified and mapped all of the outcrops, I registered Mars Orbiter Laser Altimeter (MOLA) elevation data for both gridded and ground-track(s) elevation data [*Smith et al.*, 2001] to the compositional data. I determined the average elevation of approximately 60 of the largest most prominent outcrops from the gridded elevation data based on locations identified in Figure 3.1. I also examined single point elevation data to ensure that the gridded values were representative of the actual outcrop elevations. Additionally, estimates for the thicknesses of these outcrops have been made through the use of both gridded MOLA elevation data and ground-track data where available. The outcrop thicknesses are estimated from the minimum and maximum elevations of each outcrop and the standard deviation of the elevation for all of the individual gridded outcrop elevations. However, these thicknesses should be considered minimum thicknesses, as it is not possible to determine the extent to which these units extend downward or the extent to which they have been eroded.

I created several topographic cross sections (Figure 3.3) to determine if exposures were laterally continuous (indicating that they are all part of the same unit) and if so, to determine the orientation of that unit. However, because most of average elevation data for individual outcrops did not lie directly along each topographic profile, a different approach was required. The average outcrop elevation for each of these locations was extracted (a maximum of up to ~50-80km away from the topographic profile line) and then projected orthogonally to the defined topographic cross section line. This method allows for a generalized depiction of outcrop elevation in relation to general topography. If the topographic line crosses a high or a low point in the canyon, such as a hill or crater, and outcrops are in the canyon walls, the relationship between the outcrop elevation and the topographic profile line may not be well represented. For example, in the aforementioned case, the outcrop elevations would appear below and above the topographic profile line, respectively. However, it is the overall trend of the points that is the most significant and useful data and not necessarily their exact relationship to the topographic profile.

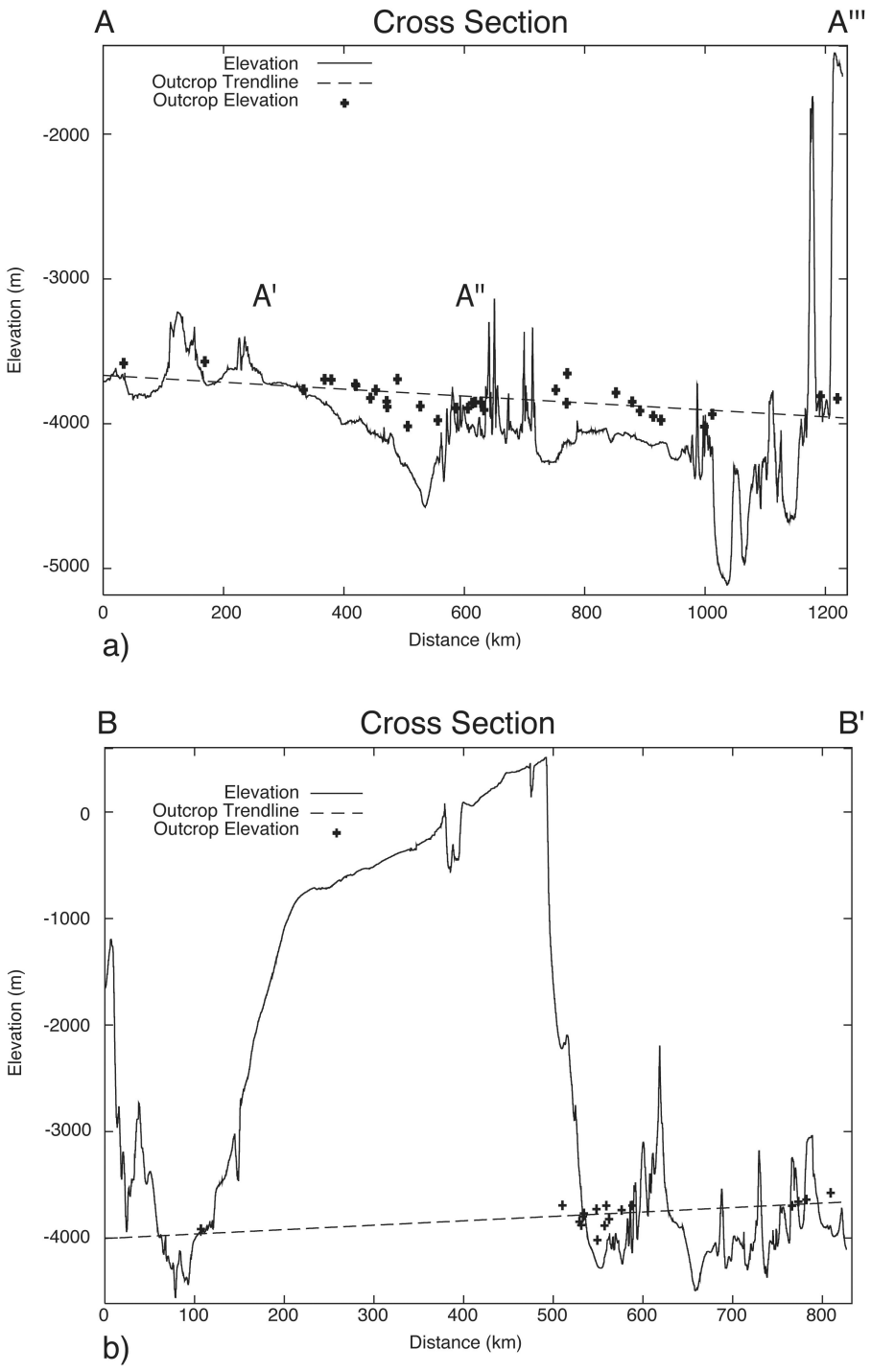

Figure 3.3. Three cross sections (A-A''', B-B', and C-C') illustrate the relief between outcrops. **A)** A-A''' illustrates the relationship between the canyon floor

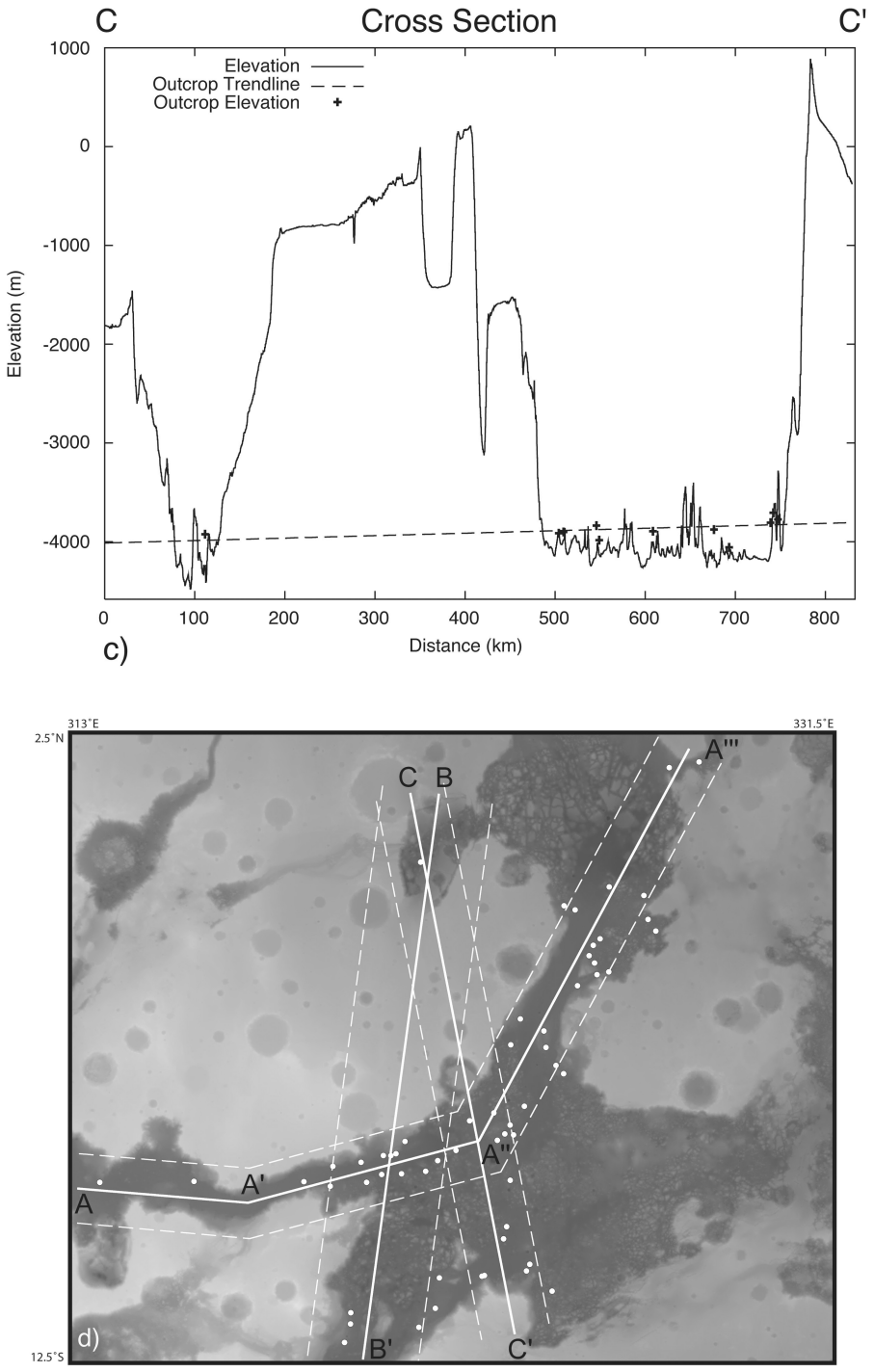

Figure 3.3. continued

and the outcrops, showing that olivine-enriched outcrops are always elevated above the canyon floor. **B)** B-B' illustrates that these outcrops persist through

Figure 3.3. continued

topographically high areas and appear in predictable locations. This cross section also illustrates the north-dipping trend of the outcrops. **C)** C-C' also illustrates the north-dipping trend of the outcrops and shows that these outcrops persist through topographically high areas. **D)** MOLA topographic elevation data at 128 ppd for the entire study region (2.5˚ N-12.5˚ S and 313˚ E-331.5˚ E). The locations of outcrops are plotted as white circles, while the locations for cross sections and topographic profiles are plotted as solid white lines. Dashed white lines illustrate the maximum lateral distance from the topographic profile line from which outcrop elevation points were collected.

3.3 Results

The olivine-enriched outcrops identified in this study extend over ~1,100 km near the eastern end of Valles Marineris in Ganges and Eos Chasmata. They are exposed up to 200 m above the canyon floor and typically ~3.5-4 km below the rim of the canyon, often forming linear arrangements parallel to the canyon walls in addition to large (often >200 km^2) flat-lying benches. Most outcrops have elevated thermal inertia compared to the surrounding canyon floor indicating they are composed of more consolidated, rocky material than mobile aeolian sediment. Through the use of MOLA elevation data and THEMIS and TES compositional data, I obtained three-dimensional information on the spatial distribution of these outcrops. The regional THEMIS mosaic (Figure 3.1a) shows the full extent of the olivine-enriched basalt unit. To the southwest of the study area (~100 km) additional olivine-enriched material has been identified associated with impact crater ejecta. These materials were not included in this study as they are not in place material and their relationship to the primary outcrops identified is uncertain. However, this excavated material may indicate that the primary olivine-enriched unit identified in this study is more extensive than mapped. As dust cover increases to the north and west of Ganges and Eos Chasmata, the full extent of this unit may be unmappable as the homogenous dust easily obscures the underlying bedrock composition in the thermal infrared wavelengths [e.g. *Ruff and Christensen*, 2002] and the overlying plateau provides few windows to the depth of these outcrops. Therefore these units may continue further than mapped in this study.

The composition of five outcrops was verified using TES spectral ratios following the method described by *Christensen et al.* [2003b]. An example of our TES analysis is shown in Figure 3.4, where an outcrop centered at 0.2˚ S, 321.8˚ E (identified by the northernmost arrow in Figure 3.1), approximately 450 km from the outcrop initially studied by *Christensen et al.* [2003b] (identified by the southernmost arrow in Figure 3.1) is compared to the spectral ratio from *Christensen et al.* [2003b] and a laboratory spectrum of olivine with a composition Fo_{68}. The outcrop analyzed with TES data by *Christensen et al.* [2003b] occurs in central Ganges Chasma whereas the outcrop chosen for this study occurs outside the main canyon, (Figure 3.1) near Ravi Vallis, allowing for constraints on changes in the olivine composition and abundance of these outcrops to be made.

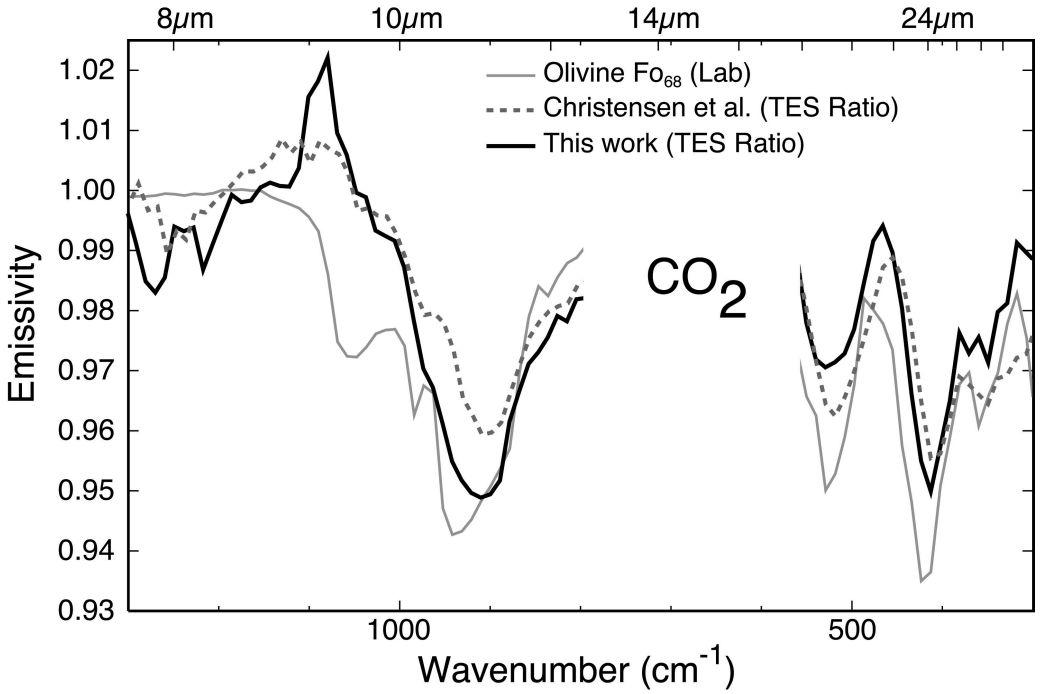

Figure 3.4. One example TES spectral ratio from this is plotted with the original *Christensen et al.* [2003b] TES spectral ratio and an example laboratory spectrum of olivine with a composition of Fo_{68}. Both TES spectral ratios have been processed with 3x1 boxcar filter to emphasize the broad absorption features associated with olivine. Both ratios have olivine compositions consistent with the laboratory spectrum, indicating a relatively constant composition over long distances, as these spectra are separated by ~450 km. A small shift in short wavelength absorption features is observed in both TES spectral ratios and indicates that this $Fo_{\#}$ is not a perfect match and actual forsterite content may be higher or lower than Fo_{68}.

Although ~80 instances of olivine-enriched material have been identified, the elevations of the ~60 most prominent outcrops have been determined using the combination of MOLA elevation data and THEMIS compositional data. The remaining ~20 instances were not mapped due to several limiting factors including: the limited areal extent of a particular outcrop, thermal inertia values indicative of a surface dominated by unconsolidated material, an association with a landform not likely a natural outcropping of bedrock (e.g. mass wasted material) and poor data quality (e.g. low surface temperature, poor image calibration due to factors such as long duration between image acquisition and shutter closing calibration images, etc). Typically, olivine-enriched outcrops are exposed in small hills or slightly raised areas that occur near the sides of the canyons, as well as in the walls of the canyon. They commonly occur in a linear arrangement with small (generally <5-10 km in length), repeated, and elongated outcrops occurring parallel to the direction of the canyon walls. Groupings of these small outcrops generally range from several km up to 50 km and more in length. However, the unit does not always crop out in a linear fashion, as seen in Figures 3.1b and 3.1c where the unit forms large flat benches. This unit also crops out in a side canyon in the north of Figure 3.1 as a larger bench. These benches range in size from ~50 km^2 to ~800 km^2 and have elevated thermal inertias (>600 $JK^{-1}m^{-2}s^{-1/2}$), indicating that they are in place outcrops of olivine-enriched material and not the result of some mobilization mechanism (e.g. aeolian, mass wasting). There are no examples of the unit cropping out further up in the canyon walls, but there are several possibilities for why other layers are not seen elsewhere, including limited

spatial resolution available on the slopes of cliffs, where they may be present but not visible or they may not be present at all.

High-resolution imagery from the Mars Orbiter Camera (MOC) [*Malin et al.*, 1998] and the High Resolution Imaging Science Experiment (HiRISE) [*McEwen et al.*, 2007] help illustrate small-scale morphologies and albedo differences associated with these outcrops; however, Figures 3.1b and 3.1c are some of the only areas covered with high-resolution data (~1.5 m/pixel and ~0.5 m/pixel, respectively) at this time, making it difficult to ascertain the small-scale morphologies and associated features for many of the outcrop locations. The available images (Figure 3.5, 3.6a) show that the olivine-enriched outcrops have a higher albedo than the smoother surrounding canyon floor and filled depressions (Figure 3.5). TES albedo values for Ganges and Eos Chasmata are typically ~0.13, indicating little dust cover throughout the region [*Christensen et al.*, 2001]. MOC and HiRISE visible imagery (Figure 3.5, 3.6a) show that the olivine-enriched material has a fairly rough and pitted surface while the olivine-poor material has a mantled and smoother appearance. These morphologic characteristics are similar to those reported for other olivine-enriched terrains, including those found in Ares Vallis [*Rogers et al.*, 2005], Gusev Crater [*Ruff et al.*, 2007], Isidis Planitia [*Tornabene et al.*, 2008], and Nili Fossae [*Hamilton and Christensen*, 2005; *Mustard et al.*, 2007], (Figures 3.6b-e, respectively). In addition to this morphologic difference, the olivine-enriched material in Ganges and Eos Chasmata is elevated above the surrounding floor material, which have a thermal inertia and morphology (dune forms are observed throughout the area in

high resolution imagery) consistent with aeolian materials. However, there are areas in the olivine-enriched outcrops that have been infilled with some amount of aeolian material, identified by small-scale dunes in many small pits and hollows.

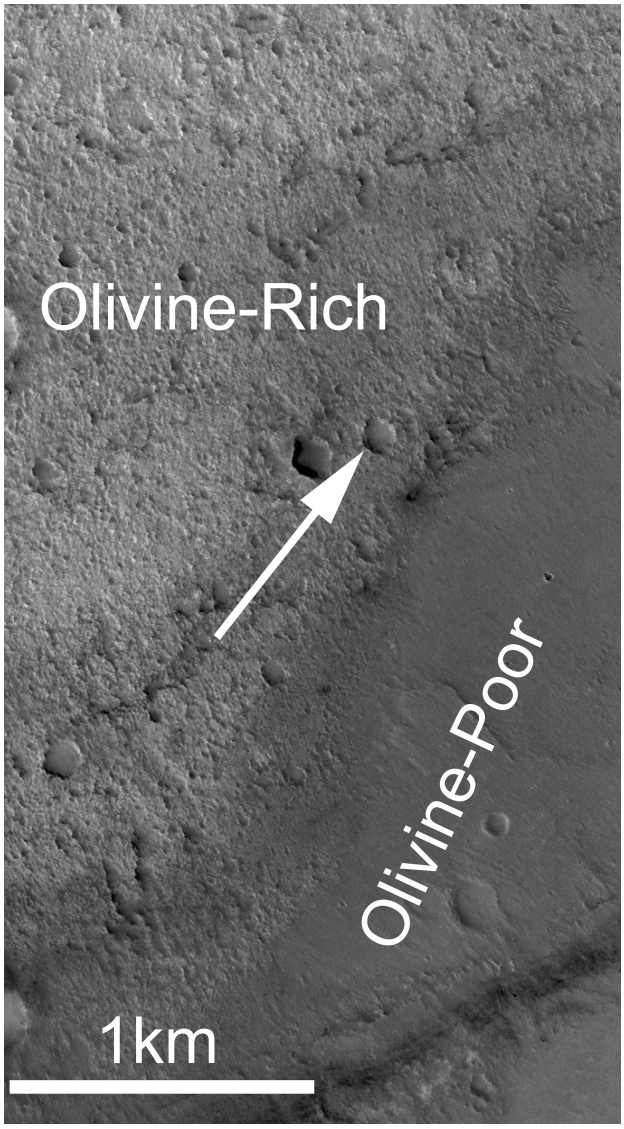

Figure 3.5. MOC Image R0802721 (centered near 325.5˚E, 3˚S) covers the contact between the olivine-enriched outcrops and the canyon floor (see Figure1). The olivine-enriched material has an albedo of ~0.13, rough pitted appearance, and is largely unmantled with lower albedo aeolian materials infilling small pits and craters (see arrow), while the olivine-poor material has a smooth appearance and seems to be dominated by aeolian material, as evidenced by dune forms.

Additionally, I have characterized the physical nature of the outcrops using thermal inertia. *Christensen et al.* [2003b] note that olivine-enriched outcrops have a high nighttime temperature when compared to the surrounding canyon floor (~10 K higher). The thermal inertia of the primary outcrop investigated by *Christensen et al.* [2003b] was determined to be ~700 J K^{-1} m^{-2} $s^{-1/2}$ [*Christensen et al.*, 2003b], which is a thermal inertia value near that of rock and is significantly higher than for unconsolidated material. While this thermal inertia is not consistent with completely unmantled bedrock, this value is likely lowered due to sub-pixel mixing with lower inertia aeolian materials (~250-300 J K^{-1} m^{-2} $s^{-1/2}$, [e.g. *Putzig et al.*, 2005; *Fergason et al.*, 2006a]) present in hollows and pits observed on the outcrops (Figure 3.5). In this study, thermal inertia was calculated for individual THEMIS nighttime temperature images (to assess image quality and calibration) [*Fergason et al.*, 2006a] that covered several of the outcrops under investigation, including Figures 3.1b and 3.1c. Many of the outcrops in question have a much higher thermal inertia than the surrounding floor material, typically ranging from ~400 to ~600 J K^{-1} m^{-2} $s^{-1/2}$, with several outcrops having thermal inertia values of greater than ~600 J K^{-1} m^{-2} $s^{-1/2}$, sometimes reaching thermal model limits of 1400 J K^{-1} m^{-2} $s^{-1/2}$.

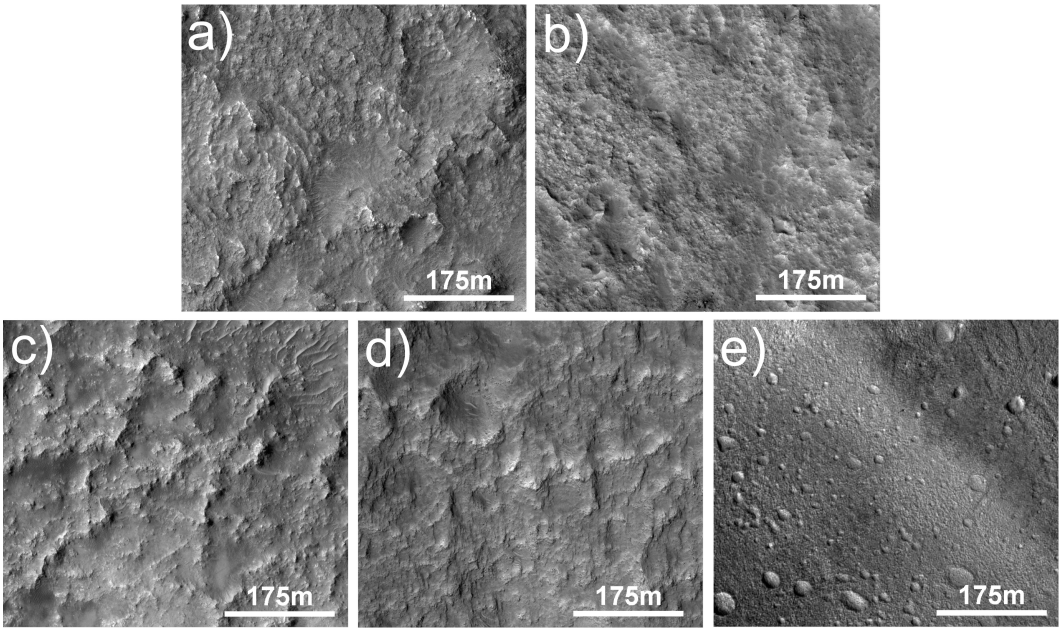

Figure 3.6. HiRISE imagery of a variety olivine-enriched units identified on Mars [e.g. *Hamilton and Christensen*, 2005; *Rogers et al.*, 2005; *Mustard et al.*, 2007; *Ruff et al.*, 2007; *Tornabene et al.*, 2008]. All images are displayed at the same scale (~56 cm/px) for easy morphologic comparison between areas. Olivine-enriched material in: **A)** Eos Chasma (HiRISE image: PSP_001798_1685, centered near 322˚ E, 10˚ S), **B)** Ares Vallis (HiRISE Image: PSP_004118_1865, centered near 341˚ E, 6.5˚ N), **C)** Gusev Crater (HiRISE Image: PSP_002133_1650, centered near 175.5˚ E, 14.5˚ S), **D)** Isidis Basin (HiRISE Image: PSP_002756_1830, centered near 85˚ E, 3˚ N), and **E)** Nili Fossae (HiRISE Image: PSP_001754_2020, centered near 78˚ E, 22˚ N). All localities exhibit the rough, pitted texture observed in Ganges and Eos Chasma (a), but the scale of these textures is variable, where Ares Vallis (b) and Nili Fossae (e) exhibits smaller scale features and Gusev Crater (c) and Isidis Basin (d) exhibits larger scale features than the Ganges and Eos Chasma unit.

Although the olivine-enriched outcrops in this study have a variety of thermal inertia values that are high (often times >600 J K^{-1} m^{-2} $s^{-1/2}$), they are not necessarily consistent with a thermal inertia of unmantled bedrock (>1200 J K^{-1} m^{-2} $s^{-1/2}$) as defined by *Edwards et al.* [2005]. However, upon examination of these occurrences with high-resolution imagery, which display a rough, pitted surface, I conclude that these outcrops are in place, exposed rock. The explanation for this discrepancy between the morphologic observations and the calculated thermal inertias, comes from the aforementioned aeolian materials (identified by dune forms) that infill some of the depressions in the exposed rock. These lower inertia materials would have the effect of lowering the overall thermal inertia as the thermal inertia data from a single THEMIS pixel is integrated over 10,000 m^2 [e.g. *Fergason et al.*, 2006a]. This relatively high thermal inertia, along with the rocky and unmantled morphologies observed in high-resolution imagery, indicate that this is an in place unit, which has been modified (e.g. aeolian processes, impact cratering, mass wasting) but is not a mobile aeolian material.

Through the use of MOLA single point elevation data and gridded data, the minimum outcrop thicknesses are estimated to range from ~60 m to ~220 m, with an average value of ~150 m. Additionally, by plotting the average outcrop elevation data and spatial data together, it is possible to determine the continuity, orientation, dip, and extent of the olivine-basalt outcrops (Figure 3.2). The uppermost surfaces of individual outcrops typically occur within ~200 m of the canyon floor, often forming small hills or benches in the canyon. Cross section

A-A'", which was constructed along the main canyon system floor (Figure 3.3a), illustrates that the topographic profile of the canyon floor, depicted as a solid line, is nearly always lower than the points of average elevation for each of the outcrops. Other cross sections (B-B' and C-C', Figures 3.3b and 3.3c) display a similar trend, where the olivine-enriched unit persists between topographically high areas and appears only at a restricted range of elevations in or near the walls of the canyon.

MOLA elevation and THEMIS multi-spectral data indicate that these olivine-enriched outcrops are not just located at similar elevations near the bottom of Ganges and Eos Chasmata, but they form a contiguous, rocky layer that is visible between topographically high areas and outcrops at consistent locations in the canyon system. In addition, this layer is relatively thin (typically <~200 m) when compared to the ~4.5 km of overlying materials.

If these outcrops are, in fact, representative of a large contiguous layer, calculating the layer's dip angle and dip azimuth could help constrain both the emplacement mechanism and the amount of crustal deformation the area has undergone. For example, elevation variations may be explained by volcanic fallout [e.g. *Wilson and Head*, 1994; *Wilson and Head*, 2007] if the layer appears to drape pre-existing topography or the unit may be offset due to faulting as a result of the regional tectonic environment [e.g. *Phillips et al.*, 2001]. Cross sections B-B' and C-C' (Figures 3.3b and 3.3c) were specifically chosen to illustrate the dip angle and azimuth of this layer, in addition to the continuity and extent of the unit. Through the analysis of these cross sections, I find that the

layer dips slightly to the northeast. By using the best linear fit to the A-A'" (Figure 3.3a) data, the dip angle was measured at ~0.013±0.004˚ (95% confidence interval) to the northeast, which is essentially flat-lying when compared to the large extent of this unit. The topographic profile line A-A'" (Figure 3.3a) indicates that the canyon floor was measured to dip to the northeast, with a dip angle of ~0.045±0.001˚ and an azimuth consistent with the outcrops. These measured dips also correspond with the large scale MOLA topography where the highest location in this scene occurs in the southwest corner and the lowest occurs in the northeast section. However, the plateau was measured to dip at a noticeably higher angle (~0.293±0.005˚) but in a similar azimuth to the canyon floor and the olivine-enriched outcrops. The differential dip between the plateau surface and the olivine layer suggests that several regional tectonic events have affected the stratigraphic column or deposition of the olivine-rich layer may have occurred on an inclined surface.

In addition to the regional tilt of this layer, there are small-scale variations (±200 m) in the data but these variations are small when compared to the overall extent of the layer (>1,100 km) thus, this layer is relatively flat-lying over large distances. These relatively small variations indicate that any vertical offset of this layer was minimal. The linear arrangement of many outcrops helps affirm that the unit is a continuous layer within the canyon walls. The outcrops that occur outside of the main canyon system (e.g. the outcrop near Ravi Vallis, used as the example location for the TES spectral analysis discussed earlier and the small craters with olivine-enriched ejecta to the southwest of the study area) suggest a

more extensive, continuous layer that persists underneath topographically high areas such as the overlying plateau between Ganges Chasma and Ravi Vallis and only outcrops at specific predictable elevations (e.g. Figures 3.3b and 3.3c). For instance, the lowest elevation in southernmost area of Shalbatana Vallis (1˚ N, 315˚ E) is higher than the expected outcrop elevation and is consistent with the lack of an olivine-enriched unit in this canyon. However, it is not possible to determine if this location is a western limit on the extent of the unit because the unit may be present in the subsurface.

Although most olivine-enriched outcrops occur near the walls of the canyon and have morphologies and thermal inertias consistent with in place, rocky materials, I have observed some evidence of transport as well. Olivine-enriched material has been carried as debris into the canyon floor by mass wasting, which can be seen in two locations in Figure 3.1a near the western edge of Ganges Chasma (318.7˚ E, 8.2˚ S; 315.5˚ E, 8.4˚ S, Figure 3.7). Although aeolian materials are observed in high-resolution imagery, they do not have a spectral signature consistent with a relative enrichment in olivine. It is not likely that aeolian materials are the primary source for this unit, rather aeolian processes only aid in eroding the outcrop and allow for transportation of these eroded materials over small distances.

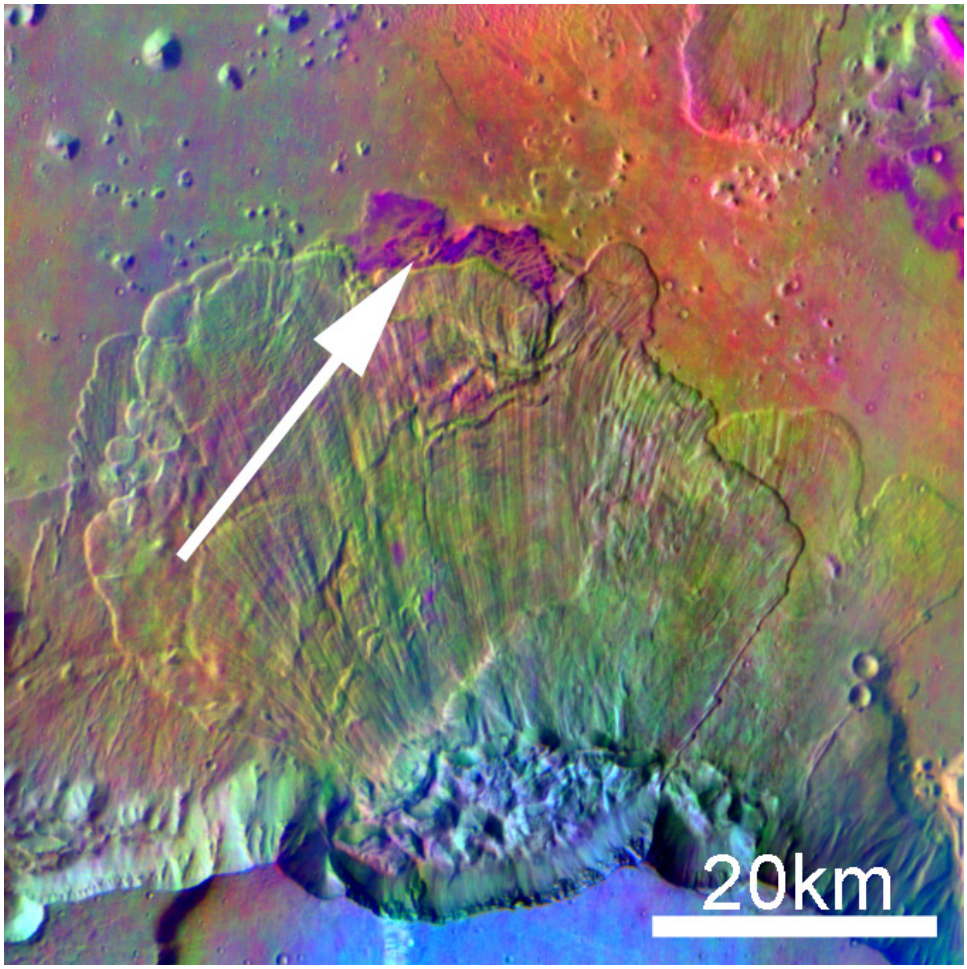

Figure 3.7. A decorrelation stretch radiance mosaic of THEMIS bands 8, 7, and 5 centered on 315.5˚ E, 8.4˚ S, where purple tones indicate the presence of olivine. Olivine-enriched material has been carried to the center of the canyon floor by a mass-wasting event, indicated by the white arrow.

3.4 Discussion

The identification and mapping of this regionally extensive unit poses some interesting questions as to the volume of material it represents, relationship to other olivine-enriched basalts in the area and globally, and its geologic origin.

3.4.1 Volume

Assuming that the maximum extent of the unit corresponds to the maximum extent of the observed outcrops, an estimate of the minimum volume of olivine-enriched material can be calculated by fitting an ellipse to a region enclosing all of the identified outcrops. The area of the ellipse of maximum extent is ~6.6×10^5 km^2. Using the average thickness of 150m, a volume of ~9.9×10^4 km^3 has been estimated. In addition to the uncertainty in the thickness estimated for this layer, the calculated volume is considered a minimum estimate since the layer may continue further under the plateau where it cannot be observed. Additionally, small craters in the floor of Eos Chasma, to the southwest of the study area, appear to excavate olivine-enriched material from below the surface and indicate that this layer likely continues further than the mapped outcrops. The full extent of this unit is also likely unknown due to increasing dust cover to the north and west of Ganges and Eos Chasmata, obscuring the underlying bedrock composition, further emphasizing that the volume estimate stated above is a minimum value.

Large igneous provinces on Earth, for example the Siberian Traps or the Deccan Traps, have total magma emplacement volumes of 1×10^6 km^3 [*Officer et*

al., 1987] to $4x10^6$ km^3 [*Courtillot et al.*, 1999] and $2x10^6$ km^3 [*Widdowson et al.*, 1997] to $4x10^6$ km^3 [*Courtillot et al.*, 1999], respectively. All of these volumes are more than an order of magnitude larger than the estimated volume of the Ganges and Eos Chasmata unit. These terrestrial cases represent the total volume of magma erupted, which consist of many different units erupted over long time periods (e.g. ~0.9±0.8 Ma for the Siberian Traps [*Campbell et al.*, 1992]). The Ganges and Eos Chasmata case is a single unit likely composed of several different eruptive events within what has been interpreted as a massive sequence of lava flows exposed in the canyon walls [*McEwen et al.*, 1999]. This comparison to large igneous provinces on Earth illustrates that the size of this martian unit is not unique for other planetary bodies in the solar system. Additionally, if the Ganges and Eos Chasmata olivine-enriched basalts are only a single unit, corresponding to a distinct period in martian history, the volume estimates for this unit are consistent with what may be expected for a single unit in large igneous provinces on Earth.

3.4.2 Comparison to Other Olivine Basalts

By comparing an example TES spectral ratio from this work and the ratio performed by *Christensen et al.* [2003b] to several laboratory-measured olivine spectra [*Salisbury et al.*, 1992; *Christensen et al.*, 2000b; *Koeppen and Hamilton*, 2008], both spectral ratios are a good match to the three main absorption features of olivine (Figure 3.4). However, an important property of olivine is that higher wavelength spectral features systematically shift to either shorter or longer wavelengths as a function of Mg and Fe content of the olivine [*Salisbury et al.*,

1992; *Hamilton et al.*, 1997; *Koeppen and Hamilton*, 2008]. This is typically represented by forsterite content ($Fo_{\#}$, the Mg-rich endmember of the solid solution series) defined as (Mg/(Mg+Fe)). This systematic shift makes it possible to estimate the forsterite content of this specific olivine unit. A forsterite content of ~0.68 (Fo_{68}) proved to be the best match of all the laboratory olivine spectra examined (with major at absorptions at ~10.6, ~19.0, and ~23.5 μm) for both the ratio performed in this work and the ratio performed by *Christensen et al.* [2003b]. However, there is a small shift in some of the shorter wavelength absorption features for both TES spectral ratios, indicating that this $Fo_{\#}$ is not a perfect match and may be slightly higher or lower than Fo_{68}. Not only is this unit olivine-enriched but the composition of the olivine remains relatively constant over large distances, as the ratio in this study and the *Christensen et al.* [2003b] ratio match each other well despite being separated by over ~450 km. *Koeppen and Hamilton* [2008] have created global maps utilizing TES spectral data illustrating the distribution of olivine for a variety of $Fo_{\#}$ compositions. *Koeppen and Hamilton* [2008] found that the best match for Ganges and Eos Chasmata is the olivine index that corresponds to $Fo_{58\text{-}74}$. These data further strengthen the argument that this is a single, extensive compositionally uniform unit and is not composed of several smaller olivine-enriched members of differing composition, as no layering is observed in high-resolution MOC or HiRISE imagery. However, distinguishing detailed compositional information is limited to the scale of a single TES pixel (3 by ~6 km), as sub-pixel mixing of material with different

forsterite content may be present but not resolvable by TES or distinguishable by the lower spectral resolution data available from THEMIS.

McSween et al. [2006] have identified picritic olivine basalts in Gusev in individual samples examined by instruments on the Mars Exploration Rovers, including Panoramic Camera (PanCam) [*Bell et al.*, 2006], Mini-Thermal Emission Spectrometer (mini-TES) [*Christensen et al.*, 2004b], Mössbauer Spectrometer [*Morris et al.*, 2004] and Alpha Particle X-ray Spectrometer [*Gellert et al.*, 2004]. It is likely that these basalts are derived from more primitive, less fractionated magmas. The proportion of the olivine described by *McSween et al.* [2006] and *Koeppen and Hamilton* [2008] on Mars ranges from 0% abundance for large sections of the planet to an extreme of 20-30% abundance, indicating that the olivine basalts identified in this study (with an abundance of ~10 to >15%) have higher than typical olivine content on Mars when viewed from orbit. Although the rocks at Gusev crater do not occur in the primary region where olivine is found on Mars, Eos and Ganges Chasmata are located in one of the areas where higher olivine concentrations are commonly found [*Koeppen and Hamilton*, 2008]. In addition, *Koeppen and Hamilton* [2008] have found that the forsterite composition of olivine on Mars can vary dramatically with olivine of Fo_{91} occurring in small occurrences near Argyre and Hellas basins and widespread occurrences of a more intermediate forsterite content (e.g. $Fo_{70\text{-}40}$), consistent with what is observed in Ganges and Eos Chasmata. However, no confident occurrences of olivine with $<<Fo_{30}$ were

identified, due to large inaccuracies in the spectral index used caused primarily by atmospheric contributions [*Koeppen and Hamilton*, 2008].

Abundant olivine rich rocks are also found near the Columbia Hilis in Gusev Crater. *Ruff et al.* [2007] identified an olivine-enriched terrain utilizing the mini-TES, which has been described as "Rubble Terrain" due to the appearance in PanCam and HiRISE images. Large rounded boulders and knobs of rubbly, layered, olivine-enriched materials have led *Ruff et al.* [2007] to hypothesize that this may be a volcaniclastic deposit. However, an alternate possibility is that these materials are impact-derived deposits similar to those suggested for the Nili Fossae region originating from the Isidis Basin impact event [*Mustard et al.*, 2007; *Tornabene et al.*, 2008]. The terrain identified also has an elevated nighttime temperature [*Ruff et al.*, 2007] implying a rockier material. When viewed using high-resolution imagery, there are significant morphological similarities between the Gusev crater "Rubble Terrain" and the unit under investigation in this study. Figure 3.6a illustrates this similarity as the olivine-enriched terrain has a rough and pitted texture similar to that described by *Ruff et al.* [2007] (Figure 3.6c).

Another example location where an olivine (Fo_{60}) basalt has been identified utilizing TES and THEMIS data is Ares Valles [*Rogers et al.*, 2005]. The outcrop of olivine in this location has a relatively high thermal inertia (575-840 J K^{-1} m^{-2} $s^{-1/2}$) and appears to occur in two primary layers. Rogers *et al.* [2005] conclude that the emplacement mechanism for this olivine-bearing unit (with an olivine abundance of >15%) could be explained by an intrusive and/or

extrusive event. There are several similarities with the olivine basalts identified in this study including the relatively high thermal inertia, morphologic evidence, olivine forsterite content and the olivine abundance of >15% which all agree well with the olivine basalt identified in this study. In addition to these similarities, both deposits are relatively close to each other, separated by ~600km and occur at roughly similar elevations, giving rise to the possibility that the emplacement of these two units may be related.

The region around the Nili Fossae is another location where olivine-enriched material has been identified [*Hamilton and Christensen*, 2005; *Mustard et al.*, 2005; *Mustard et al.*, 2007] utilizing THEMIS, TES, and Observatoire pour la Minéralogie, l'Eau, les Glaces, et l'Activité (OMEGA) spectral data. This deposit is to the northeast of the Syrtis Major volcanic shield, and contains a ~30,000 km^2 contiguous olivine-enriched outcrop. This deposit is associated with concentric fractures that may be related to the Isidis basin impact event. This olivine-enriched locality has similar characteristics to those identified in this study where outcrops of this unit have a rough and pitted appearance and appear to be largely free of aeolian material. However, sand dunes are prevalent in this area and appear to overly a hard substrate of olivine-enriched material. *Hamilton and Christensen* [2005] have determined that the composition the olivine in this location is ~Fo_{68-75} and often has elevated thermal inertias (~455 J K^{-1} m^{-2} $s^{-1/2}$) when compared to the olivine-poor materials. Additionally, this olivine-enriched unit displays similar characteristics to what is observed in southwest Isidis basin

[2008], where an olivine-enriched unit has been mapped and characterized using compositional, thermophysical and morphologic data.

Morphologies associated with the olivine-enriched materials found in Nili Fossae generally agree with those in Ganges and Eos Chasmata, with the exception of the curved lineaments identified by *Hamilton and Christensen* [2005]. These lineaments are associated with flat-lying layering in Nili Fossae, which has not been observed in the Ganges and Eos Chasmata unit. However, when this area was characterized using OMEGA and HiRISE [*Mustard et al.*, 2007], these lineaments appear to be related to the underlying phyllosilicate material in the region which pre-dates the overlying olivine-enriched unit. *Mustard et al.* [2007] propose that this olivine-enriched material represents an impact melt deposit related to the Isidis Basin formation event. As no lineaments have been observed in or near the Ganges and Eos Chasmata olivine-enriched unit, this indicates that there are no correlated layered phyllosilicate materials present in this location, unlike those found in Nili Fossae [*Mustard et al.*, 2007]. Alternatively, Tornabene et al. [*Tornabene et al.*, 2008] have proposed that the underlying phyllosilicate-rich terrain identified in Nili Fossae is more likely representative of ejecta associated with the Isidis Basin impact event. If this interpretation is correct, it is also consistent with the lack of these features in Ganges and Eos Chasmata, as there are no clear large impact basins within 1000's of km of these localities. Additionally this result is supported directly by OMEGA data, which did not identify phyllosilicate materials in Ganges and Eos Chasmata [*Bibring et al.*, 2006].

The Ares Vallis olivine-enriched bedrock [*Rogers et al.*, 2005] displays the most similarities to the Ganges and Eos Chasmata unit where olivine abundances, composition, morphology and thermal inertia correlate best. In addition, this site is relatively close (~600 km) to the Ganges and Eos Chasmata unit and crops out at a similar elevation, which may indicate even more widespread olivine-enriched basaltic volcanism than hypothesized in this study. However, of specific note are the striking similarities (e.g. olivine abundance, forsterite content, thermal inertia data, morphologies) between all of the previously discussed olivine-enriched units, which are spread out over large distances on the surface [e.g. *Hamilton and Christensen*, 2005; *Rogers et al.*, 2005; *Mustard et al.*, 2007; *Ruff et al.*, 2007; *Tornabene et al.*, 2008] and the Ganges and Eos Chasmata layer. Figure 3.6 highlights the morphologic similarities (especially rough, pitted textures) of these units, with HiRISE imagery shown for several sites where olivine-enriched units have been identified. However, the scale of the identified textures is variable, with Ares Vallis (6b) and Nili Fossae (6e) exhibiting smaller scale features and Gusev Crater (6c) and Isidis Basin (6d) exhibiting larger scale features than the Ganges and Eos Chasmata unit (6a). This variability may be due to different weathering conditions or differences in regional histories. Additionally, Nili Fossae shows significantly more aeolian dune forms than other areas, indicating that this area may be subject to more gradational processes or is composed of more friable material than other areas.

Most in place olivine-enriched units have olivine abundances which are typically >15% and have intermediate forsterite content (~0.68). Additionally,

these units typically have elevated thermal inertia (>500 J K^{-1} m^{-2} $s^{-1/2}$), which are not necessarily consistent with unaltered bedrock, but are likely lowered due to finer-grained aeolian materials commonly observed in hollows on these surfaces or the presence of an olivine lag eroded from a cap unit [*Christensen et al.*, 2005; *Mustard et al.*, 2007; *Tornabene et al.*, 2008]. In addition to these localized regional examples, *Koeppen and Hamilton* [2008] indicate that olivine with a forsterite content of ~0.68 are most common in the southern highlands, which is consistent with the findings in this study. Several martian meteorite samples (e.g. Chassagny and ALH 77005) which are olivine-rich also have the best spectral matches with Fo_{68} [*Hamilton et al.*, 2003] further strengthening the argument that olivine bearing materials with this forsterite content are common on Mars. Compositions and olivine abundance are similar for many examples of *in situ* olivine on Mars, and when considering unit age, most olivine-enriched units (including the Ganges and Eos Chasmata layer) were likely emplaced during the Noachian [e.g. *Rogers et al.*, 2005; *Mustard et al.*, 2007; *Tornabene et al.*, 2008], early in martian history. Additionally, it is likely that when martian meteorites (e.g. the Nahklites and Chassignites, with crystallization ages of ~1.3 Gyrs [*Nyquist et al.*, 2001]) were ejected from the surface, they sampled lower stratigraphy (where olivine-enriched units with this forsterite content appear to be more common), which is also consistent with what is observed in Ganges and Eos Chasmata.

3.4.3 Geologic Origin of the Unit

There are several geologic processes that could produce a layer such as that observed in this study, including: 1) an intrusive mafic sill, 2) volcanism associated with tectonic rifting of the Valles Marineris system, 3) a volcaniclastic flow deposit, or 4) a discrete episode in martian history during which flood lavas were erupted onto the surface. Emplacement as a sill can explain the contrasting composition of the unit relative to regional material. The source for the sill may have been derived from more primitive magmas than the igneous units that are presumed to comprise the regional material, which show no olivine-enrichment indicative of primitive magmas. However, I do not favor this explanation, primarily due to the large lateral extent of the unit. On Earth some of the largest sills extend for thousands of square kilometers [e.g. *Francis*, 1982; *Kavanagh et al.*, 2006], significantly smaller than the Ganges and Eos Chasmata unit, which has an areal extent of ~6.6×10^5 km^2. Additionally, on Earth, large sills are commonly associated with crustal thinning and continental breakup [e.g. *Francis*, 1982]. Evidence that further strengthen this argument is the lack of any feeder dike structures in high-resolution imagery and the absence of any thermally metamorphosed materials commonly associated with intrusive events (e.g. clays from hydrothermal alteration) [*Bibring et al.*, 2005]. Rifting and crustal thinning associated with the formation of Valles Marineris provide another possibility for the formation of this unit. Extension associated volcanism (usually basic) typically occurs in the final stages of rifting where the canyon is already opened allowing lavas to spread onto the pre-existing canyon floor. If the unit was

emplaced via this mechanism, olivine-enriched basalts would occur primarily on the floor of the canyon and not in the walls, as observed. An extensive episode of flood lava eruptions or volcaniclastic flows deposited on the surface in a relatively short time period could explain the distribution of outcrops observed in the canyon system, the estimated volume of material erupted, and composition. In this case, these flows have likely been buried under a large sequence of other flows [*McEwen et al.*, 1999]. This hypothesis can effectively explain the small variations in outcrop elevations and the seemingly single layered nature of the unit.

Variations in elevation of this unit (seen in Figure 3.3b-d) are relatively small when compared to the lateral extent of this unit; however, this layer does not appear to lie on a perfect plane requiring some other explanation for the observed variations. If a series of flood lavas or a volcaniclastic deposit were the source of this unit, variations in the average elevation data can be explained by flows filling or draping pre-existing features such as canyons, grabens, or craters. If the unit was emplaced by an intrusive mechanism, the observed irregularities can be attributed to magma preferentially following weaknesses in the country rock. Tectonic activity [*Phillips et al.*, 2001], such as faulting observed in the Valles Marineris region by previous studies [e.g. *Peulvast et al.*, 2001] may have also occurred, providing another possible explanation for the observed elevation variations; however, no direct evidence for faults has been observed in this study.

Characterizing the magma evolution of a relatively thin olivine-enriched lava flow or volcaniclastic deposit depends largely on the nature of the olivine in

the material. Olivine included as phenocrysts versus xenocrysts (foreign crystals incorporated into the magma) or magma chamber cumulate materials likely have different parent magmas, describe different crystallization sequences, and have different petrogenic histories [*McSween et al.*, 2006]. Magma with olivine included as cumulates or xenocrysts may have undergone more fractional crystallization than magma with primary olivine phenocrysts. High-pressure experiments [*Bertka and Holloway*, 1994] have placed constraints on the stable mineral phases at depth, indicating that the martian mantle is likely composed of olivine, orthopyroxene, and spinel at ~75 km below the surface. If I consider an eruption direct from the martian mantle, then to retain much of this primary phase assemblage, little fractional crystallization, little to no assimilation of evolved materials and low degrees of partial melting (all lowering the overall olivine fraction of the magma) must have occurred to form the olivine-enriched basalts found in Ganges and Eos Chasmata. Although other minerals associated with this assemblage (orthopyroxene and spinel) are not directly detected in this work, evidence for orthopyroxene in this area has been noted by several earlier studies [e.g. *Bandfield*, 2002; *Hamilton et al.*, 2003; *Bibring et al.*, 2005; *Rogers and Christensen*, 2007]. If the olivine is included as primary phenocrysts, then it is likely that these are primitive magmas that were erupted on the surface as picritic basalts, providing additional evidence that the martian mantle is likely undepleted with respect to iron content [e.g. *McSween*, 1994]. This is assuming that the formation of the olivine is a primary process and the magma was not significantly modified to include olivine cumulate materials or xenocrysts. However, the most

likely scenario is that these basalts represent primitive magmas, as suggested for the Gusev Crater olivine basalts [*McSween et al.*, 2006]. Unfortunately, it is difficult to distinguish the inclusion style of olivine utilizing ground-based measurements onboard the Mars Exploration Rovers [*McSween et al.*, 2006], making them even less distinguishable from the orbital data available in this study.

If these are lava flows, then potential eruptive centers must be considered. However, there are no evident sources for these flows, but on Earth and the Moon the source vents for flows are typically buried and the small areas exposed in the martian unit make the detection of source vents unlikely. One possibility is that these flows may be related to the initiation of Tharsis volcanism, yet not necessarily associated with any of the landforms observed today. If this were the case, these flows would likely be some of the first lavas erupted which were subsequently buried by more evolved and fractionated, olivine-depleted lavas, that obscured the source vent or caldera. A similar hypothesis has been formed for Syrtis Major and the Isidis Basin region, where Noachian to Hesperian picritic lavas were erupted in the early stages of volcanism at Syrtis major [*Tornabene et al.*, 2008]. Tornabene et al. [2008] do not identify stratigraphically higher flows indicating that the formation of picritic lavas did not occur again in the history of Syrtis Major. The observed terrain may then be interpreted as heavily impacted ancient terrain, which has been more recently exposed. Additionally, this is a plausible scenario for the Ganges and Eos Chasmata picritic flows, which likely occurred during a discrete time early in martian history (early to middle

Noachian), as flows are not observed higher in the stratigraphic section, most outcrops occur near the same elevation (low in the canyon stratigraphy) and all outcrops are relatively thin when compared to the overlying stratigraphy [*McEwen et al.*, 1999].

The exact timing of this event cannot be determined as observations of a nadir-pointing THEMIS instrument are limited on the steep slopes of the canyon walls. There may be more events of a similar composition emplaced throughout martian history captured in the walls of the canyon but they may not be able to be imaged by nadir-pointing THEMIS observation. If more events occurred throughout martian history in this location, bench-forming morphologies similar to those observed for the identified unit would be expected to occur at a variety of locations in the canyon walls; however, this is not observed supporting the conclusion that the layer identified in this study is the largest occurrence of olivine-enrichment noted to date.

3.5 Conclusions

- I have identified an *in situ*, olivine-enriched stratigraphic layer, which extends laterally over a distance of >1,100 km and has a minimum volume of ~9.9×10^4 km^3. Additionally, olivine-enriched material outside the primary study area has been observed as ejecta from small craters in the canyon floor, giving rise to the possibility that this layer is even larger than estimates given here. This layer was characterized and identified utilizing TES spectral data and THEMIS multi-spectral images, along with THEMIS nighttime temperature data to determine

the thermophysical properties of the outcrops. Most outcrops have elevated thermal inertia values (often >~600 J K^{-1} m^{-2} $s^{-1/2}$, with extremes of >1200 J K^{-1} m^{-2} $s^{-1/2}$), which indicates that this unit is not a mobile sediment and is an in place rocky unit. These observations agree well with morphologic evidence from high-resolution imagery, which display a relatively unmantled, rough and pitted surface associated with the olivine-enriched material, with some aeolian bedforms infilling the hollows and pits of the surface observed by HiRISE and MOC imagery (Figure 3.5).

- In addition to infrared data, I also used MOLA elevation data to constrain the vertical dimension of this layer, allowing for the continuity, extent, dip and orientation to be constrained. This layer is continuous over >1,100km and the olivine-enriched outcrops seem to define a layer that is essentially flat-lying. This unit persists underneath topographically high areas appearing only in expected, elevation-dependent locations, and is one of the largest continuous compositional units found on Mars to date with an estimated volume of ~9.9×10^4 km^3.
- Four possibilities for the geologic origin of the olivine-enriched unit include: 1) volcanism associated with tectonic rifting of the Valles Marineris system, 2) a volcaniclastic flow deposit, 3) an intrusive mafic sill, or 4) a discrete episode in martian history during which flood lavas were erupted onto the surface. The most likely explanation

for the geologic origin of this layer is an eruptive event consisting of compositionally uniform olivine-enriched flood lavas originating from a primitive mantle source region.

- When the Ganges and Eos Chasmata unit is compared to other olivine-enriched units on Mars, namely those identified in Ares Vallis [*Rogers et al.*, 2005], Gusev Crater [*Ruff et al.*, 2007], Isidis Planitia [*Mustard et al.*, 2007; *Tornabene et al.*, 2008], and Nili Fossae [*Hamilton and Christensen*, 2005], striking compositional (>15% olivine abundance and ~Fo_{68}), morphologic (commonly rough, pitted textures) and thermophysical (typically >500 J K^{-1} m^{-2} $s^{-1/2}$) similarities are observed. Additionally many of these units are hypothesized to have been emplaced early in martian history. These similarities in age and characteristics lead to the possibility that there was a discrete period of time early in Mars history, when compositionally uniform and extensive olivine-enriched basalts were erupted onto the surface.

CHAPTER 4

GLOBAL EVIDENCE FOR A WIDESPREAD OLIVINE-ENRICHED BEDROCK LAYER ON MARS: IDENTIFICATION OF THE BOREALIS BASIN FORMING IMPACT EJECTA DEPOSIT?

The identification and mapping of an ancient, thin, and extensive olivine-enriched basalt layer indicates an early widespread process on Mars that has gone previously undocumented. The formation of this layer is likely related to early voluminous volcanism, a magma ocean, or the Borealis basin forming impact event. While we favor the impact hypothesis, the identification of this unit provides clues into the early stages of Mars' evolution, where the responsible process could have altered the martian climate through the release of volatiles and formed the enigmatic global dichotomy.

4.1 Introduction

Exposures of ancient materials on planetary surfaces are rare and difficult to positively identify without *in situ* measurements. Planetary processes that bury, obscure, and alter these materials further complicate the identification of these materials from orbit. However, a detailed characterization of these materials, their distribution, and geologic history can provide fundamental constraints on a poorly understood period of planetary evolution through the identification processes, providing constraints on their duration, and quantifying the lasting effects these processes have in shaping the Mars we view today.

On Mars, a significant fraction of the landscape is dominated by heavily cratered terrain from the late heavy bombardment (LHB) or the relatively smooth northern lowlands that were modified subsequent to the LHB. On Earth, fast crustal recycling, abundant water, widespread volcanism, and gradational processes associated with plate tectonics have largely erased the most ancient materials from the geologic record. Many of the same processes occur on Mars, where volcanism (e.g. Tharsis, Elysium, plains units), tectonics (e.g. Valles Marineris), and outflow channels (e.g. Ares Vallis) have buried or eroded much of the ancient crust. Nonetheless, a significant fraction of the surface is ancient (Noachian or early Hesperian) and represents a portion of geologic time largely erased from Earth's surface.

Mars is a largely volcanic planet dominated basaltic lava flows [*McEwen et al.*, 1999; *Christensen et al.*, 2000a] and volcaniclastic deposits [*Robbins et al.*, 2011], with important but minor variations in the basaltic composition at the global scale [*Rogers and Christensen*, 2007]. The majority of Mars' mineralogical variability occurs at a small scale, covers a minor area of the surface, and is commonly associated with aqueous alteration [*Poulet et al.*, 2005; *Ehlmann et al.*, 2008; *Squyres et al.*, 2008].

4.2 Olivine On Mars

Against the backdrop of volcanic uniformity and localized aqueous alteration, a series of unique olivine-enriched deposits have been identified and mapped globally [*Koeppen and Hamilton*, 2008] and regionally [*Hamilton and Christensen*, 2005; *Rogers et al.*, 2005; *Mustard et al.*, 2007; *Edwards et al.*,

2008] using Thermal Emission Spectrometer (TES), Thermal Emission Imaging System (THEMIS) and Compact Reconnaissance Imaging Spectrometer for Mars (CRISM) data. Materials with elevated olivine content (>15% areal abundance) such as those found in Nili Fossae [*Hamilton and Christensen*, 2005; *Mustard et al.*, 2007], Ares Valles [*Rogers et al.*, 2005], Ganges and Eos Chasmata [*Edwards et al.*, 2008], Mare Serpentis [*Rogers et al.*, 2009], and Isisdis Basin [*Tornabene et al.*, 2008] are found in small outcrops and have the highest thermal inertia (TI) values on the planet (>500 J K^{-1} m^{-2} $s^{-1/2}$) [*Bandfield et al.*, 2011].

A thin (~60-200 m) and extensive (~1,100 km) olivine-enriched layer identified in the walls of Ganges and Eos Chasmata beneath >6 km of overlying material represents ancient material exposed on Mars [*Edwards et al.*, 2008]. Outcrops of this unit are characterized by high olivine content >15% of composition Fo_{68} (Figure 4.1a and 4.1b), elevated thermal inertia (>600-800 J K^{-1} m^{-2} $s^{-1/2}$), and a rough and pitted morphology [*Edwards et al.*, 2008]. Expanding on the original study region, I have found this olivine-enriched unit with similar thermophysical (Figure 4.2), compositional (Figure 4.3) and morphologic properties (Figure 4.4) can be mapped globally (Figure 4.1).

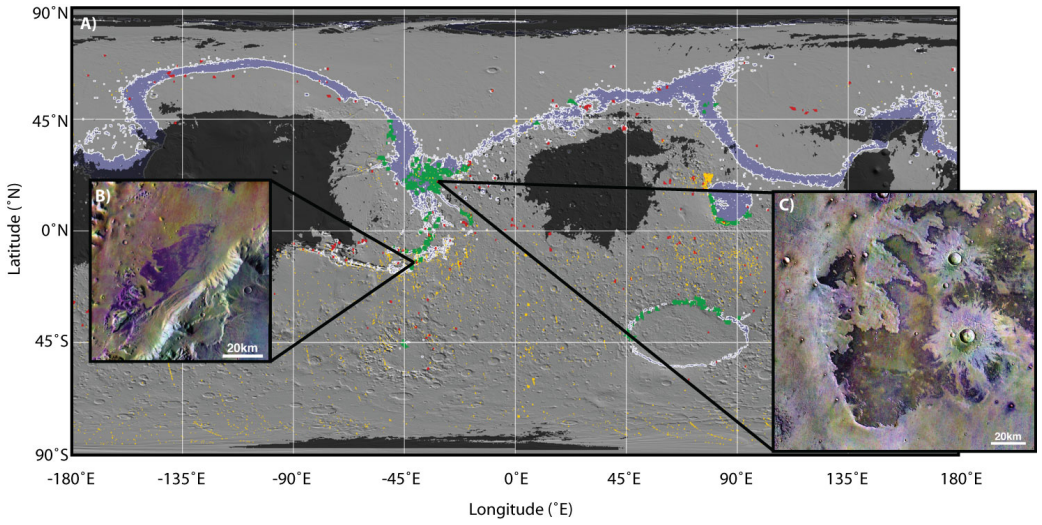

Figure 4.1. A) A MOLA shaded relief map where locations with TES Lambert albedo >0.25 are grayed out and a blue shape highlights elevations from -3900 m to -3600 m. Green shapes are olivine-enriched outcrops identified using THEMIS and TES (restricted to -5000 m to -2000 m due to the large number of observations), red shapes are olivine-enriched outcrops identified using CRISM over the entire planet, not associated with a morphologic feature (e.g. crater floor, ejecta, etc.) and orange shapes are TES pixels with a Fo_{58}-Fo_{74} index value [*Koeppen and Hamilton*, 2008] >1.01 (not restricted by elevation), **B)** THEMIS decorrelation stretch mosaic of bands 8, 7, and 5 (where olivine-enriched materials are purple) of an outcrop in Ganges and Eos Chasmata (-11.25˚ N, 322˚ E), and **C)** a location 2,000 km to the northeast of Figure B (21.75˚ N, 323.75˚ E), where two fresh impact craters have excavated below the olivine-enriched layer exposing olivine-poor material in the ejecta blanket. A small crater to the southeast has excavated olivine rich material, indicating the layer persists in the subsurface. High TI materials at the edges of the outcrop where the unit erodes back also show the strongest olivine signature.

All of this unit's remotely sensed properties can be used to determine the characteristics of the layer and constrain its emplacement, petrology, and modification history. Additional olivine-enriched bedrock locations that I consider to be related include identifications in Ares Valles [*Rogers et al.*, 2005], Isidis Basin [*Tornabene et al.*, 2008], and Ganges and Eos Chasmata [*Edwards et al.*, 2008]. This layer has compositions consistent with typical plagioclase and pyroxene abundances of martian basaltic material with an enrichment in olivine as the primary compositional distinction. This mineralogy indicates the source material that generated the unit underwent little fractional crystallization and assimilated few evolved materials [*Bertka and Holloway*, 1994]. The high TI olivine-enriched outcrops (>500 to 1400 J K^{-1} m^{-2} $s^{-1/2}$) compared to the lower TI olivine-poor regolith (Figure 4.2) indicates that the olivine-enriched materials are *in situ* exposures of bedrock and have not been significantly transported or altered. This is further supported by the fine-scale morphology, where olivine-enriched materials occur as fractured bedrock or blocky surfaces (Figure 4.4) and mobile olivine-poor materials infill local depressions.

The type examples of olivine-enriched bedrock occur in Ganges and Eos Chasmata and the outflow channels around Chryse Planitia (Figures 1b,c), with numerous additional occurrences along the dichotomy boundary. The thickness of the olivine-enriched layer (~200-300 m) is determined where lower TI, olivine-poor materials can be observed both above and below the high-TI, olivine-enriched material (Figure 4.1c, Figure 4.2). Previous work has shown that this unit is continuous over great distances (~1,100 km) and it is only observed where

it has been exposed by erosion that has removed the overlying igneous and sedimentary material. Global mapping has revealed that this unit, where exposed, occurs consistently at ~3,800 ± 500 m below datum over its >4,000 km extent. Olivine-enriched materials, located at similar elevations in the walls of Hellas Basin, may also be related; however, the extensive alteration, impact and glaciation history in Hellas makes the correlation of olivine-enriched outcrops difficult.

4.3 Instrument Description and Methods

Olivine-enrichment is straightforward to identify in a variety of spectral data acquired of Mars including those from THEMIS, TES and CRISM. The THEMIS thermal infrared imager is a 9 spectral channel, 320 by 240 element uncooled, micro-bolometer array that covers a wavelength range of 6.7-14.8 μm. It has 100 m/pixel spatial sampling from the 420 km altitude orbit of the 2001 Mars Odyssey spacecraft [*Christensen et al.*, 2004a]. The TES instrument onboard the 1997 Mars Global Surveyor spacecraft consists of several instruments including a broadband thermal bolometer (covering 5.1-150 μm), visible/near-infrared (0.3-2.9μm) radiometers and a Michelson interferometric spectrometer (5.8-50μm with 5 or 10cm^{-1} spectral sampling) with a six-element array of uncooled deuterated triglycine sulfate (DTGS) pyroelectric detectors [*Christensen et al.*, 2001] and has a ~3x6 km footprint on the surface per detector. The CRISM visible/near-infrared instrument onboard the Mars Reconnaissance Orbiter spacecraft is a grating imaging spectrometer, with two detectors (a silicon photodiode and a cooled HgCeTd 640x480 element array) that sample from 0.4-1

μm and 1.0-4.0 μm at 6.55 nm spectral sampling with full resolution images reaching ~15-38 m/pixel spatial sampling [*Murchie et al.*, 2007].

THEMIS multi-spectral data are the primary means used here to identify outcrops of the olivine-rich layer because of their nearly global coverage, high spatial resolution, and ability to easily discriminate olivine-bearing materials from typical basaltic compositions (Figure 4.1a) observed on Mars [e.g. *Hamilton and Christensen*, 2005; *Rogers et al.*, 2005; *Edwards et al.*, 2008]. THEMIS nighttime infrared data, converted to thermal inertia [*Fergason et al.*, 2006a] were used to facilitate the identification of bedrock units, and provided a very effective means to identify these materials (Figure 4.2). A TES spectral index [*Koeppen and Hamilton*, 2008] designed highlight olivine of various forsterite compositions (Figure 4.3, Fo_{58-74}) was used where the outcrop was large enough and high quality TES data were available. CRISM FRT/HRL/HRS targeted data were used where available and provide high spatial resolution observations for many of the smaller outcrop locations. Where High Resolution Image Science Experiment (HiRISE) data or Mars Orbiter Camera (MOC) data were available, the morphology of the olivine-rich outcrops was assessed using the highest resolution images available allowing for the determination of fine scale (0.5-3m) morphologies.

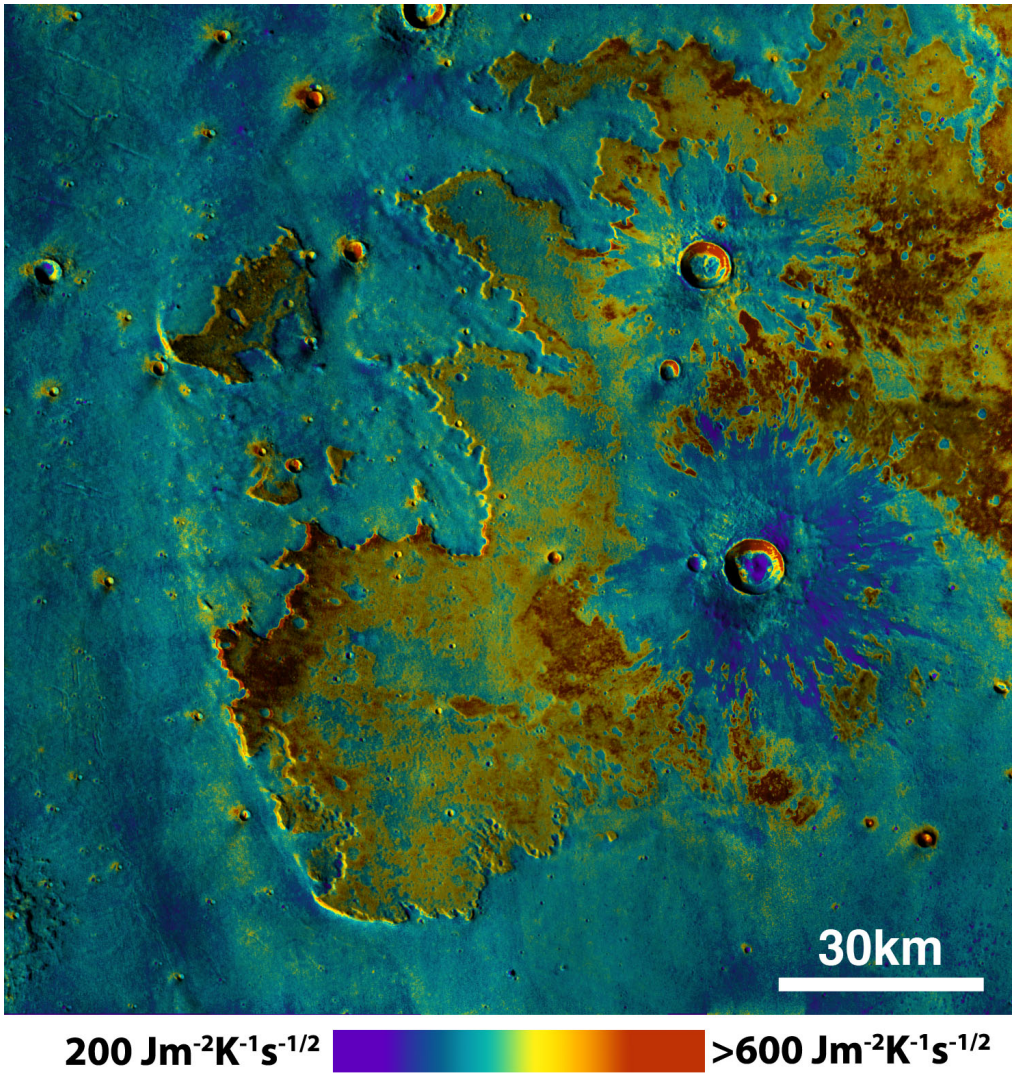

Figure 4.2. A colorized THEMIS TI [*Fergason et al.*, 2006a] mosaic over daytime temperature illustrates high TI values (>600 J K^{-1} m^{-2} $s^{-1/2}$, red tones with a maximum of ~800 J K^{-1} m^{-2} $s^{-1/2}$) are associated with the edges of the unit and the highest olivine content. The lowest TI values (~200 J K^{-1} m^{-2} $s^{-1/2}$, blue tones) are associated with ejecta, pits, and the lower surrounding plains. Flat sections of the olivine-enriched unit are likely mantled by aeolian materials and exhibit a similar spectral and thermophysical character to the surrounding olivine poor plains.

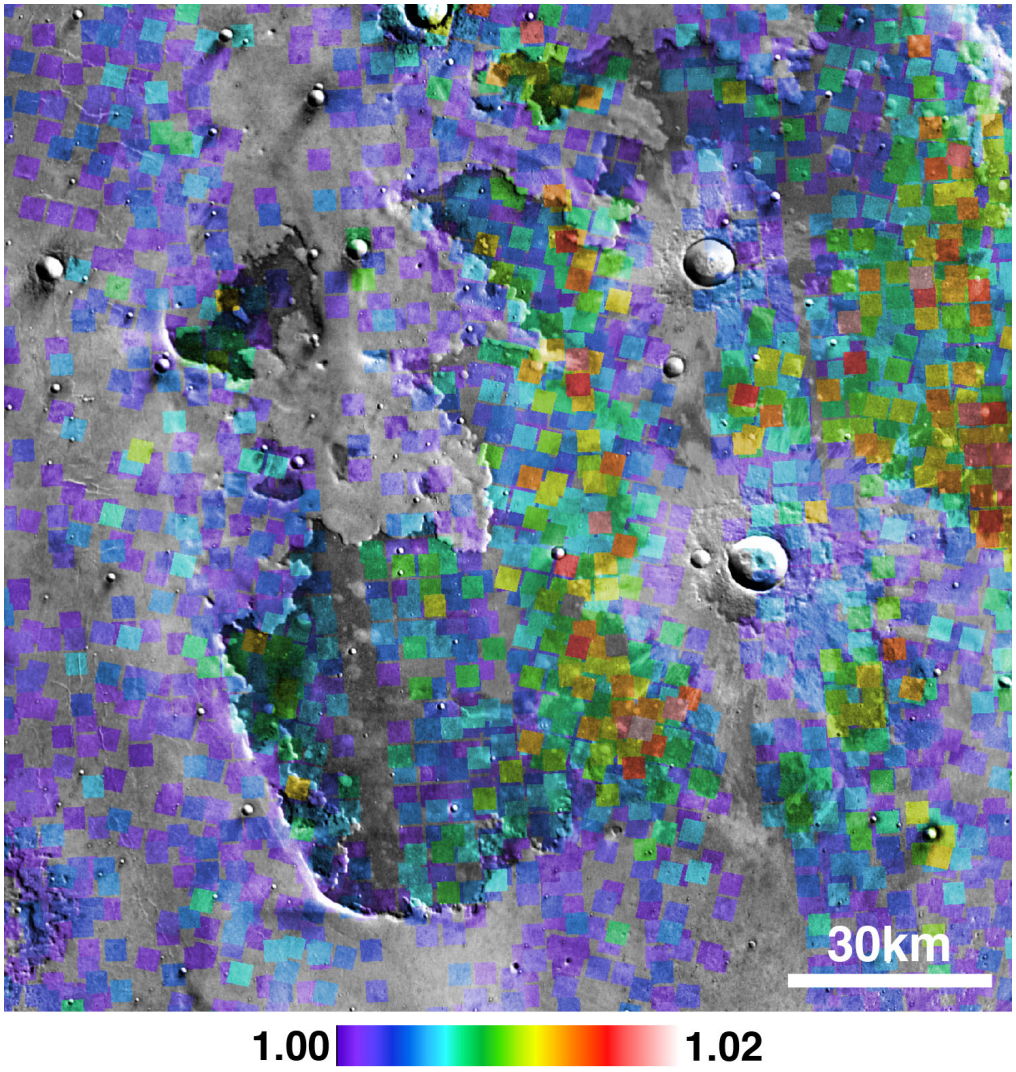

Figure 4.3. A colorized spectral index of TES data highlights olivine with forsterite compositions ranging from ~58 to ~74 [*Koeppen and Hamilton*, 2008] overlain on a THEMIS daytime infrared mosaic of the same location as Figure 1c. In this case the highest index values (>1.02, red tones) correspond with the strongest identification of olivine with a composition of Fo_{58-74}, while the lowest index values (<1.00, blue and purple tones) indicate a weak or non-existent olivine identification. Figure 1c and this figure have good agreement regarding the locations with the strongest identification of olivine.

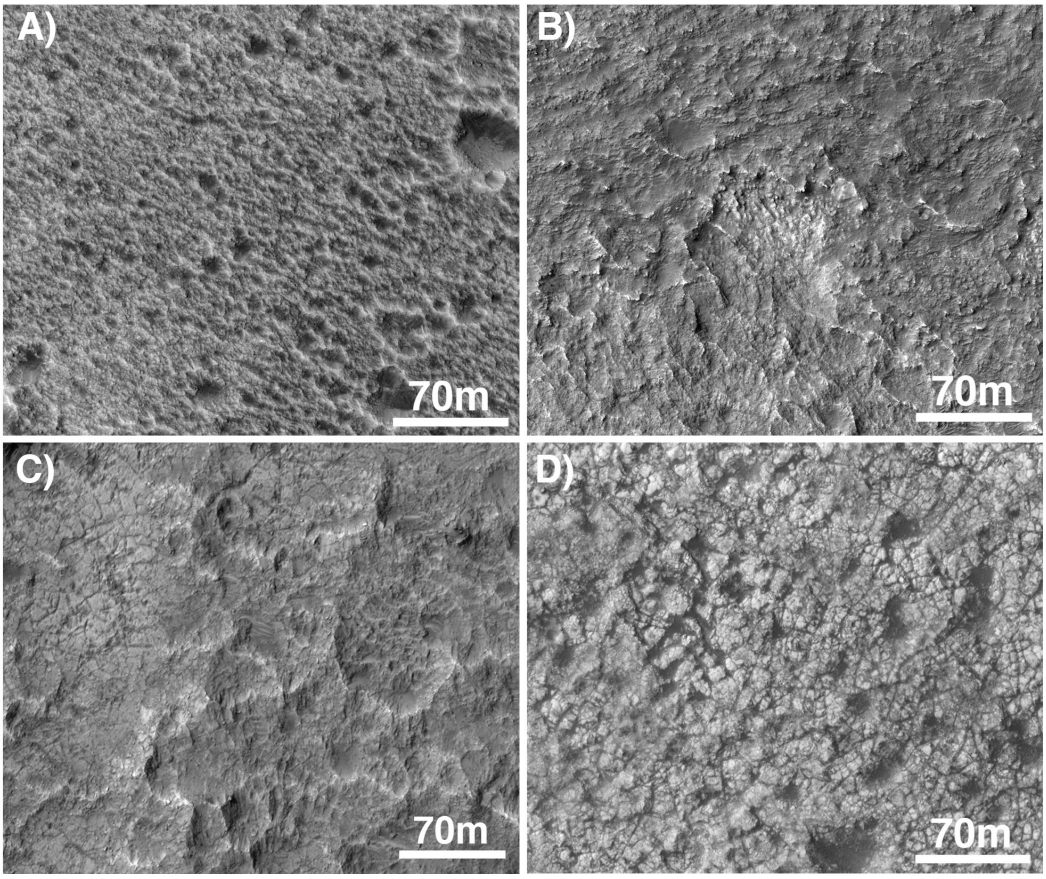

Figure 4.4. HiRISE showing the range of fine-scale morphologies observed for various outcrops, where darker material infills topographic lows and have a weaker olivine signature than the lighter toned, blocky and pitted olivine-enriched materials. **A)** Chryse Planitia (ESP_017278_2020), **B)** Eos Chasma (PSP_001798_1685), **C)** Ravi Vallis (PSP_008628_1800), and **D)** Ares Vallis (PSP_007889_1865). Textural variability may be from different weathering environments, as these images sample a range of latitudes and contexts (e.g. channel floors vs. flat plains).

4.4 Key Observations

4.4.1 Composition

Using a variety of spectral data, I have constrained the composition of an olivine-rich, rocky unit with typical outcrops having >10% areal abundance of olivine. Olivine-rich deposits on Mars have been discussed in detail in the literature and many of these locations coincide with outcrop identifications made in this study [*Hamilton and Christensen*, 2005; *Rogers et al.*, 2005; *McSween et al.*, 2006; *McDowell and Hamilton*, 2007; *Mustard et al.*, 2007; *Edwards et al.*, 2008; *Koeppen and Hamilton*, 2008; *Tornabene et al.*, 2008; *Rogers et al.*, 2009; *Edwards et al.*, 2010; *Rogers and Fergason*, 2011]. In general, these olivine-rich outcrops have plagioclase and pyroxene compositions within the range of typical basaltic materials on Mars [e.g. *Rogers and Christensen*, 2007] and differ primarily in higher olivine (Fo_{58-74}) abundances (>10% to 20%) then are found in regional basaltic lava units abundances.

The magma that generated the olivine-rich materials must be derived almost directly from the martian mantle and have undergone little fractional crystallization and little to no assimilation of more evolved materials. If more evolved materials were included in the melt, the olivine content of the materials would be significantly lower than what is observed [*Bertka and Holloway*, 1994]. While the context and crystal size of the olivine in the rock is not well constrained, the olivine must have sufficiently large crystals and be pervasive through the rock to exhibit characteristic vibrational modes in the thermal infrared

at the 100 m/px scale. This indicates that the melt must have cooled at a rate slow enough to crystallize olivine-rich basalt and not a quenched basaltic glass.

4.4.2 Physical Nature

Assessing the competence and physical characteristics of material that composes the olivine-rich outcrops helps constrain the mobility of the outcrop material. In general olivine-rich outcrops identified in this study have thermal inertia values >500 to 1400 J K^{-1} m^{-2} $s^{-1/2}$ and always have a higher thermal inertia than the surrounding olivine-poor martian materials (Figure 4.2). The elevated thermal inertia associated with the olivine-rich outcrops indicates that the material is relatively immobile and the derived thermal inertia values are consistent with some of the rockiest materials on the planet [*Edwards et al.*, 2009].

The relationship between the high thermal inertia olivine-rich outcrops and the typically lower thermal inertia olivine-poor martian may be related to weathering and alteration processes in some cases [*Bandfield and Rogers*, 2008; *Bandfield et al.*, 2011]. However, in the cases I present here, there is no visible transition (either physically or mineralogically/chemically) from olivine-rich, high thermal inertia to olivine-poor, low thermal inertia materials. Therefore I conclude that based on these observations, the olivine-rich materials identified are likely in-place and have not been significantly displaced from their original locations.

4.4.3 Morphology

The morphology associated with olivine-rich outcrops (Figure 4.4) exhibit a variety of different textures and fine scale morphologies. Olivine-rich outcrops are commonly lighter toned than the surrounding olivine poor material and typically exhibit a rough and pitted texture with olivine-poor aeolian material infilling local depressions. This range of morphologies is common to other high thermal inertia materials [*Edwards et al.*, 2009], as well as other olivine rich materials [*Edwards et al.*, 2008]. In some cases, the outcrops exhibit fractured and blocky textures (Figures 4c and d) though the range of these textures may be related to the range of latitudes and planetary settings in which the identified olivine-rich outcrops are found.

4.4.4 Thicknesses

The only method by which the thicknesses of the identified outcrops can be constrained is through the positive identification of olivine-poor, low thermal inertia material both above and below the outcrops. In Ganges and Eos Chasmata the olivine-rich materials were characterized where possible through these means and typical outcrop thicknesses were found to be ~200 m [*Edwards et al.*, 2008]. In Figure 4.1c, two impacts that occurred in the olivine-rich material have exposed olivine-poor material from the subsurface that was incorporated as ejecta. In a location to the southeast in Figure 4.1c, a small impact crater exhibits a prominent olivine signature indicating that the olivine rich material at approximately the same elevation as the high thermal inertia olivine bench to the northwest is present below the olivine poor surface. These types of observations

help constrain the vertical extent of this layer, indicate that it is relatively thin, and is likely present but masked in many instances.

4.4.5 Additional Observations of Olivine

While many processes on Mars result in olivine enrichment, (e.g. volcanism [*Hamilton and Christensen*, 2005], post-impact volcanism, and impact ejecta [*Mustard et al.*, 2007]) for all of the cases identified in this study I have not been able to associate a geologic process likely responsible the emplacement of the olivine-rich material. Several locations of previously identified materials that I consider related are: Ares Valles [*Rogers et al.*, 2005], Isidis Basin [*Tornabene et al.*, 2008], and Ganges and Eos Chasmata [*Edwards et al.*, 2008], as well as other anomalous basaltic regions that occur in Surface Type 2 regions [*Rogers and Christensen*, 2003]. The locations identified in all of these cases, have striking similarities to those outcrops originally identified in Ganges and Eos Chasmata, where they have ~Fo_{68} olivine with >10% areal abundance, elevated thermal inertia values (>800 J K^{-1} m^{-2} $s^{-1/2}$ in Ares Valles) and have a rough and pitted fine scale morphology that is often fractured at the 10s of meters scale. In addition to positive identifications of olivine, many of the anomalous basaltic locations originally identified using TES data only [*Rogers and Christensen*, 2003], are co-located and highly correlated with positive identifications of olivine-rich materials in this study. In other cases, olivine-rich materials that occur near volcanic centers [*Hamilton and Christensen*, 2005] or as proposed impact ejecta deposits [*Mustard et al.*, 2007], are not considered related and often

have different fine-scale morphologies and can be readily associated with geologic features.

4.4.6 The Distribution of Olivine-rich Outcrops

The olivine-rich outcrops identified in this study are widespread and occur over a wide range of locations on the martian surface. However, the most common location for these materials to crop out is the dichotomy boundary, where the ancient crustal materials are well exposed. These outcrops occur at remarkably similar elevations (approximately 3,800 ± 500 m below the martian datum) over the ~4,000 km or more extent of this unit.

Olivine-rich materials are also observed in walls of Hellas Basin. While the elevation of olivine-rich materials in Hellas is within ~1000 m of those in other locations, the elevations of outcrops are more variable. However, this variability could result from the complex history of impact, alteration, and glaciation that has occurred in Hellas. It is difficult to discern materials that were present before the Hellas Basin impact event and those materials that have been emplaced after its formation. These exposures do not appear to be related to any distinguishable geologic feature and are commonly exposed as small hills with elevated thermal inertia on the rim of Hellas Basin.

The observations of olivine-rich outcrops are not complete on all areas of the planet primarily due to increased dust cover that precludes orbital compositional studies in places like Arabia Planitia and the Tharsis Montes. In addition, other geologic processes can make positive identifications difficult including mass wasting, erosional, or impact processes that can either bury or

erode through the layer or other depositional processes such as volcanism. However, the location of these olivine-rich outcrops is not necessarily coincident with the major volcanic provinces on Mars and more often outcrops occur hundreds to thousands of kilometers away.

As it has been mapped, this layer records a unique, large-scale geologic process that has not previously been noted and is unlike any other geologic layer identified to date on Mars. Because a large majority of outcrops occur at similar elevations over large distances, are relatively thin and occur at depth within the crust, I conclude that this unit is a discrete, major geologic layer emplaced over a relatively short period of time early in martian history.

4.5 Formation Models

Any model for the formation of this large-scale, olivine-enriched layer must satisfactorily explain its: 1) unique composition (>10%-25% ~Fo_{68}), 2) ancient age (>6 km of heavily cratered overlying material), 3) large-scale ($1.5x10^6$ km^3 to >$5x10^6$ km^3) and observed continuity (>4,000 km laterally), and 4) rocky nature (elevated TI and fine-scale morphology). I present three scenarios and the supporting and opposing evidence under which a layer with these characteristics could form.

4.5.1 Magma Ocean

First, the formation of an olivine-enriched layer may be related to an early magma ocean with significant density stratification. A magma ocean could be responsible for producing the earliest martian crust within ~30-50 Myr after

accretion [*Elkins-Tanton et al.*, 2005]. In this scenario, several crustal compositions, consistent with what is observed from orbit, would be produced, including olivine and pyroxene rich materials [*Elkins-Tanton et al.*, 2005]. This model explains the observed surface compositions and constrains the formation to early Mars history. Furthermore, if two different melt source regions were present, a magma ocean might also explain the origin of the enigmatic dichotomy and the widespread distribution of the olivine-enriched materials [*Zhong and Zuber*, 2001; *Elkins-Tanton et al.*, 2005].

Although a magma ocean may have played a significant role in martian history, this model fails to satisfactorily explain an olivine-enriched layer with the observed thickness. A cumulate overturn/magma ocean model predicts a massive compositionally uniform layer hundreds of kilometers thick [*Elkins-Tanton et al.*, 2005] where olivine-enriched materials would make up the lower portion of the crust, and not the observed continuous thin layer. While model parameters such as mantle composition, solid and melt fractions [*Elkins-Tanton et al.*, 2003], and timing are difficult to constrain, this process may be responsible for the genesis of the more typical martian crust over millions to tens of million of years [*Elkins-Tanton et al.*, 2003; *Elkins-Tanton et al.*, 2005] and the observed olivine-enriched layer may be related to a later event that was short lived by comparison.

4.5.2 Compositionally Distinct Volcanism

Second, I propose a period of intense and widespread volcanism or near-surface intrusions that may have occurred shortly after crustal formation, possibly as a result of enhanced surface heat flux associated with core formation (~3.5-4

Ga) [*Solomon*, 1979]. However, Hf-W isotope anomalies in SNC martian meteorites [*Lee and Halliday*, 1997; *Kleine et al.*, 2002] suggest the martian core and crust formed contemporaneously within ~30 Myr of solar system formation, shortly after accretion and not later in martian history, moving the time of peak heat flux earlier.

The distribution and thickness of the layer necessitates that volcanism with a unique composition occurred once and briefly over much of the martian surface, with peak heat flux as the driving mechanism to partially melt the mantle. However, reconciling the timing of peak heat flux, crustal differentiation, and solidification and the necessity for a differentiated and solid crust by the time of the olivine-enriched layer's emplacement is difficult. While this and the magma ocean model may predict a massive deposit rather than a thin layer, basal sections may be thinner olivine-enriched cumulates consistent with observations. The improbability of a discrete period in early martian history of widespread, compositionally distinct volcanism over much of the planet's surface is the major argument against this hypothesis, though early planetary processes are not well understood and these events may be commonplace

4.5.3 Mega-Impact Ejecta

As the final scenario, an impact that formed the Borealis basin may have produced the regional to global olivine-enriched layer. A high-energy impact would excavate the crust and upper mantle and distribute these materials over the planet's surface, with distribution and volume as a function of impact energy and angle [*Marinova et al.*, 2008]. Head-on impacts generate large volumes of melt

(up to ~80km global equivalent layer depth) and would likely erase all evidence of impact features [*Marinova et al.*, 2008]. However for conditions in the early solar system with bodies >1,000 km in diameter traveling in roughly parallel orbital planes at similar velocities [*Wilhelms and Squyres*, 1984], a glancing impact is more likely [*Marinova et al.*, 2008]. If the borealis basin was formed by an impact [*Marinova et al.*, 2008], its very existence argues for a glancing impact of an object ~2,000 km diameter [*Marinova et al.*, 2008] that would produce 6-20 km global equivalent depth of melt [*Marinova et al.*, 2008]. Total melt volume decreases with impact angle and except for the most energetic impacts, 50-70% of the melt would be concentrated in the excavation area and 10-30% ejected from the planet altogether [*Marinova et al.*, 2008]. The remaining 20-30% mantle rich melt material would be deposited on the planet in a layer ~1.2 to ~6 km thick, with all or part of this material comprising the olivine-enriched layer.

This model explains many aspects of the olivine-enriched layer. The Borealis basin likely formed shortly after accretion and crust formation explaining the ancient age [*Solomon et al.*, 2005]. Impact melt that includes martian mantle is consistent with an olivine-enriched composition [*Marinova et al.*, 2008] and the large impact can account for the layer's widespread distribution. Additionally, the excavation boundary —a 10,600 km by 8,500 km ellipse centered at 67˚ N, 208˚ E [*Andrews-Hanna et al.*, 2008]—is coincident with many outcrops of this layer. Some olivine-enriched materials found northward of the excavation boundary do not form a distinguishable a layer, but they could be an exposed olivine unit that formed from melt within the impact structure.

The Borealis impact ejecta model also best explains the relatively thin nature of the layer. If the layer is continuous between outcrops, its extent and thickness imply a total volume >$3x10^6$ km^3 and may be as large >$2x10^7$ km^3 if outcrops observed in Hellas Basin are included. The melt volumes predicted by numerical impact models [*Marinova et al.*, 2008] are ~1-1.5 orders of magnitude larger than what is calculated for the olivine-enriched layer, but this discrepancy may be insignificant as the layer may be olivine cumulate materials from a more voluminous ejecta deposit. While the expected stratigraphy from the contemporaneous deposition of ejecta and crustal thickening has not been modeled, an olivine cumulate is consistent with what would likely form at the base of a thick, molten eject unit. Subsequent to the impact, basaltic crustal materials were emplaced superposed on the existing dichotomy, cratered during the LHB, and degraded with the subsequent deposition of materials derived and eroded from the southern highlands onto the northern lowlands [*Solomon et al.*, 2005]. This sequence of events and compositions, matches the observed geology well. Given the testable and observable aspects of each model, I conclude that the mega-impact ejecta model is the most reasonable mechanism by which a thin, olivine-enriched layer from early in Mars history could form.

4.7 Implications

- Regardless the formation mechanism, this ancient, rocky, olivine-enriched layer on Mars has significant implications for the early history of the planet. While I favor the Borealis-impact model, the presence of an extensive layer of unique composition indicates a significant planet-wide

event. In our view, this layer provides evidence for and constraints on the Borealis impactor. If the materials observed in the walls of Hellas are part of this unit, the layer must pre-date the Hellas impact event and the layer is likely a global deposit. The significance of the layer as a marker for early Mars history is unique among current observations.

- In all the models considered, the formation of this layer would be associated with significant planetary heating and may have depleted the mantle of volatiles, affecting the global water cycle in later history. The layer's relatively uniform elevation indicates a nearly spherical early Mars with little topographic variability, indicating that today's topographic variability is entirely due to subsequent volcanism, tectonism, and large impact events.
- In addition to providing constraints on martian dichotomy formation models, this olivine-enriched layer likely represents some of the most ancient material present on the surface of Mars and has properties consistent with material derived from a primitive mantle source region. These materials could provide important constraints on the differentiation of Mars, mantle, and core chemistry, the source material of some SNC meteorites, and the timing of the Borealis basin forming event. Any site where olivine-enriched material has been identified by this work provides a unique sampling site for future sample return or rover missions. Analysis of these materials either by a lander or sample return mission could help illuminate early planetary processes that are poorly understood.

CHAPTER 5

IMPACT RELATED DECOMPRESSION MELTING: THE FORMATION OF WIDESPREAD INFILLED CRATERS AND INTER-CRATER PLAINS ON MARS

Infilled craters on Mars have been observed since the first spacecraft viewed the surface and early work characterized these craters as infilled by sedimentary materials. Later work using THEMIS thermal inertia determined these craters contain some of the rockiest materials on the planet and not sedimentary materials. Here I investigate the distribution, physical properties (morphology and thermal inertia), and composition of these craters over the entire planet. The majority of the ~3,300 rocky crater floors identified are concentrated in the low albedo (0.1-0.17), cratered southern highlands. These craters are associated with the highest thermal inertia values (> 500 to 2000 J m^{-2} K^{-1} $s^{-1/2}$), some of the most mafic materials on the planet (enriched in olivine/pyroxene vs. high-Si phases/plagioclase, often with >10-15% olivine areal abundance), and formed ~3.5 billion years ago. Several processes could be responsible for the formation of the crater floors, though the most likely scenario is volcanic infilling through fractures created in the impact event. Furthermore, the generation of the primitive magma source directly results from decompression melting of the martian mantle by the removal of the crustal material excavated by the impactor. This process only occurred in early Martian history, during or shortly after the Late Heavy Bombardment when the crust was still relatively thin and heat flow

was high. This process was widespread and responsible for the eruption of significant volumes of primitive material, both inside and outside of craters. Decompression melting accounts for the unusual infilling of martian crater sand is an important planetary process that has gone previously undocumented.

5.1 Introduction

Deeply infilled crater were first observed by Mariner 4 in 1965 and have remained an enigma ever since. Various processes to fill martian craters have been proposed, including aeolian sedimentation [e.g. *Arvidson*, 1974; *Christensen*, 1983; *McDowell and Hamilton*, 2007], lacustrine sedimentation [e.g. *Newsom et al.*, 1996; *Cabrol and Grin*, 1999; *Fassett and Head*, 2005; *Pondrelli et al.*, 2005] and impact processes such as impact melt ponding [e.g. *Schultz*, 1976; *Smrekar and Pieters*, 1985; *Wilhelms et al.*, 1987]. However, these explanations are unsatisfying because nearby similar sized craters are often unfilled, the surrounding terrains are typically unmantled, and the process by which environmental conditions necessary to form widespread aeolian or fluvial deposition were created has not been adequately identified.

In this paper, I investigate the physical and compositional properties of the crater-filling materials and conclude that a different process – impact induced decompression melting of the martian mantle – is responsible for the inter crater materials as well as extensive regions of the intra-crater plains.

5.2 Background

High-thermal inertia surfaces (>1200 J K^{-1} m^{-2} $s^{-1/2}$) interpreted as exposed bedrock have been characterized High-thermal inertia surfaces (>1200 J K^{-1} m^{-2} $s^{-1/2}$) interpreted as exposed bedrock have been characterized and mapped on Mars from 75˚ S to 75˚ N [*Edwards et* al., 2009] using Thermal Emission Imaging System (THEMIS) [*Christensen et al.*, 2004a] nighttime infrared data. *Edwards et al*. [2009] have identified three distinct morphologies associated with outcrops of in-place rocky material, including: 1) valley and crater walls on steep slopes, 2) flat crater floor surfaces with higher-thermal inertia material present in the crater floor than the crater walls, and 3) plains surfaces not related to any major topographic feature, which commonly show wind scouring morphologies, such as rough and pitted textures. The distribution of these features suggests several factors that control the exposure, creation, and destruction of bedrock, including high-latitude periglacial processes and dust mantling [*Edwards et* al., 2009]. However, there are many locations on the martian surface that meet conditions where bedrock is expected to occur yet it is not observed, leading to the possibility that large-scale crustal processing, reworking, and/or mantling has destroyed or masked a majority of the bedrock on Mars [*Edwards et* al., 2009].

One of the three high-thermal inertia morphologies identified was flat crater floor materials [*Edwards et* al., 2009]. Some of these infilled craters were identified previously identified using Viking Infrared Thermal Mapper (IRTM) data [*Christen*sen, 1983] and Mariner 9 visible imaging data [*Arvid*son, 1974]. The crater floors were characterized by their elevated thermal inertia, low albedo

splotches occurring on the downwind side of the crater, and their flat-floors and lack of central peaks [*Arvidson*, 1974; *Christensen*, 1983]. The characteristics of these craters include several fundamental and unique parameters not common to other martian impact craters, with: 1) a flat-floor with no discernable central peak and a rough, pitted fine-scale (meter scale) morphology and aeolian materials infilling topographic lows, 2) elevated thermal inertia in the crater floor as compared to the surrounding terrain and crater walls, and 3) extensive post-impact modification, with shallow sloped walls, little-to-no visible ejecta material, and occasional gullies and impact craters on both the walls and floor [*Edwards et al.*, 2009].

The original mechanism proposed for the infilling of these craters was largely considered to be aeolian [*Arvid*son, 197*4; Christen*sen, 1983]. However, the high-thermal inertia values derived from THEMIS suggest that these deposits are instead in-place rocky material and not mobile sediment [*Edwards et* al., 2009]. *Edwards et al*. [2009] proposed that these craters were filled with lithified sediment or with volcanic materials. In this work, I expand our study to include all infilled craters with elevated floor thermal inertia values and diameters >1 km that are visible using the 100 m/pixel THEMIS global mosaics [*Edwards et al.*, 2011b] (Figure 5.1). Similar infilled craters have been identified on the Moon [e.g. *Schultz*, 1976; *Smrekar and Pieters*, 1985; *Wilhelms et al.*, 1987] and may have formed by the infilling of impact melt or through impact related volcanism. However, on Mars, no evidence for flow features commonly associated with impact melt has been identified in association with this crater type.

Approximately 3,300 craters have been identified (Figure 5.2) and several fundamental questions arise regarding high-thermal inertia, infilled craters: 1) What is the geologic origin of the high-thermal inertia crater floor material (e.g. sedimentary, volcanic, impact melt)? 2) What geologic process or processes are responsible for the emplacement of these materials? and 3) What does the spatial and temporal distribution of infilled craters indicate about the planetary evolution of Mars?

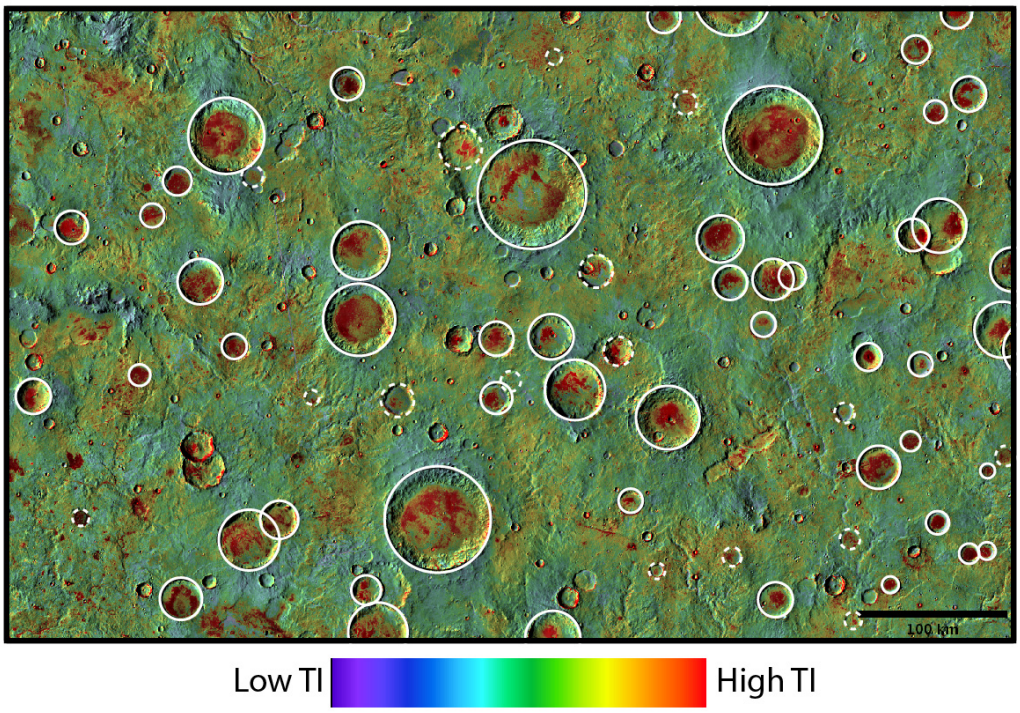

Figure 5.1. Colorized THEMIS nighttime temperature overlain on THEMIS relative daytime temperature from the THEMIS global mosaic [*Edwards et al.*, 2011b, and references therein] of a region of the southern highlands centered near 83.5˚ E, 45˚ S. In this view, blue tones indicate lower nighttime temperatures and relatively low-thermal inertia surfaces while, red tones indicate higher nighttime temperatures and relatively high-thermal inertia and rockier surfaces. Temperatures are normalized and are only relative. Craters classified with elevated floor thermal inertia values are identified by a solid white circle while potential candidates which were not examined in detail are identified by a dashed white circle

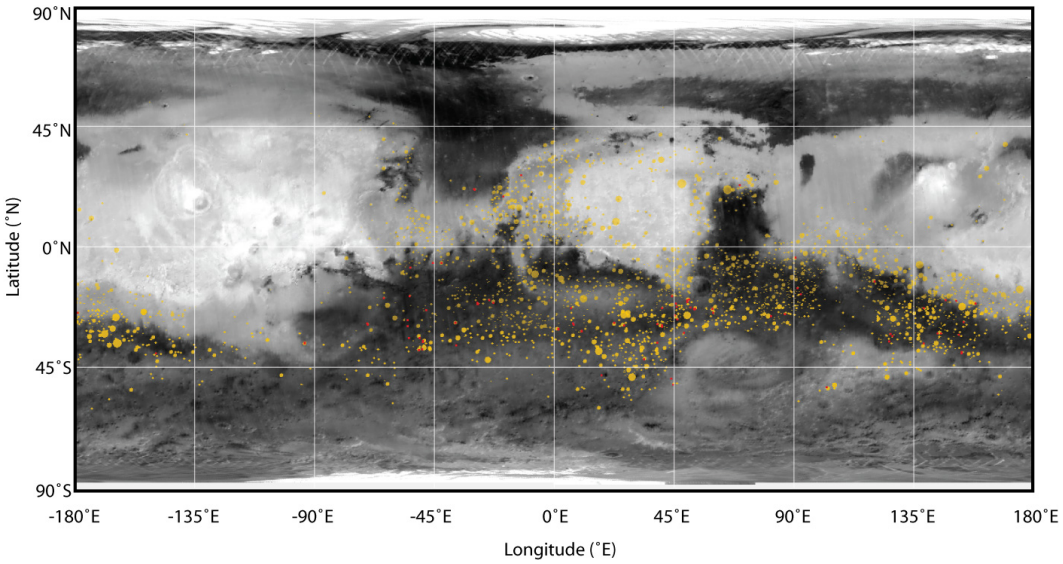

Figure 5.2. The global distribution of craters with floors that have a relatively high-thermal inertia as compared the surrounding terrain on a TES Lambert albedo map. The yellow circles are craters identified as having a relatively high-thermal inertia from the THEMIS nighttime global mosaic. The red dots are locations that were identified by *Edwards et al.* [2009] as crater floors that are consistent with bedrock exposures.

While representative portions of the southern cratered highlands containing many infilled craters such as Mare Serpentis [*Rogers et* al., 2009] and Tyrrhena and Iapygia Terrae [*Rogers and Ferga*son, 2011] have been characterized in detail [*Rogers et al.*, 2009; *Rogers and Fergason*, 2011], no study has specifically focused on the thermophysical and compositional properties of infilled craters.

Detailed localized compositional studies of small regions from orbit [e.g. *Hamilton and Christensen*, 2005; *Rogers et al.*, 2005; *Mustard et al.*, 2007; *Edwards et al.*, 2008; *Tornabene et al.*, 2008; *Ehlmann et al.*, 2009; *Rogers et al.*, 2009; *Rogers and Fergason*, 2011; *Wray et al.*, 2011] provide important and fundamental understanding of geologic processes on Mars, but global-scale studies have the ability to fundamentally change the current understanding of and synthesize planetary evolution, as well as identify wide-scale processes on planetary surfaces. In this study, I examine the composition of all infilled craters on Mars that have flat-floors, no central peak and elevated thermal inertia as compared to the surrounding terrain, following similar techniques as those used in other studies [e.g. *Bandfield*, 2002; *Rogers et al.*, 2005; *Rogers and Christensen*, 2007; *Rogers et al.*, 2009; *Rogers and Fergason*, 2011] using Thermal Emission Spectrometer (TES, [*Christensen*, 1999]), Compact Reconnaissance Imaging Spectrometer for Mars (CRISM, [*Murchie et al.*, 2007]), THEMIS spectral data in combination with THEMIS thermal inertia data [*Fergason et al.*, 2006a] and crater age dates [*Neukum and Wise*, 1976; *Neukum and Hiller*, 1981; *Hartmann and Neukum*, 2001; *Ivanov*, 2001; *Neukum et al.*, 2001], with the aim of

constraining the process or processes responsible for the formation of high-thermal inertia infilled craters.

5.2 Method

5.2.1 Crater Selection Criteria

The morphologic and thermophysical criteria used to identify infilled craters originally, were: 1) higher-thermal inertia inside the crater than the surrounding terrain and crater walls, 2) relatively flat-floors with no identifiable visible central peak, 3) degraded rims with highly eroded or non-existent ejecta deposits, and 4) no other identifiable source for the high-thermal inertia material (e.g. volcanic centers, and sedimentary mounds such as that observed in Gale Crater, etc.).

In order to map the global distribution of craters with these characteristics, I used the THEMIS daytime and nighttime relative temperature mosaics [*Edwards et al.*, 2011b] to first assess the morphology and qualitatively examine the thermal inertia differences between the crater floors and the surrounding terrain. While the THEMIS global mosaics only map the relative temperature, as they are normalized for season, atmospheric conditions, and local time, they are extremely valuable for determining relative differences in thermophysical properties [*Edwards et al.*, 2011b]. I examined every location on the planet from 75˚S to 75˚N for locations where crater floors show warmer nighttime temperatures than the surrounding wall materials. In all I identified ~3,300 craters that met these criteria using the THEMIS global mosaics and were flagged for further

investigation. I included all regions, including the typically dusty provinces of Elysium, Tharsis and Arabia, and did not include a crater size restriction other than the limit of the 100 m/pixel resolution of the THEMIS global mosaics [*Edwards et al.*, 2011b]. Crater center location and diameter were recorded and mapped for craters that met the above criteria.

5.2.2 Surface Property Datasets

5.2.2.1 Compositional Data

5.2.2.1.1 THEMIS

THEMIS is an infrared and visible multispectral imager onboard the 2001 Mars Odyssey spacecraft. In this work I used THEMIS multi-spectral daytime infrared data at 100-meter per pixel spatial sampling to assess the compositional variability of the high-thermal inertia crater floors. THEMIS bands 8, 7, and 5 (11.79, 11.04 and 9.35 μm respectively) can be used to emphasize the strong absorptions due to olivine and other mafic minerals such as pyroxenes [e.g. *Christensen et al.*, 2003b; *Edwards et al.*, 2008; *Rogers et al.*, 2009] that are lacking in the surrounding lower-thermal inertia inter-crater plains and crater walls. A running-decorrelation stretch [*Gillespie et al.*, 1986; *Edwards et al.*, 2011b] was performed on the multi-band THEMIS images to emphasize spectral differences; using the 8, 7, and 5 band combination, the olivine-enriched materials appears purple. All THEMIS data were processed using a variety of advanced image processing techniques including, time-dependent focal plane temperature variation removal, temperature variation across the THEMIS calibration flag

removal, line- and row-correlated noise removal and uncorrelated random noise removal noise removal [*Bandfield et al.*, 2004a; *Edwards et al.*, 2011b]. For a more detailed discussion of advanced THEMIS data processing techniques see *Edwards et al.* [2011b].

5.2.2.1.2 TES

The Mars Global Surveyor Thermal Emission Spectrometer consists of several different instruments including a broadband thermal bolometer (covering 5.1-150 μm), visible/near-infrared (0.3-2.9 μm) bolometer and a Michelson interferometer (5.8-50 μm with 5 or 10 cm^{-1} spectral sampling) with a six-element array of uncooled deuterated triglycine sulfate (DTGS) pyroelectric detectors [*Christensen et* al., 2001], each yielding a ~3x8 km footprint on the surface. I primarily used the thermal infrared interferometer for compositional work, along with the visible/near-infrared bolometer to derive surface Lambert albedo.

Two different approaches were taken with TES data: 1) a full removal of atmospheric components and derivation of mineral abundances [e.g. *Ramsey and Christensen*, 1998; *Bandfield et al.*, 2000a; *Smith et al.*, 2000; *Rogers et al.*, 2007; *Rogers and Aharonson*, 2008] for several example sites, and 2) a spectral index for large-scale mapping and comparison with THEMIS thermal inertia data. In the first case, a limited set of warm surface (>255 K), clear atmosphere (9 μm dust extinction <0.15 and 11 μm ice extinction <0.04), low albedo (<0.17) TES data were selected, with emission angles <5˚, no solar panel or image motion compensator mirror motion, and orbit counter keeper (OCK) values <7000. Once the data of interest were identified, I removed the atmospheric contribution by

fitting each TES spectrum with a library of mineral spectra (Table 5.1) and atmospheric components [*Bandfield et al.*, 2000b] using the linear deconvolution surface-atmosphere separation routine documented by *Smith et al*. [2000].

I used the 507cm^{-1} spectral index developed by *Rogers and Fergaso*n [2011] to map global variability in mafic-ness as this index is directly affected by the abundances of olivine and/or pyroxene relative to the plagioclase and/or high-silica phases present on the surface [*Rogers and Ferga*son, 2011]. While any spectral index will not explicitly determine the mineral abundances, the 507 cm^{-1} is able to place constraints on the mafic-ness of a surface and measures the non-atmospherically corrected emissivity slope between 423-434 cm^{-1} and 497–508 cm^{-1} (TES bands 27–28 and 34–35) [*Rogers and Ferga*son, 2011].

When I performed spectral index mapping, the quality parameters listed above were relaxed (including data with higher dust and water-ice extinctions, higher albedo, and lower surface temperature values) to allow for greater surface coverage. This is acceptable as the 507 cm^{-1} spectral index is not very sensitive to atmospheric variability and works well on lower surface temperature data [*Rogers and Ferga*son, 2011]. This spectral index was applied widely over the planetary surface and was used to systematically compare high-thermal inertia crater floors to typical martian surfaces, without the need to derive TES surface emissivity spectra and introduce a more complicated metric for assessing the mafic-ness of the planet.

Table 5.1. Spectral Library used in quantitative mineral abundance determination from TES data after *Rogers and Fergason* [2011]

[a]*Reference Number/Source*	*Spectrum Identifier*	*Assigned Mineral Group*
ASU	Quartz BUR-4120	Quartz
ASU	Microcline BUR-3460	Alkali feldspar
ASU	Albite WAR-0235	Plagioclase
ASU	Oligoclase BUR-060D	Plagioclase
ASU	Andesine WAR-0024	Plagioclase
ASU	Labradorite BUR-3080A	Plagioclase
ASU	Bytownite WAR-1384	Plagioclase
ASU	Anorthite BUR-340	Plagioclase
1	Shocked anorthosite	Plagioclase
	at 17 GPa	Plagioclase
	at 21 Gpa	Plagioclase
	at 25.5 Gpa	Plagioclase
	at 27 Gpa	Plagioclase
	at 38 Gpa	Plagioclase
	at 56.3 Gpa	Plagioclase
ASU	Bronzite NMNH-93527	Orthopyroxene
ASU	Enstatite HS-9.4B	Orthopyroxene
ASU	Hypersthene NMNH-B18247	Orthopyroxene

Table 5.1. continued

2	Average Lindsley pigeonite	Low-Ca clinopyroxene
ASU	Diopside WAR-6474	High-Ca clinopyroxene
ASU	Augite NMNH-9780	High-Ca clinopyroxene
ASU	Augite NMHN-122302	High-Ca clinopyroxene
ASU	Hedenbergite manganoan DSM-HED01	High-Ca clinopyroxene
ASU	Forsterite BUR-3720A	Olivine
ASU	Fayalite WAR-RGFAY01	Olivine
3	KI 3362 Fo60	Olivine
3	KI 3115 Fo68	Olivine
3	KI 3373 Fo35	Olivine
3	KI 3008 Fo10	Olivine
4	Illite Imt-1 < 0.2 mum (pellet)	Phyllosilicates
ASU	Ca-montmorillonite solid STx-1	Phyllosilicates
5	Saponite (Eb-1) < 0.2 mum (pellet)	Phyllosilicates
4	Swy-1 < 0.2 microns (pellet)	Phyllosilicates
6	K-rich glass	Glass

Table 5.1. continued

6	SiO2 glass	Glass
7	Opal-A (01-011)	Amorphous silica
8	Al-Opal	Amorphous silica
9	Average Meridiani and Aram Hematite (TT derived)	Oxide
ASU	Anhydrite ML-S9	Sulfate
ASU	Gypsum ML-S6	Sulfate
10	Kieserite	Carbonate
ASU	Calcite C40	Carbonate
ASU	Dolomite C20	Zeolite
11	Crystalline heulandite	Zeolite
11	Crystalline stilbite	Zeolite

[a]Spectral library after *Rogers and Fergason* [*2011*] where, individual mineral spectra are from the ASU spectral library available online at http://speclib.asu.edu [2000b], except as indicated as from alternate sources: (1) *Johnson et al.* [2002]; (2) *Wyatt et al.* [2001]; (3) *Koeppen and Hamilton* [2008]; (4) *Michalski et al.* [2006]; (5) *Michalski et al*. [2005]; (6) Wyatt et al. [2001]; (7) *Michalski et al*. [2003]; (8) provided by M.D. Kraft; (9) *Glotch et al.* [2004]; (10) *Baldridge* [2007]; (11) *Ruff* [2004]

5.2.2.1.3 CRISM

CRISM, onboard the Mars Reconnaissance Orbiter spacecraft is a grating imaging spectrometer with two detector arrays and a maximum of 15 m/pixel spatial sampling from 0.4-4.0 μm at 6.55 nm spectral sampling. CRISM spectral data were utilized primarily to help provide compositional information at high spatial resolution to provide context for fine-scale morphology from High-Resolution Imaging Science Experiment (HiRISE) [*McEwen et* al., 2007] and Mars Orbiter Camera (MOC) [*Malin et* al., 1998] images. The low-Ca pyroxene and high-Ca Pyroxene spectral indices (LCPINDEX and HCPINDEX) [*Pelkey et* al., 2007], as well as the modified olivine spectral index (OLINDEX2) [*Salvatore et* al., 2010] were the primary indices utilized in locations where craters had CRISM coverage. The limited spatial coverage of CRISM full resolution targeted data precluded a more systematic and detailed global study.

5.2.2.2 Physical Properties

5.2.2.2.1 THEMIS Thermal Inertia

Thermal inertia is defined as $I = (\kappa\rho c)^{1/2}$, where κ is the thermal conductivity, r is the bulk density of the material, and c is specific heat. I used the KRC thermal model [*Kieffer*, submitted] to model surface temperatures and derive thermal inertia given a variety of observational and planetary conditions, including local time, solar longitude, atmospheric dust opacity, surface slopes, and broadband visible albedo following Fergason et al. [2006a] and Edwards et al. [2009].

Thermal inertia on Mars is strongly controlled by the thermal conductivity [*Kieffer et al.*, 1973; *Jakosky*, 1986; *Presley and Christensen*, 1997a; c; b; *Piqueux and Christensen*, 2011]. Assuming the material in question is homogeneous and an unconsolidated particulate, thermal inertia derived from spacecraft data can be related to effective particle size using laboratory experiments and physical models [*Kieffer et al.*, 1973; *Piqueux and Christensen*, 2009; *Piqueux and Christensen*, 2011], and has been used quantitatively determine the physical properties of the upper several decimeters of surface material. Under Martian environmental conditions, surfaces with lower-thermal inertia are interpreted as having smaller effective particle sizes.

I used the approach described *by Edwards et al*. [2009], where minimum, maximum and average thermal inertia values were derived from each THEMIS image framelet (256 line segment of a THEMIS infrared image; approximately 32 by 26 km at 100 m/pixel sampling) and stored in a database. This approach allows for global coverage while preserving some information about the small-scale variability by identifying the highest, minimum, and average value of each surface location.

In order to ensure high quality and well-calibrated thermal inertia data were used in this study, I restricted nighttime surface temperatures to >160K, avoiding interfering effects from seasonal CO_2 frost. Other constraints following the method used by *Edwards et al*. [2009] included limiting the study to nadir-looking images with <10% data dropouts, nighttime data with a solar incidence angle of >95˚ (below the local horizon), and local solar times earlier than 0630.

No data poleward of 60˚ latitude were allowed as the thermophysical properties in these regions are often dominated by CO_2 and H_2O ices that complicate the interpretation of thermal inertia values [e.g. *Bandfield and Feldma*n, 2008; *Piqueux et al*., 2008].

Additional steps to ensure well calibrated thermal inertia data include limiting the difference between TES average atmospheric radiance with a spatial sampling of 2 pixels per degree (convolved with the THEMIS band 10 spectral response function) and THEMIS band 10 average framelet radiance to less than $\pm 2 \times 10^{-5}$ W m^{-2} sr^{-1} μm^{-1} [*Edwards et* al., 2009]. Differences between average THEMIS framelet thermal inertia and TES binned at 2 pixels per degree thermal inertia were limited to less than ±220 J m^{-2} K^{-1} $s^{-1/2}$ because a difference of this magnitude may indicate a highly non-homogenous surface or the inaccuracy of either dataset [*Edwards et* al., 2009]. Framelets with an average or minimum thermal inertia values of zero J m^{-2} K^{-1} $s^{-1/2}$ or 2000 J m^{-2} K^{-1} $s^{-1/2}$ and framelets with maximum or average thermal inertia values of zero J m^{-2} K^{-1} $s^{-1/2}$ were also discarded [*Edwards et* al., 2009].

For THEMIS thermal inertia mosaics that were created for individual crater sites, I used the method described by *Fergason et al.* [2006a] with the constraints described above to convert every individual pixel in a band 9 THEMIS nighttime infrared image from brightness temperature to thermal inertia. I then mosaicked the ~20 resulting thermal inertia images together *Edwards et al.* [2011b]. Further details regarding the methods used and their associated uncertainties are available in *Edwards et al.* [2011b] and *Fergason et al.* [2006a].

5.2.2.2.2 Fine-Scale Morphology

HiRISE, Context Imager (CTX) [*Malin et* al., 2007], and MOC high-resolution visible images (~0.3 m/px, ~5 m/px, and 1.5-6 m/px respectively) were used when available to assess the fine-scale morphology of identified craters. I also related these fine-scale data to compositional data from CRISM and THEMIS to establish relationships between in-place and mobile aeolian materials.

5.2.2.3 Comparison of TES Compositional and THEMIS Thermophysical Data

In order to directly compare TES spectral index data to THEMIS thermal inertia data, they must be at the same spatial resolution. In order to map THEMIS framelet thermal inertia data, I binned the maximum THEMIS thermal inertia value for each THEMIS framelet (32 by 26 km, ~2 ppd at the equator) to a 16ppd (~3.5k m) global map [e.g. *Edwards et al*., 2009]. A similar process was done for TES 507 cm^{-1} index data, where the maximum index value in each bin is used. This allows for the direct comparison of these two datasets either globally or for individual crater floors defined by an ellipse, despite the desperate native measurement spatial resolutions.

5.2.3 Age Dating of Crater Floor Surfaces

A selected subset of 154 crater floors were selected for age dating by crater counting in order to investigate possible variations in the composition, morphology, and thermophysical properties of the infilled craters with age. This selection included all the bedrock crater locations (54) originally identified

[*Edwards et* al., 2009] and a random sampling of craters >30 km in diameter with elevated thermal inertia values (100). All locations had sufficient coverage with CTX images to allow for robust cratering statistics. Only smaller craters >100 m in diameter on the flat-floor of the large crater under examination were counted. I specifically excluded craters that were present on the walls of the larger crater and did not include craters that were superposed on modification features such as landslides or bedforms. I excluded ~40 total crater floors from the final results (114 total craters remaining) for a variety of reasons including those with insufficient CTX coverage or floors that experienced modification processes (e.g. mass wasting, aeolian bedforms, etc.) over a significant fraction of the surface.

Finally, only crater floors with similar thermophysical characteristics were chosen to ensure the surfaces would have similar crater retention properties. In this work, I am not specifically interested in an absolute date for each crater, but are instead concerned with the relative timing of the formation of each cater floor and the subsequent modification of the primary crater floor surface.

Following standard crater counting methods [*Hartmann and Neukum*, 2001; *Ivanov*, 2001; *Neukum et al.*, 2001; *Michael and Neukum*, 2010 and references therein], I plotted the cumulative crater frequency per square kilometer against the crater diameter in kilometers [*Michael and Neu*kum, 2010] and fit surface ages using standard Mars cumulative cratering frequency isochrons and production curves [e.*g. Hartmann and Neu*kum, 200*1; Iva*nov, 2001]. I applied a resurfacing correction [*Michael and Neu*kum, 2010] for those craters above the characteristic resurfacing 'kink' where a good fit was not achievable and our

cumulative crater frequency plot had a lower slope than the typical production isochrons.

5.3 Results

5.3.1 Composition and Thermal Inertia of an Example Site

In order to establish the validity of global trends using THEMIS thermal inertia and TES compositional data (Table 5.2), an example site that best typifies the characteristics in this study was examined. The site chosen had: 1) an elevated thermal inertia associated with the crater floor (Figure 5.3), 2) highly degraded morphology, and 3) was located in the low albedo, ancient cratered southern highlands at equatorial to moderate latitudes (<30˚). Multiple techniques and datasets were used to assess the composition (Figures 5.4-5.7) and the thermophysical properties (Figure 5.3) of the example site.

Spectral deconvolution results from TES (Figure 5.7, Table 5.2) provide the most quantitative determination of olivine and pyroxene abundance. These results clearly show that the crater floor material is enriched in olivine (15% areal abundance) as compared to the lower-thermal inertia inter-crater plains (no modeled olivine). Figure 5.6 shows 507 cm^{-1} spectral index values over the same region as the THEMIS thermal inertia values shown in Figure 5.3. The TES 507 cm^{-1} (Figure 5.6) has significantly higher values over the locations associated with higher olivine and pyroxene abundances as observed by quantitative TES deconvolution (Figure 5.7), THEMIS DCS (Figure 5.4), and CRISM OLINDEX2 (Figure 5.5).

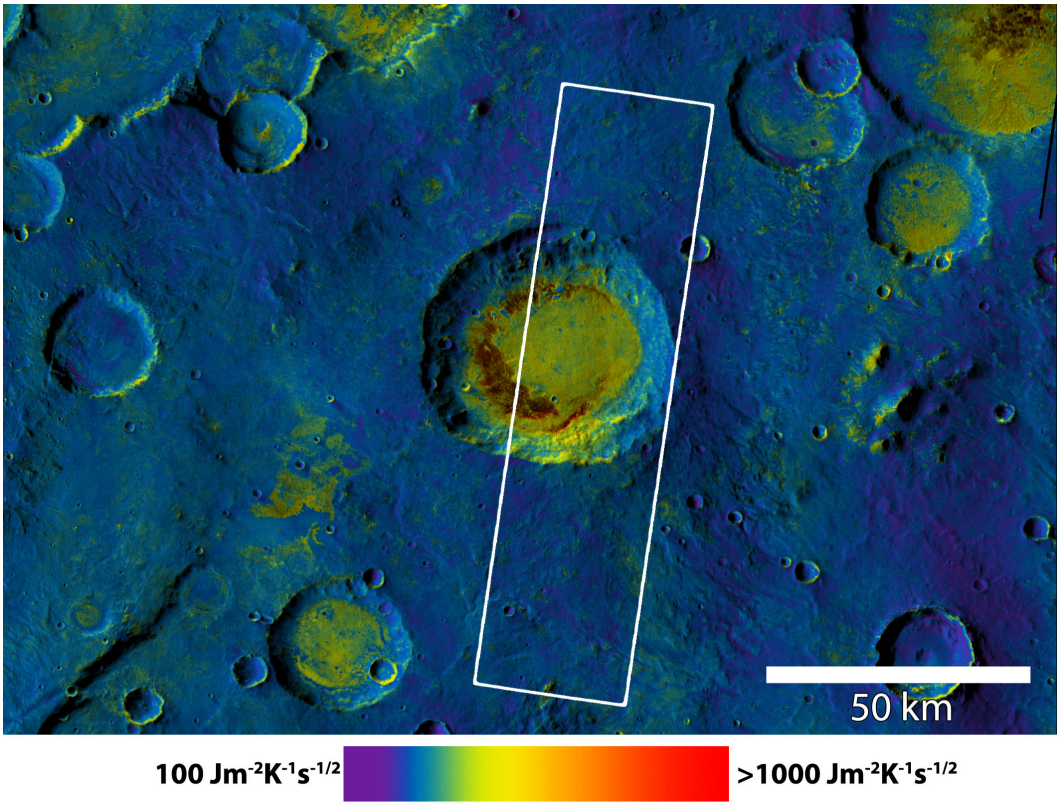

Figure 5.3. THEMIS colorized thermal inertia mosaic overlain on a THEMIS daytime temperature mosaic centered near 41.0˚ E, 21.5˚ S. The blue-purple tones in this data represent low-thermal inertia values (~100-250 J m^{-2} K^{-1} $s^{-1/2}$) consistent with fine particulate martian regolith. Red tones represent high-thermal inertia values (>1000 J m^{-2} K^{-1} $s^{-1/2}$) consistent with in-place rocky materials, which are concentrated in the crater floors of the region and rarely are present in the walls of craters or inter-crater plains. The center crater is the location of detailed analyses of THEMIS, CRISM and TES data. The location Figure 5.4 is shown as the white box.

Table 5.2. Modeled Mineral abundances and other properties

Mineral Group	*Typical Plains (%)*	*Crater Floor (%)*
Feldspar	29 (5)	35 (6)
Pyroxene	33 (6)	21 (5)
Olivine	-	14 (4)
High-Si	20 (8)	17 (7)
[a]Other	17 (2)	11 (3)

Additional Properties:

[b]Mafic Index	Low 507cm^{-1} Index (<1.0004)	High 507cm^{-1} Index (>1.006)
[c]CRISM OLINDEX2	Low OLINDEX2	High OLINDEX2
THEMIS DCS (8, 7, and 5) color	pink, green	magenta, purple
[d]Thermal Inertia (J m^{-2} K^{-1} s$^{-1/2}$)	~200	>800

[a]Other includes: sulfate, carbonate, hematite, quartz

[b]The 507cm^{-1} is described in *Rogers and Fergason* [2011]

[c]OLINDEX2 is described in *Salvatore et al.* [2010]

[d]THEMIS thermal inertia was calculated following *Fergason et al.* [2006a]

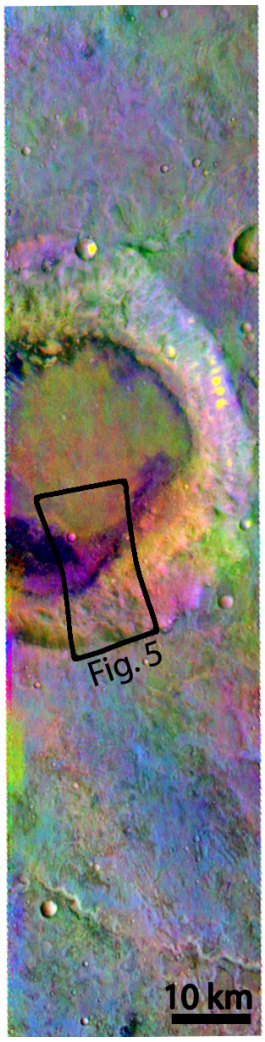

Figure 5.4. THEMIS bands 8-7-5 (projected as red, green, and blue respectively) decorrelation stretch of the image (I41931002) outline identified in Figure 5.3. Purple tones are consistent with olivine-enriched materials. Locations with the largest band 7 (11.04 μm) absorptions (due to the presence of olivine) are highly correlated with the locations that exhibit the highest thermal inertia values shown in Figure 5.3. Green/blue/pink tones are consistent with martian basaltic materials (Figure 5.7). The outline of a CRISM image (HRL00013311_07, Figure 5.5) is shown for reference.

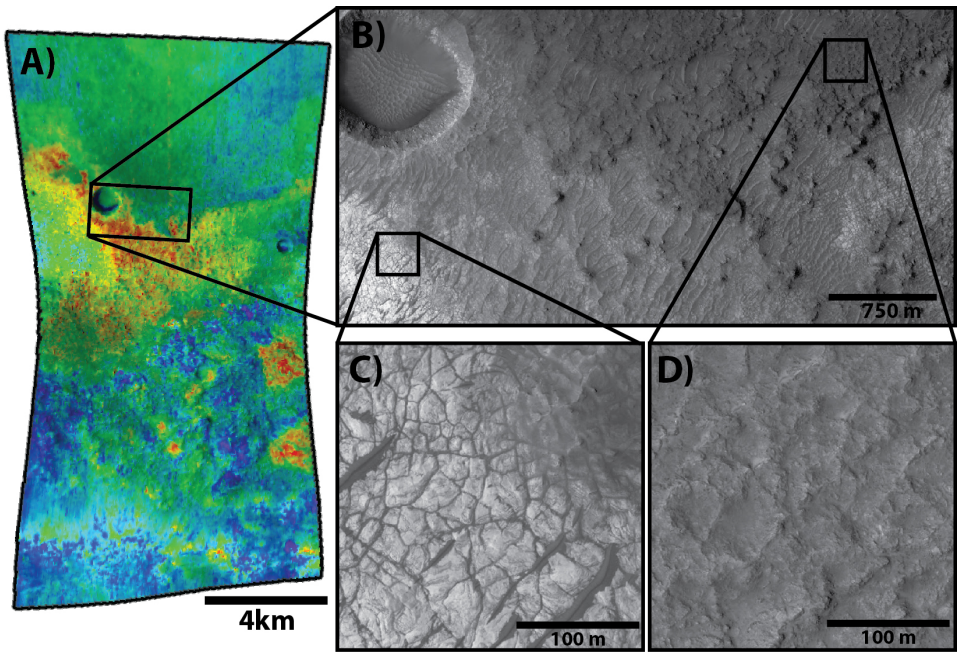

Figure 5.5. A) CRISM (HRL00013311_07) OLINDEX2 parameter colorized where blue tones have relatively low index values and red tones have relatively high index values. This image shows the same trend as the THEMIS image shown in Figure 5.4, where the strongest olivine identifications are consistent with the locations that have the highest thermal inertia values. **B)** A section of a HiRISE image (ESP_013504_1580) that shows the fine-scale surface morphologies associated with olivine-enriched **(C)** and olivine-poor **(D)** materials. C**)** A close up view of a typical olivine-enriched surface, where the fractured and lighter toned material is coincident with the strongest olivine absorptions in both CRISM and THEMIS data, and is likely in-place bedrock. **D)** A close up view of a typical olivine-poor surface, where the material is relatively dark, and appears somewhat rough, with little to no blocks or fractures visible on the surface.

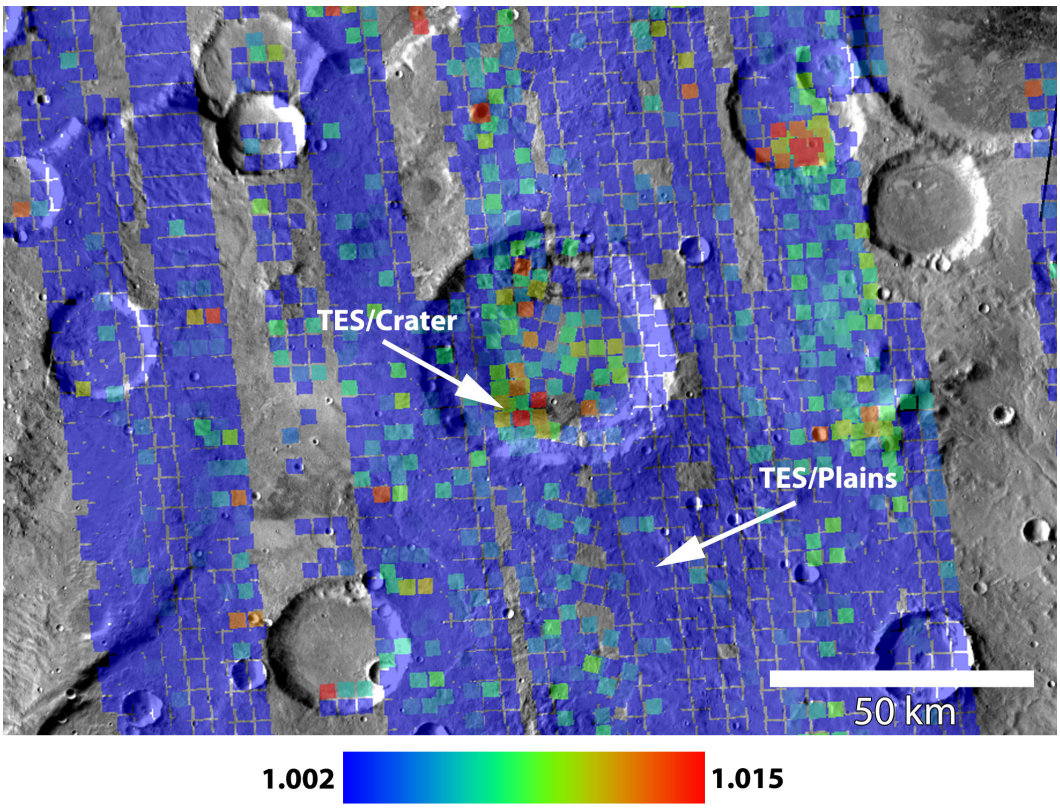

Figure 5.6. TES 507 cm^{-1} spectral index [*Rogers and Ferga*son, 2011] colorized and overlain on a THEMIS daytime temperature mosaic centered at 41.0˚ E, 21.5˚ S. The blue tones in this data represent data with low index values (<1.002) and are consistent with material that have low pyroxene/olivine abundances. Red tones are data values >1.015 and have high pyroxene/olivine abundances. The areas with the highest index values are consistent with the areas associated with the highest thermal inertia values (Figure 5.3) and olivine absorptions present in both CRISM and THEMIS images. The trend in this example is present in many high-thermal inertia crater floors (Figure 5.9).

The darkest purple tones in the THEMIS DCS images indicate the presence of elevated olivine abundances (Figure 5.4) and correlate well with the highest thermal inertia units shown in Figure 5.8. The highest CRISM OLINDEX2 [*Salvatore et* al., 2010] values (Figure 5.5a) are directly correlated with elevated olivine abundances in the THEMIS decorrelation stretch image. Similar trends have been noted in other detailed studies [*McDowell and Hamilton*, 2007; *Rogers et al.*, 2009; *Rogers and Fergason*, 2011] that included a compositional and thermophysical analysis of a selection of craters on Mars. The results from this sample site are consistent with previous work and the compositions derived from THEMIS (Figure 5.4), CRISM (Figure 5.5) and TES (Figure 5.6 and 5.7) agree well and all indicate that the highest thermal inertia materials (> 800 J m^{-2} K^{-1} $s^{-1/2}$, Figure 5.8) correspond directly to the most mafic materials in the region.

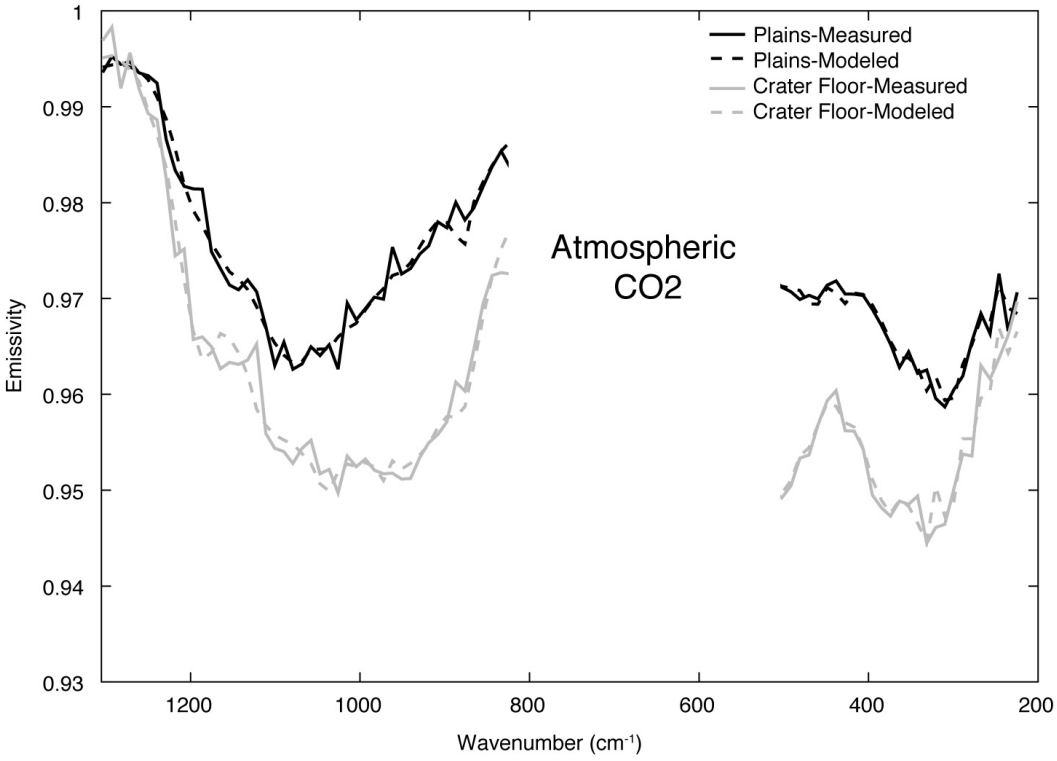

Figure 5.7. Atmospherically corrected TES surface emissivities of crater floor materials and the surrounding plains. I have modeled (dashed lines) the observed TES data (solid lines) using linear spectral deconvolution techniques [*Ramsey and Christensen*, 1998; *Rogers and Aharonson*, 2008]. I derive areal abundances that indicate the crater floor material is enriched in olivine (~14%) over the surrounding plains (with no modeled olivine). The crater floor also has a complementary decrease in high-silica, other minor phases, and an increase in plagioclase when compared to the surrounding plains. The locations from where the spectra were acquired are indicated in Figure 5.6.

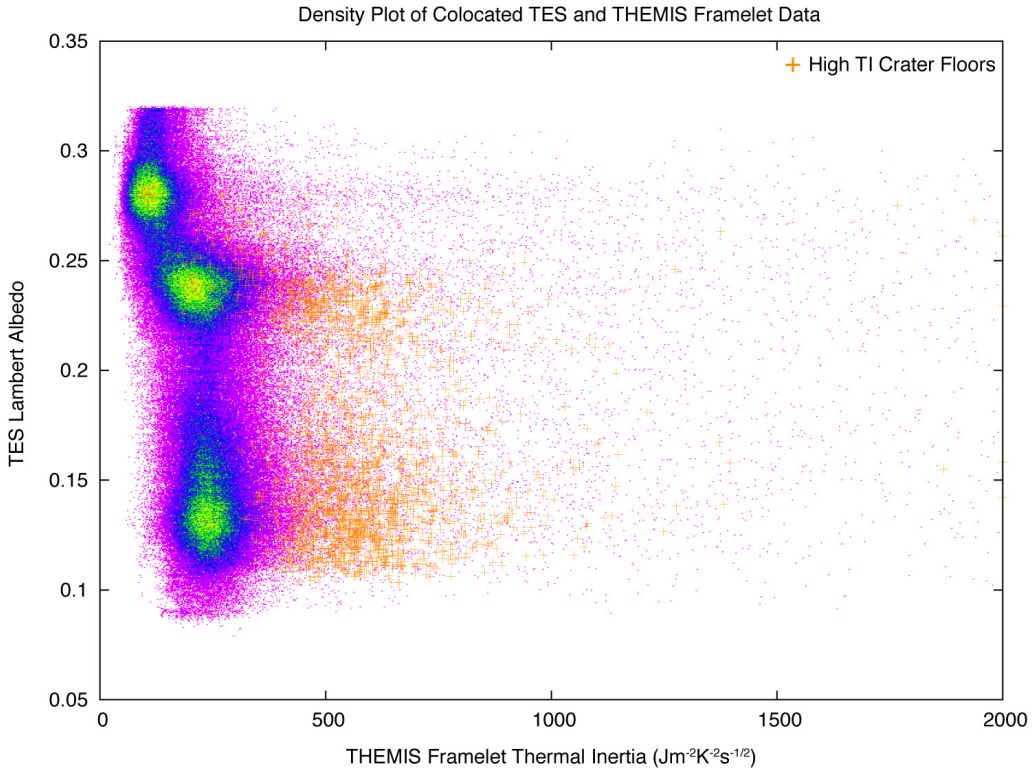

Figure 5.8. A density plot with values ranging from 1 count (purple) to 43 counts (red) of THEMIS average framelet thermal inertia versus TES Lambert albedo over all locations that meet quality constraints documented in the Methods section. The orange crosses are the maximum THEMIS framelet thermal inertia versus the average TES albedo under each crater identified (Figure 5.2) where both data are available. The majority of martian surfaces group in moderate (~200-300 J m^{-2} K^{-1} $s^{-1/2}$) thermal inertia values over a wide range of albedo values. As the albedo increases, the average thermal inertia generally decreases. Of particular interest is that while the crater floors do not exhibit any significant albedo trends and have same groupings as the rest of planet, the thermal inertia values associated with the craters are significantly higher (typically >400 J m^{-2} K^{-1} $s^{-1/2}$) than typical martian surfaces.

5.3.2 Global Properties

5.3.2.1 Distribution

The majority of the infilled high-thermal inertia craters were identified (> ~3,300) in the relatively low albedo (0.1-0.17) southern highlands (Figure 5.2). This pattern likely results from the thermal inertia constraint, as a thermal inertia difference between the crater floor and surrounding walls and plains must be observed for a positive identification to be made. In dusty locations like Arabia, positive identifications are difficult due to the relatively homogenous regional thermal inertias and pervasive dust mantling. However, a smaller fraction of craters occur in regions that have elevated albedo values (0.2-0.25) and bordering the major dust provinces of Arabia, Tharsis, and Elysium. The absolute THEMIS thermal inertia for individual craters is variable with maximum values within each crater ranging from ~300 to >2000 J m^{-2} K^{-1} $s^{-1/2}$ (with the thermal inertia lookup table having limits of 20 to 2000 J m^{-2} K^{-1} $s^{-1/2}$).

In rare cases (<10), craters were identified in the major dust covered areas and are likely due to the initial identification method using only the relative temperature THEMIS global mosaics. While crater floors in these high albedo areas exhibit a higher thermal inertia (~200 J m^{-2} K^{-1} $s^{-1/2}$) than the surrounding plains (often <100 J m^{-2} K^{-1} $s^{-1/2}$) they still have overall low-thermal inertia values when compared to other craters common to those found in the low albedo regions (often >800-1200 J m^{-2} K^{-1} $s^{-1/2}$). These thermal inertia values are inconsistent

with in place rocky material, although minor amounts of mantling materials would easily obscure any rocky material present.

5.3.2.2 TES 507 cm^{-1} Index

The majority of the planet occurs in a relatively low 507 cm^{-1} spectral index (~1.004) and a low-moderate thermal inertia cluster (Figure 5.9). However, the infilled craters have a higher thermal inertia (~450 J m^{-2} K^{-1} $s^{-1/2}$) and TES 507 cm^{-1} index (~1.01) that indicates craters with flat-floors are typically more consolidated or rocky than the average martian surface and are also significantly more mafic than typical locations on the planet's surface (Figure 5.9).

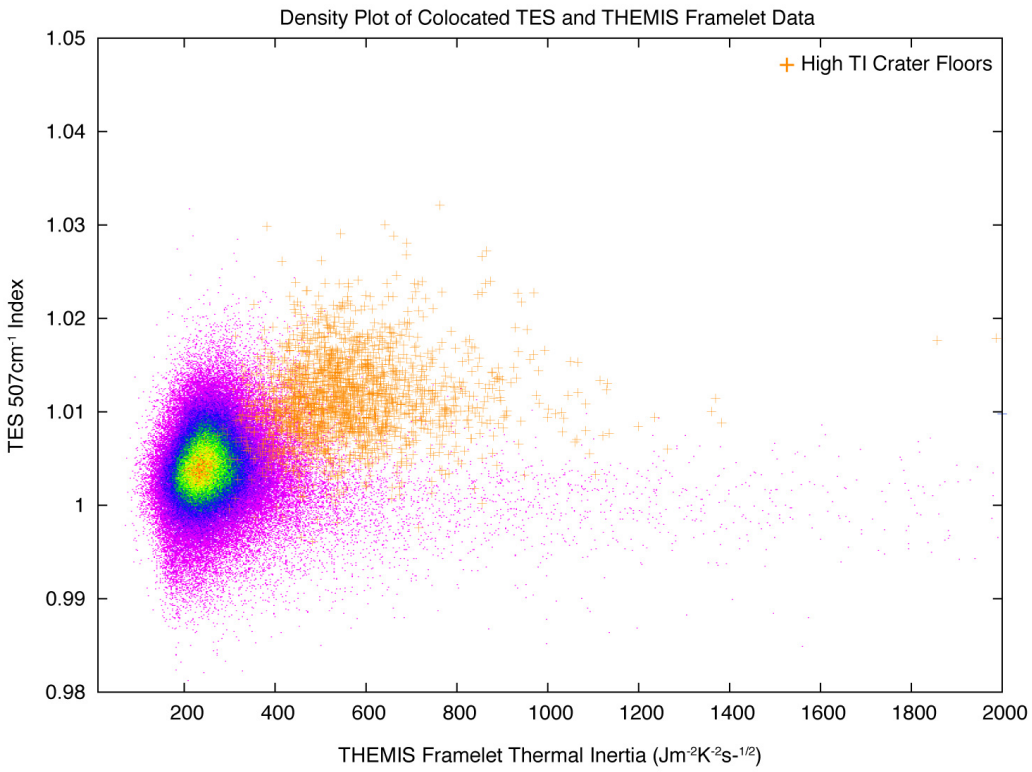

Figure 5.9. A density plot with values ranging from 1 count (purple) to 29 counts (red) of THEMIS average framelet thermal inertia versus TES 507 cm^{-1} mafic index [*Rogers and Fergas*on, 2011] where both datasets overlap and meet quality control constraints established in the Methods section. The orange crosses are the maximum THEMIS framelet thermal inertia versus the maximum 507 cm^{-1} mafic index of crater identified (Figure 5.1) where both data are available. The majority of martian surfaces when viewed through these data group as a cluster centered at ~250 J m^{-2} K^{-1} $s^{-1/2}$ and a value of ~1.004 in the mafic index. The crater floors cluster above these values in both datasets (~500 $Jm^{-2}K^{-1}s^{-1/2}$ and ~1.01 mafic index). This is similar to the trend I observe at local scales in Figures 5.3 and 5.6 and is occurring over many of the ~3,300 craters identified by visual examination.

5.3.2.3 THEMIS Thermal Inertia

In an assessment of the physical properties of the infilled craters in question, it is found that many craters do not have thermal inertia values consistent with bedrock (>1200 J m^{-2} K^{-1} $s^{-1/2}$; Figure 5.10) and other locations on the planet can often have thermal inertia values associated with rockier materials. However, the absolute thermal inertia values are less important than the relative interior-exterior differences, given all the factors, such as dust and sediment mantles that can affect the absolute thermal inertia value. It is therefore significant that infilled craters nearly always have higher thermal inertia floors than the surrounding terrain (Figures 5.10 and 5.11). Infilled craters commonly have higher thermal inertia values than the majority of the martian surface from 60˚S to 60˚N (Figure 5.10).

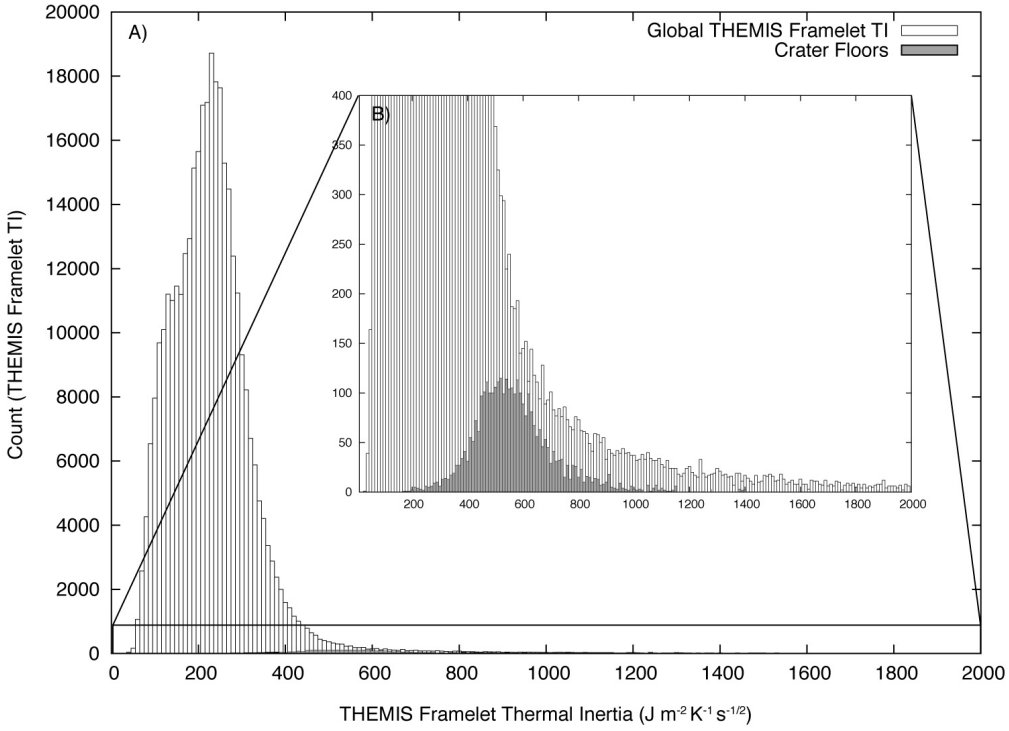

Figure 5.10. A) A histogram of the distribution of THEMIS framelet maximum thermal inertia (dark gray) for all data that meet the quality control constraints established in the Methods section. The black outlined histogram is the binned average THEMIS maximum framelet thermal inertia of all the craters identified. **B)** A zoom in of Figure 5.10a, where the histogram of the crater floors is more easily seen. While the craters are not the only features on the planet that exhibit high-thermal inertia [e.*g. Edwards et* al., 2009], on average, they have values above typical martian surfaces.

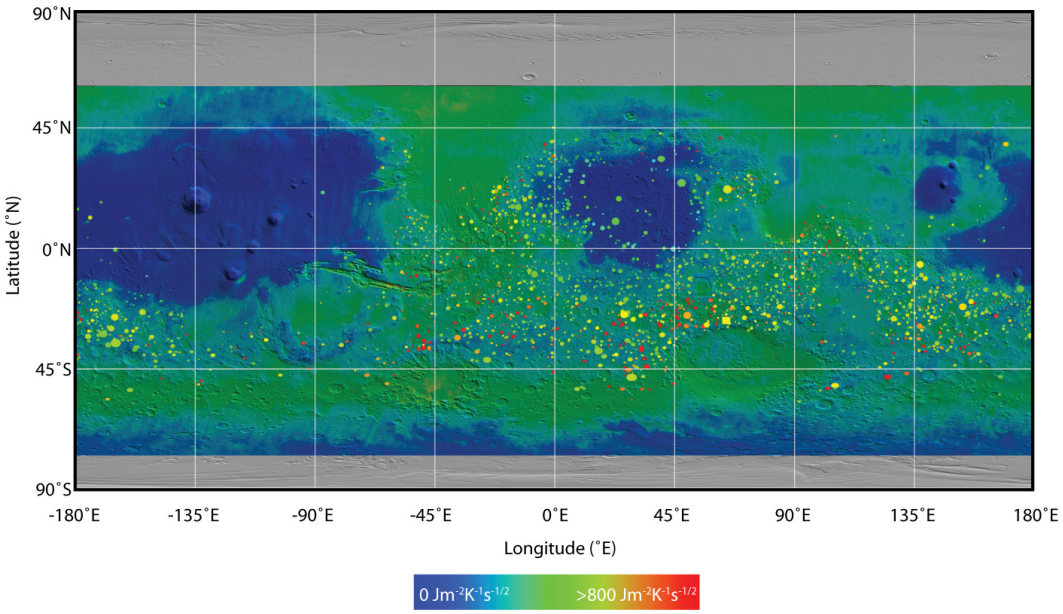

Figure 5.11. TES colorized thermal inertia map overlain on MOLA shaded relief for context. Circles are colorized THEMIS maximum thermal inertia of crater floors using the same color scale as the TES map. The comparison of the crater floors to their surrounding terrain indicates that the crater floors typically have higher-thermal inertia values than the surrounding plains. Locations in Figures 5.8 and 5.10, where the absolute value of thermal inertia is lower than the majority of the observations, may still be consistent as craters in the major low inertia regions (Tharsis, Arabia, and Elysium) are elevated above the typical surrounding terrain. This is most readily observed in the Arabia Terra region, where many green circles, with TI of ~200-300 J m^{-2} K^{-1} $s^{-1/2}$ are surrounded by surfaces with thermal inertia values of ~100-200 J m^{-2} K^{-1} $s^{-1/2}$.

5.3.2.4 Fine-Scale Morphology

HiRISE images (Figures 5.5b-d and 5.12, Table 5.3) show that the more mafic and higher thermal inertia crater floors are often dominated by in-place rock or blocky material. These outcrops are generally lighter toned than the lower thermal inertia and less mafic terrain. They often have fractures that are spaced by 10s to 100s of meters (Figures 5.12f-h), which is common to other rocky surfaces on the planet [e.*g. Edwards et* al., 2009]. Although typically fractured, these surfaces are not highly disrupted and megabreccia is not typically observed. Pits and hollows in the high-thermal inertia surfaces are often infilled with other materials that commonly exhibit bedforms; these materials are likely mobile aeolian sediment. A range of thermal inertia values associated with infilled crater floor morphologies are shown in Figure 5.12. Based on the fine-scale morphology variations, the likely cause of the thermal inertia variations is due to changes in the amount of mantling materials, where lower thermal inertia surfaces have more sediment than higher thermal inertia surfaces. Therefore, the measured THEMIS thermal inertia is the lower limit of the thermal inertia of the rocky crater floor material.

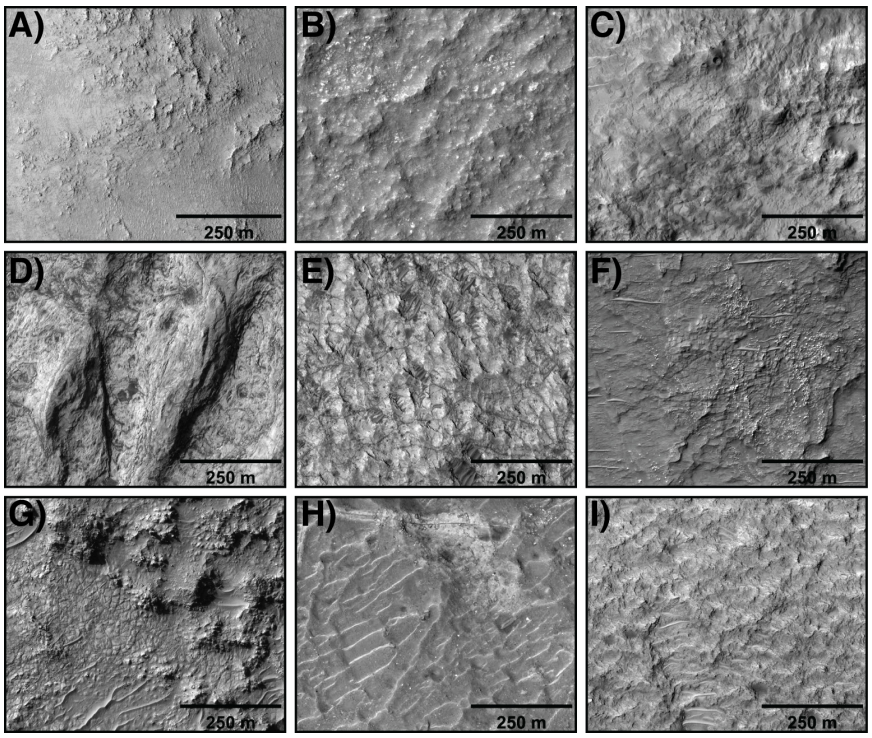

Figure 5.12. Nine examples of typical fine-scale morphologies commonly associated with crater floor material. These images span the majority of the range of thermal inertia values, with the top left figure **(A)** having the lowest THEMIS thermal inertia and the bottom right **(I)** having the highest THEMIS thermal inertia. Table 5.3 lists the images, locations, and the associated THEMIS thermal inertia values. While the range of textures observed is quite varied blocks and outcrops of fractured bedrock are often present. However, in general, lower thermal inertia examples exhibit a smoother and more mantled morphology with prevalent aeolian bedforms, while the higher thermal inertia examples appear denuded with bare rock constituting a significant fraction of the surface material. Figure 5.12d appears to show subtle layering in some of the topographic highs.

Table 5.3. HiRISE image identification and thermophysical properties for Figure 5.12

Figure #	*HiRISE Image ID*	*Longitude (˚E)*	*Latitude (˚N)*	*[a]THEMIS Thermal Inertia ($JK^{-1}m^{-2}s^{-1/2}$)*
A	PSP_009732_1960	55.56	15.83	~410
B	ESP_013946_1415	215.9	-38.215	~630
C	PSP_006789_1560	140.83	-23.81	~710
D	PSP_006962_1520	97.52	-27.91	~810
E	PSP_004192_1550	46.05	-24.66	~1130
F	ESP_017300_1565	87.0	-23.59	~1260
G	PSP_009735_1490	140.83	-23.81	~1630
H	ESP_022619_1495	313.25	-30.42	> ~2000
I	ESP_024855_1785	102.05	-1.68	> ~2000

[a]THEMIS thermal inertia values are derived from the maximum of the crater floor. All HiRISE images were taken from approximately the same locations as the THEMIS thermal inertia data.

5.3.2.5 Crater Floor Formation and Modification Ages

The majority of high-thermal inertia infilled craters on Mars occur in the cratered southern highlands, suggesting an old age for the process that filled the craters. In addition, these craters are large, with an average size of 42.1±22.6 km in diameter with the smallest crater having a diameter of ~8 km and the largest having a diameter of ~180 km (Table 5.4). While the crater infilling could be much younger than the crater itself, the fact that the infilling primarily occurs in old, larger craters suggests that the infilling processes is also old. Numerous examples exist of young fresh-looking craters that are not infilled. Figure 5.13 illustrates the contrast between young and old craters, where the more highly degraded crater with no ejecta blanket or central peak is significantly infilled with rocky material, while the fresh-looking crater still has a clearly visible central peak and ejecta blanket indicating it has not been significantly modified or infilled since it formed (Figure 5.13).

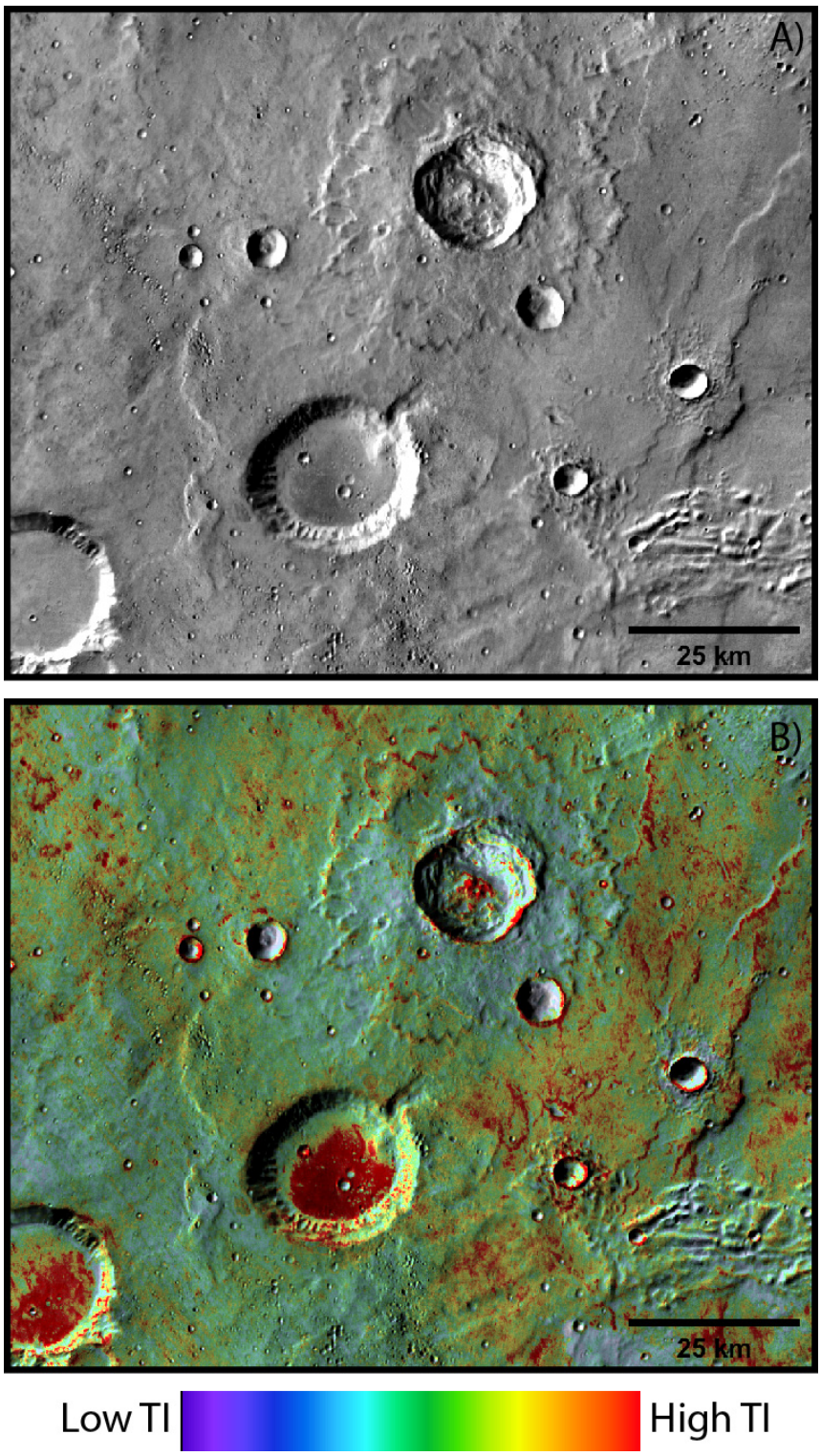

Figure 5.13. THEMIS daytime global mosaic **(A)** and THEMIS colorize nighttime temperature global mosaic overlain on the THEMIS daytime global

Figure 5.13. continued

mosaic **(B)** centered at 312.5˚ E, 21.8˚ S that shows both a fresh-looking and highly modified infilled crater floor. The highly degraded crater has no visible ejecta blanket, central peak or rim, and has been significantly infilled with high-thermal inertia materials. In contrast, the fresh crater has a clearly visible ejecta blanket, central peak, well-defined rim, and has not been significantly modified or infilled. This is typical of what is observed, where fresh-looking craters, despite being of similar size, are not typically infilled with high-thermal inertia materials, indicating that the process responsible for infilling occurred in early martian history.

.

An independent estimate of the age of the infilling process can be determined using crater abundances on the crater floor materials. Figure 5.14 shows the distribution of both the primary and secondary crater floor surface ages measured in this work and all ages with error bars, as well as geographic location, crater diameter and area counted are show in Table 5.4. Two distinct peaks in primary surface age are observed in the histogram (Figure 5.14), with the majority of the crater floors being formed early in martian history at ~3.5 Ga. Approximately 75% of all craters counted in this study have primary surface ages between 3.2 Ga and 4.0 Ga, with another 15% having primary surface ages between 2.0 Ga and 3.0 Ga. Most craters in the 3.2-4.0 Ga age range have error bars <100-200 Ma and typically have good model age fits to the observed data, the craters in the 2.0-3.0 Ga age range commonly have larger error bars (upwards of 500 Ma), indicating that the number of craters counted for the given area may be insufficient or significant resurfacing has occurred (Figure 5.14). Figure 5.15 shows the distribution of both the crater floor ages over the planet's surface, where no geographic correlation with crater floor age is identified.

Four example isochrones, including the resurfacing correction, are shown in Figure 5.16. In most cases, two distinct isochrons can be clearly distinguished, where a characteristic resurfacing event is observed as a 'kink' in the cumulative crater frequency plot (Figure 5.16a and b). However, in some cases, only minor 'kinks' are observed and the slope of the cumulative crater frequency plot is lower than that of the isochrons, indicating that the surfaces counted are retaining more

craters than what is predicted by the typical martian crater production function [e.g. *Hartmann and Neukum*, 2001; *Ivanov*, 2001; *Michael and Neukum*, 2010].

Based on the crater counting results (Figures 5.14-5.16) and the typical morphologic differences between fresh-looking and highly degraded craters (Figure 5.13), the majority of craters in this study occurring over much of the planet's surface were infilled in early martian history (~3.5 Ga). Furthermore, the process responsible for infilling the craters appears to have only operated in early martian history, during or shortly after the LHB and has not operated over large regions of the planet's surface since.

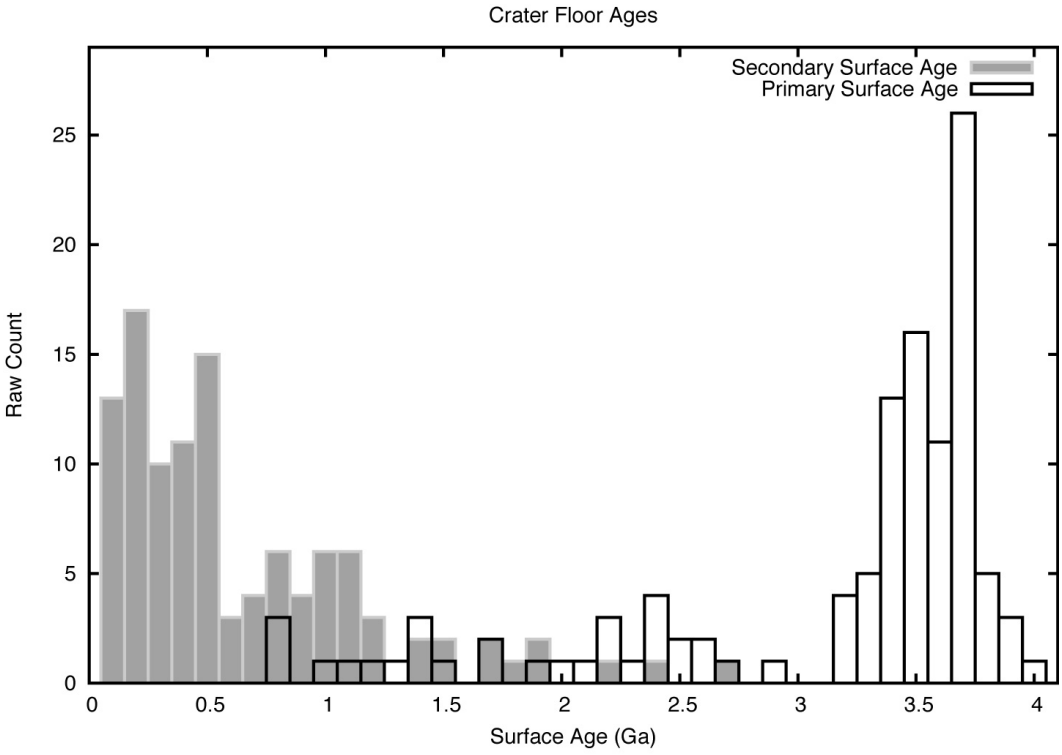

Figure 5.14. The majority of primary crater surface ages occur at ~3.7 Ga, though another minor peak occurs at ~2.25 Ga and occurrences as young as ~0.75 Ga are present. It is likely that most of these craters formed during the Late Heavy Bombardment and were subsequently resurfaced shortly thereafter. The secondary surface age is more widely distributed with the majority of the resurfacing occurring from ~100 Ma to 1.25 Ma.

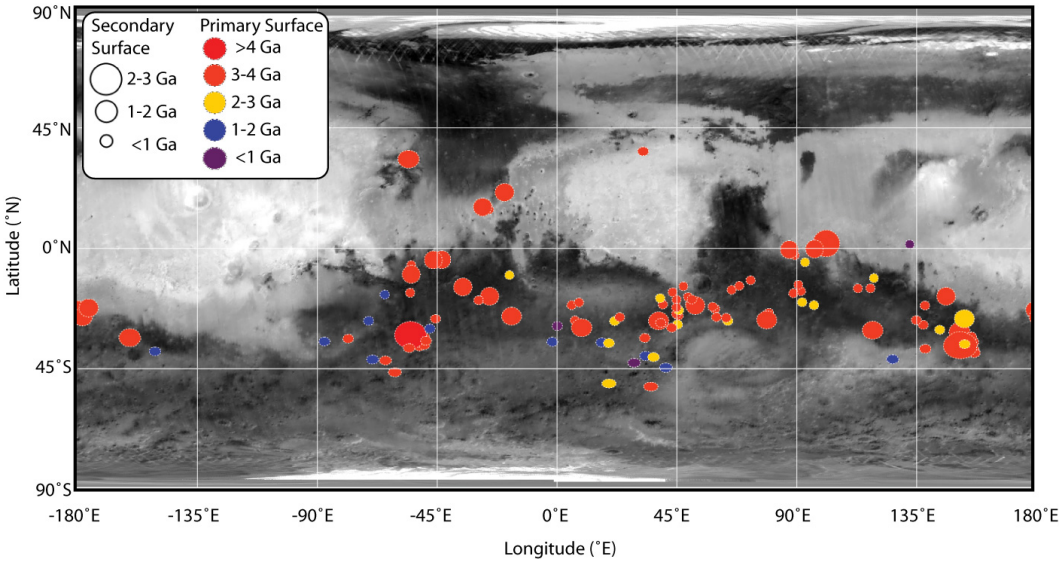

Figure 5.15. A map of all the craters dated in this study where the base map is TES Lambert Albedo, the size of the circle corresponds to the secondary surface age, and the color of the circle corresponds to the primary surface age. There is no clear geographic correlation between secondary surface age and primary surface age. Craters with a variety of primary surface ages occur in the same geographic regions (see the circum-Hellas area). Craters that experienced resurfacing at a variety of times are also present in the same geographic areas (to the east of Hellas).

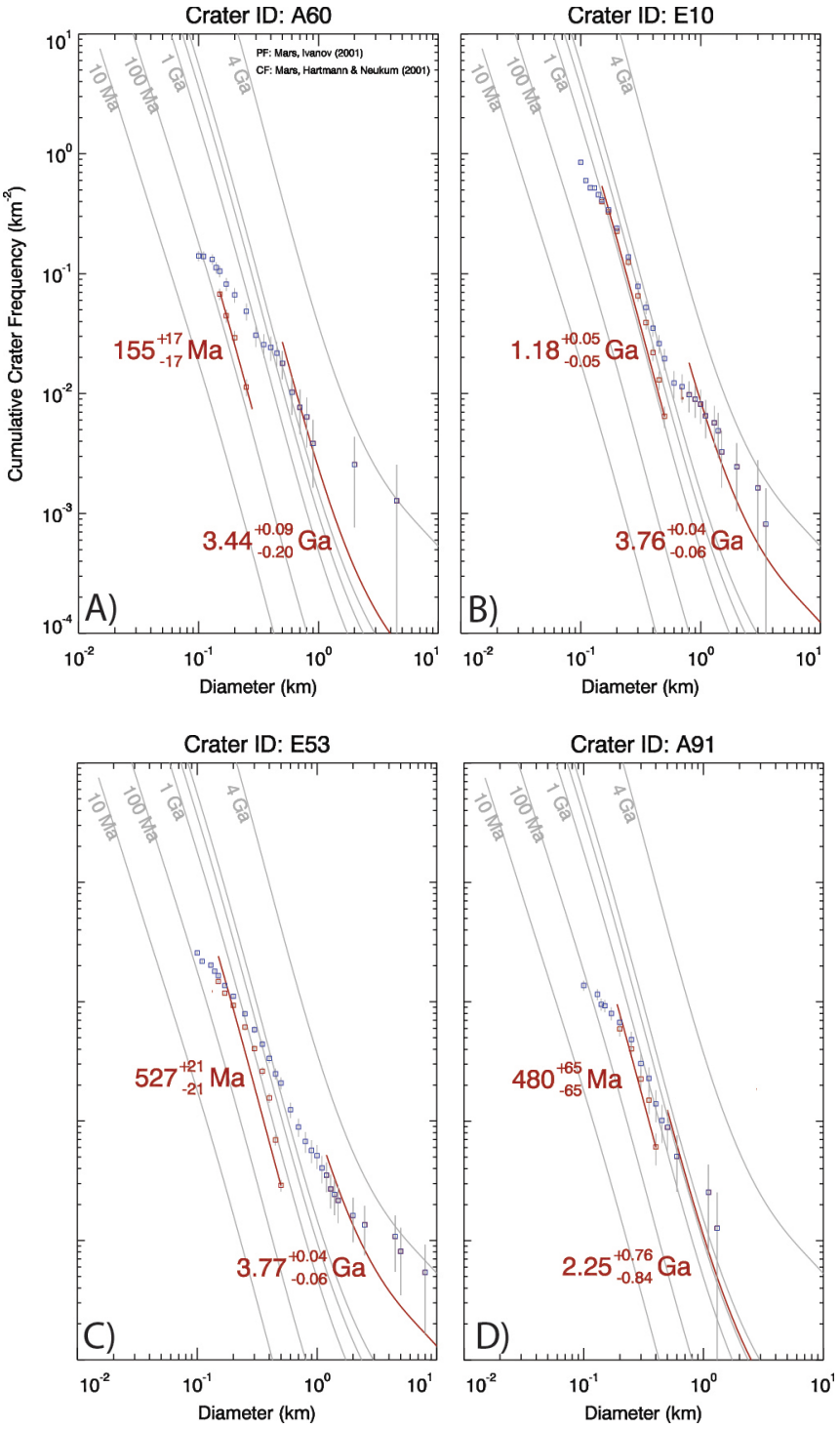

Figure 5.16. Four example cumulative distribution crater frequency plots illustrating the range of variability in crater distribution. All early ages were fit using the resurfacing correction described by *Michael and Neukum* [2010].

Figure 5.16. continued

A) The younger resurfacing age has a shallower slope than the production function isochrons above the resurfacing 'kink', indicating some fraction of existing craters were removed. Several points are not well fit below the characteristic resurfacing 'kink' likely indicating the surface had a complex early history. **B)** The resurfacing correction in this example is relatively minor as compared to Figure 5.16a and the older age is well modeled. The resurfacing 'kink' in this example is easily recognized and allowed for the easy separation of the two ages. **C)** Again a large resurfacing correction is applied in this case to the points which lie above the very minor 'kink' at ~800Ma. Separating the early from ancient ages is difficult in some cases, as the slope of the cumulative crater frequency may be significantly lower than that of the production function isochrons, indicating that smaller craters were not easily destroyed in many cases and are present at levels above the predicted resurfacing. **D)** In instances where error bars are large for the older date, I can generally attribute this to a having only a few large craters or having a small area that was counted.

Table 5.4. Table of all craters counted in this study with, including our unique identifier, planetary coordinates, crater diameter, and the area of the region counted. The primary and secondary (resurfacing) surface ages are reported including their error bars.

ID	*Lon (°E)*	*Lat (°N)*	*Diam (km)*	*Area (km^2)*	*Secondary Surface Age (Ga -/+)*		*Primary Surface Age (Ga -/+)*	
E02	341.44	20.81	60	953.8	1.760	(-0.070 / 0.070)	3.64	(-0.160 / 0.080)
E04	41.07	-21.37	50	917.6	0.296	(-0.028 / 0.028)	3.46	(-0.360 / 0.100)
E05	44.75	-16.73	36	549.8	0.116	(-0.023 / 0.023)	3.97	(-0.200 / 0.080)
E06	46.20	-19.57	32	338.3	0.286	(-0.062 / 0.062)	3.81	(-0.110 / 0.060)
E07	50.53	-18.54	74	2587.6	0.290	(-0.020 / 0.020)	3.64	(-0.070 / 0.040)
E09	51.31	-21.30	29	411.9	0.641	(-0.068 / 0.068)	3.77	(-0.280 / 0.090)
E10	53.25	-21.69	67	1225.8	1.180	(-0.050 / 0.050)	3.76	(-0.060 / 0.040)
E11	60.69	-22.97	62	1584.3	0.720	(-0.036 / 0.036)	3.70	(-0.090 / 0.050)
E12	59.80	-22.17	66	2165.7	0.598	(-0.029 / 0.029)	3.72	(-0.090 / 0.060)
E14	46.91	-25.55	51	714.9	0.574	(-0.047 / 0.047)	3.54	(-0.740 / 0.110)
E15	46.12	-24.88	67	1520.0	0.341	(-0.010 / 0.010)	3.71	(-0.080 / 0.050)
E16	39.47	-27.53	36	464.1	1.810	(-0.100 / 0.100)	3.90	(-0.070 / 0.050)
E17	40.27	-28.23	84	844.0	0.590	(-0.042 / 0.041)	3.71	(-0.090 / 0.050)
E21	22.89	-27.58	81	2325.9	0.282	(-0.017 / 0.017)	2.65	(-0.470 / 0.390)
E22	8.04	-27.41	106	4960.6	0.534	(-0.018 / 0.018)	3.78	(-0.110 / 0.060)
E23	10.48	-30.09	35	376.5	1.040	(-0.080 / 0.080)	3.39	(-0.400 / 0.110)

Table 5.4. continued

E24	1.34	-29.45	69	889.5	0.360	(-0.051 / 0.051)	0.83	(-0.060 / 0.040)
E26	311.39	-33.82	72	1974.3	0.399	(-0.023 / 0.023)	3.47	(-0.280 / 0.100)
E27	309.38	-37.12	61	630.3	0.275	(-0.033 / 0.033)	3.70	(-0.140 / 0.070)
E28	311.31	-36.59	94	2120.2	0.327	(-0.210 / 0.210)	3.46	(-0.370 / 0.110)
E29	309.38	-32.20	77	2567.5	0.925	(-0.031 / 0.031)	3.79	(-0.100 / 0.060)
E33	290.33	-27.53	57	822.8	0.158	(-0.015 / 0.015)	1.03	(-0.200 / 0.200)
E34	306.07	-32.80	23	87.2	2.740	(-0.270 / 0.240)	4.03	(-0.080 / 0.050)
E35	209.95	-39.00	45	859.4	0.816	(-0.054 / 0.054)	1.90	(-0.440 / 0.440)
E36	154.16	-38.20	42	685.1	0.517	(-0.045 / 0.045)	3.53	(-0.470 / 0.110)
E37	152.66	-31.60	51	752.8	1.080	(-0.060 / 0.060)	3.70	(-0.070 / 0.050)
E38	145.26	-30.84	65	1506.1	0.412	(-0.019 / 0.019)	2.62	(-0.240 / 0.230)
E45	154.51	-26.70	35	581.1	1.990	(-0.100 / 0.100)	2.99	(-0.220 / 0.150)
E48	147.64	-18.31	46	275.5	1.220	(-0.120 / 0.120)	3.96	(-0.200 / 0.080)
E49	181.35	-23.38	56	983.1	1.140	(-0.060 / 0.060)	3.65	(-0.120 / 0.070)
E50	139.69	-21.74	45	936.8	0.885	(-0.052 / 0.052)	3.83	(-0.160 / 0.070)
E51	93.02	-16.35	45	375.2	0.805	(-0.084 / 0.084)	3.76	(-0.300 / 0.090)
E53	80.91	-24.55	94	3700.3	0.527	(-0.021 / 0.021)	3.77	(-0.060 / 0.040)
E54	92.01	-13.95	39	623.5	0.515	(-0.050 / 0.050)	3.66	(-0.160 / 0.070)
E55	120.48	-11.42	79	1975.2	0.271	(-0.013 / 0.013)	2.49	(-0.350 / 0.330)
E59	337.20	-19.23	57	1021.0	0.210	(-0.230 / 0.230)	3.70	(-0.100 / 0.080)
E60	335.84	-18.30	50	503.6	1.100	(-0.090 / 0.090)	3.78	(-0.270 / 0.090)

Table 5.4. continued

E61	331.69	-19.79	56	1573.1	0.538	(-0.030 / 0.030)	3.72	(-0.160 / 0.070)
E63	305.95	-16.95	45	614.2	0.551	(-0.047 / 0.047)	3.73	(-0.110 / 0.060)
E64	296.41	-17.66	50	934.9	0.041	(-0.004 / 0.004)	1.75	(-0.480 / 0.480)
E65	317.85	-4.52	60	703.0	1.740	(-0.080 / 0.080)	3.42	(-0.220 / 0.090)
E66	314.66	-4.62	38	563.6	1.100	(-0.070 / 0.070)	3.78	(-0.090 / 0.060)
E67	306.38	-6.49	34	452.3	0.650	(-0.064 / 0.064)	3.73	(-0.150 / 0.070)
E68	90.78	-2.86	61	1407.9	0.466	(-0.033 / 0.033)	3.53	(-0.170 / 0.080)
E73	34.48	-40.67	87	999.1	0.204	(-0.021 / 0.021)	1.21	(-0.310 / 0.310)
E75	6.71	-21.59	30	204.4	0.462	(-0.075 / 0.075)	3.59	(-0.210 / 0.090)
A03	182.65	-26.03	56	1137.5	1.120	(-0.050 / 0.050)	3.71	(-0.070 / 0.050)
A04	120.01	-31.05	36	495.4	1.000	(-0.070 / 0.070)	3.70	(-0.220 / 0.080)
A06	305.34	33.27	36	625.2	1.240	(-0.070 / 0.070)	3.24	(-0.660 / 0.170)
A07	74.11	-12.22	36	434.4	0.342	(-0.039 / 0.039)	3.52	(-0.230 / 0.090)
A08	18.02	-35.66	39	473.0	0.193	(-0.016 / 0.015)	1.39	(-0.400 / 0.400)
A11	300.21	-46.85	56	158.0	0.254	(-0.055 / 0.055)	3.64	(-0.170 / 0.080)
A12	103.98	2.84	37	502.4	0.273	(-0.016 / 0.016)	3.43	(-0.110 / 0.060)
A13	335.63	14.30	36	494.1	0.460	(-0.026 / 0.026)	3.47	(-0.190 / 0.080)
A14	282.66	-34.20	48	1090.6	0.484	(-0.038 / 0.038)	3.27	(-0.570 / 0.150)
A15	52.04	-19.44	50	1187.3	0.324	(-0.026 / 0.026)	3.47	(-0.110 / 0.060)
A18	40.02	-18.98	48	735.5	0.330	(-0.018 / 0.018)	2.28	(-0.580 / 0.560)
A19	102.52	1.56	43	824.8	2.210	(-0.080 / 0.080)	3.49	(-0.060 / 0.040)

Table 5.4. continued

A22	80.15	-27.16	37	396.4	1.050	(-0.120 / 0.120)	3.87	(-0.090 / 0.050)
A23	37.54	-41.13	44	553.7	0.114	(-0.012 / 0.012)	2.04	(-0.560 / 0.560)
A24	291.81	-42.07	41	325.7	0.130	(-0.021 / 0.021)	1.40	(-0.490 / 0.490)
A25	306.37	-10.02	41	429.7	1.030	(-0.040 / 0.040)	3.74	(-0.090 / 0.330)
A26	20.75	-35.87	34	435.3	0.748	(-0.063 / 0.063)	2.17	(-0.760 / 0.730)
A27	343.31	-10.34	30	398.2	0.402	(-0.036 / 0.036)	2.40	(-0.590 / 0.550)
A28	325.77	-14.78	30	298.1	1.510	(-0.120 / 0.120)	3.77	(-0.290 / 0.090)
A29	46.57	-28.88	38	625.4	0.298	(-0.029 / 0.029)	2.37	(-0.570 / 0.530)
A30	149.91	-34.73	35	467.0	0.531	(-0.056 / 0.056)	3.51	(-0.160 / 0.080)
A31	344.12	-25.75	58	1055.6	1.050	(-0.050 / 0.050)	3.49	(-0.080 / 0.050)
A33	66.91	-15.88	37	481.6	0.502	(-0.063 / 0.063)	3.62	(-0.090 / 0.060)
A34	98.10	-0.55	42	788.9	1.100	(-0.030 / 0.030)	3.66	(-0.120 / 0.060)
A35	296.68	-42.42	50	858.4	0.335	(-0.033 / 0.033)	3.42	(-0.800 / 0.130)
A37	114.45	-15.30	41	631.7	0.505	(-0.031 / 0.031)	3.58	(-0.040 / 0.030)
A39	315.50	-26.74	44	879.4	0.971	(-0.058 / 0.058)	3.52	(-0.180 / 0.080)
A40	273.70	-35.27	44	487.5	0.243	(-0.033 / 0.030)	1.47	(-0.650 / 0.650)
A41	94.56	-5.52	32	147.8	0.409	(-0.036 / 0.036)	2.79	(-0.380 / 0.290)
A42	34.27	-33.92	60	1272.2	0.540	(-0.059 / 0.059)	3.55	(-0.220 / 0.090)
A43	9.51	-20.62	54	1265.5	0.428	(-0.022 / 0.022)	3.56	(-0.130 / 0.070)
A44	311.96	-34.96	54	996.3	0.318	(-0.035 / 0.035)	3.31	(-0.420 / 0.130)
A45	33.63	36.20	46	889.8	0.943	(-0.054 / 0.054)	3.64	(-0.200 / 0.080)

Table 5.4. continued

A46	305.55	-37.73	46	581.0	0.194	(-0.028 / 0.028)	3.32	(-0.950 / 0.170)
A48	333.23	15.21	56	829.2	1.440	(-0.070 / 0.070)	3.45	(-0.490 / 0.110)
A49	65.49	-27.56	27	174.7	0.109	(-0.017 / 0.017)	2.42	(-1.200 / 0.820)
A50	61.23	-26.13	38	415.5	0.084	(-0.019 / 0.019)	3.24	(-0.120 / 0.120)
A51	139.02	-29.00	38	701.1	0.417	(-0.028 / 0.028)	3.58	(-0.100 / 0.060)
A52	133.95	1.21	41	609.7	0.146	(-0.012 / 0.012)	0.84	(-0.200 / 0.200)
A53	88.63	-0.73	42	627.0	1.530	(-0.090 / 0.090)	3.52	(-0.500 / 0.110)
A54	42.16	-45.10	47	508.9	0.036	(-0.008 / 0.008)	1.11	(-0.420 / 0.420)
A55	184.96	-22.64	30	329.3	1.900	(-0.120 / 0.120)	3.49	(-0.280 / 0.100)
A57	64.89	-26.37	32	350.0	0.862	(-0.061 / 0.061)	3.70	(-0.090 / 0.060)
A58	359.45	-35.41	39	554.2	0.199	(-0.012 / 0.012)	1.57	(-0.220 / 0.220)
A59	69.84	-14.38	39	526.3	0.790	(-0.110 / 0.110)	3.86	(-0.090 / 0.050)
A60	139.83	-38.05	48	782.2	0.155	(-0.017 / 0.017)	3.44	(-0.200 / 0.090)
A62	47.04	-23.53	37	495.8	0.217	(-0.030 / 0.030)	2.28	(-1.300 / 0.950)
A63	46.19	-22.45	48	910.1	0.827	(-0.050 / 0.050)	3.64	(-0.110 / 0.060)
A65	136.41	-27.23	40	822.1	0.948	(-0.062 / 0.062)	3.71	(-0.060 / 0.040)
A66	157.98	-38.42	43	709.3	0.679	(-0.051 / 0.051)	3.69	(-0.120 / 0.070)
A67	119.16	-15.26	57	1883.4	0.241	(-0.018 / 0.018)	3.71	(-0.050 / 0.040)
A68	30.27	-43.27	65	1040.7	0.165	(-0.010 / 0.010)	0.90	(-0.270 / 0.270)
A69	90.16	-17.16	43	564.2	0.771	(-0.059 / 0.059)	3.52	(-0.230 / 0.090)
A71	155.70	-35.52	34	453.9	1.420	(-0.090 / 0.090)	3.50	(-0.200 / 0.080)

Table 5.4. continued

A72	97.91	-21.65	34	471.4	0.368	(-0.029 / 0.029)	2.41	(-0.510 / 0.480)
A75	313.34	-30.42	40	339.3	0.188	(-0.015 / 0.015)	1.47	(-0.730 / 0.730)
A76	93.45	-20.52	39	443.8	0.555	(-0.024 / 0.024)	2.59	(-0.440 / 0.390)
A77	158.30	-39.59	35	425.4	0.295	(-0.039 / 0.039)	3.75	(-0.080 / 0.050)
A78	36.50	-52.22	55	442.0	0.066	(-0.011 / 0.011)	3.39	(-0.320 / 0.110)
A79	200.47	-33.84	34	460.3	1.250	(-0.060 / 0.060)	3.64	(-0.170 / 0.080)
A80	157.12	-33.43	38	593.3	0.402	(-0.018 / 0.018)	3.20	(-0.210 / 0.110)
A81	48.77	-14.48	37	481.2	0.836	(-0.046 / 0.046)	3.34	(-0.780 / 0.150)
A82	152.95	-36.71	49	695.6	2.430	(-0.017 / 0.017)	3.82	(-0.600 / 0.540)
A84	44.39	-30.13	47	961.4	0.294	(-0.027 / 0.027)	3.54	(-0.130 / 0.070)
A90	154.63	-36.24	50	874.0	0.184	(-0.009 / 0.009)	2.53	(-0.310 / 0.290)
A91	20.80	-51.06	52	787.6	0.480	(-0.065 / 0.065)	2.25	(-0.840 / 0.760)
A92	24.85	-26.16	59	1116.1	0.518	(-0.034 / 0.034)	3.57	(-0.110 / 0.060)
A93	127.52	-41.93	38	409.1	0.296	(-0.020 / 0.020)	1.74	(-0.500 / 0.500)

Craters with the prefix “E” are a subset of instances of high thermal inertia crater floors identified in [*Edwards et al.,* 2009]. Craters with the prefix “A” are instances of craters floors identified in this work as encompassing a representative range of craters. All craters selected were >30 km in diameter and had CTX coverage over a majority of the crater floor to ensure a large enough area was covered for statistically significant crater count results.

5.4 Discussion

Any model for the formation of infilled high-thermal inertia craters on Mars must adequately explain: 1) the elevated thermal inertia and rockiness of the crater floor as compared to the surrounding terrain, 2) the enrichment in mafic minerals associated with the rocky material, 3) the typical morphology, including the lack of a central peak, relatively flat-floor, and blocky/fractured fine-scale morphology, 4) the global distribution of craters with similar characteristics, and 5) the typical primary formation ages for the crater floor materials of ~3.2-4.0 Ga.

I present three different potential formation mechanisms for the geologic origin of martian infilled, high-thermal inertia craters including: 1) the lithification/induration of sediments, 2) the ponding of crustal melt material generated by heating during the impact process, and 3) infilling by volcanic materials. The similarities in the compositional, morphological, and thermophysical data strongly suggest that a similar set of processes are responsible for the creation of the majority of infilled craters on Mars.

5.4.1 Geologic Formation

The processes responsible for the formation of infilled craters primarily occurred early in martian history (between 3.2 and 4.0 Ga) near the end of the Late Heavy Bombardment. This process/processes is responsible for the creation of rocky and mafic (pyroxene and olivine enriched) material relative to the surrounding cratered southern highlands that typically have moderate thermal inertia and are basaltic in composition. This process often creates the rockiest

material on the planet with thermal inertia values in excess of 1000 J m^{-2} K^{-1} $s^{-1/2}$ and is responsible for some of the most mafic material observed on Mars with olivine areal abundances >15%.

Crater age date observations indicate that the mechanism by which many of the infilled craters formed occurred at the end of the Late Heavy Bombardment (~3-4 Ga) and did not occur over widespread areas of the planet again in martian history. It is possible that the ~10-25% of crater floors that formed within the last 1-3 Ga respectively may have different formation mechanisms such as infilling and induration of sediments, or they may have been significantly modified and the primary surface age has been completely obscured. I specifically discuss the timing of events and the observational constraints as directly related to specific formation mechanisms in the following sections.

5.4.1.1 Lithification/Induration of Sediments

The lithification/induration of sedimentary material derived from either inside or outside of the crater has been suggested previously [*McDowell and Hamilton,* 2007] for the formation of infilled craters in southwestern region Margaritifer Terra. Indurated and lithified sedimentary materials have been observed at both Meridiani Planum and Gusev Crater by the Mars Exploration Rovers [e.g. *Squyres et al.*, 2004b; *Squyres et al.*, 2004a; *McLennan et al.*, 2005; *Squyres and Knoll*, 2005; *Squyres et al.*, 2006]. Water (either ground or surface) could infiltrate the loose sediments, cementing them with dissolved mineral salts, such as sulfates, as is likely the case in Meridiani Planum [*McLennan et al.*, 2005; *Squyres and Knoll*, 2005; *McDowell and Hamilton*, 2007].

Although *McDowell and Hamilton* [2007] favor an induration hypothesis, I find several lines of evidence that argue against it. First, it is likely that the majority of infilling the sediments would be derived from either inside or nearby the crater. The surrounding materials (Figures 5.4, 5.6, and 5.7) are commonly less mafic than the high-thermal inertia crater floor material. It is unlikely that less mafic sediments can be lithified into more mafic bedrock, unless a transport process existed to concentrate mafic materials in the derived sediments. Such a concentrating process is unlikely especially given the high instability of olivine and the lack of direct evidence for water at these sites. In addition, layering is not commonly observed in the high-thermal inertia crater floor material, although visible layering is not required for a deposit to be sedimentary. However, layers are observed in the interior layered deposits of Valles Marineris [*Fergason et al.*, 2006a] and typical crater mounds, such as those found in Arabia Terra [*Fergason and Christen*sen, 2008], and the lack of significant layering at HiRISE scales in the crater infill argues against a sedimentary origin of these materials.

The thermal inertia on Mars observed *in situ* at the Mars Exploration Rover (MER) Spirit landing site in Gusev Crater indicates that dense Adirondack class basaltic rocks have thermal inertia values of $> \sim 1200$ J m^{-2} K^{-1} $s^{-1/2}$ and typical Columbia Hills volcaniclastic or lithified sedimentary rocks have much lower thermal inertia values (~ 600 J m^{-2} K^{-1} $s^{-1/2}$) as observed by the Mini-Thermal Emission Spectrometer (Mini-TES) [*Christensen et al.*, 2003a; *Fergason et al.*, 2006b]. The thermal inertia for the Adirondack class basalts was derived from a single rock (Bonneville Beacon) and does not take into account the

surrounding lower thermal inertia regolith (~200-300 J m^{-2} K^{-1} $s^{-1/2}$). However, when viewed by THEMIS, significant sub-pixel mixing of rock and regolith or aeolian material is likely to occur. Therefore, when high-thermal inertia values (>600 J m^{-2} K^{-1} $s^{-1/2}$) are observed at THEMIS scales (100 m/px), it is likely a combination of regolith and rocky material (clearly observed in HiRISE images), indicating that the rockiest crater floor materials are not consistent with lithified sediments but are instead more likely to be composed of dense crystalline, volcanic rocks [*Edwards et* al., 2009].

Sedimentary infilling cannot adequately explain the enhanced mafic composition and the very high thermal inertia values. The blocky and fractured textures commonly observed are also inconsistent with other known sedimentary or layered deposits, such as those present in Gale crater, Meridiani Planum, and Valles Marineris interior layered deposits. Based on the morphologic, thermophysical and compositional evidence, I conclude that this formation mechanism is not likely to be responsible for the overall infilling and emplacement of the more mafic, high thermal inertia crater floor materials.

5.4.1.2 Impact Melt

There is potential for impact melt to create high-thermal inertia crater floors. In all large (10s of km scale) impact craters, the amount of impact melt should be significant [e.g. *Schultz and Mustard*, 2004; *Osinski*, 2006] and with increasing crater size, the volume of melt remaining inside the crater walls increases significantly primarily due to the non linear increase in melt production with crater diameter [*Cintala and Gri*eve, 199*8; Osinski et* al., 2008].

Additionally, massive melt sheets should partially infill the crater [*Cintala and Gri*eve, 199*8; Osinski et* al., 2008] with the remainder ejected from the crater [*Schultz and Must*ard, 2004].

If I consider the amount of impact melt generated in an impact event [e.g. *Cintala and Griev*e, 1998], the volumes would not be sufficient to completely fill these craters to their current depths. Most craters in the diameter ranges identified (e.g. >10 km) should have central peaks and the volumes of melt required to completely overtop and cover the central peaks would not be generated [e.g. *Cintala and Griev*e, 1998]. Furthermore, impact melts are rarely restricted to crater floors and are typically present on crater walls, rims and on surfaces outside the crater.

If the melt sheet were significant enough, it is possible that a glassy melt would not remain, but rather the melt could cool slowly enough to form material that is sufficiently crystalline to be recognized by spectroscopic methods as mineralogically distinct. This material would likely have a thermal inertia consistent with in-place bedrock (> 1200 J m^{-2} K^{-1} $s^{-1/2}$) [*Edwards et* al., 2009]. Because the majority of these impact craters likely formed during the Late Heavy Bombardment at ~3.9 Ga, the surface ages I measure are roughly in agreement with the formation of the crater floors at the time of the crater formation itself.

This impact melt emplacement mechanism adequately explains several of our observations, including the blocky fractured textures, the extremely high-thermal inertia values, the crater floor age dates, and their global distribution. However, it does not explain the compositional difference between the crater floor

and the surrounding less mafic basaltic inter-crater plains. The impact event would have melted the typical cratered southern highlands basaltic material and re-crystallized a material with a nearly identical bulk composition and mineralogy. This melting and re-crystallization would not result in an increase in the olivine/pyroxene abundances as observed by TES, especially if the regolith is already altered as this would increase the amount of silica available in the melt, resulting in a lower 507 cm^{-1} index. In addition, I do not observe any obvious flow features on the crater walls or crater floors consistent with impact melt, though evidence of flow features may have likely been long since eroded, especially when considering the ancient age and highly eroded nature of most of the craters under examination. Based on the distribution, morphology, volume of material, and compositional evidence, I conclude that while impact melt was likely generated and may have filled portions of the crater floor, but it is not responsible for the filling of craters with of the more mafic, high-thermal inertia materials.

5.4.1.3 Volcanic Infilling

Volcanic infilling is another scenario for the formation of the more mafic, high-thermal inertia crater floors. In this formation mechanism, surface flows or material injected through sub-surface fractures [e.g. *Schultz*, 1976; *Schultz*, 1978; *Schultz and Orphal*, 1978] would have infilled the crater floor. In this model, the impact event is responsible for fracturing the crust and subsurface and likely created the pathways for magma to reach the surface [*Schultz*, 1976; *Schultz*, 1978; *Schultz and Orphal*, 1978]. Depending on the volume of magma released,

the erupted material could have overtopped the central peak and potentially flowed over the crater rim.

If the melt source regions were sufficiently primitive and largely unfractionated (e.g. derived from the martian mantle), it is possible that material more mafic (enriched in olivine and pyroxene) than the typical inter-crater highlands would be erupted onto the crater floor surface. These effusive volcanic products would be thermophysically consistent with Adirondack class basalts from Gusev, with thermal inertia values (e.g. > 1200 J m^{-2} K^{-1} $s^{-1/2}$) consistent with in-place bedrock. Volcanic infilling would likely produce materials consistent with the blocky morphologies of the mafic materials found on the floors of older craters. The high-thermal inertia and fractured morphology is consistent with effusive volcanic products and the isolation of the crater fill material in topographic lows is typical of ponding lavas. While similar processes have been suggested previously (e.g. Mare Serpentis [*Rogers et* al., 2009], Tyrrhena and Iapagia Terra [*Rogers and Ferga*son, 2011]), the source of the volcanic infilling material has remained largely unclear.

Both the sedimentary infilling and impact melt arguments cannot adequately explain the significantly different compositions, high-thermal inertia values, and fine-scale morphology. Based on the lack of evidence for either the sedimentary infilling and the impact melt hypotheses, only the volcanic infilling hypothesis is considered further. All observations and predictions, including the elevated thermal inertia values and morphology are in agreement with the volcanic infilling hypothesis.

5.4.2 Implications for Ancient Mars

Volcanic infilling associated with cratering is a unique and widespread process that effects large impact craters (> ~10 km) that formed early in martian history (> 3 Ga), across large areas of the southern highlands. This process likely occurred planet-wide, but I am only able to view locations where significant modification (e.g. the resurfacing of the northern lowlands, magmatism associated with Tharsis and Elysium, polar and periglacial processes, and the deposition of dust over regions such as Arabia Terra) has not occurred later in martian history.

5.4.2.1 Magma Source for Volcanic Infilling

The volcanic materials filling the craters could have come from outside or within the crater. There is typically no evidence for surface flows that overtopped the crater rim, and while it is possible that significant erosion could have removed the evidence of these rim-topping flows in some cases, it is highly unlikely to have removed it in all of the thousands of craters examined. Given the lack of evidence for this type of event, I do not address it further.

Impact related decompression melting of the martian mantle is a likely source to generate widespread magmatism on early Mars, where the impact event removes several kilometers of crustal material and magma is generated from decompression melting of the mantle. The majority of the crater floors were infilled early in martian history when higher crustal heat flow and a relatively thin crust on top of the Fe/Mg-rich martian mantle were present [*Zuber*, 2001, and references therein]. When these conditions are combined with the removal of several kilometers of crustal material by the impactor [e.*g. Boyce and Garb*eil,

2007], decompression melting of the martian mantle could occur. Figure 5.17 is an illustration of the pressure/temperature path decompression melting may take compared to a range of possible conditions for the early and present day base of the martian crust [e.g. *Spohn*, 1991; *Zuber*, 2001; *Morschhauser et al.*, 2011]. The main differences between the early and present day martian crustal properties is that the current crust is significantly thicker and cooler than earlier conditions [e.g. *Morschhauser et al*., 2011]. A thicker crust or lithosphere (consistent with present day conditions) makes it more difficult to generate and mobilize melt to the surface by the removal of several km of surface material, while a thinner crust and higher geothermal gradient (ancient conditions) makes it easier to generate and mobilize melt.

While phase transitions (Figure 5.17b) are somewhat important as erupted materials (e.g. Adirondack class basalts) [*Monders et al*., 2007] can be directly derived form the olivine, orthopyroxene, and melt field, the most important factor is the amount of melt generated. The fraction of melt increases regardless of phase transitions and is related to the distance from the solidus (Figure 5.17a). Once the removal of surface material by the impactor occurs, all points along the crustal column at all depths experience a corresponding drop in pressure and additional melt is likely generated along the full column of material. If the melt fraction at any point along this column is high enough to mobilize the melt, then an eruption at the surface is likely. This impact generated mantle melt would be primitive and crystallize high amounts of olivine and pyroxene, though the exact

composition is dependent on the depth of the mantle source [*Bertka and Holloway*, 1994; *McSween et al.*, 2006].

With this magma source as a reasonable possibility, it is unnecessary to involve large- or regional-scale magma bodies, as the development of the melt is directly related to the impact process. The generation of this magma would likely cease later in martian history as the martian crust thickened and geothermal gradient decreased to present day values [e.g. *Zuber et al.*, 2000; *Zuber*, 2001; *Andrews-Hanna et al.*, 2008]. This prediction is consistent with the observation of infilled craters only having degraded and highly eroded morphologies, indicating their ancient age, which is further constrained by crater age dates in this work of 3-4 Ga. Additionally, craters with well-preserved rims and ejecta blankets, such as that displayed in Figure 5.13, are not typically infilled by these materials. The infilled craters and their mafic blocky interiors are a direct consequence of impacts into a relatively thin martian crust with high heat flow in early martian history, likely during or just after the Late Heavy Bombardment.

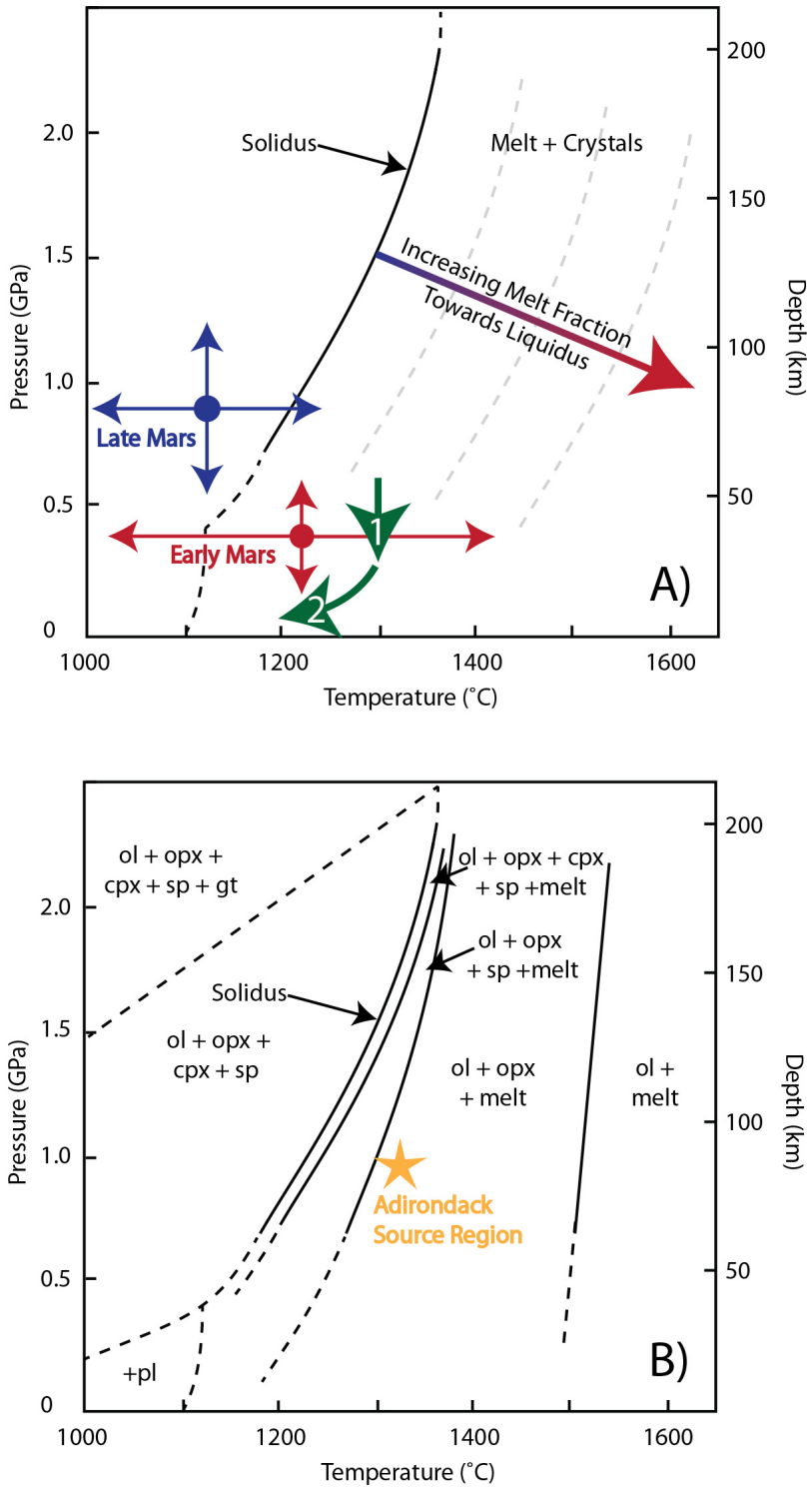

Figure 5.17. A set of pressure/temperature diagrams after *Bertka and Holloway* [1994] with a martian mantle composition of *Dreibus and Wanke* [1985],

Figure 5.17. continued

that illustrate both composition and increasing melt fraction. The solid lines are determined by *Bertka and Hollowa*y [1994] using high pressure/temperature experiments. Dashed lines are extrapolations of the solid lines where experiments were not conducted to constrain actual compositions. These phase diagrams are used to illustrate a range of conditions and potential options for the generation of a magma from impact related decompression melting. **A)** The two sets of colored arrows represent estimates of typical early (red) and possible present day (blue) martian crustal conditions [e.g. *Spohn*, 1991; *Zuber*, 2001; *Morschhauser et al.*, 2011]. Temperature and pressure ranges are estimates based on crustal evolution models [*Morschhauser et al*., 2011] and may not represent actual values. Green arrow #1 represents an example path that the removal of crustal material would take. The pressure would be lowered and it is possible to cross phase transitions shown in B) (e.g. into the field from which picritic olivine-rich Adirondack basalts [*McSween et al.*, 2006] were likely generated [*Monders et al*., 2007]). Regardless of phase transitions, the further the arrow travels away from the solidus, the more melt is generated. Once a critical point is reached where a sufficient fraction of melt is present, the melt can be mobilized and then follows a path similar to arrow #2 where the pressure continues to decrease and the temperature decreases as the magma migrates towards the surface. **B)** Minerals stable in each field are labeled and are from *Bertka and Hollowa*y [1994]. The star represents the potential source composition for olivine-rich Adirondack class basalts determined experimentally [*Monders et al*., 2007].

5.4.2.2 Magma Composition and Relative Rockiness

The discrepancy between the surrounding bulk crustal compositions and that of the rockier, more mafic crater floor materials also has implications for the martian crust as a whole. This observation is especially important if I consider that the bulk of the martian crust may not be significantly altered and where alteration occurs, it typically occurs in isolated locations (e.g. Nili Fossae, crater central peaks, massively layered terrain, etc.). Typical martian magmas that formed the moderate thermal inertia southern highlands are generally depleted in olivine and pyroxene and enriched in plagioclase/high-Si phases [e.*g. Rogers and Ferga*son, 2011] as compared to the higher thermal inertia crater floors and high-thermal inertia inter crater plains. This may indicate a variety of magma source regions and different levels of melt fractionation or partial melting were commonplace in early Mars, possibly based on crater size. This fractionation, while somewhat limited, was capable of producing largely mafic and ultra-mafic rocks that dominate the majority of the martian surface. The less rocky martian regolith may be derived from ash and pyroclastic deposits resulting from explosive volcanism and may be derived from a less mafic, more fractionated magma source.

5.4.2.3 Missing Infilled Craters

Volcanic infilling of crater floors by decompression melting of the mantle was likely occurring over much of the surface in early martian history. This process occurred anywhere when the impactor was sufficiently large to remove

several kilometers of material and the crust was relatively thin (e.g. Figure 5.17). Locations where mafic high-thermal inertia crater floors are not observed are locations where significant surface morphology alteration has occurred. For example, I observe a significantly lower fraction (Figure 5.2) of high-thermal inertia crater floors next to volcanic centers (e.g. Tharsis and Elysium), areas with enhanced glaciation (e.g. Hellas Basin [e.*g. Holt et al.,* 2008], Deuteronilus Mensae [e.*g. Head et al*., 2006]), high latitude regions where periglacial processes are be prevalent [e.*g. Kreslavsky et al*., 2008], areas with large numbers of channels, areas that have been resurfaced including the northern lowlands, and high albedo dusty regions where indurated materials [*Christen*sen, 1982] likely bury and mask the high-thermal inertia values. Widespread aeolian and mantling material is likely responsible for lowering the average thermal inertia of many crater floor surfaces and is a significant driving factor that serves to create the variability in thermal inertia and compositions I observe through the various crater floors.

The overall population of high-thermal inertia materials decreases at latitudes poleward of ~50˚ are reached [*Edwards et al.*, 2009]. This is likely due to enhanced regolith formation associated with an active layer [*Kreslavsky et* al., 2008], subsurface ice [*Bandfield*, 2007; *Bandfield and Feldman*, 2008; *Smith et al.*, 2009] and other polar processes [e.*g. Edwards et al.,* 2009]. These observations are consistent with the distribution of bedrock surfaces [*Edwards et al., 2009]* and though there are infilled craters present at higher latitudes (e.g.

poleward of 60˚), I do not observe any craters with higher thermal inertia material associated with crater floors.

5.4.2.4 Large Scale Fracturing of the Crust and the Formation of Inter-Crater Plains

Crater fractures would likely extend to the first 10s of km of the upper crust and could provide pathways for dikes and sills to erupt onto the surface outside of the crater. The eruption of these materials may be responsible for a significant fraction of the basaltic lavas and pyroclastics thought to constitute the majority of the southern highlands [e.*g. McEwen et* al., 1999]. Much of the southern highlands cannot be traced back to volcanic centers and this may be a viable way for the emplacement of significant volumes of material. It is common to find high-thermal inertia and more mafic locations in the inter-crater plains in conjunction with the craters identified here [e.g. *Rogers et al.*, 2009; *Rogers and Fergason*, 2011]. The fractures from the impact events may also be responsible for the emplacement of this material, which typically have no clear source.

Along with providing conduits for magma to erupt onto the surface, the highly fractured crust may provide pathways for groundwater to circulate in the deep crust. Local hydrothermal systems could be setup directly after the impact [e.*g. Abramov and Kr*ing, 200*5; Schwenzer and Kr*ing, 2009], but later hydrothermal systems derived from alternate heat sources including adjacent magma bodies and other impact events, may utilize these pervasive fractures to alter the martian crust at depth [e.g. *Michalski and Niles*, 2010; *Ehlmann et al.*,

2011b]. This alteration would likely occur early in martian history as significant heat from various impact events, higher than present geothermal gradients [*Zu*ber, 2001], and abundant water that carved channels [*Carr and C*low, 1981] were present during this period of martian history [e.g. *Bibring et al.*, 2006; *Ehlmann et al.*, 2011b].

5.5 Conclusions

In this study, I have shown that:

- Highly eroded craters with flat-floors composed of material with elevated thermal inertia values (e.g. > 500 to 2000 J m^{-2} K^{-1} $s^{-1/2}$) are prevalent in the ancient low albedo cratered southern highlands. The thermal inertia of the crater floors does not necessarily need to be consistent with bedrock (with thermal inertia values > 1200 J m^{-2} K^{-1} $s^{-1/2}$) [e.*g. Edwards et al*., 2009], but are instead elevated as compared to the surrounding inter-crater plains. The high-thermal inertia crater floors material has experienced similar weathering and alteration events as the inter-crater plains that are typically composed of less competent materials. These craters contain some of the rockiest materials on the planet and likely represent a unique widespread process that occurred early in martian history.
- The fine-scale morphologies associated with the high-thermal inertia crater floors commonly show a rough and pitted texture,

with boulders and in-place fractured rock exposed on the surface. Mobile aeolian materials commonly infill local depressions in the exposed rocky surfaces, reducing the observed thermal inertia. Where thermal inertia values are not consistent with in-place bedrock, I find it is most directly related to the fraction of fines versus bedrock and not the physical nature of the bedrock.

- Crater floor age dates derived from crater counting statistics yield modeled surface ages of ~3-4 Ga for the more than 110 crater floors measured in this study. Crater floors also have a resurfacing age of less than ~1 Ga indicating that they likely formed early in martian history and were subsequently altered/resurfaced in the more recent past.
- I also observe the rocky material in the crater floors is significantly more mafic (globally constrained using the TES 507cm^{-1} spectral index [*Rogers and Ferga*son, 2011]) and enriched in olivine/pyroxene versus plagioclase/high Si-phases when compared to the surrounding typical inter-crater plains.
- Based on the surface properties described here, three mechanisms are considered for the formation of infilled, high-thermal inertia crater floors on Mars including: 1) the lithification/induration of sediments, 2) the ponding of crustal melt material related to the heat generated during the impact process, and 3) infilling by

volcanic materials. Of these three possibilities, only volcanic infilling can produce features with the observed morphological, thermophysical, and compositional characteristics, along with the widespread occurrence and ancient ages. In this scenario, crustal material below the crater is heavily fractured providing a pathway for magma to reach the surface. This magma would be directly sourced from the decompression melting of the martian mantle due to the removal of several kilometers of overlying crustal material by the impactor. As the ancient martian crust was likely thin [e.*g.* *Zu*ber, 2001] and the geothermal gradients were significantly higher than present day, the decompression melting of the mantle would be more likely to occur than under present day conditions. This is borne out by the ancient ages (~3-4 Ga) of the crater floors that indicates their formation early in martian history and not after the crustal thickening of the southern highlands and reduction of the geothermal gradient.

The fractures in the upper crust created by these large impact events may provide pathways for the lavas that form the Hesperian ridged plains or rocky mafic exposures visible throughout the southern highlands [e.g. *Edwards et al.*, 2009; *Rogers et al.*, 2009; *Rogers and Fergason*, 2011]. Many of these flows have no easily observable volcanic edifices and could be fed directly from dikes that utilized the highly fractured crust as pathways for magma to breach the

surface. Furthermore, groundwater and hydrothermal systems could also use these fractures as pathways to circulate through and alter the martian crust.

CHAPTER 6

MICROSCOPIC EMISSION AND REFLECTANCE THERMAL INFRARED SPECTROSCOPY: INSTRUMENTATION FOR QUANTITATIVE *IN SITU* MINERALOGY OF COMPLEX PLANETARY SURFACES

The diversity of investigations of planetary surfaces, especially Mars, using *in situ* instrumentation over the last decade is unprecedented in the exploration history of our solar system. The style of instrumentation able to be supported by landed spacecraft is dependent on several parameters, including weight and power consumption, instrument complexity and cost, and desired measurement outcome (e.g. chemistry, mineralogy, petrology, morphology, etc.), all of which must be evaluated when deciding an appropriate spacecraft payload. I present a laboratory microscopic emission and reflectance spectrometer for the analysis of martian analog materials as a strong candidate for the next generation of *in situ* instruments designed to definitively assess sample mineralogy and petrology while preserving geologic context. I discuss the instrument capabilities, signal and noise, and overall system performance. Furthermore, I evaluate the ability of this instrument to quantitatively discriminate and determine sample mineralogy including bulk mineral abundances. This capability is greatly enhanced from existing emission spectrometers, as the number of mineral components observed at any microscopic measurement spot is low (typically <3). Since this style of instrument is based on a long heritage of thermal infrared emission spectrometers sent to orbit (the Thermal Emission Spectrometer), sent to

planetary surfaces (the Mini-Thermal Emission Spectrometers), and evaluated in laboratory environments, direct comparisons to existing data are uniquely possible with this style of instrument. Furthermore, the ability to obtain bulk mineralogy and atmospheric data, much in the same manner as the Mini-Thermal Emission Spectrometers, is of significant additional value and provides the ability to maintain the long history of atmospheric monitoring for Mars. Miniaturization of this instrument has also been demonstrated as the same microscope objective has been mounted to a flight-spare Mini-Thermal Emission Spectrometer. Further miniaturization of this instrument is straightforward with modern electronics and the development of this instrument as an arm-mounted device is the end goal.

6.1 Introduction

Over the last several decades the range and volume data returned from planetary exploration missions has increased exponentially. The orbital missions responsible for the bulk of this data have traveled throughout our solar system to nearly every planetary scale body, including most recently MESSENGER, Venus Express, Lunar Reconnaissance Orbiter, Hyabusa, Chandrayaan-1, Mars Global Surveyor, 2001 Mars Odyssey, Mars Express, Mars Reconnaissance Orbiter, and Cassini-Huygens. These orbiters have carried a wide range of specialized instruments ranging from high-resolution imaging visible cameras, radar, laser altimeters, magnetometers, and a wide range of spectrometers, including gamma ray and neutron spectrometers, thermal emission spectrometers, and visible/near-infrared reflectance spectrometers. While fundamental observations have been made from these orbital instruments, the next generation of instruments to be

deployed throughout the solar system will build on the remotely sensed characterization of planetary surfaces to perform *in situ* characterization of planetary material.

6.1.1 In Situ and Remote Sensing Observations of Mars from Lander Data

The trajectory towards *in situ* instrumentation is largely underway in the case of the martian surface. A concerted effort has been made over the last decade to characterize the surface *in situ* and in unprecedented detail. Beginning with the Mars Pathfinder as a lander technology demonstration and continuing with the Mars Exploration Rovers (MER) [*Squyres et al.*, 2003], the Phoenix lander, and the Mars Science Laboratory (MSL), the martian surface has been characterized using a variety of *in situ* and landed remote sensing techniques. For example onboard the Mars Exploration Rovers, a broad suite of instruments including the Alpha-Particle X-ray Spectrometer (APXS) [*Gellert et al.*, 2006], Mössbauer [*Morris et al.*, 2004], Microscopic Imager (MI) [*Herkenhoff et al.*, 2003], the Mini-Thermal Emission Spectrometer (Mini-TES) [*Christensen et al.*, 2003a], and the Panoramic Camera (PanCam) [*Bell et al.*, 2006] have characterized in detail both Meridiani Planum and a section of the floor of Gusev Crater. The combination of *in situ* (e.g. MI, APXS, Mössbauer) and remote sensing (e.g. PanCam, Mini-TES) instruments have proved to be especially successful in both identifying potential targets at a distance and characterizing those targets in detail [*Gellert et al.*, 2004; *Klingelhöfer et al.*, 2004; *McLennan et al.*, 2005; *Golombek et al.*, 2006; *Ruff et al.*, 2006; *Squyres et al.*, 2007; *Lewis et al.*, 2008; *Rogers and Aharonson*, 2008; *Squyres et al.*, 2008; *Ruff et al.*, 2011]. Many of these

observations have fundamentally changed our understanding of Mars and Mars surface processes.

Following the relatively modest MER instrument suite, the MSL instruments suite includes a host of largely *in situ* instruments designed to assess the habitability of past and present Mars. These instruments include the Mast Camera (Mastcam), a Laser Induced Breakdown Spectrometer (LIBS) for remote elemental composition (ChemCam), a microscopic imager (MAHLI), an Alpha-particle X-ray spectrometer (APXS), chemistry and mineralogy by powder X-ray diffraction and X-ray fluorescence (CheMin), as well as a quadrupole mass spectrometer, a gas chromatograph and a tunable laser spectrometer (SAM). This suite of instruments onboard MSL will characterize the martian surface in unprecedented detail, rivaling what can be done in the laboratory on Earth. However, the time to make many of the measurements is exceedingly long, including sample preparation of several hours and integration times for the ChemMin instrument of many of hours for a single measurement. Additionally the power requirements for highly complex instruments and long measurement times is prohibitively costly and requires the use of a radioisotope thermoelectric generator (RTG), which dramatically increases the cost of planetary missions due to the increased mass and system complexity over solar panels.

While these instruments will characterize a small fraction of the martian surface in great detail, the majority of the martian surface will never be explored and examined at the scales possible from lander and rover data. Complementary techniques from orbit and at lander scales can allow for the extrapolation of the

findings from landers to the rest of the planetary surface. To date, only one set of complementary instruments (spectral sampling and wavelength range) has been sent to orbit and the surface (the Thermal Emission Spectrometer (TES) [*Christensen et al.*, 1998] and Mini-TES, respectively). However the scales of these measurements are quite disparate, where Mini-TES samples outcrop scale variability (centimeter to meter spot sizes) and TES samples regional scale variability (~3x8 km spots when the instrument is nadir looking).

6.1.2 Vibrational Spectroscopy

Vibrational spectroscopy (e.g. Mini-TES, TES, Thermal Emission Imaging System (THEMIS) [*Christensen et al.*, 2004a], Compact Reconnaissance Imaging Spectrometer for Mars (CRISM) [*Murchie et al.*, 2007] and Observatoire pour la Minéralogie, l'Eau, les Glaces, et l'Activité (OMEGA) [*Bibring et al.*, 2005]) is commonly utilized to quantitatively determine mineralogical properties of observed materials on planetary bodies. Vibrational spectroscopy is based on the principle that energy is emitted/reflected at specific frequencies related to the vibrational motions of the material's crystal lattice, which in turn are directly related to the crystal structure and elemental composition of the material in question [e.g. *Wilson et al.*, 1955; *Farmer*, 1974]. Several methods of vibrational spectroscopy are commonly utilized in remote sensing, including infrared emission and reflectance, near-infrared reflectance, Raman, and attenuated total reflectance spectroscopy. For most geologic materials, fundamental vibrational frequencies typically occur in the thermal infrared (~2-100 μm) range of the electromagnetic spectrum, making the use of thermal infrared emission

spectroscopy highly applicable to the examination of planetary surfaces, due to its low power constraints and relatively simple measurement technique (interferometry). These techniques have been used extensively [*Farmer*, 1974; *Hunt and Salisbury*, 1976; *Mustard and Hays*, 1997; *Bandfield et al.*, 2000a; *Hamilton and Christensen*, 2000; *Glotch et al.*, 2004; *Ruff*, 2004] to investigate the properties of rock forming minerals in the laboratory and properties of planetary surfaces from orbit and landed spacecraft.

Thermal Emission spectroscopy is typically a bulk analysis method, as most rocks and surfaces are not homogenous at the spot size that typical instruments are capable of measuring (typically ~0.5-1 cm diameter spot for laboratories). However, the measurement of materials in a laboratory is not currently the primary case where emission spectroscopy is used. In general, emission spectroscopy is used in remote sensing applications on planetary bodies and Earth with typical instruments (e.g. THEMIS, TES, Advanced Spaceborne Thermal Emission and Reflection Radiometer [*Yamaguchi et al.*, 1998]) having spot sizes or spatial sampling of hundreds of meters to kilometers [e.g. *Bandfield et al.*, 2000a; *Christensen et al.*, 2003b; *Christensen et al.*, 2005; *Glotch and Christensen*, 2005; *Rogers et al.*, 2005]. At this scale there is no a compositionally/mineralogically uniform surface; rather, endmembers in the thermal infrared spectral range (e.g. 6-100 μm), to first order, add linearly with aerial abundance [*Ramsey and Christensen*, 1998]. It is possible to use a linear unmixing model for thermal infrared emission spectroscopy, where an endmember library of pure minerals [e.g. *Salisbury et al.*, 1992; *Christensen et*

al., 2000b] is used as a reference to determine quantitative mineral abundances based on their respective contributions (using a linear least squares method) to the measured spectrum. This method has been used extensively in the laboratory to determine the bulk compositions of unknown samples [e.g. *Ruff et al.*, 1997] and on spacecraft data to characterize the composition of Earth and other planetary bodies, including Mars [e.g. *Bandfield et al.*, 2000a; *Christensen et al.*, 2005; *Hamilton and Christensen*, 2005; *Koeppen and Hamilton*, 2008; *Bandfield et al.*, 2011].

However, this method is not without problems, as it is dependent on the mineral phases available in the endmember library spectra, meaning if the endmember is not in the library it cannot be included in the modeled spectrum. This leads to difficulties in the interpretation of mineralogically complex surfaces as the primary silicate absorption features related to the stretching of Si and O occur from ~8 to 14μm. Furthermore, not every possible mineral has an easily accessible pure component that can bet measured in the laboratory to make up a diverse and comprehensive endmember library. Further complicating matters, spectral features vary as solid solution series minerals vary in composition, so often times a range of compositions are needed for individual minerals like olivine, where the major spectral absorptions move to either higher or lower wavelength as a function of forsterite number [e.g. *Koeppen and Hamilton*, 2008; *Lane et al.*, 2011].

A large body of work has been completed to interpret and quantitatively analyze thermal emission spectra, from unmixing spectral endmembers for

quantitative mineral abundance determination to studying the effects of particle size and porosity on spectra [e.g. *Salisbury and Eastes*, 1985; *Moersch and Christensen*, 1995; *Mustard and Hays*, 1997; *Ramsey and Christensen*, 1998]. This measurement technique is highly valuable and spacecraft missions that carried emission spectrometers have yielded a wealth of quantitative mineralogical data of the surface of Mars [e.g. *Bandfield et al.*, 2000a; *Hamilton et al.*, 2003; *Ruff*, 2004; *Hamilton and Christensen*, 2005; *Ruff et al.*, 2006]. However, this work often lacks direct petrographic context for samples in question, which can significantly aid in determining the geologic mode of origin and type of alteration the samples have undergone. Instead, inferences about the nature of materials must be made from other instruments and techniques including such optical microscopy [*Herkenhoff et al.*, 2003], high-resolution morphology and grain size information determined from thermal inertia data [e.g. *Presley and Christensen*, 1997b].

6.1.3 Microscopic Emission Spectroscopy

In this work, I present the design and implementation of a laboratory microscopic emission and reflectance spectrometer with the aim to bridge the gap between remote sensing and *in situ* techniques. Furthermore, the laboratory instrument has been mated with an existing Mini-TES flight-spare instrument using the same microscopic fore optic and performs comparably to the laboratory setup with the commercially available spectrometer.

The microscopic laboratory instrument presented here has a spot size of ~85 μm, a factor of 100x better than currently available instruments and operates roughly at the scale of individual mineral phases in a medium grained volcanic sample. This small scale spot size allows for not only the reduction of spectral mixing in samples, reducing the need to perform linear deconvolution with large numbers of endmembers, but also will allow for *in situ* measurements of individual grains and their properties while retaining geological and spatial context of the sample under examination.

This technique can also help scale some of the other measurements that are typically made in the laboratory, on a lander, and from orbit. For example, it will be possible to better quantify how individual spectra observed in a single scene combine together to form a bulk rock spectrum and subsequently how bulk rock spectra relate to bulk planetary surface spectra from orbit. Currently the spectral behavior individual mineral grains as related to bulk rock and planetary surface spectra is not well constrained. This new instrument allows for the further characterization and quantification of bulk emission spectroscopy measurements.

One of the most significant advantages of this type of instrumentation is the extremely limited sample preparation required. This instrument is a non-contact measurement, requires no sample grinding or powdering, and can directly measure natural surfaces in place. When paired with a tool to remove the outermost rock rind, such as the rock abrasion tool (RAT) on the MER rovers, this instrument could characterize the primary mineralogy of the sample. When the minimal sample preparation is combined with the relatively quick acquisition

times (~5-10 minutes per spot) this instrument has significant advantages over techniques that take hours to days to measure a single sample. These advantages make this instrumentation a good candidate for *in situ* mineralogical studies on planetary surfaces, where it would be based on lander and/or rover style of spacecraft. It should be possible to reduce the form factor of this instrument sufficiently to allow for the mounting of this instrument on a rover arm, much like the APXS and Mössbauer instruments of MER.

6.2 Instrumentation and Experiment Apparatus

I present the instrument design and implementation that allows for the automated acquisition of thousands of emission spectra with an instrument resolution of ~85 μm over a specified sampling area. In this section I present all the components necessary to make the measurements at this scale. A labeled three-dimensional model that precisely describes the locations of every component is presented as Figure 6.1. Additionally, the details for each additional component are available in Table 6.1.

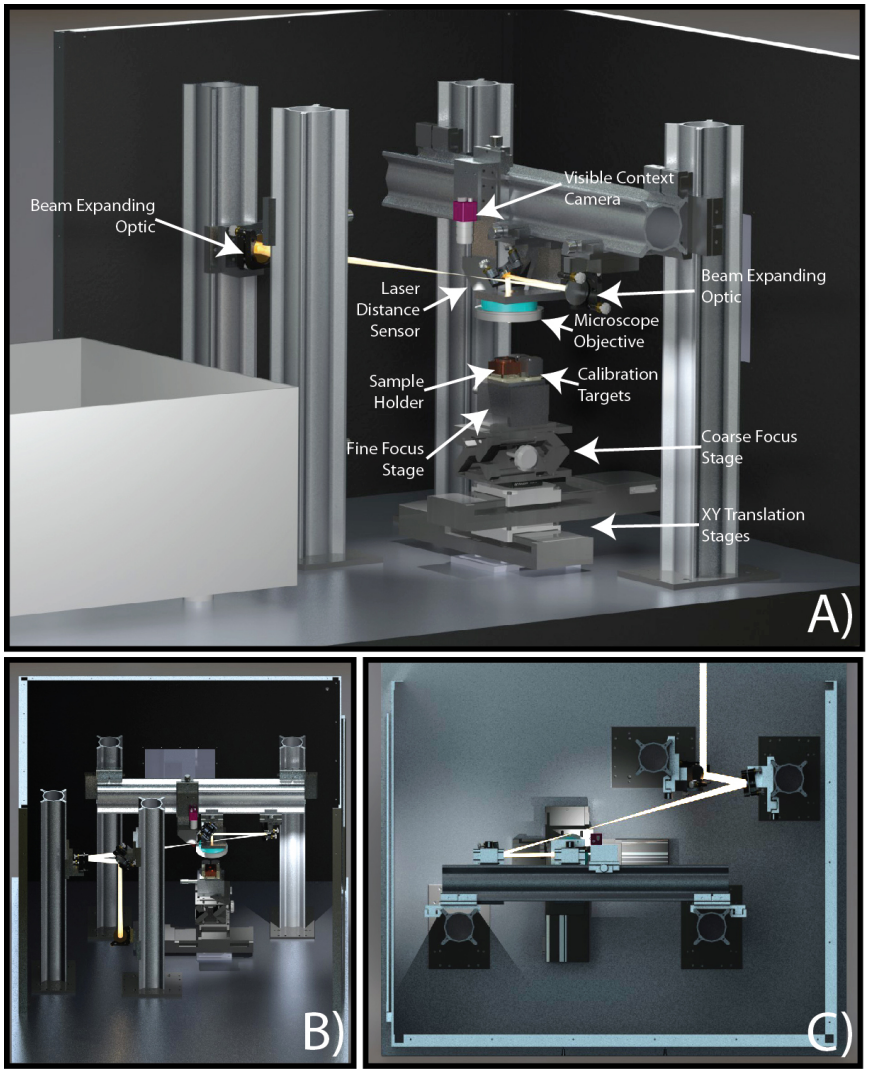

Figure 6.1. Three rendered views of the instrument solid model where major components are labeled in Figure 1a. **A)** A perspective view where the microscope objective is shown in blue and the ray trace of the extreme rays is shown in yellow. The top and side enclosing walls of the environmental chamber have been removed from this drawing. **B)** Side view of the instrument where additional components, including the relay optics that direct the beam into the spectrometer can be observed. **C)** Top down view of the instrument optical path where the beam entering the spectrometer leaves towards the top of the image.

6.2.1 System Components

6.2.1.1 Spectrometer

A commercially available interferometric spectrometer supplied by ThermoFisher/Nicolet is used as the base for this instrument (Figure 6.1 and Table 6.1). The spectrometer is originally indented to be used as a transmission spectrometer, though with the removal of a cover port and an internal mirror, the instrument can collect light from outside its environmental housing. The spectrometer purchased is equipped with a Cesium Iodide (CsI) beamsplitter with an operating range of 6400-200 cm^{-1} (Table 6.1) and operates as Michelson Interferometer where the beamsplitter directs and recombines light from both a fixed and precisely controlled moving mirror where signals are recombined to create a constructive and deconstructive interference pattern. After the light is modulated it is directed to either a pyroelectric or quantum detector. The modulated energy in the form of an interferogram with intensity related to moving mirror position (Figure 6.2a) is converted to an uncalibrated power spectrum (Figure 6.2b) by a discrete Fourier Transform.

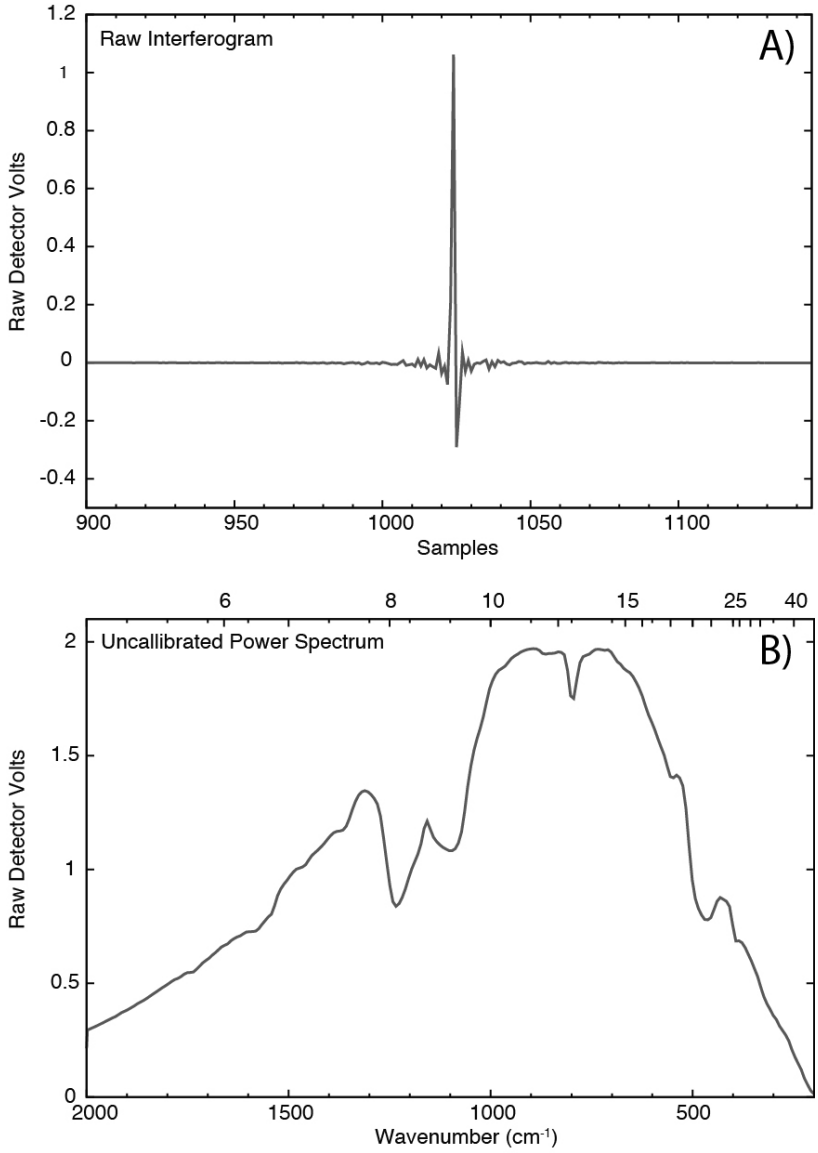

Figure 6.2. A) The raw interferogram generated from a ~85μm spot is shown along with **B)** the raw uncalibrated power spectrum of quartz. The data in each plot are related to one another by a discrete Fast Fourier Transform. The power spectrum of two known blackbody targets are then used to calibrate the data from this instrument in a full aperture calibration to radiance with units of W cm^{-2} sr^{-1} (section 6.2.2).

6.2.1.2 Infrared Detectors

In this setup I utilize two separate detectors depending on the type of measurement the user wishes to make. I have implemented both a Mercury Cadmium Telluride (MCT) quantum detector and Deuterated L-alanine doped Triglycene Sulfate (DLaTGS) pyroelectric detector in this system. While the pyroelectric detector is comparable to what is currently utilized on many spacecraft interferometers (e.g. TES, mini-TES), it has a sensitivity of ~5-10x lower than the cryogenically cooled MCT quantum detector. However, adding a cryogenically cooled detector to spacecraft instruments adds significant complexity and increases the potential for detector failure if the cooler ceases to operate. Furthermore the spectral range covered by the MCT detectors is often limited to ~600cm^{-1}, though they can measure to lower wavenumbers using special coatings but with reduced signal to noise (SNR). These longer wavelengths (>20μm) often provide valuable and diagnostic absorption features for primary mafic and secondary alteration mineralogy [e.g. *Ruff et al.*, 2007; *Koeppen and Hamilton*, 2008; *Lane et al.*, 2011] and are important for mineralogical studies of planetary surfaces.

In this instrumental setup I utilize the MCT detector as a quick reconnaissance tool to evaluate the mineralogical diversity of the sample in a laboratory setting and then utilize the pyroelectric DLaTGS detector to collect the full spectral range allowable by the beamsplitter and optics combination. Furthermore the pyroelectric detector is a better match for the capabilities of the

performance that can be expected for this style of instrument on a planetary surface.

6.2.1.3 Optical Design

The optical design of the system is straightforward, utilizing a collimated beam throughout the system (Figure 6.3). The microscope is a diamond turned Schwarzchild objective with an F-number of ~0.4 and a focal length of 9.81mm (Figure 6.4, Table 6.1). This objective minimizes spherical aberration, coma and astigmatism as the primary and secondary surfaces are matched spherical components. Depending on the position of the secondary mirror, it is possible to manipulate the nature of the light exiting the optic. For example in the version mounted to the flight spare mini-TES instrument, a back F-number of 12 is used as it matches the original design of the mini-TES Cassegrain telescope [*Christensen et al.*, 2003a].

Table 6.1. Microscopic emission instrument characteristics and supporting components, including translational stages, context imager, sample and calibration targets.

Spectrometer	
Spectrometer Manufacturer	ThermoFisher/Nicolet
Interferometer Type	Michelson
Beamsplitter Material	Cesium Iodide (CsI)
Typical Spectral Range	4000 – 200 cm^{-1} (1.56 – 50 μm)
Spectral Sampling	1-16 cm^{-1}
Samples/Interferogram	8192
Interferometer Beam Size	~2.5 cm (through beamsplitter)

Detectors	
DLaTGS Detector	
Temperature Control	Thermo-Electric Temperature Stabilized
Detector Size	0.5 mm diameter
*Detector D**	> $2.4x10^{8}$ cm•$Hz^{1/2}$•$Watt^{-1}$ (20 Hz)
Interferometer Mirror Velocity	0.1581 cm/sec
Spectral Range	6400-200 cm^{-1}

Table 6.1. continued

MCT-B

Temperature Control	Cryogenic Liquid Nitrogen Cooled
Detector Size	1 mm by 1 mm square
*Detector D**	> 8.0×10^{9} cm•$Hz^{1/2}$•$Watt^{-1}$ (20 Hz)
Interferometer Mirror Velocity	1.8988 cm/sec
Spectral Range	11,700-400 cm^{-1}

Fore-Optics

Microscope Objective Design	Schwarzschild objective
Spot Size	~85 μm (approaching diffraction limit)
Numerical Aperture/f-number	0.8/~0.4
Microscope Field of View	120°
Working Distance	~9.81 mm
Depth of Field	~20 μm

Sample/Calibration Specifics

Maximum Sample Size	2 x 2 cm
Sample Temperature	Heated to 100˚C > background
Calibration Blackbody Targets	(1) "hot" 130˚C , (1) "warm" 110˚C, 5 mm spherical Blackbody cavity w/0.5 mm diameter entrance

Table 6.1. continued

DLaTGS SNR (5 min acq., @380K, 10µm)	~80
MCT-B SNR (5 min acq., @380K, 10µm)	~120
Silicon Nitride Infrared Source	>1200˚K for reflectance mode

Supporting Systems

X Stage Translation	10 cm
Y Stage Translation	10 cm
Z Stage Translation	1.25 cm
Coarse Z Stage Translation	5.5 cm
X-Y-Z Stage Micro-step Size	< 2 µm (including hysteresis/backlash)
Laser Displacement Sensor Resolution (Z)	1-3 µm (at the center of measurement)
Context Camera (1.5 Megapixels)	Color CCD (<4x6 µm resolution)

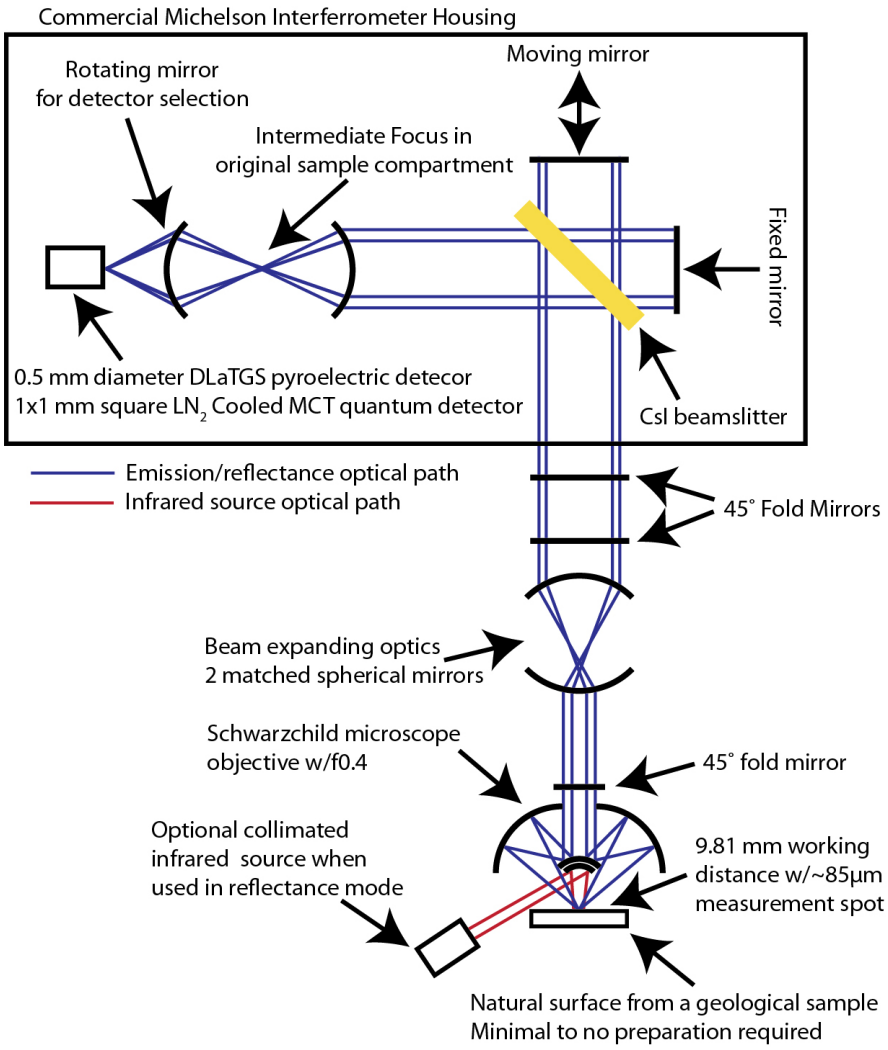

Figure 6.3. A schematic layout of the optical system for the microscopic emission and reflectance spectrometer represents all the major components of this optical system. The blue lines represent the extreme light rays of the spectrometer optical system, where the relative size of the rays represent the true scaling and path of the light in the system. The black shapes represent different optical or system components in the system and are labeled accordingly. The red lines represent the emitted energy of the infrared source when the system is used in reflectance mode.

However, for the laboratory setup, the position of the secondary mirror was adjusted so the microscope objective (Figure 6.4) outputs a collimated beam ~1 cm in diameter which is upsized by beam expanding optics to ~2 cm inches in diameter to better match the desired input of the Nicolet spectrometer. The relay/beam expanding optics are a pair of matched spherical mirrors with focal lengths of 75 cm and 150 cm also designed to minimize spherical aberration, coma, and astigmatism to ensure the image formed on the detector is crisp and accurately represents a small circular spot measured on the sample. Several other flat fold mirrors are utilized to direct the beam from the high measurement location to the level of the spectrometer. All mirrors in the system are gold coated and flat to ¼ wavelength in the visible wavelengths, making them excellent reflectors in the infrared, with reflectivity > 0.995 over nearly the entire spectral range [e.g. *Bennett and Ashley*, 1965]. Furthermore, in principle the optical design of this system is quite similar, with the exception of the microscope objective and the relay optics required to achieve the ~85 μm measurement spot size, to that of a suite of existing emission spectrometers used extensively by the planetary science community to evaluate and characterize data returned from spacecraft missions [e.g. *Ruff et al.*, 1997; *Feely and Christensen*, 1999; *Bandfield et al.*, 2000a; *Christensen et al.*, 2000b; *Rogers et al.*, 2005; *Rogers and Christensen*, 2007; *Edwards et al.*, 2008; *Koeppen and Hamilton*, 2008].

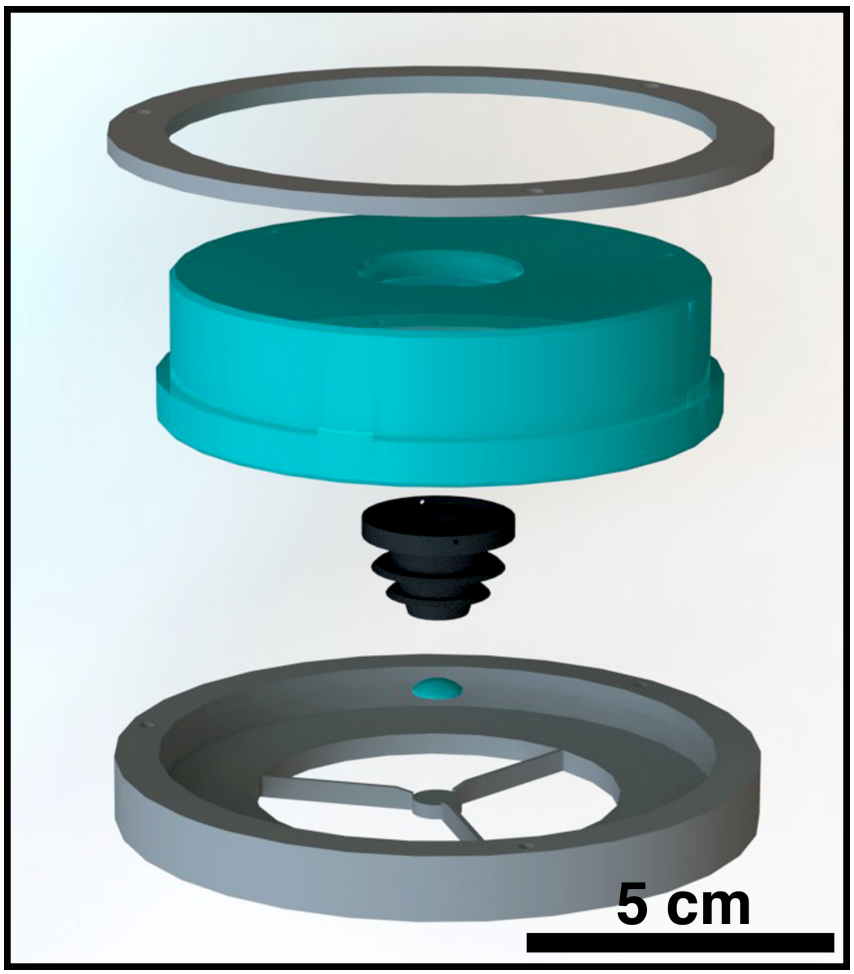

Figure 6.4. An expanded view of the solid model of the Schwarzschild objective is shown in this figure. The blue components represent diamond turned optics, while the silver components are the supporting spider and compression ring used to physically locate and hold the secondary mirror (small convex surface). The objective is mounted onto a specialized mounting bracket using a three-point mount directly to the primary mirror (large concave surface). Additionally, a baffle (black) designed to minimize stray light is mounted at the exit of the primary mirror and extends into the primary mirror cavity with a maximum light allowance diameter matched to the secondary mirror.

Once the collimated energy is directed into the Nicolet spectrometer by the last fold mirror, the energy passes through a CsI beamsplitter oriented at 45˚ (Figure 6.3) which separates the equally light into two directions with different path lengths, one fixed and one variable. The specifics of Michelson interferometry are described in Section 2.1.1. However, this signal measured by the detector is not purely derived from the sample. I use a full aperture calibration (described below) that accounts for the instrument response function as well as radiance contributed by the instrument itself [e.g. *Ruff et al.*, 1997]. Furthermore the environment is also emitting and a portion of that energy is reflected off of the sample and captured by the optical system, also known as downwelling radiance [e.g. *Ruff et al.*, 1997]. The specifics of instrument calibration are discussed in Section 2.2.

6.2.1.4 Supporting Systems

A variety of support systems are required for the acquisition and calibration of spectral data at the sub-100μm scale (Figure 6.1, Figure 6.5, Table 6.1). In order to accurately measure a spectrum, I must control the X, Y, and Z position of the sample to within ~1-2 μm with little or no physical movement of the sample. To do this I use translational stages capable of high precision movement.

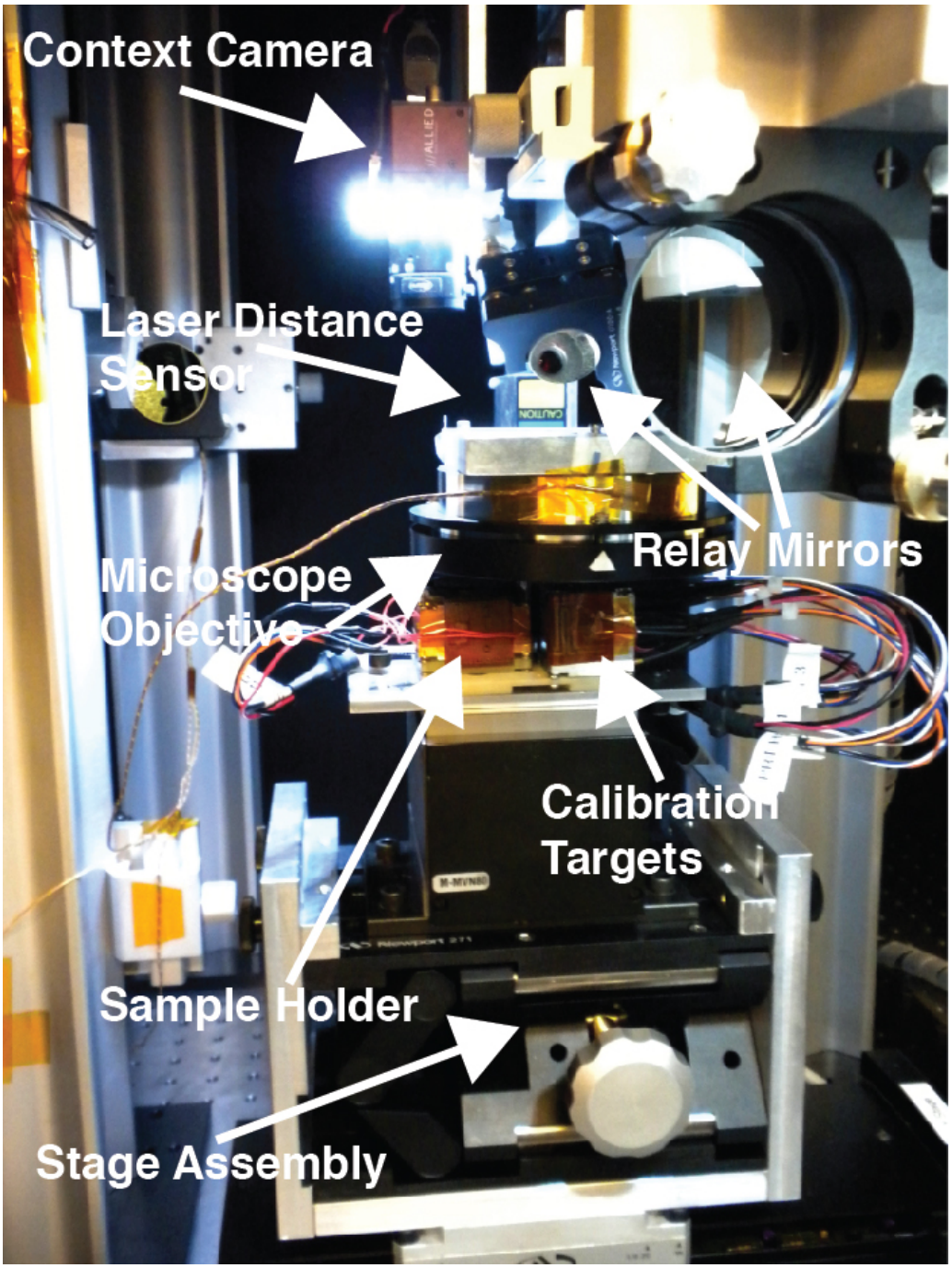

Figure 6.5. A side view of the XYZ position system, microscope objective and supporting systems, including the laser displacement sensor and the context camera. For reference, the relay mirrors are 2 inches in diameter.

Due to the extremely fast (small depth of field) Schwarzschild objective, it is necessary to position the sample within ~20 μm of the best focus in the Z-axis. To accomplish this I use a laser displacement sensor capable of accurately and precisely measuring distances to within several microns. The desired sample spot is moved under this sensor and the Z stage is moved until the best focus is established, generally within 3-5 μm (Figure 6.6a and 7a). This system works well for both solid and particulate samples. Where a best focus cannot be found (due to low reflectivity, oriented crystal faces that prevent the return of a laser signal to the sensor detector, etc.), the location is recorded and the previous best focus is used. This assumption is generally reasonable where the sample is not a particulate and the surface is generally smooth over the data spacing. When this is not the case, a spectrum of a defocused (and enlarged spot) is acquired.

A visible imaging context camera with ~7 μm/pixel resolution is also used to identify desired measurement locations (Figure 6.6b and 7b) and control the acquisition grid. This grid can be constructed as any combination of X by Y samples and calibration targets may be acquired at any interval, though generally at the end of a column of measurements.

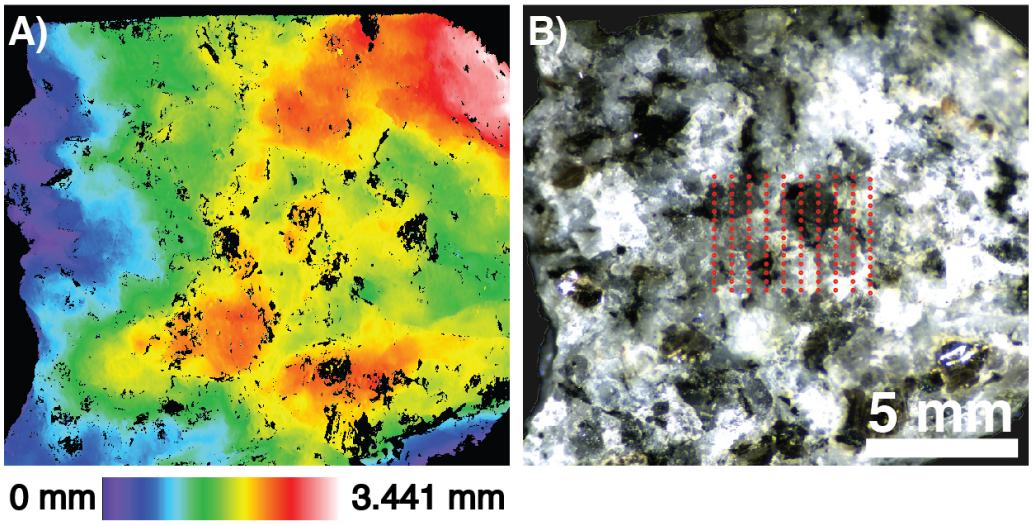

Figure 6.6. A) Example of a micro-topography map of a solid sample used to find the microscope focal point within ~5 μm. Black locations indicate the absence of good laser returns. In these cases I use an interpolated value for best focus. **B)** Co-aligned visible context image with a microscope sampling pattern overlain (red circles). The circles are to scale with the spot size of the instrument and are the exact locations where thermal emission data are acquired.

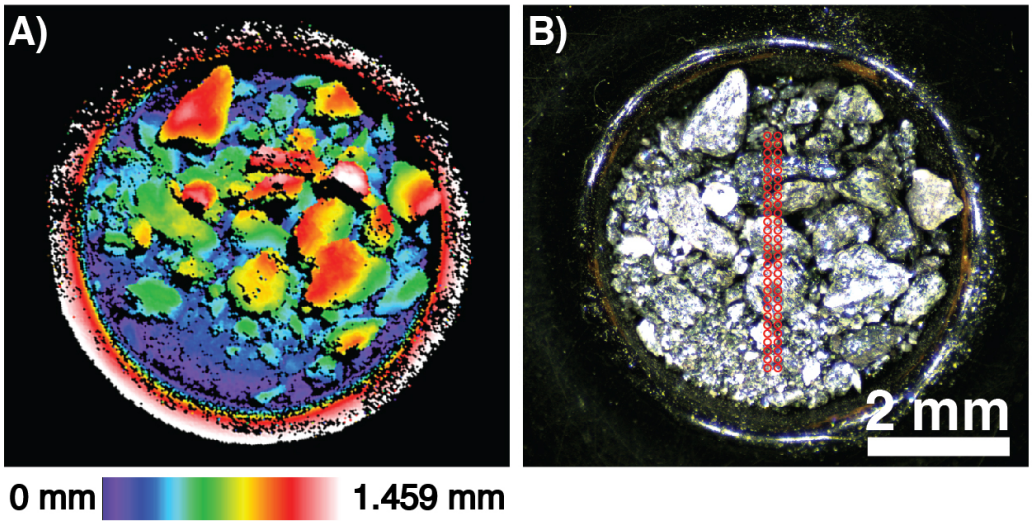

Figure 6.7. A) Example of a micro-topography map of a particulate sample used to find the microscope focal point within ~5 µm. Black locations indicate the absence of good laser returns. In these cases I use an interpolated value for best focus. **B)** Co-aligned visible context image with a microscope sampling pattern overlain (red circles). The circles are to scale with the spot size of the instrument and are the exact locations where thermal emission data are acquired.

These X, Y, and Z translation stages were physically referenced to each test location (context image, focus, and microscope) by a thin wire (~35 μm in diameter) cross hair that can be heated to ~600˚ K to reference the spectrometer with a high level of signal at the detector. Once each test position has been established in relational space, it is possible to accurately move to each test position with a sample and measure the identical spot to within ~5 μm in absolute position, which is less than the individual pixel size of the context imager.

The sample in the emission setup is heated above room temperature to enhance signal to noise for individual measurements [e.g. *Ruff et al.*, 1997]. While this process can result in the dehydration of some clays and sulfates, in general most rock forming minerals do not significantly change their crystal structure with a moderate (100˚ K) increase in temperature. Furthermore it is not uncommon for geologic materials, especially on airless bodies to experience temperatures above 350˚ K [e.g. *Vasavada et al.*, 2012]. While it is not explicitly necessary to heat the sample to ~390˚ C, it aids in reducing measurement time and significantly increases the signal to noise as emitted radiance is proportional to temperature to the fourth power. However as an alternative to heating samples, I have developed a thermal infrared reflectance mode for this instrument (Section 6.2.1.5).

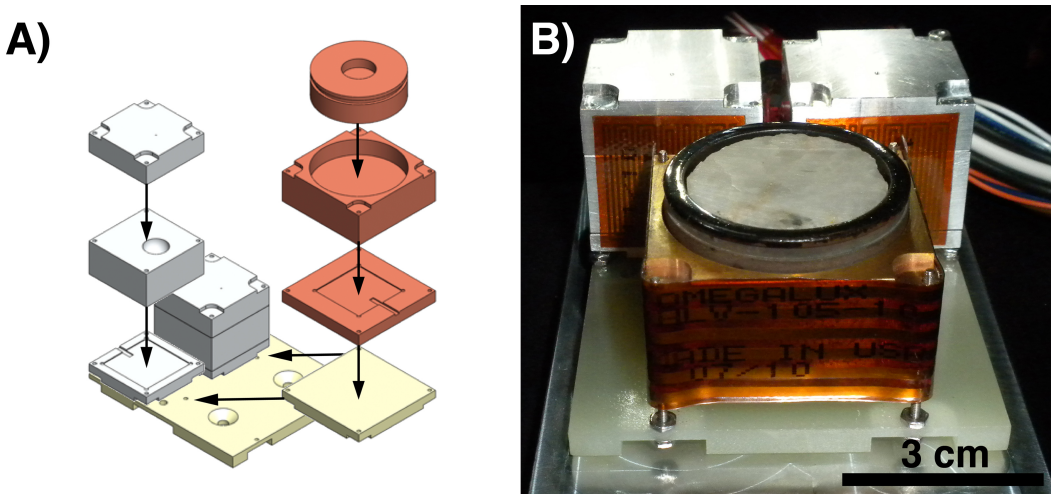

Figure 6.8. A model of the sample holder (orange) and blackbody calibration targets (gray) **(A)** with the individual components expanded for clarity. The sample holder is constructed of copper because of its extremely high thermal conductivity, while the blackbodies are constructed of aluminum because aluminum has a high reflectivity over the thermal infrared wavelength region and any unpainted surfaces will reflect the majority of the incident energy. **B)** The final completed sample holder and blackbody calibration targets with a quartz standard used to compare the instruments calibration to existing laboratory equipment.

Two blackbody cavities (5 mm spheres with a 0.5 mm entrance) are used as targets for the instruments full aperture calibration (Figure 6.8). These blackbodies are controlled to ~0.1˚ K precision and accuracy at 400˚ K and 380˚ K bracketing the typical temperature (~390˚ K) of a sample in this instrument. These calibration targets are mounted directly next to the sample holder, which allows for multiple calibration points throughout the measurement to capture any instrument drift or changes in the environment. The calibration targets are instrumented with two platinum resistance thermistors (PRT) each (one above and below the spheres) and allow the precise determination of the temperature of the sphere. These differentially mounted PRTs typically show a measured temperature difference of 0.05˚ K, which is significantly below the accuracy and precision of the PRTs. The PRTs have an absolute calibration accuracy of ~0.1˚ K from 90˚ K to 780˚ K.

Furthermore an instrumented environmental chamber (Figure 6.1), where water vapor and CO_2 have been scrubbed from the atmosphere, encompasses the entire instrument. The interior of this chamber is painted with Krylon Ultra Flat Black 1602 paint that has an emissivity >0.95 over the entire thermal infrared wavelength region [*Stierwalt et al.*, 1963]. I monitor relative humidity, environmental air temperature, and the temperatures of various system components. Any dramatic changes in these parameters are logged throughout the acquisition of sample data and can be used to identify data that may be poorly calibrated.

6.2.1.5 Reflectance Mode

As an alternative to directly heating the sample to >100˚ K above ambient temperature, I have developed a micro-reflectance attachment for this instrument (Figure 6.3, Table 6.1). In this case rather than the sample being heated from below, the sample is illuminated by an infrared source (a >1200˚ K silicon nitride emitter) with relatively uniform spectral response over 2000-200 cm^{-1}. While this is not the primary mode of this instrument, as the goal is to make direct comparisons to existing laboratory and spacecraft data, it is a unique measurement that could easily be applied to a landed spacecraft thermal infrared micro-spectrometer.

Many commercial microscopic reflectance instruments are available, but they typically use cooled detectors and modulate (which occurs when light passes through the interferometer) the light prior to its interaction with the sample. The experimental setup I have developed here is significantly different in that unmodulated light is directed at the sample in a nearly perpendicular orientation. This light is then reflected off of the sample approximately into a hemisphere for Lambertian surfaces, which is expected as typical sample surfaces do not highly forward- or back-scatter. This unmodulated reflected light is captured by the same optical system that captures the emitted energy when the sample is directly heated. The value of this method is that both an emission and reflectance measurement can be made of the identical spot. If different fore-optics were utilized with this system (an off-axis parabola or Schwarzschild objective with a larger f-number), the reflectance mode can be used to quickly acquire high SNR

micro-spectra while a defocused spot can be utilized to make bulk emission measurements. The variety of measurements (point counting of individual mineral grains with primary geologic context and bulk mineralogy measurements at the outcrop scale) makes this style of instrumentation unique in its capabilities and a strong candidate for a rover or lander platform as a quantitative mineralogy instrument.

6.2.2 Calibration and Data Acquisition

6.2.2.1 Automated Acquisition

The microscopic emission spectrometer allows the investigator to easily acquire large volumes of spectroscopic data with little input. The investigator defines the acquisition parameters, including number of spots in the X and Y directions (Figures 6.6b and 6.7b), the spacing between these spots, the sample and blackbody calibration target temperatures, and the calibration interval. Once the sample is loaded the system automatically acquires all the specified data and necessary ancillary measurements including the temperature of the environmental chamber, relative humidity, instrument temperature and sample temperature. In order to ensure measurement stability, several parameters, including sample and blackbody temperatures, relative humidity, and microscope temperature are monitored until they reach the set points. Furthermore, anytime the sample is moved a significant distance (e.g. to the calibration targets), the instrument pauses until stability conditions are met (typically 5 minutes).

6.2.2.2 Spectral Calibration

By in large the calibration of raw data to emissivity have not been significantly modified from [*Ruff et al.*, 1997] and the majority of the equations and measurements necessary to accurately account fro all the factors that effect thermal emission have been presented previously including the energy related to sample emission, reflection, and background sources [e.g. *Kember et al.*, 1979; *DeBlase and Compton*, 1991; *Rewick and Messerschmidt*, 1991; *Christensen and Harrison*, 1993; *Ruff et al.*, 1997]. The major difference between the method used by *Ruff et al.* [1997] and the method described here is the use of numerous blackbody calibration measurements over the span of the entire spectral acquisition. Depending on the number of acquisition points the investigator specifics for the microscopic emission spectrometer (>200-1000), lengthy (>1 day) measurements can arise necessitating the use of multiple blackbodies to account for changes in the instrument response and environmental parameters. Here I present the updated method for calibration of thermal emission data acquired form this instrument.

After *Christensen and Harrison* [1993] and *Ruff et al.* [1997], I use the following equations to solve for the emissivity of the sample, accounting for a time varying term using a cubic spline interpolation for each spectral point with a sample at an unknown temperature (definitions for all variables used can be found in Table 6.2). I do not show the cubic spline interpolation in the following equations but rather include the solutions for all equations at wavelengths λ, temperature T, and time t_{samp}, where the values at each time have been

interpolated with the cubic spline or a linear approximation if enough data points are not available for cubic interpolation. Furthermore, this equation set derives a temperature independent emissivity using a time-interpolated calibration, though throughout it is useful to consider the idealized and temperature dependent spectral radiance (*B*) and emissivity (ε) as inseparable. These variables are generally represented as $\varepsilon(\lambda)B(\lambda,T,t_{samp})$ and are typically manipulated as a group, until the final derivation of emissivity.

Table 6.2. Definition of variables used in the equations to derive calibrated emissivity

λ	Wavelength
T	Temperature
t_{samp}	Time at a given point between two calibration measurements when the sample was acquired. The corresponding function value is calculated using a cubic spline.
E_{inst}	Emissivity of the instrument
B_{inst}	Idealized radiance of the instrument
F	Instrument response
ε_{env}	Emissivity of the environment
B_{env}	Idealized radiance of the environment
ε_{samp}	Emissivity of the sample
B_{samp}	Idealized radiance of the sample
$R_{samp}=1-\varepsilon_{samp}$	Reflectivity of the sample is equivalent to 1-emissivity by Kirchhoff's law
V_{samp}	Measured sample voltage
B_{bb}	Idealized radiance of the blackbody calibration targets
V_{bb}	Measured blackbody voltage
cf	Christiansen feature wavelength

Table 6.2. continued

σ_V	Standard deviation of detector voltage
SNR	Signal to Noise
n	Number of spectral co-additions
h	Planck's constant
c	Speed of light
k	Boltzmann's constant

First I take the initial equation from *Christensen and Harrison* [1993] that defines all the important parameters that contribute to the measured voltage of the Fourier transform spectrometer:

$$V_{meas}\left(\lambda,T,t_{samp}\right)=\begin{bmatrix}\varepsilon_{samp}\left(\lambda\right)B_{samp}\left(\lambda,T,t_{samp}\right)\\+R_{samp}\left(\lambda\right)\varepsilon_{env}\left(\lambda\right)B_{env}\left(\lambda,T,t_{samp}\right)\\-\varepsilon_{inst}\left(\lambda\right)B_{inst}\left(\lambda,T,t_{samp}\right)\end{bmatrix}F(\lambda,t_{samp}) \tag{6.1}$$

By using blackbodies at two known and temperatures and raw voltages measured by the detector for each calibration target, I can compute an instrument function [e.g. *Hanel et al.*, 1972; *Ruff et al.*, 1997] (Figure 6.9a). Equation 6.2 assumes that that the emissivity of the blackbodies is 1 at all wavelengths and there is no reflected component. The time varying instrument response function is a critical component to the calibration procedure as it allows for the conversation of uncalibrated volts measured by the detector to calibrated spectral radiance (W cm^{-2} sr^{-1}). Additionally the time varying component allows for small changes in the instrument behavior to be captured during long data acquisition runs.

$$F\left(\lambda,t_{samp}\right)=\frac{V_{bb}(\lambda,T_1,t_{samp})-V_{bb}(\lambda,T_2,t_{samp})}{B_{bb}(\lambda,T_1,t_{samp})-B_{bb}(\lambda,T_2,t_{samp})} \tag{6.2}$$

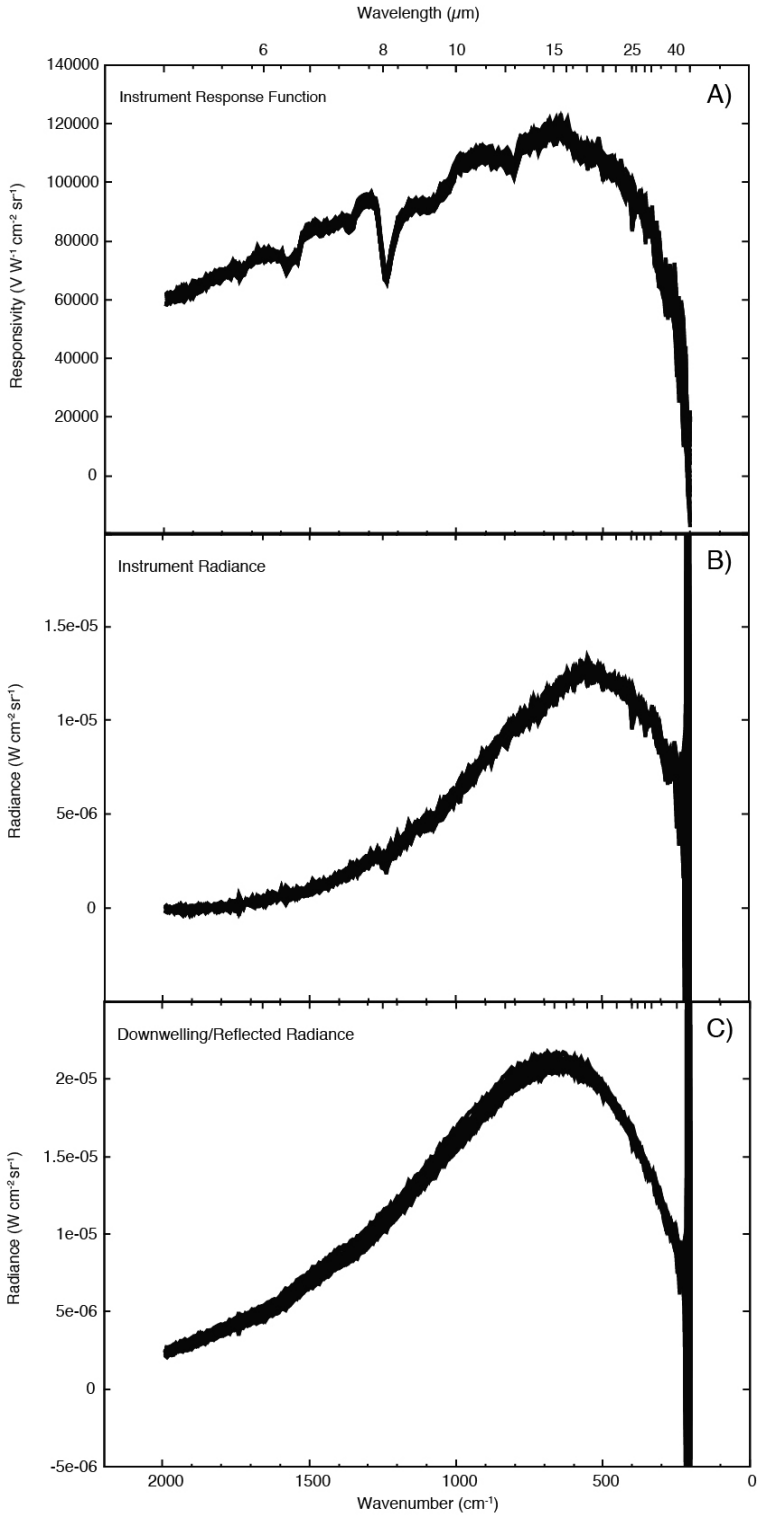

Figure 6.9. Typical instrument calibration and response parameters are shown. **A)** 25 different instrument response functions over 10 days. **B)** 25 different

Figure 6.9. continued

instrument radiance curves over 10 days **C)** 25 different down welling radiance measurements over 10 days. The variability in all cases is less than a few percent. To help capture the changing environment as many samples can be acquired between calibration measurements, I interpolate the instrument response function and instrument radiance using cubic-splines based on time for each individual sample.

Equation 6.3 is the derivation of the instrument radiance term (Figure 6.9b). Using Equation 6.2 and a single blackbody measurement it is possible to derive the instrument radiance. The instrument radiance is the energy that reaches the detector that did not originate at the sample [e.g. *Ruff et al.*, 1997], including detector and background energy from the emitting components inside the spectrometer. As a further simplification, the instrument emissivity ($\varepsilon_{inst}(\lambda)$) is commonly assumed to be 1 and the instrument radiance term is replaced by an ideal blackbody of the measured instrument temperature [*Ruff et al.*, 1997]; however, in the case of this instrument I use the derived instrument radiance and not an ideal radiance, as the instrument radiance is a combination of blackbodies of several temperatures for this instrument.

$$\varepsilon_{inst}(\lambda) B_{inst}(\lambda, T, t_{samp}) = \frac{B_{inst}(\lambda, T_1, t_{samp}) - V_{bb}(\lambda, T_1, t_{samp})}{F(\lambda, t_{samp})} \tag{6.3}$$

Calculating calibrated radiance for a sample is accomplished by rearranging Equation 6.1 to the form shown in Equation 6.4. In this case all of the radiance (both emitted and reflected) are moved to a single side of the equation. In order to simplify this equation and derive a temperature independent emissivity, it is necessary to determine the sample temperature from a non-contact method (as is typical for spacecraft missions) [e.g. *Lyon*, 1962]. In order to solve for temperature, I assume that over some portion of the spectrum the emissivity is 1 and the reflectivity is zero, which is best met at the Christiansen frequencies in the spectrum. This is the frequency where the index of refraction (n) for the sample is equal to the index of refraction for the surrounding medium [*Henry*,

1948]. This frequency is often coincident with low extinction coefficients (k) for geologic materials and produces an emissivity near 1.0 [*Ruff et al.*, 1997]. In a complicated system such as the microscopic emission spectrometer where many environmental sources of a variety of temperatures are being reflected off of the sample, I use a diffuse gold reflector in place of a sample to accurately measure the typical downwelling/reflected spectral component (Figure 6.9c). In this case I then apply a scaled version of this measured downwelling radiance as the mixed variable group $\varepsilon_{env}(\lambda)B_{env}(\lambda,T,t_{samp})$. This allows for spectral features present in the downwelling radiance as well as temperature variability to be accounted for robustly.

$$\begin{bmatrix} \varepsilon_{samp}(\lambda)B_{samp}(\lambda,T,t_{samp}) \\ +R_{samp}(\lambda)\varepsilon_{env}(\lambda)B_{env}(\lambda,T,t_{samp}) \end{bmatrix} = \begin{bmatrix} \dfrac{V_{samp}\left(\lambda,T,t_{samp}\right)}{F\left(\lambda,t_{samp}\right)} \\ +\varepsilon_{inst}(\lambda)B_{inst}(\lambda,T,t_{samp}) \end{bmatrix} \tag{6.4}$$

If I calculate a brightness temperature for all radiances (Equation 6.5, assuming there are no emissivity absorption features) for all wavelengths using the Planck equation in the form of Equation 6.6, the maximum temperature of the sample temperature is likely the best match for the position of the Christiansen frequency. *Ruff et al.* [1997] includes a detailed discussion of the effect of deriving the wrong Christiansen frequency on the absolute calibration of spectral data, though the effects are generally minimal in terms of absolute emissivity, they are not negligible.

$$B_{samp@cf}(\lambda,T,t_{samp}) = \frac{V_{samp@cf}\left(\lambda,T,t_{samp}\right)}{F\left(\lambda,t_{samp}\right)} + \varepsilon_{inst}(\lambda)B_{inst@cf}\left(\lambda,T,t_{samp}\right) \tag{6.5}$$

$$T = \frac{hc}{\ln\left[\frac{2hc^2}{\lambda^5 B_{samp@cf}} + 1\right]k} \tag{6.6}$$

The final step for calibration is the calculation of a temperature independent emissivity. This is accomplished by again rearranging Equation 6.1 using the time interpolated instrument response function, downwelling radiance, and instrument energy variables that were solved for in Equations 6.2-6.6.

$$\varepsilon_{samp}(\lambda) = \frac{\frac{V_{samp}\left(\lambda, T, t_{samp}\right)}{F\left(\lambda, t_{samp}\right)} - \varepsilon_{env}(\lambda) B_{env}\left(\lambda, T, t_{samp}\right) + \varepsilon_{inst}(\lambda) B_{inst}\left(\lambda, T, t_{samp}\right)}{B_{samp}\left(\lambda, T, t_{samp}\right) - \varepsilon_{env}(\lambda) B_{env}\left(\lambda, T, t_{samp}\right)} \tag{6.7}$$

The validity of this method is well established and a detailed discussion and error analysis of many components of this calibration routine is performed by *Ruff et al.* [1997]. Furthermore, I utilize a full-aperture calibration, with the blackbody calibration targets placed at the same position as the sample. With this setup, the same number of components (e.g. mirrors, baffles, optomechanical components) and instrument orientation (e.g. field of view, sample/calibration target position) are used and allow for all of the components to contribute in the same way to the raw measured spectrum. These contributions are then incorporated into the instrument response function and instrument radiance, allowing them to be completely removed in the calibration routine with no assumptions about the reflectivity of various mirrors or contribution of other components required.

6.3 Instrument Results

6.3.1 Signal to Noise

The signal to nose ratio of this system is dependent on several factors including detector responsivity, the temperature of the target material, the number of spectra that are co-added together (scales as the square root of the number of samples), the spectral sampling, and the overall throughput of the optical system. In order to assess the SNR of a complicated optomechanical system such as that presented in this work, I measure many individual spectra with no co-adding of the same spot under the same conditions for each detector. I measured a quartz standard and each blackbody calibration target (Figure 6.10). In order to calculate the SNR of the system a moving window standard deviation of 20 spectra divided by the IRF and averaged together. An ideal blackbody at the specified target temperature is then divided by the average windowed standard deviation (Equation 6.8). The SNR is calculated in this manner as this removes any time dependent variations in the instrument that may be due to temperature controller instability or a changing environment and instrument temperature.

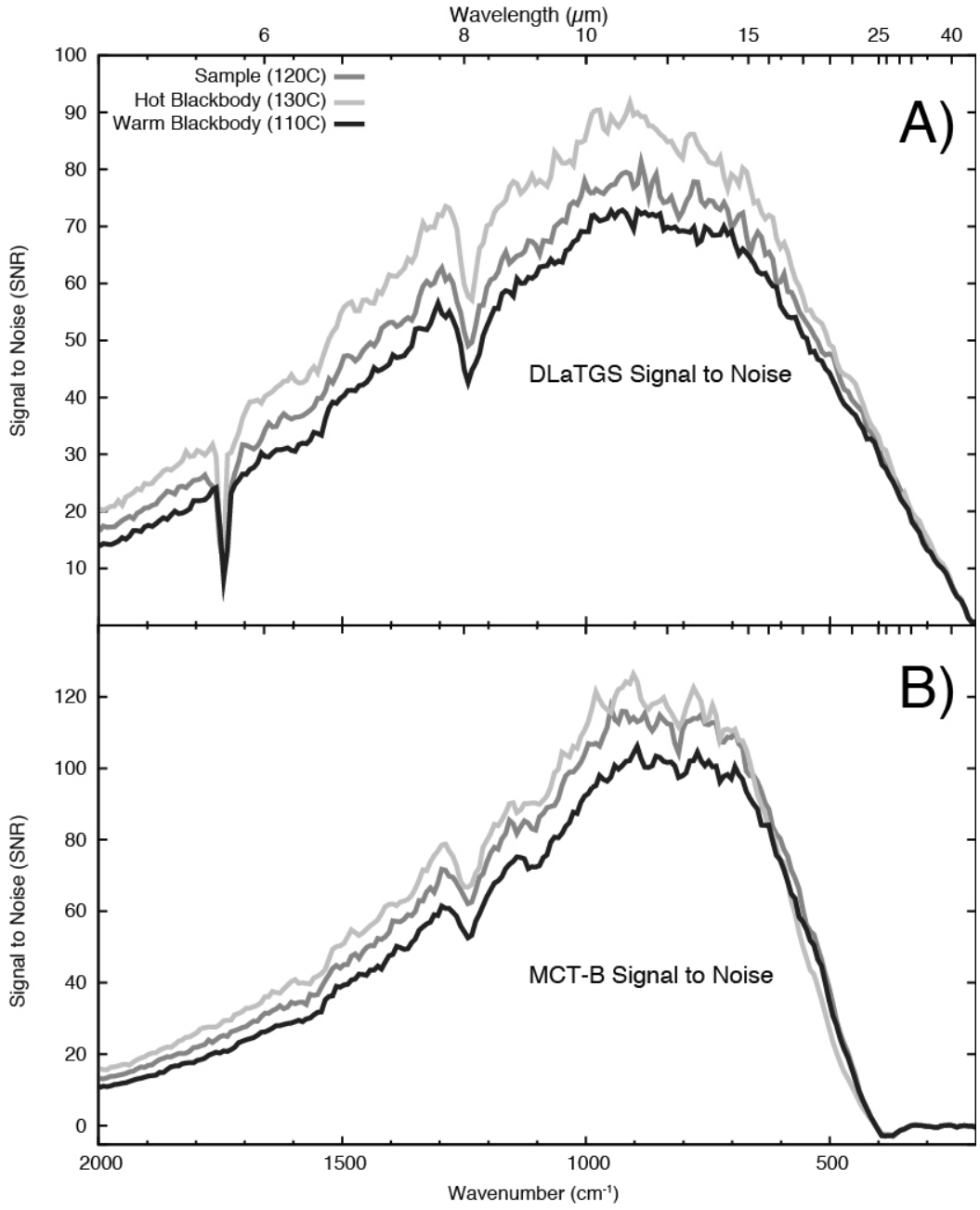

Figure 6.10. Signal to noise for each detector in the micro-emission and reflectance spectrometer instrument. The SNR is shown for each of the blackbody calibration targets and a quartz sample. The SNR is directly correlated to sample temperature in all cases. In each case I co-added 1000 individual spectra to make the plots. However a reduction of 500 scans results in a reduction

Figure 6.10. continued

in SNR by <10%. **A)** DLaTGS detector. **B)** MCT-B detector. The slightly higher peak SNR for the MCT-B detector is largely attributed to the enhanced sensitivity as a result of the detector cooling. However, the SNR increase is significantly less than order of magnitude expected by comparing detector D*. This is likely due to the elevated background signal present from the environment as the MCT-B detector is highly sensitive to any room temperature radiation. A cold stop to remove any excess energy from the system would likely increase SNR significantly.

$$SNR(\lambda,T) = \frac{B_{samp}(\lambda,T)}{\left[\left(\frac{\sum_{i=1}^{n-20}\sigma_V(\lambda,T)_i \ldots \sigma_V(\lambda,T)_{i+20}}{n}\right)\cdot\left(\frac{1}{F(\lambda,T)}\right)\right]} \quad (6.8)$$

The derived instrument SNR at 900cm^{-1} for the DLaTGS detector is ~70-90 for target temperatures ranging from 380-400˚ K. The SNR at 900cm^{-1} for the MCT-B detector is slightly higher at ~100-120 for target temperatures ranging from 380-400˚ CK. The increase in signal for the MCT-B detector is not the predicted ~2-3 times improvement expected, though this is likely due to the lack of a cold field stop that would prevent stray light and extreme rays from entering the detector. Since the noise of a DLaTGS is fixed with the area of the detector, it is not as affected by the stray light/extreme rays of the system as the MCT-B detector that has noise that scales with the number of photons that interact with the detector. So a warm instrument and environment, coupled with extreme rays derived from room temperature materials, which do not greatly affect the DLaTGS SNR likely greatly affect the MCT-B detector as many more photons from locations other than the sample are measured, increasing the detector noise.

6.3.2 Calibration Evaluation

6.3.2.1 Comparison to Existing Laboratory Measurements

By comparing the results of a standard target in existing laboratory [e.g. *Ruff et al.*, 1997] equipment and the microscopic emission spectrometer, the level of absolute calibration can be assessed. Figure 6.11 is the average of 100 micro-

emission spectra compared to the bulk measured spectrum of the quartz standard (Figure 6.8b) of a ~1x1 cm square area. Several observations can be made when comparing these two data. First, the overall contrast between instruments is well matched, indicating that the downwelling radiance is well accounted for. Furthermore the position and shape of the absorption features are also well matched. The only major variability in the spectrum shown occurs on the shorter wavelength side of major absorption features (e.g. ~1200 cm^{-1}, Figure 6.11). This broadening of absorption features is similar to what is observed in a bi-directional reflectance setup, such as that used by *Salisbury et al.* [1992] to measure the reflectance of pure geologic materials.

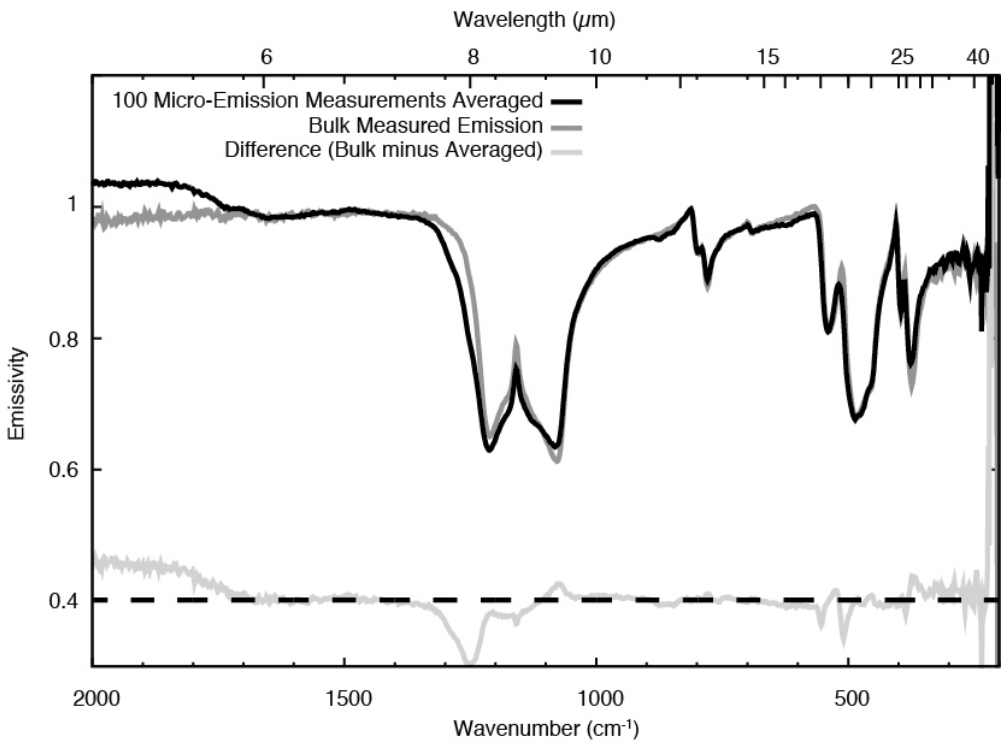

Figure 6.11. A demonstration of the absolute calibration of the micro-emission instrument is made using a well known sample of vein quartz. One hundred individual micro-emission spectra (of 500 co-adds each) over a 1x1 cm grid are averaged together and compared to a bulk measurement made with existing laboratory equipment that has been used characterize a variety of rock forming minerals [e.g. *Ruff et al.*, 1997; *Christensen et al.*, 2000b] for the analysis of martian TES data [e.g. *Bandfield et al.*, 2000a; *Christensen et al.*, 2001; *Ruff*, 2004; *Hamilton and Christensen*, 2005; *Edwards et al.*, 2008; *Koeppen and Hamilton*, 2008]. The difference between the existing laboratory and average micro-emission data are most pronounced as the widening of spectral features (e.g. 1250 cm^{-1}). However, the depth and shape of absorption features is matched extremely well.

At very high wavenumbers (>1750 cm^{-1}, Figure 6.11) a significant divergence in the micro-emission and bulk measured spectra is observed. This divergence generally occurs at wavelengths shorter than the Si-O stretching region and is introduced by an unaccounted for component in the calibration. I have determined that this emissivity excess is likely due to the anodized support structure (high emissivity) spider for the secondary mirror of the Schwarzschild being reflected onto the sample. If I include a small off axis mirror on the back of the spider to both prevent the emitted sample energy from being reflected back onto the sample, and the low emissivity of the mirror from reflecting on to the sample, this feature lessens in magnitude. Further work is underway to better characterize the effect of this calibration artifact.

6.3.2.2 Crystallographic Orientation Effects

Since the majority of emission and reflectance measurements to date are bulk measurements of many randomly oriented crystals [e.g. *Ruff et al.*, 1997] the measurement of single crystals in an unknown orientation will likely result in the observation of only one vibrational mode for the sample in question [e.g. *Lane*, 1999]. Figure 6.12a is the measurement of a quartz crystal oriented down the c-optical axis in the micro-emission spectrometer and the bulk emission spectrometer, compared to a bulk spectrum of randomly oriented quartz grains. While the micro-emission oriented quartz spectrum shows many orientation effects (including missing doublets), an additional feature at ~550 cm^{-1} is visible in the oriented micro-emission spectra and randomly oriented bulk measurement. This may be due to the high angle from which the photons are collected (emission

angle ~60˚). Furthermore the emission microscope collects energy form 360˚ simultaneously at the high emission angle, making this measurement more akin to a hemispherical or bi-directional reflectance measurement than a typical emission measurement. In an oriented quartz crystal (Figure 6.12a), I not only view the c-optical axis but also observe emitted energy from the a-optical axis simultaneously due to the high angle. This is a significant difference from many bulk emission measurements as they typically observe energy from < 15˚ emission angle, enhancing the effect of optical axis orientation. Figure 6.12b shows the variability of a quartz component from a natural sample. Again the major changes occur at ~550 cm^{-1} and do not significantly affect the identification of these samples as quartz. Furthermore while some variability, similar to what is shown in Figure 6.12b is expected for every measured spectrum, I predict that minerals with simple crystal structures (e.g. 2 optical axes) will show the strongest effect, as this instrument will not likely observe perfectly oriented crystals.

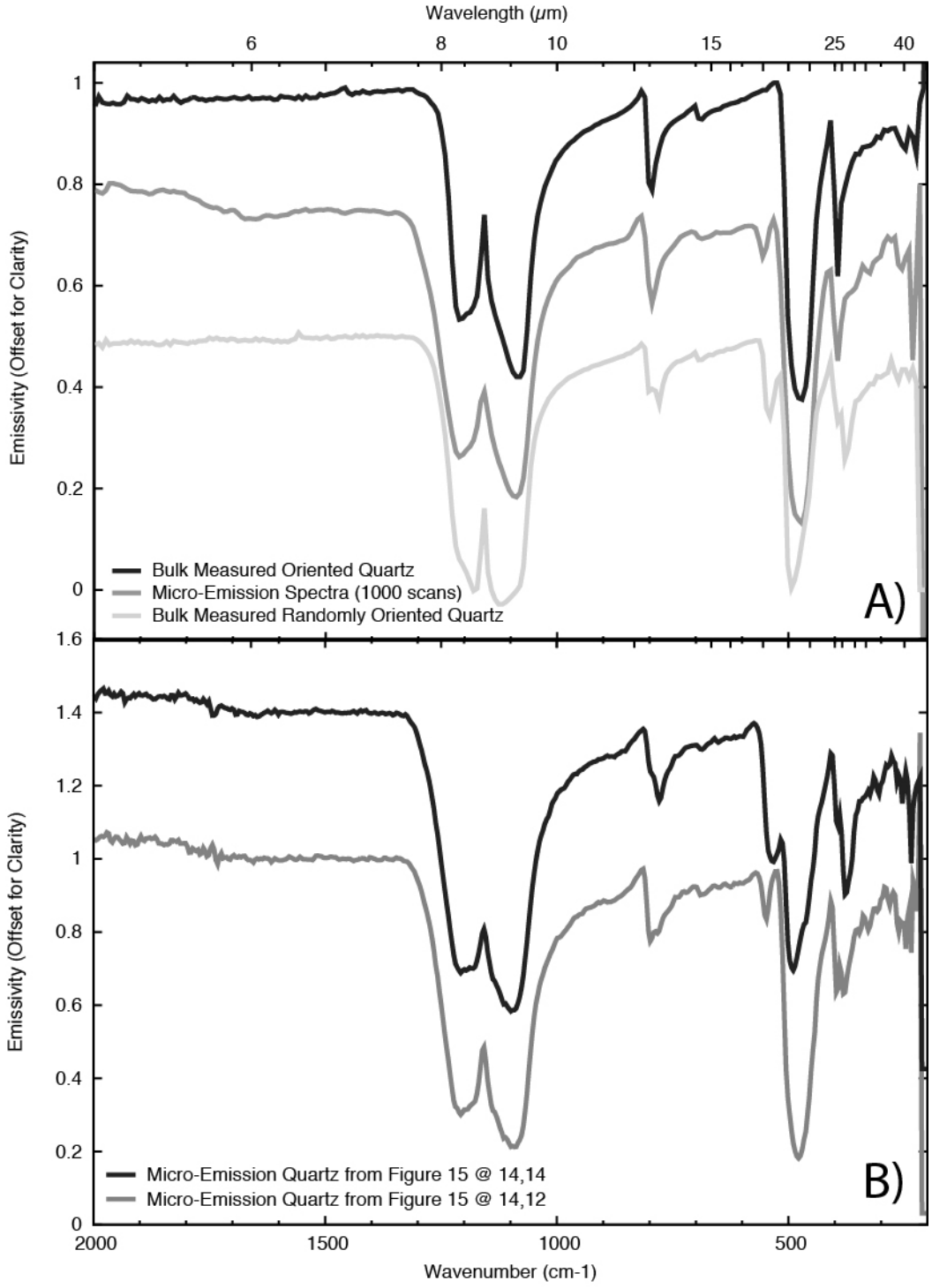

Figure 6.12. A) A bulk emission spectrum of randomly oriented quartz grains and a quartz crystal oriented down the c optical axis compared to the micro-emission spectrum of the same oriented quartz crystal. In general, the oriented quartz

Figure 6.12. continued

crystals are lacking some of the prominent quartz doublets at ~800 cm^{-1} and ~400 cm^{-1}. However, in the oriented quartz microscopic emission spectrum, the doublet at ~550cm^{-1} appears although at a different position than in the randomly oriented quartz. This doublet does not appear in the bulk measured oriented quartz and indicates that while some crystallographic orientation effects are preserved in the microscopic emission system, the effects are not as extreme as with other optical designs. **B)** Two quartz spectra extracted from the data shown in Figure 15 illustrate the typical variability of quartz orientation effects in a natural sample. By in large the effects are minimal and are most easily seen at the ~550 cm^{-1} doublet.

A perfectly oriented crystal is the worst-case scenario for the micro-emission spectrometer and any slight deviation in this perfect orientation in the crystal will result in additional optical axes being observed by the instrument and a reduction of the effect on the spectral data (Figure 6.12b). While this allows the spectrometer to produce data that have many similarities to bulk emission measurements, the typical simplification of the Fresnel equations [e.g. *Pollack et al.*, 1990; *Lane*, 1999] to ignore orientation effects, typically represented as Θ, are not possible with this setup and the full Fresnel equations accounting emission angle must be solved to derive the real and imaginary indices of refraction.

6.3.2.3 Repeatability

Overall when measuring a consistent and uniform sample, the microscopic emission spectrometer yields consistent results over long time periods, over various environmental conditions and instrument conditions. Furthermore, a spectrum from one sample, acquired from the same locality over the course of several days to weeks does not change significantly in spectral shape or contrast. The variability in a mostly uniform sample such as that shown in Figures 6.8b and 6.13, which is 100 spots acquired over 4 days, is most likely due to small-scale variability of the sample rather than changes in downwelling radiance or instrument energy. The standard deviation of these data is very small, typically 2-8% of the depth of the major absorption features, where its effect is most significant. Furthermore, the average of these 100 spots, matches the bulk emission measurement of the same sample (Figure 6.11), lending to the idea that the small-scale variability is included, but not separable, in the bulk measurement.

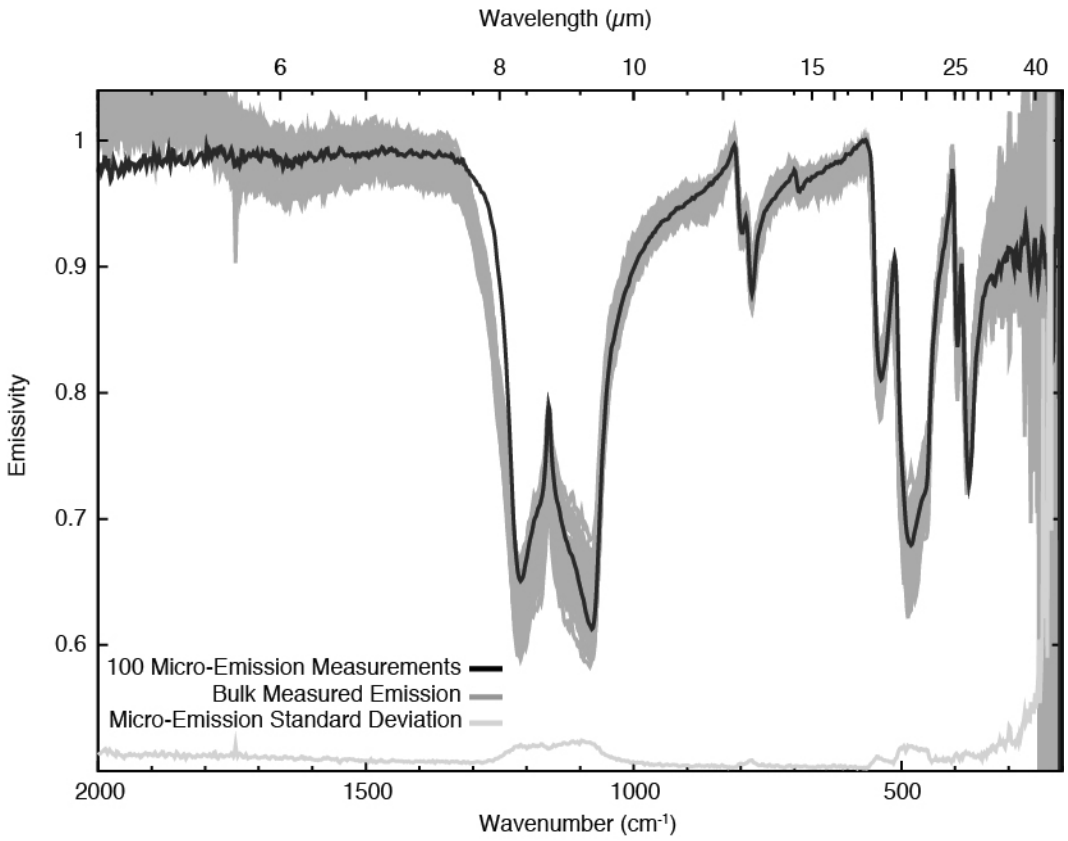

Figure 6.13. The 100 individual micro-emission spectra (500 co-adds each) are compared to the same bulk measurement in Figure 11. The variability in the data is likely due to small-scale (<1 mm) variability in the vein quartz sample. The standard deviation of the data are also shown and is typically <<5% of the lab data.

6.3.2.4 Emission versus Reflectance Measurements

When I compare the microscopic emission results to microscopic reflectance measurements (Figure 6.14), in general, I find good agreement with the spectral shape and position of major absorption features. While there are significant mismatches in the Si-O stretching (700-1200 cm^{-1}) and bending (150-600 cm^{-1}) regions, these are not directly correlated to spectral absorption features, but rather spectral slope and the width of the features. These mismatches likely stem directly from the rudimentary calibration of the reflectance mode when compared to the calibration of the emission data. However, even with the rudimentary reflectivity calibration, the quality of the spectral data is high making this technique a valuable addition to the instrument's wide range of capabilities. In the future, refinement of the reflectivity calibration will yield data that agree even better with the emission data. While I do not discuss this measurement style in detail as it is primarily a demonstration of a novel method to acquire reflectance data, this technique could prove to be especially powerful for situations where sample heating is not permissible due to power constraints (e.g. spacecraft applications) or sample constraints (e.g. loss of volatiles at low temperatures).

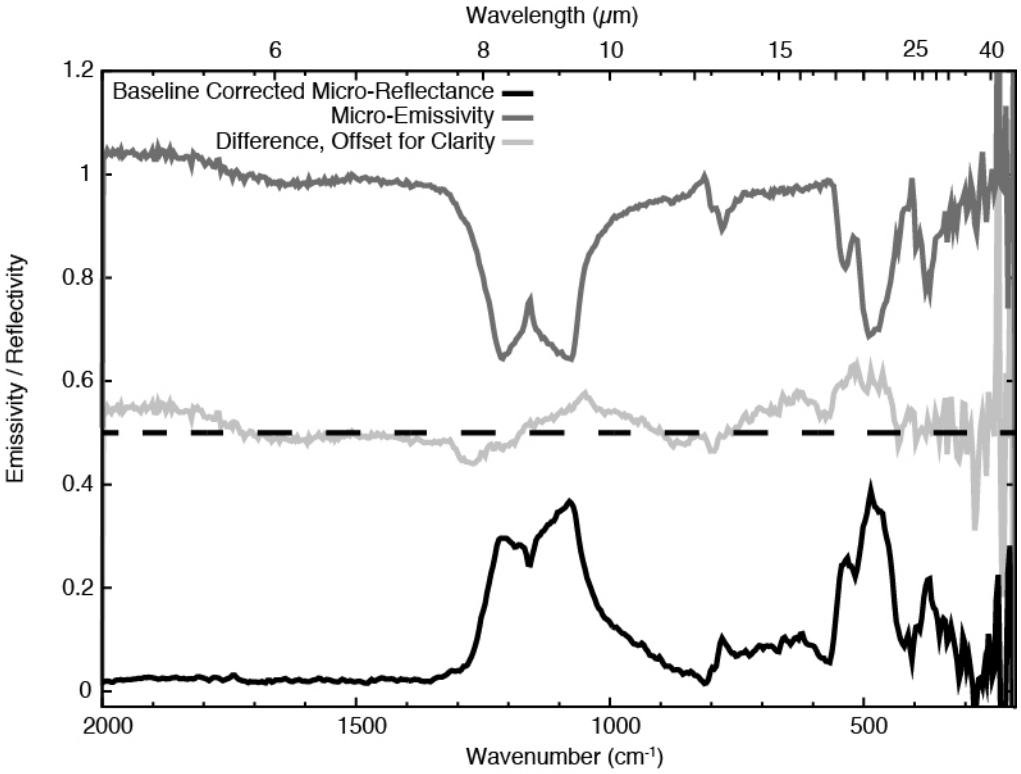

Figure 6.14. Microscopic-emission and reflectance data are shown as well as their differences. The reflectance data where calibrated using a diffuse gold reflector and have been baseline corrected to remove any spectral slope. The microscopic emission data were calibrated using the two spherical blackbody targets. In general the spectral shapes of these two different measurements match extremely well with all primary spectral features being well matched. While some difference exists with these two measurements, the reflectance data are considered preliminary and with a more robust calibration routine, the majority of the difference between these data should be eliminated based on Kirchoff's Law which states E = 1 – R where E is emissivity and R is reflectivity.

6.3.3 Rock Sample

The significant strength of this instrument is to performance petrographic analysis of the sample in question. This *in situ* quantitative non-destructive mineralogical analysis of an unknown sample is a powerful tool. This technique retains geologic context (Figure 6.15a), which is fairly unique to microscopic spectrometers. In many cases, the sample must be cored, ground into a powder, and delivered to the instrument directly, removing all geologic context. However, Figure 6.15 shows a fairly typical analysis of a quartz-monzonite, where I have identified 4 major components throughout the sample and one accessory component (Figure 6.15b). Bulk emission measurements (Figure 6.16) did not detect, due to the low areal abundance of titanite (the accessory component) in the sample (likely < 1%). While individual microscopic emission data spots are not necessarily composed of a single component, they are general simple mixtures of only a few components, which should be identical temperatures (removing aniso-thermality induced slopes) and are easy to separate.

The spectral discrimination of minerals in this sample is well demonstrated (Figure 6.15) and the identification of these components is straightforward. A spectral index map, decorrelation stretch [e.g. *Gillespie et al.*, 1986], deconvolution [e.g *Feely and Christensen*, 1999; *Ramsey et al.*, 1999; *Rogers and Aharonson*, 2008] of individual points, or spectral classification are powerful tools for mapping the variability and locations of individual components in the sample. While there is some variability in the individual measurements, by

in large, spectral features and shape along with the spectral contrast matches the bulk emission measurement extremely well (Figure 6.16) for a complicated natural geologic material. This further illustrates that the individual spectral components (e.g. 400 micro-emission measurements averaged together) can adequately represent the bulk emission measurement. The individual spectral components in this case include orientation effects, roughness effects and the mineralogical variability.

However, I find the maximum variability of the individual components in this sample is generally attributed to crystallographic orientation effects (e.g. Figure 6.12b) and mineralogical variability and not instrumentation effects, or sample roughness. This allows for the quantitative identification of each component and their respective contributions to the bulk-measured spectrum to be well characterized. If I compare deconvolution results [e.g. *Ramsey et al.*, 1999] of the bulk measured spectrum, using a simple endmember spectral library (Table 6.3), to the spectral deconvolution point counting method of the microscopic emission spectrometer described below, I find excellent agreement between the two datasets (Figure 6.17).

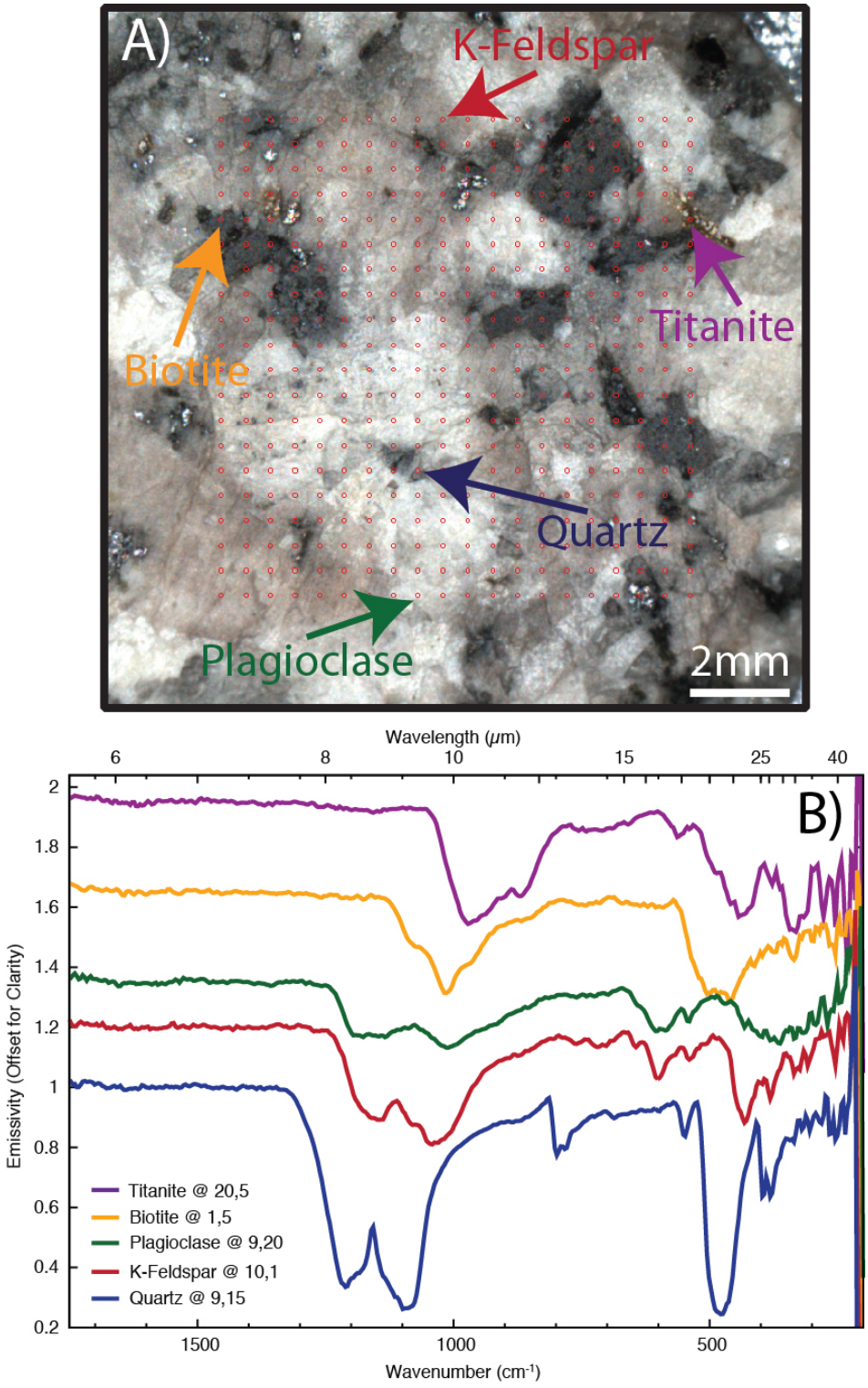

Figure 6.15. The locations **(A)** of microscopic-emission spectra **(B)** for a quartz-monzonite thick section. The red open circles are locations of individual

Figure 6.15. continued

measurements. In this sample, four major components are identified, plagioclase feldspar (white tones), potassium feldspar (pink tones), biotite (dark tones), and quartz (translucent). Quartz is not easily discernable in the visible image as it is somewhat translucent and often appears as the color of the material surrounding or below it. A minor phase, titanite (orange-gold tones), is also identified and constitutes only ~3 pixels of the 400 measured. Minor variations in individual spectra may be due to slight differences in optical axis orientation.

In order to perform spectral point counting, I use the same spectral library (Table 6.3) and unmix every individual spectrum. After the unmixing of the spectral data, I then sum all the concentrations normalized for blackbody contributions together and normalize back to 100%, which results in the areal abundance of that individual spectral component. In this case, I were not interested in the variability within individual mineral groups so all results are grouped according to Table 6.3. To test the overall sensitivity of this method to components with low abundances, I exclude components with low abundances from individual spot unmixing results (Figure 6.17) and then normalize the sum of all spots to 100%. In general I find that this exclusion, up to abundances <50% does not change the derived spectral deconvolution point counting abundances more than ~5-6% for any given mineral group. While the absolute mineral abundances of this sample are not known, the individual determination of mineral abundances to within ~5% through the disparate methods of spectral point counting and bulk spectral deconvolution, lends to the precision of emission spectroscopy for the quantitative determination of the mineralogy of natural geologic materials.

Table 6.3. Spectral Library used in quantitative mineral abundance determination for the quartz-monzonite sample in Figures 6.14-6.16.

[a]*Reference Number/Source*	*Spectrum Identifier*	*Assigned Mineral Group*
ASU	Quartz BUR-4120	Quartz
ASU	Microcline BUR-3460	K-Feldspar
ASU	Orthoclase WAR-RGSAN01	K-Feldspar
ASU	Albite WAR-0235	Plagioclase
ASU	Oligoclase BUR-060D	Plagioclase
ASU	Andesine WAR-0024	Plagioclase
ASU	Labradorite BUR-3080A	Plagioclase
ASU	Anorthite BUR-340	Plagioclase
ASU	Biotite BUR-840	Mica
ASU	Chlorite WAR-1924	Mica
ASU	Muscovite WAR-5474	Mica
ASU	Phlogopite HS-23.3B	Mica

[a]Spectral library after *Feely and Christensen* [*1999*] where, individual mineral spectra are from the ASU spectral library available online at http://speclib.asu.edu [*Christensen et al.*, 2000b].

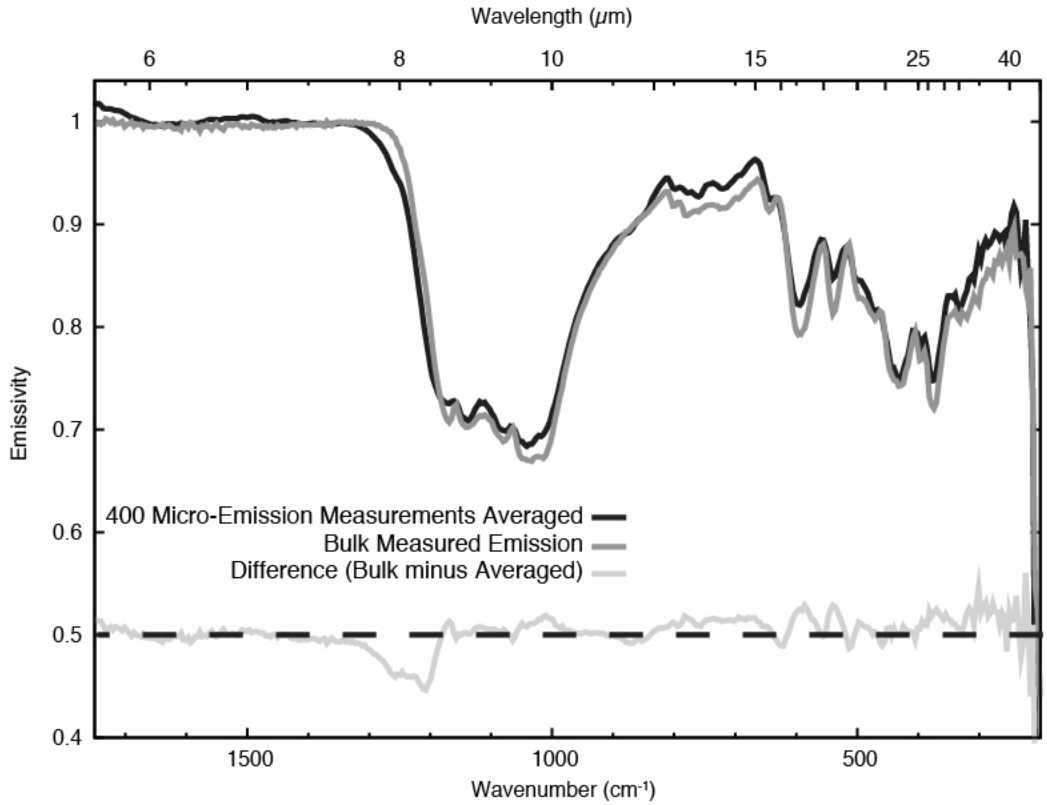

Figure 6.16. Four hundred individual micro-emission spectra over a 1x1 cm grid are averaged together and compared to a bulk measurement made with existing laboratory equipment. The difference between the existing laboratory and average micro-emission data are most pronounced as the widening of spectral features (e.g. 1225 cm^{-1}). However, the depth and shape of absorption features is matched extremely well.

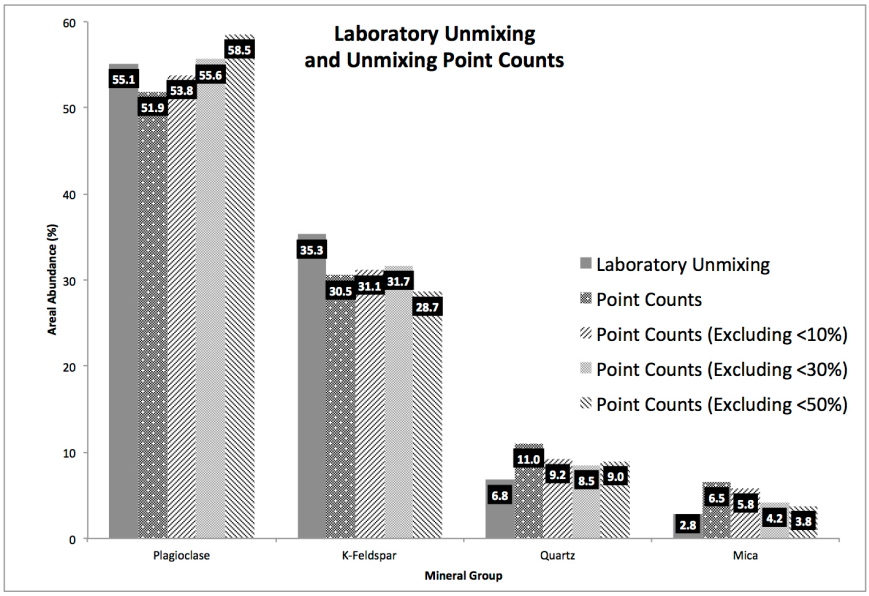

Figure 6.17. A histogram of the bulk emission laboratory deconvolution mineral abundances and derived microscopic emission point count abundance. I present several methods for deriving microscopic emission point counts, where I simply deconvolve each individual spot with a simple library (Table 3) covering the variability in the sample, and then sum the abundances and normalize back to 100%. In this case, I do not exclude minor components, as I am confident that individual pixels are generally well modeled as they are commonly a combination of one to three endmembers. In subsequent methods I exclude deconvolution results that have abundances less than 10, 30, and 50%. In each of these cases, the results do not change significantly varying by <5% derived mineral abundances. Furthermore the comparison to laboratory unmixing results is quite good and provides a high level of confidence in bulk spectral deconvolution and the point counting methods used to determine sample mineralogy.

6.4 Conclusions

I have presented a brief summary of various *in* situ instruments that have, to date, been used on planetary surfaces and detailed the development of a laboratory microscopic emission and reflectance spectrometer. While in its present form, the laboratory instrument is large and somewhat complicated, primarily due to commercial instrument constraints, a flight prototype has been constructed where an identical microscope objective has been mounted to a flight spare Mini-TES instrument, illustrating the straightforward instrument design and long heritage of thermal emission spectrometers. Further miniaturization of this instrument is straightforward with modern electronics and the development of this instrument as an arm-mounted device is the end goal.

I find this style of instrumentation has several obvious advantages over other *in situ* instrumentation proposed for planetary surface investigations including, APXS, Mössbauer, microscopic imagers, X-rad diffraction and X-ray florescence spectrometers, and Raman spectrometers [e.g. *Blacksberg et al.*, 2010]. These advantages include a simple and tested instrument design, a long heritage of instruments sent to planetary surfaces and orbit, the ability to make direct comparisons to existing and past instruments, as well as the ability to quantitatively determine the bulk sample mineralogy while retaining the geologic and petrologic context. Very few, if any, instruments mentioned above are capable doing *in situ* petrology. I find the capability of this instrument to do *in situ* petrology to be a major strength of this instrument. This style of instrument could also be used for the derivation of atmospheric opacities [e.g. *Smith et al.*,

2004] to help maintain the long record of atmospheric conditions obtained from orbiting and landed spacecraft. Furthermore, with a different microscope objective (an off-axis parabola instead of the Schwarzschild objective) that results in only a marginally larger spot size (e.g. ~200-300 μm), it is possible to defocus the measurement spot to gain outcrop scale measurements comparable to existing Mini-TES spatial sampling.

CHAPTER 7

CONCLUSIONS

The work presented in this manuscript contributes to the state of knowledge of the early geologic history of Mars. In the course of examining early Mars processes, I present algorithm development for the advanced processing of returned spacecraft data, novel techniques for the analysis of compositional data, the analysis of a variety of ancient rocky surfaces on Mars, and I include a discussion of the initial work for a next generation instrument designed for *in situ* mineralogical and petrological investigation of planetary surfaces.

I have focused my attention on data processing, instrumentation and early planetary processes for several reasons:

- By developing new and novel techniques for the processing and mosaicking of compositional and imaging datasets, more specifically THEMIS data, I have enhanced the ability to quantitatively assess the geology and geologic history of large areas of the martian surface.
- Early planetary evolution and processes are poorly understood. Using a variety of image and data processing techniques, such as those presented in Chapter 1, I have examined a variety of *in situ,* ancient rocky surfaces with the goal of constraining several early planetary evolutionary processes on Mars.
- The development of new instrumentation for *in situ* investigations of planetary surfaces has the ability to greatly enhance our ability to

examine planetary surfaces from landed spacecraft. Furthermore, the development of instruments that preserve petrologic context using similar remote sensing methods to existing orbital and landed instruments can help further the understanding of existing datasets and allow for the application of lessons learned at the few landed sites to the remainder of the planet.

Chapter 2 represents a significant improvement in the algorithms and data processing techniques used to mosaic tens of thousands of THEMIS infrared images, as well as other imaging datasets from other planetary bodies, including the Moon and Earth.

- I present algorithms for several common instrument effects, such as the temperature variation across the calibration flag correction, random noise removal, and running stretches designed specifically for THEMIS, though these algorithms and data processing techniques are not limited to THEMIS data and may be applied to past, current, and future data. The use of these techniques must be carefully validated for each dataset to quantify the effects that may be introduced to the data.
- The techniques for the creation of small-scale and large-scale mosaics presented in Chapter 2 provide the ability to view the surface of Mars and other planetary bodies, as well as geologic problems, through many different perspectives. For example, one can obtain high-resolution visible imagery of an area, which may help illuminate

compositional and thermophysical data, providing a more complete view of geologic processes on Mars.

- The mosaicking ability and techniques presented in Chapter 2 provides an unprecedented amount of flexibility to the end user to produce both quantitative and qualitative large-scale seamless products of most map-projected datasets. These products can be constructed relatively easily and scientific investigations are not limited to the extent of a single image; rather, they can be combinations of tens to several thousands of images as is the case with the THEMIS global mosaics.
- I also address the data selection, mosaicking procedure, quality control measures, and the registration considerations for the THEMIS daytime and nighttime relative temperature global mosaics. The THEMIS mosaics constructed of Mars are the highest resolution (100m/pixel) global scale datasets available to date.

The algorithms and data processing and mosaicking techniques described in Chapter 2 were essential to the next several chapters as these techniques enabled the quantitative and qualitative assessment of large regions of the surface of Mars for compositional and thermophysical variability. In **Chapter 3,** I present the findings from a regional study that aimed to characterize early compositionally distinct volcanism on Mars.

- An *in situ*, olivine-enriched stratigraphic layer, which extends laterally over a distance of >1,100 km and has a minimum volume of ~9.9×10^4 km^3 was identified and characterized by its compositional and

thermophysical properties using TES and THEMIS data. Initially I identified locations outside of the primary study region that may also be related to this *in situ* layer, making these size estimates a minimum.

- Outcrops of these materials commonly have elevated thermal inertia values (often >~600 J K^{-1} m^{-2} $s^{-1/2}$, with extremes of >1200 J K^{-1} m^{-2} $s^{-1/2}$), which indicates that this unit is not a mobile sediment and is an in-place rocky unit.
- The fine-scale morphologic observations agree well with thermophysical data that suggest these surfaces are relatively unmantled, rough and pitted surface associated with the olivine-enriched material, with some aeolian bedforms infilling the hollows and pits of the surface observed by HiRISE and MOC imagery.
- MOLA elevation data was also used to constrain the vertical dimension of this layer, allowing for the continuity, extent, dip and orientation to be constrained. I found this layer to be continuous over >1,100 km and essentially flat-lying. This unit persists underneath topographically high areas appearing only in expected, elevation-dependent locations, and is one of the largest continuous compositional units found on Mars.
- If I considered only this region, four possibilities for the geologic origin of the olivine-enriched unit include: 1) volcanism associated with tectonic rifting of the Valles Marineris system, 2) a volcaniclastic flow deposit, 3) an intrusive mafic sill, or 4) a discrete episode in

martian history during which flood lavas were erupted onto the surface.

Based on the evidence available at the time of the writing of Chapter 3, I concluded the most likely explanation for the geologic origin of this layer is an eruptive event consisting of compositionally uniform olivine-enriched flood lavas originating from a primitive mantle source region. However, when the Ganges and Eos Chasmata unit is compared to other olivine-enriched units on Mars, namely those identified in Ares Vallis [*Rogers et al.*, 2005] and Isidis Planitia [*Mustard et al.*, 2007; *Tornabene et al.*, 2008] among other locations such as Chryse Planitia, striking compositional (>15% olivine abundance and ~Fo_{68}), morphologic (commonly rough, pitted textures) and thermophysical (typically >500 J K^{-1} m^{-2} $s^{-1/2}$) similarities are observed. Additionally many of these units are hypothesized to have been emplaced early in martian history. I suggest these similarities in age and characteristics are indicative of a discrete period of time early in Mars history, when compositionally uniform and extensive olivine-enriched basalts were emplaced onto the surface.

In **Chapter 4**, I further investigate this compositional layer and extended the study region in all directions. I found that this layer was significantly larger and proposed that any model for the formation of this large-scale, olivine-enriched layer must satisfactorily explain its: 1) unique composition (>10%-25% ~Fo_{68}), 2) ancient age (>6 km of heavily cratered overlying material), 3) large-scale ($1.5x10^6$ km^3 to >$5x10^6$ km^3) and observed continuity (>4,000 km laterally), and 4) rocky nature (elevated TI and fine-scale morphology).

The models I propose include:

- An early magma ocean with significant density stratification capable of producing several crustal compositions consistent with what is observed from orbit, including olivine and pyroxene rich materials.
- A period of intense and widespread volcanism or near-surface intrusions that may have occurred shortly after crustal formation, possibly as a result of enhanced surface heat flux associated with core formation.
- An impact that formed the Borealis basin that excavated the crust and upper mantle and distribute these olivine-enriched materials over the planet's surface into a regional or global layer.

While I favor the Borealis-impact model, the presence of an extensive layer of unique composition indicates a significant planet-wide event that likely shaped the martian landscape. This process could have depleted the mantle of volatiles affecting the martian atmosphere and later hydrologic cycle. The olivine-rich materials identified in this study could provide important constraints on the differentiation of Mars, mantle, and core chemistry, the source material of some SNC meteorites, and the timing of the Borealis basin forming event.

In **Chapter 5,** I examine another widespread and ancient process on Mars that has previously gone undocumented. This chapter focuses on the analysis of ubiquitous and widespread flat-floored craters on Mars. I propose that large impacts (causing >10 km diameter craters) on early Mars generated widespread

magmatism as a result of impact related decompression melting of the martian mantle. I find that:

- Highly eroded craters with flat-floors composed of material with elevated thermal inertia values (e.g. > 500 to 2000 J m^{-2} K^{-1} $s^{-1/2}$) are prevalent in the ancient low albedo cratered southern highlands. Some of the rockiest materials on Mars occur in the bottom of these craters and likely represent a unique widespread process that occurred early in martian history.
- The fine-scale morphologies associated with the high thermal inertia crater floors commonly show a rough and pitted texture, with boulders and in-place fractured rock exposed on the surface. Mobile aeolian materials commonly infill local depressions in the exposed rocky surfaces, reducing the observed thermal inertia.
- The rocky crater floor material is significantly more mafic (globally constrained using the TES 507 cm^{-1} spectral index [*Rogers and Ferga*son, 2011]) and enriched in olivine/pyroxene versus plagioclase/high Si-phases when compared to the surrounding typical inter-crater plains.
- Crater counting model ages of the crater floor material for >110 craters have ages that range from 3 to 4 Ga (early Hesperian to late Noachian, approximately consistent with the LHB). Crater floors also have a resurfacing age of less than ~1 Ga indicating that they likely formed early in martian history and were subsequently altered/resurfaced in

the more recent past.

Based on the surface properties described here, I propose three possible mechanisms for the formation of flat-floored, high thermal inertia crater floors across the surface of Mars including: 1) the lithification/induration of sediments, 2) the ponding of crustal melt material related to the heat generated during the impact process, and 3) infilling by volcanic materials. Of these three possibilities, I find only volcanic infilling can produce features with the observed morphological, thermophysical, and compositional characteristics, along with the widespread occurrence and ancient ages.

- As a result of the impact event, crustal material below the crater is heavily fractured providing a pathway for magma to reach the surface.
- The magma is directly sourced from the decompression melting of the martian mantle due to the removal of several kilometers of overlying crustal material by the impactor. As the ancient martian crust was likely thin [e.*g.* *Zu*ber, 2001] and the geothermal gradients were significantly higher than present day, the decompression melting of the mantle would be more likely to occur than under present day conditions.
- This model is consistent with the ancient ages (~3-4 Ga) of the crater floors and indicates their formation occurred early in martian history and not after the crustal thickening of the southern highlands and reduction of the geothermal gradient.
- The fractures in the upper crust created by these large impact events

may provide pathways for the lavas that form the Hesperian ridged plains or rocky mafic exposures visible throughout the southern highlands [e.g. *Edwards et al.*, 2009; *Rogers et al.*, 2009; *Rogers and Fergason*, 2011].

- Many of the lava flows on the martian inter-crater plains have no easily observable volcanic edifices and could be fed directly from dikes that utilized the highly fractured crust as pathways for magma to breach the surface. Furthermore, groundwater and hydrothermal systems could also use these fractures as pathways to circulate through and alter the martian crust.

The view of early martian history as described through this work is one of an active planet with a variety of somewhat unique processes occurring in the first several hundred million years. Large-scale impact processes were common throughout the early solar system and Mars preserves evidence of such events in its geologic record. Furthermore, the generation of large volumes of magma through mantle decompression melting by the removal of crustal material during large impacts is a process that I propose did not just occur on Mars. This process was likely widespread throughout the solar system, occurring on planets such as Mercury, Venus, Earth and possibly even Earth's Moon. The materials erupted by these events likely represent significantly more primitive materials as they likely had little time to equilibrate or incorporate other martian crustal materials. The ability to use Mars as a window into the ancient history of our solar system by advanced data processing and state of the art space borne instrumentation is a

venue of research that should be further explored. The next generation of instruments should build on this strong legacy of exploration and remain complementary to data returned by current missions.

In **Chapter 6**, I present the design, construction, performance and calibration of a microscopic (~85 μm sample size) thermal infrared emission and reflectance laboratory instrument. This instrument represents one possibility for a next generation landed instrument designed specifically to characterize the mineralogy of the surface by *in situ* measurements. In its present form, the laboratory instrument is large and somewhat complicated, though miniaturization of this instrument is straightforward with modern electronics and the development of this instrument as an arm-mounted device is the end goal.

This style of instrumentation has several advantages over other *in situ* instrumentation proposed for planetary surface investigations including, APXS, Mössbauer, microscopic imagers, X-rad diffraction and X-ray florescence spectrometers, and Raman spectrometers [e.g. *Blacksberg et al.*, 2010].

These advantages include:

- A simple and tested instrument design, a long heritage of instruments sent to planetary surfaces and orbit, the ability to make direct comparisons to existing and past instruments, as well as the ability to quantitatively determine the bulk sample mineralogy while retaining the geologic and petrologic context.
- Very few, if any, instruments mentioned above are capable of doing *in situ* petrology, which enables a more through examination

of the geologic history of a sample, as the mineral context is preserved.

- This style of instrument could also be used for the derivation of atmospheric opacities [e.g. *Smith et al.*, 2004] to help maintain the long record of atmospheric conditions obtained from orbiting and landed spacecraft.
- Furthermore, with a different microscope objective (an off-axis parabola instead of the Schwarzschild objective) that results in only a marginally larger spot size (e.g. ~200-300μm), it is possible to defocus the measurement spot to gain outcrop scale measurements comparable to existing Mini-TES spatial sampling.

Throughout this work, an effort was made to cover a wide range of topics and develop a diverse set of skills with the goals of obtaining a better understanding of the data returned from the martian surface, as well as how to use these data to characterize the early history of Mars. The approaches used included the development of a proto-flight *in situ* mineralogy instrument, the detailed analysis of data from nearly all spacecraft orbiting Mars, including THEMIS, TES, MOC, CRISM, HiRISE, CTX, MOLA, GRS and HRSC, and the development of advanced image and processing algorithms for correcting instrument artifacts and mosaicking tens of thousands of images together.

Future work will continue to build on this skill set, with the goal of using the laboratory instrument developed as a part of this work, earth analog materials,

and data analysis of current and future spacecraft data to better constrain the ancient history of Mars.

REFERENCES

Abramov, O., and D. A. Kring (2005), Impact-induced hydrothermal activity on early Mars, *J. Geophys. Res.*, *110*, E12S09, doi: 10.1029/2005je002453.

Anderson, J. A., S. C. Sides, D. L. Soltesz, T. L. Sucharski, and K. L. Becker (2004), Modernization of the integrated software for imagers and spectrometers.

Andrews-Hanna, J. C., M. T. Zuber, and W. B. Banerdt (2008), The Borealis basin and the origin of the martian crustal dichotomy, *Nature*, *453*(7199), 1212-U1227, doi:10.1038/nature07011.

Arvidson, R. E. (1974), Windblown streaks, splotches, and assorted craters on Mars: Statistical analysis of Mariner 9 photographs, *Icarus*, *21*(1), 12-27, doi:10.1016/0019-1035(74)90086-4.

Baldridge, A. M. (2007), Thermal infrared spectral studies of sulfates and chlorides: Applications to salts on the Martian surface, Ph.D. Dissertation, 204 pp, Arizona State University, Tempe.

Bandfield, J. L. (2002), Global mineral distributions on Mars, *J. Geophys. Res.*, *107*, doi: 10.1029/2001JE001510.

Bandfield, J. L. (2007), High-resolution subsurface water-ice distributions on Mars, *Nature*, *447*(7140), 64-67, doi:10.1038/nature05781.

Bandfield, J. L. (2008), High-silica deposits of an aqueous origin in western Hellas Basin, Mars, *Geophys Res Lett*, *35*(12), doi:10.1029/2008GL033807.

Bandfield, J. L., and W. C. Feldman (2008), Martian high latitude permafrost depth and surface cover thermal inertia distributions, *J. Geophys. Res*, *113*, E08001, doi:10.1029/2007JE003007.

Bandfield, J. L., and A. D. Rogers (2008), Olivine dissolution by acidic fluids in Argyre Planitia, Mars: Evidence for a widespread process?, *Geology*, *36*(7), 579-582, doi: 10.1130/G24724A.1

Bandfield, J. L., V. E. Hamilton, and P. R. Christensen (2000a), A global view of Martian volcanic compositions, *Science*, *287*(5458), 1626-1630, doi: 10.1126/science.287.5458.1626.

Bandfield, J. L., M. D. Smith, and P. R. Christensen (2000b), Spectral dataset factor analysis and endmember recovery: Application to analysis of

martian atmospheric particulates, *J. Geophys. Res.*, *105*, 9573-9588, doi:10.1029/1999JE001094.

Bandfield, J. L., A. D. Rogers, and C. S. Edwards (2011), The Role of Aqueous Alteration in the Formation of Martian Soils, *Icarus*, *211*(1), 157-171, doi: 10.1016/j.icarus.2010.08.028.

Bandfield, J. L., V. E. Hamilton, P.R.Christensen, and H. Y. McSween, Jr. (2004a), Identification of quartzofeldspathic materials on Mars, *J. Geophys. Res.*, *109*, doi :10.1029/2004JE002290.

Bandfield, J. L., A. D. Rogers, M. D. Smith, and P.R.Christensen (2004b), Atmospheric correction and surface spectral unit mapping using Thermal Emission Imaging System data, *J. Geophys. Res.*, *109*, E10008, doi:10.1029/2004JE002289.

Bell, J. F., J. Joseph, J. N. Sohl-Dickstein, H. M. Arneson, M. J. Johnson, M. T. Lemmon, and D. Savransky (2006), In-flight calibration and performance of the Mars Exploration Rover Panoramic Camera (Pancam) instruments, *Journal of Geophysical Research*, *111*, E02S03, doi:10.1029/2005JE002444

Bennett, J. M., and E. Ashley (1965), Infrared reflectance and emittance of silver and gold evaporated in ultrahigh vacuum, *Applied optics*, *4*(2), 221-224, doi: 10.1364/AO.4.000221.

Bertka, C. M., and J. R. Holloway (1994), Anhydrous partial melting of an iron-rich mantle I: subsolidus phase assemblages and partial melting phase relations at 10 to 30 kbar, *Contributions to Mineralogy and Petrology*, *115*(3), 313-322, doi: 10.1007/BF00310770.

Bibring, J.-P., Y. Langevin, A. Gendrin, B. Gondet, F. Poulet, M. Berthé, A. Soufflot, R. Arvidson, N. Mangold, J. Mustard, P. Drossart, and Omega-Team (2005), Mars Surface Diversity as Revealed by the OMEGA/Mars Express Observations, *Science*, *307*, 1576-1581, doi:10.1126/science.1108806.

Bibring, J.-P., Y. Langevin, J. F. Mustard, F. Poulet, R. Arvidson, A. Gendrin, B. Gondet, N. Mangold, P. Pinet, F. Forget, O. t. the, M. Berthe, J.-P. Bibring, A. Gendrin, C. Gomez, B. Gondet, D. Jouglet, F. Poulet, A. Soufflot, M. Vincendon, M. Combes, P. Drossart, T. Encrenaz, T. Fouchet, R. Merchiorri, G. Belluci, F. Altieri, V. Formisano, F. Capaccioni, P. Cerroni, A. Coradini, S. Fonti, O. Korablev, V. Kottsov, N. Ignatiev, V. Moroz, D. Titov, L. Zasova, D. Loiseau, N. Mangold, P. Pinet, S. Doute, B. Schmitt, C. Sotin, E. Hauber, H. Hoffmann, R.

Jaumann, U. Keller, R. Arvidson, J. F. Mustard, T. Duxbury, F. Forget, and G. Neukum (2006), Global Mineralogical and Aqueous Mars History Derived from OMEGA/Mars Express Data, *Science*, *312*(5772), 400-404, 10.1126/science.1122659.

Blacksberg, J., G. R. Rossman, and A. Gleckler (2010), Time-resolved Raman spectroscopy for in situ planetary mineralogy, *Applied optics*, *49*(26), 4951-4962, doi: 10.1364/AO.49.004951.

Bourke, M. C., K. S. Edgett, and B. A. Cantor (2008), Recent aeolian dune change on Mars, *Geomorphology*, *94*(1-2), 247-255, doi:10.1016/j.geomorph.2007.05.012

Boyce, J. M., and H. Garbeil (2007), Geometric relationships of pristine Martian complex impact craters, and their implications to Mars geologic history, *Geophys. Res. Lett.*, *34*, L16201, doi:10.1029/2007GL029731.

Boynton, W. V., W. C. Feldman, W. Squyres, T. H. Prettyman, J. Brückner, L. G. Evans, R. C. Reedy, R. Starr, J. R. Arnold, D. M. Drake, P. A. J. Englert, A. E. Metzger, I. Mitrofanov, J. I. Trombka, C. d'Uston, H. Wänke, O. Gasnault, D. K. Hamara, D. M. Janes, R. L. Marcialis, S. Maurice, I. Mikheeva, G. J. Taylor, R. Tokar, and C. Shinohara (2002), Distribution of hydrogen in the near surface of Mars: Evidence for subsurface ice deposits, *Science*, *297*(81), 81-85, DOI: 10.1126/science.1073722.

Boynton, W. V., G. J. Taylor, L. G. Evans, R. C. Reedy, R. Starr, D. M. Janes, K. E. Kerry, D. M. Drake, K. J. Kim, R. M. S. Williams, M. K. Crombie, J. M. Dohm, V. Baker, A. E. Metzger, S. Karunatillake, J. M. Keller, H. E. Newsom, J. R. Arnold, J. Bruckner, P. A. J. Englert, O. Gasnault, A. L. Sprague, I. Mitrofanov, S. W. Squyres, J. I. Trombka, L. d'Uston, H. Wanke, and D. K. Hamara (2007), Concentration of H, Si, Cl, K, Fe, and Th in the low- and mid-latitude regions of Mars, *J. Geophys. Res.*, *112*(E12S99, doi:10.1029/2007JE002887.), doi: 10.1029/2007je002887.

Byrne, S., and A. P. Ingersoll (2003), Martian climatic events on timescales of centuries: Evidence from feature morphology in the residual south polar ice cap, *Geophys Res Lett*, *30*(13), 1696, doi:1610.1029/2003GL017597.

Cabrol, N. A., and E. A. Grin (1999), Distribution, Classification, and Ages of Martian Impact Crater Lakes, *Icarus*, *142*(1), 160-172.

Campbell, I. H., G. K. Czamanske, V. A. Fedorenko, R. I. Hill, and V. Stepanov (1992), Synchronism of the Siberian Traps and the Permian-Triassic Boundary, *Science*, *258*(5089), 1760-1763, doi: 10.1126/science.258.5089.1760.

Carr, M. H., and G. D. Clow (1981), Martian channels and valleys: Their characteristics, distribution, and age, *Icarus*, *48*, 91-117, doi: 10.1016/0019-1035(81)90156-1.

Chase, S., Jr., E. Miner, G. Münch, and G. Neugebauer (1970), Infrared radiometry experiment for Mariner Mars 1971, *Icarus*, *12*, 46-47.

Christensen, P. R. (1982), Martian dust mantling and surface composition: Interpretation of thermophysical properties, *J. Geophys. Res.*, *87*(B12), 9985-9998, doi: 10.1029/JB087iB12p09985.

Christensen, P. R. (1983), Eolian intracrater deposits on Mars: Physical properties and global distribution, *Icarus*, *56*(3), 496-518, doi:10.1016/0019-1035(83)90169-0.

Christensen, P. R. (1988), Global albedo variations on Mars: Implications for active aeolian transport, deposition, and erosion, *J. Geophys. Res.*, *93*(B7), 7611-7624, doi:10.1029/JB093iB07p07611.

Christensen, P. R. (1999), Calibration Report for the Thermal Emission Spectrometer (TES) for the Mars Global Surveyor Mission*Rep.*, 228 pp, Mars Global Surveyor Project, NASA Jet Propulsion Laboratory, Pasadena, CA.

Christensen, P. R. (2002), Calibration Report for the Thermal Emission Imaging System (THEMIS) for the 2001 Mars Odyssey Mission*Rep.*, 2001 Mars Odyssey Project, NASA Jet Propulsion Laboratory, Pasadena, CA.

Christensen, P. R., and S. T. Harrison (1993), Thermal infrared emission spectroscopy of natural surfaces: Application to desert varnish coatings on rocks, *J. Geophys. Res.*, *98*(B11), 19,819-819,834, doi: 10.1029/93JB00135.

Christensen, P. R., J. L. Bandfield, M. D. Smith, V. E. Hamilton, and R. N. Clark (2000a), Identification of a basaltic component on the martian surface from Thermal Emission Spectrometer data, *J. Geophys. Res.*, *105*(E4), 9609-9622, doi: 10.1029/1999JE001127.

Christensen, P. R., N. Gorelick, S. Anwar, S. Dickenshied, C. S. Edwards, E. Engle, and T. S. Team (2007), New Insights About Mars From the Creation and Analysis of Mars Global Datasets, *Eos Trans. AGU*, *88*(52), Fall Meet. Suppl., Abstract P11E-01.

Christensen, P. R., J. L. Bandfield, V. E. Hamilton, D. A. Howard, M. D. Lane, J. L. Piatek, S. W. Ruff, and W. L. Stefanov (2000b), A thermal emission

spectral library of rock forming minerals, *J. Geophys. Res.*, *105*, 9735-9738, doi:10.1029/1998JE000624

Christensen, P. R., B. M. Jakosky, H. H. Kieffer, M. C. Malin, H. Y. McSween, Jr., K. Nealson, G. L. Mehall, S. H. Silverman, S. Ferry, M. Caplinger, and M. Ravine (2004a), The Thermal Emission Imaging System (THEMIS) for the Mars 2001 Odyssey Mission, *Space Science Reviews*, *110*(1), 85-130, doi: 10.1023/B:SPAC.0000021008.16305.94.

Christensen, P. R., D. L. Anderson, S. C. Chase, R. T. Clancy, R. N. Clark, B. J. Conrath, H. H. Kieffer, R. O. Kuzmin, M. C. Malin, J. C. Pearl, T. L. Roush, and M. D. Smith (1998), Results from the Mars Global Surveyor Thermal Emission Spectrometer investigation, *Science*, *279*(5357), 1692-1698, doi: 10.1126/science.279.5357.1692

Christensen, P. R., H. Y. McSween, Jr., J. L. Bandfield, S. W. Ruff, A. D. Rogers, V. E. Hamilton, N. Gorelick, M. B. Wyatt, B. M. Jakosky, H. H. Kieffer, M. C. Malin, and J. E. Moersch (2005), Evidence for igneous diversity and magmatic evolution on Mars from infrared spectral observations, *Nature*, *436*, 504-509, doi:10.1038/nature03639.

Christensen, P. R., G. L. Mehall, S. H. Silverman, S. Anwar, G. Cannon, N. Gorelick, R. Keehn, T. Tourville, D. Bates, S. Ferry, T. Fortuna, J. Jeffryes, W. O'Donnell, R. Peralta, T. Wolverton, D. Blaney, R. Denise, J. Rademacher, R. V. Morris, and S. Squyres (2003a), The Miniature Thermal Emission Spectrometer for the Mars Exploration Rovers, *J. Geophys. Res.*, *108*(E12), 8064, doi:10.1029/2003JE002117.

Christensen, P. R., J. L. Bandfield, J. F. Bell, III, N. Gorelick, V. E. Hamilton, A. Ivanov, B.M. Jakosky, H. H. Kieffer, M. D. Lane, M. C. Malin, G. L. Mehall, T. McConnochie, A. S. McEwen, H. Y. McSween, Jr., J. E. Moersch, K. H. Nealson, J. W. Rice, Jr., M. I. Richardson, S. W. Ruff, M. D. Smith, T. N. Titus, and W. Wyatt (2003b), Morphology and composition of the surface of Mars: Mars Odyssey THEMIS results, *Science*, *300*(2056), 2056-2061, doi: 10.1126/science.1080885.

Christensen, P. R., S. W. Ruff, R. L. Fergason, A. T. Knudson, R. E. Arvidson, J. L. Bandfield, D. L. Blaney, C. Budney, W. M. Calvin, T. D. Glotch, M. P. Golombek, T. G. Graff, V. E. Hamilton, A. Hayes, J. R. Johnson, H. Y. McSween, Jr., G. L. Mehall, L. K. Mehall, J. E. Moersch, R. V. Morris, A. D. Rogers, M. D. Smith, S. W. Squyres, M. J. Wolff, and M. B. Wyatt (2004b), Initial results from the Miniature Thermal Emission Spectrometer experiment at the Spirit landing site at Gusev Crater, *Science*, *305*, 837-842.

Christensen, P. R., J. L. Bandfield, V. E. Hamilton, S. W. Ruff, H. H. Kieffer, T. Titus, M. C. Malin, R. V. Morris, M. D. Lane, R. N. Clark, B. M. Jakosky, M. T. Mellon, J. C. Pearl, B. J. Conrath, M. D. Smith, R. T. Clancy, R. O. Kuzmin, T. Roush, G. L. Mehall, N. Gorelick, K. Bender, K. Murray, S. Dason, E. Greene, S. H. Silverman, and M. Greenfield (2001), Mars Global Surveyor Thermal Emission Spectrometer experiment: description and surface science results, *J. Geophys. Res.*, *106*(E10), 23,823-823,871, doi:10.1029/2000JE001370

Cintala, M. J., and R. A. F. Grieve (1998), Scaling impact-melt and crater dimensions: Implications for the lunar cratering record, *Meteoritics & Planet. Sci*, *33*(4), 889–912, doi: 10.1111/j.1945-5100.1998.tb01695.x.

Courtillot, V., C. Jaupart, I. Manighetti, P. Tapponnier, and J. Besse (1999), On causal links between flood basalts and continental breakup, *Earth Planet Sc Lett*, *166*(3-4), 177-195.

DeBlase, F. J., and S. Compton (1991), Infrared Emission Spectroscopy: A Theoretical and Experimental Review, *Appl. Spectrosc.*, *45*(4), 611-618, doi:10.1366/0003702914337029.

Dreibus, G., and H. Wanke (1985), Mars, a Volatile-Rich Planet, *Meteoritics*, *20*(2), 367-381.

Edwards, C. S., P. R. Christensen, and V. E. Hamilton (2008), Evidence for extensive olivine-rich basalt bedrock outcrops in Ganges and Eos chasmas, Mars, *J. Geophys. Res*, *113*, E11003, doi:10.1029/2008JE003091.

Edwards, C. S., P. R. Christensen, and J. Hill (2011a), Mosaicking of global planetary image datasets: 2. Modeling of wind streak thicknesses observed in Thermal Emission Imaging System (THEMIS) daytime and nighttime infrared data, *J. Geophys. Res.*, *116*(E10), E10005, doi:10.1029/2011JE003857.

Edwards, C. S., J. L. Bandfield, P. R. Christensen, and R. L. Fergason (2005), Global distribution of bedrock on Mars using THEMIS high resolution thermal inertia, *Eos Trans. AGU*, *86(52), Fall Meet. Suppl.*, Abstract P21C-0158.

Edwards, C. S., J. L. Bandfield, P. R. Christensen, and R. L. Fergason (2009), Global distribution of bedrock exposures on Mars using THEMIS high-resolution thermal inertia, *J. Geophys. Res*, *114*, E11001, doi:10.1029/2009JE003363.

Edwards, C. S., A. D. Rogers, J. L. Bandfield, and P. R. Christensen (2010), Volcanic origin of flat floored, bedrock containing craters on Mars, *41st LPSC*, Abstract # 1543.

Edwards, C. S., K. J. Nowicki, P. R. Christensen, J. Hill, N. Gorelick, and K. Murray (2011b), Mosaicking of global planetary image datasets: 1. Techniques and data processing for Thermal Emission Imaging System (THEMIS) multi-spectral data, *J. Geophys. Res.*, *116*(E10), E10008, doi:10.1029/2010JE003755.

Ehlmann, B. L., J. F. Mustard, S. L. Murchie, J. P. Bibring, A. Meunier, A. A. Fraeman, and Y. Langevin (2011a), Subsurface water and clay mineral formation during the early history of Mars, *Nature*, *479*(7371), 53-60, Doi 10.1038/Nature10582.

Ehlmann, B. L., J. F. Mustard, S. L. Murchie, J.-P. Bibring, A. Meunier, A. A. Fraeman, and Y. Langevin (2011b), Subsurface water and clay mineral formation during the early history of Mars, *Nature*, *479*(7371), 53-60, doi:10.1038/nature10582.

Ehlmann, B. L., J. F. Mustard, S. L. Murchie, F. Poulet, J. L. Bishop, A. J. Brown, W. M. Calvin, R. N. Clark, D. J. D. Marais, and R. E. Milliken (2008), Orbital identification of carbonate-bearing rocks on Mars, *Science*, *322*(5909), 1828.

Ehlmann, B. L., J. F. Mustard, G. A. Swayze, R. N. Clark, J. L. Bishop, F. Poulet, D. J. Des Marais, L. H. Roach, R. E. Milliken, and J. J. Wray (2009), Identification of hydrated silicate minerals on Mars using MRO-CRISM: Geologic context near Nili Fossae and implications for aqueous alteration, *J. Geophys. Res*, *114*, E00D08, doi:10.1029/2009JE003339

Elkins-Tanton, L. T., E. M. Parmentier, and P. C. Hess (2003), Magma ocean fractional crystallization and cumulate overturn in terrestrial planets: Implications for Mars, *Meteorit Planet Sci*, *38*(12), 1753-1771.

Elkins-Tanton, L. T., P. C. Hess, and E. M. Parmentier (2005), Possible formation of ancient crust on Mars through magma ocean processes, *J. Geophys. Res.*, *110*(E12), 10.1029/2005je002480.

Farmer, V. C. (1974), The infrared spectra of minerals, edited by V. C. Farmer, pp. 227-331, Adlard and Son Ltd.

Fassett, C. I., and J. W. I. Head (2005), Fluvial sedimentary deposits on Mars: Ancient deltas in a crater lake in the Nili Fossae region, *Geophys. Res. Lett.*, *32*, L14201, doi:14210.11029/12005GL023456.

Feely, K. C., and P. R. Christensen (1999), Quantitative compositional analysis using thermal emission spectroscopy: Application to igneous and metamorphic rocks, *J. Geophys. Res.*, *104*, 24,195-124,210, doi: 10.1029/1999JE001034

Feldman, W. C., W. V. Boynton, R. L. Tokar, T. H. Prettyman, O. Gasnault, S. W. Squyres, R. C. Elphic, D. J. Lawrence, S. L. Lawson, S. Maurice, G. W. McKinney, K. R. Moore, and R. C. Reedy (2002), Global Distribution of neutrons from Mars: Results from Mars Odyssey, *Science*, *297*(75), 75-78, doi:10.1126/science.1073541.

Fenton, L. K., and M. T. Mellon (2006), Thermal properties of sand from Thermal Emission Spectrometer (TES) and Thermal Emission Imaging System (THEMIS): Spatial variations within the Proctor Crater dune field on Mars, *J. Geophys. Res.*, *111*, E06014, doi:10.1029/2004JE002363.

Fenton, L. K., P. E. Geissler, and R. M. Haberle (2007), Global warming and climate forcing by recent albedo changes on Mars, *Nature*, *446*(7136), 646-649, doi: 10.1038/nature05718.

Fergason, R. L., and P. R. Christensen (2008), Formation and erosion of layered materials: Geologic and dust cycle history of eastern Arabia Terra, Mars, *J. Geophys. Res.*, *113*, E12001, doi: 10.1029/2007je002973.

Fergason, R. L., P. R. Christensen, and H. H. Kieffer (2006a), High resolution thermal inertia derived from THEMIS: Thermal model and applications, *J. Geophys. Res.*, *111*, E12004, doi:10.1029/2006JE002735.

Fergason, R. L., P.R.Christensen, J. F. Bell III, M. P. Golombek, K. E. Herkenhoff, and H. H. Kieffer (2006b), Physical properties of the Mars Exploration Rover landing sites as inferred from Mini-TES-derived thermal inertia, *J. Geophys. Res.*, *111*, E02S02, doi:10.1029/2005JE002583.

Francis, E. H. (1982), Magma and sediment-I Emplacement mechanism of late Carboniferous tholeiite sills in northern Britain: President's anniversary address 1981, *Journal of the Geological Society, London*, *139*(1), 1-20.

Gellert, R., R. Rieder, J. Brückner, B. C. Clark, G. Dreibus, G. Klingelhöfer, G. Lugmair, D. W. Ming, H. Wänke, A. Yen, J. Zipfel, and S. W. Squyres (2006), Alpha Particle X-Ray Spectrometer (APXS): Results from Gusev crater and calibration report,, *J. Geophys. Res.*, *111*(E02S05), , doi:10.1029/2005JE002555.

Gellert, R., R. Rieder, R. C. Anderson, J. Brückner, B. C. Clark, G. Greibus, T. Economou, G. Klingelhöfer, G. W. Lugmain, D. W. Ming, S. W. Squyres, C. d'Uston, H. Wänke, A. Yen, and J. Zipfel (2004), Chemistry of rocks and soils at Gusev Crater from the Alpha Particle X-ray Spectrometer, *Science*, *305*(5685), 829-832, doi: 10.1126/science.1099913.

Gillespie, A. R., A. B. Kahle, and R. E. Walker (1986), Color enhancement of highly correlated images. I. Decorrelation and HSI contrast stretches, *Remote Sensing Environ.*, *20*, 209-235, doi: 10.1016/0034-4257(86)90044-1.

Glotch, T. D., and P. R. Christensen (2005), Geologic and mineralogic mapping of Aram Chaos: Evidence for a water-rich history, *J. Geophys. Res.*, *110*, E09006, doi: 10.1029/2004JE2389.

Glotch, T. D., R. V. Morris, P. R. Christensen, and T. G. Sharp (2004), Effect of precursor mineralogy on the thermal infrared emission spectra of hematite: Application to martian hematite mineralization, *J. Geophys. Res.*, *109*, E07003, doi:10.1029/2003JE002224.

Golombek, M. P., J. A. Grant, L. S. Crumpler, R. Greeley, R. E. Arvidson, I. J. F. Bell, C. M. Weitz, R. Sullivan, P. R. Christensen, L. A. Soderblom, and S. W. Squyres (2006), Erosion rates at the Mars Exploration Rover landing sites and long-term climate change on Mars, *J. Geophys. Res.*, *111*, E12S10, doi:10.1029/2006JE002754.

Greeley, R., N. Lancaster, S. Lee, and P. Thomas (1992), Martian Eolian Processes, Sediments, and Features, in *Mars*, edited by H. Kieffer, B. Jakosky, C. Snyder and M. Matthews, Univ. of Arizona Press, Tucson.

Greeley, R., R. Leach, B. White, J. Iversen, and J. Pollack (1980), Threshold windspeeds for sand on Mars: Wind tunnel Ssimulations, *Geophys. Res. Lett.*, *7*, 121-124.

Hamilton, V. E., and P. R. Christensen (2000), Determining the modal mineralogy of mafic and ultramafic igneous rocks using thermal emission spectroscopy, *J. Geophys. Res.*, *105*, 9717-9734, doi:10.1029/1999JE001113.

Hamilton, V. E., and P. R. Christensen (2004), Green Mars: Geologic Characteristics of Olivine-Bearing Terrains as Observed by THEMIS, MOC, and MOLA, *LPSC XXXV*.

Hamilton, V. E., and P. R. Christensen (2005), Evidence for extensive olivine-rich bedrock in Nili Fossae, Mars, *Geology*, *33*(6), 433-436, doi: 10.1130/G21258.1.

Hamilton, V. E., P. R. Christensen, and H. Y. McSween, Jr. (1997), Determination of martian meteorite lithologies and mineralogies using vibrational spectroscopy, *J. Geophys. Res.*, *102*(E11), 25,593-525,603.

Hamilton, V. E., P. R. Christensen, H. Y. McSween, Jr., and J. L. Bandfield (2003), Searching for the source regions of martian meteorites using MGS TES: Integrating martian meteorites into the global distribution of igneous materials on Mars, *Meteoritics and Planetary Science*, *38*(6), 871-885, doi: 10.1111/j.1945-5100.2003.tb00284.x.

Hanel, R. A., B. J. Conrath, V. G. Kunde, C. Prabhakara, I. Revah, V. V. Salomonson, and G. Wolford (1972), The Nimbus 4 infrared spectroscopy experiment 1. Calibrated thermal emission spectra, *J. Geophys. Res.*, *77*(15), 2629-2641, 10.1029/JC077i015p02629.

Hapke, B. (1986), Bidirectional reflectance spectroscopy: 4. The extinction coefficient and the opposition effect, *Icarus*, *67*(2), 264-280.

Hapke, B. (2002), Bidirectional reflectance spectroscopy 5. The coherent backscatter opposition effect and anisotropic scattering, *Icarus*, *157*(2), 523-534, 10.1006/icar.2002.6853.

Hapke, B., R. Nelson, and W. Smythe (1998), The Opposition Effect of the Moon: Coherent Backscatter and Shadow Hiding, *Icarus*, *133*(1), 89-97.

Hartmann, W. K., and G. Neukum (2001), Cratering chronology and the evolution of Mars, *Space Sci Rev*, *96*(1), 165-119, doi: 10.1023/A:1011945222010.

Head, J. W., D. R. Marchant, M. C. Agnew, C. I. Fassett, and M. A. Kreslavsky (2006), Extensive valley glacier deposits in the northern mid-latitudes of Mars: Evidence for Late Amazonian obliquity-driven climate change, *Earth Plan. Sci. Lett.*, *241*(3-4), 663-671, doi:10.1016/j.epsl.2005.11.016.

Helfenstein, P., and M. K. Shepard (1999), Submillimeter-scale topography of the lunar regolith, *Icarus*, *141*(1), 107-131.

Helfenstein, P., J. Veverka, and J. Hillier (1997), The Lunar Opposition Effect: A Test of Alternative Models, *Icarus*, *128*(1), 2-14.

Henry, R. L. (1948), The Transmission of Powder Films in the Infra-Red, *Journal of the Optical Society of America*, *38*(9), 775-787.

Herkenhoff, K. E., S. W. Squyres, J. F. Bell, III, J. N. Maki, H. M. Arneson, P. Bertelsen, D. I. Brown, S. A. Collins, A. Dingizian, S. T. Elliott, W. Goetz, E. C. Hagerott, A. G. Hayes, M. J. Johnson, R. L. Kirk, S. McLennan, R. V. Morris, L. M. Scherr, M. A. Schwochert, L. R. Shiraishi, G. H. Smith, L. A. Soderblom, J. N. Sohl-Dickstein, and M. V. Wadsworth (2003), Athena Microscopic Imager investigation, *J. Geophys. Res.*, *108*(E12), 8065, doi:10.1029/2003JE002076.

Hoefen, T., R. N. Clark, J. L. Bandfield, M. D. Smith, J. C. Pearl, and P. R. Christensen (2003), Discovery of olivine in the Nili Fossae region of Mars, *Science*, *302*(5645), 627-630, doi: 10.1126/science.1089647.

Holt, J. W., A. Safaeinili, J. J. Plaut, J. W. Head, R. J. Phillips, R. Seu, S. D. Kempf, P. Choudhary, D. A. Young, N. E. Putzig, D. Biccari, and Y. Gim (2008), Radar Sounding Evidence for Buried Glaciers in the Southern Mid-Latitudes of Mars, *Science*, *322*(5905), 1235-1238, doi: 10.1126/science.1164246

Hunt, G. R., and J. W. Salisbury (1976), Mid-infrared spectral behavior of metamorphic rocks, *Environ. Res. Paper*, *543-AFCRL-TR-76-0003*, 67.

Ivanov, B. A. (2001), Mars/Moon cratering rate ratio estimates, *Space Sci Rev*, *96*(1), 87-104, doi: 10.1023/A:1011941121102.

Jakosky, B. M. (1986), On the thermal properties of martian fines, *Icarus*, *66*(1), 117-124, doi:10.1016/0019-1035(1086)90011-90014

James, P. B., G. Briggs, J. Barnes, and A. Spruck (1979), Seasonal recession of Mars' South Polar Cap as seen by Viking, *J. Geophys. Res.*, *84*, 2889-2922.

Jaumann, R., G. Neukum, T. Behnke, T. C. Duxbury, K. Eichentopf, J. Flohrer, S. Gasselt, B. Giese, K. Gwinner, and E. Hauber (2007), The high-resolution stereo camera (HRSC) experiment on Mars Express: Instrument aspects and experiment conduct from interplanetary cruise through the nominal mission, *Planet Space Sci*, *55*, 928-952.

Johnson, J. R., F. Horz, P. G. Lucey, and P. R. Christensen (2002), Thermal infrared spectroscopy of experimentally shocked anorthosite and pyroxentie: Implications for remote sensing of Mars, *J. Geophys. Res.*, *107(E10)*, 5073, doi:10.1029/2001JE001517.

Kavanagh, J. L., T. Menand, and R. S. J. Sparks (2006), An experimental investigation of sill formation and propagation in layered elastic media, *Earth Planet Sc Lett*, *245*(3-4), 799-813.

Kember, D., D. H. Chenery, N. Sheppard, and J. Fell (1979), Fourier-transform i.r. emission studies of weakly emitting overlayers on metal surfaces; experimental and spectral-ratioing procedures and the comparative use of room temperature triglycine sulphate and low-temperature mercury cadmium telluride detectors, *Spectrochimica Acta Part A: Molecular Spectroscopy*, *35*(5), 455-459, 10.1016/0584-8539(79)80160-9.

Kieffer, H. H. (submitted), Thermal models for analysis of Mars infrared mapping.

Kieffer, H. H., and T. N. Titus (2001), TES mapping of Mars' north seasonal cap, *Icarus*, *154*(1), 162-180, doi:110.1006/icar.2001.6670.

Kieffer, H. H., T. Titus, K. Mullins, and P. R. Christensen (2000), Mars south polar cap behavior observed by TES: Seasonal cap evolution controlled by frost grain size, *J. Geophys. Res.*, *105*(E4), 9653-9700, doi:10.1029/1999JE001136.

Kieffer, H. H., J. S.C. Chase, E. Miner, G. Munch, and G. Neugebauer (1973), Preliminary report on infrared radiometric measurements from Mariner 9 spacecraft, *J. Geophys. Res.*, *78*, 4291-4312, doi: 10.1029/JB078i020p04291.

Kieffer, H. H., T. Z. Martin, A. R. Peterfreund, B. M. Jakosky, E. D. Miner, and F. D. Palluconi (1977), Thermal and albedo mapping of Mars during the Viking primary mission, *J. Geophys. Res.*, *82*, 4249-4291, doi: 10.1029/JS082i028p04249.

Kirk, R. L., E. Howington-Kraus, D. Galuszka, B. Redding, and T. M. Hare (2006), Topomapping of Mars with HRSC images, ISIS, and a commercial stereo workstation, *Int. Arch. Photogramm. Remote Sensing Spatial Inf. Sci*, *36*, 293ñ298.

Klaasen, K. P., T. E. Thorpe, and L. A. Morabito (1977), Inflight performance of the Viking visual imaging subsystem, *Applied Optics*, *16*(12), 3158-3170.

Kleine, T., C. M¸nker, K. Mezger, and H. Palme (2002), Rapid accretion and early core formation on asteroids and the terrestrial planets from HfñW chronometry, *Nature*, *418*(6901), 952-955.

Klingelhöfer, G., R. V. Morris, B. Bernhardt, C. Schröder, D. S. Rodionov, J. R.A. de souza, A. Yen, R. Gellert, E. N. Evlanov, B. Zubkov, J. Foh, E. Kankeleit, P. Gütlich, D. W. Ming, F. Renz, T. Wdowiak, S. W. Squyres, and R. E. Arvidson (2004), Jarosite and hematite at Meridiani Planum

from the Mössbauer spectrometer on the Opportunity rover, *Science*, *306*(5702), 1740-1745, doi: 10.1126/science.1104653

Koeppen, W. C., and V. E. Hamilton (2008), Global distribution, composition, and abundance of olivine on the surface of Mars from thermal infrared data, *J. Geophys. Res*, *113*, E05001, doi:10.1029/2007JE002984

Kreslavsky, M. A., J. W. Head, and D. R. Marchant (2008), Periods of active permafrost layer formation during the geological history of Mars: Implications for circum-polar and mid-latitude surface processes, *Planet Space Sci*, *56*(2), 289-302, doi: 10.1016/j.pss.2006.02.010.

Lane, M. D. (1999), Infrared optical constants of calcite and their relationship to particle size effects in thermal emission spectra of granular calcite, *J. Geophys. Res.*, *104*, 14,099-014,108, doi:10.1029/1999JE900025

Lane, M. D., T. D. Glotch, M. D. Dyar, C. M. Pieters, R. Klima, T. Hiroi, J. L. Bishop, and J. Sunshine (2011), Midinfrared spectroscopy of synthetic olivines: Thermal emission, specular and diffuse reflectance, and attenuated total reflectance studies of forsterite to fayalite, *J. Geophys. Res.*, *116*(E8), E08010, doi:10.1029/2010JE003588

Lee, D. C., and A. N. Halliday (1997), Core formation on Mars and differentiated asteroids, *Nature*, *388*(6645), 854-857.

Leighton, R. B., and B. C. Murray (1966), Behavior of carbon dioxide and other volatiles on Mars, *Science*, *153*, 136-144.

Lewis, K. W., O. Aharonson, J. P. Grotzinger, S. W. Squyres, J. F. Bell Iii, L. S. Crumpler, and M. E. Schmidt (2008), Structure and stratigraphy of Home Plate from the Spirit Mars Exploration Rover, *J. Geophys. Res*, *113*, E12S36, doi:10.1029/2007JE003025.

Lowell, P. (1896), *Mars*, Longmans and Green, London.

Lyon, R. J. P. (1962), Evaluation of infrared spectroscopy for compositional analysis of lunar and planetary soils*Rep.*, Stanford Research Institute.

Malin, M. C., M. A. Caplinger, and S. D. Davis (2001), Observational evidence for an active surface reservoir of solid carbon dioxide on Mars, *Science*, *294*, 2146-2148, DOI: 2110.1126/science.1066416.

Malin, M. C., K. S. Edgett, L. V. Posiolova, S. M. McColley, and E. Z. Noe Dobrea (2006), Present-Day Impact Cratering Rate and Contemporary Gully Activity on Mars, *Science*, *314*, 1573-1577.

Malin, M. C., W. M. Calvin, B. A. Cantor, R. T. Clancy, R. M. Haberle, P. B. James, P. C. Thomas, M. J. Wolff, J. F. Bell, and S. W. Lee (2008), Climate, weather, and north polar observations from the Mars Reconnaissance Orbiter Mars Color Imager, *Icarus*, *194*(2), 501-512, doi:510.1016/j.icarus.2007.1010.1016.

Malin, M. C., J. F. Bell, B. A. Cantor, M. A. Caplinger, W. M. Calvin, R. T. Clancy, K. S. Edgett, L. Edwards, R. M. Haberle, P. B. James, S. W. Lee, M. A. Ravine, P. C. Thomas, and M. J. Wolff (2007), Context Camera Investigation on board the Mars Reconnaissance Orbiter, *J. Geophys. Res.*, *112*, E05S04, doi:10.1029/2006JE002808. .

Malin, M. C., M. H. Carr, G. E. Danielson, M. E. Davies, W. K. Hartmann, A. P. Ingersoll, P. B. James, H. Masursky, A. S. McEwen, L. A. Soderblom, P. Thomas, J. Veverka, M. A. Caplinger, M. A. Ravine, T. A. Soulanille, and J. L. Warren (1998), Early views of the martian surface from the Mars Orbiter Camera of Mars Global Surveyor, *Science*, *279*(5357), 1681-1685, doi: 10.1126/science.279.5357.1681.

Marinova, M. M., O. Aharonson, and E. Asphaug (2008), Mega-impact formation of the Mars hemispheric dichotomy, *Nature*, *453*(7199), 1216-1219, doi: 10.1038/nature07070.

McDowell, M. L., and V. E. Hamilton (2007), Geologic characteristics of relatively high thermal inertia intracrater deposits in southwestern Margaritifer Terra, Mars, *J. Geophys. Res.*, *112*, E12001, doi:10.1029/2007JE002925

McEwen, A. S., M. C. Malin, M. H. Carr, and W. K. Hartmann (1999), Voluminous volcanism on early Mars revealed in Valles Marineris, *Nature*, *397*, 584-586, doi:10.1038/17539.

McEwen, A. S., E. M. Eliason, J. W. Bergstrom, N. T. Bridges, C. J. Hansen, W. A. Delamere, J. A. Grant, V. C. Gulick, K. E. Herkenhoff, L. Keszthelyi, R. L. Kirk, M. T. Mellon, S. W. Squyres, N. Thomas, and C. M. Weitz (2007), Mars Reconnaissance Orbiter's High Resolution Imaging Science Experiment (HiRISE), *J. Geophys. Res.*, *112*, E05S02, doi:10.1029/2005JE002605.

McLennan, S. M., J. F. B. III, W. M. Calvin, P. R. Christensen, B. C. Clark, J. P.A. De Souza, J. Farmer, D. A. Fike, R. Gellert, A. Ghosh, T. D. Glotch, J. Grotzinger, B. Hahn, K. E. Herkenhoff, J. A. Hurowitz, J. R. Johnson, S. S. Johnson, B. Jolliff, G. Klingelhöfer, A. H. Knoll, Z. Learner, M. C. Malin, J. H.Y. McSween, J. Pocock, S. W. Ruff, L. A. Soderblom, S. W. Squyres, N. J. Tosca, W. A. Watters, M. B. Wyatt, and A. Yen (2005),

Provenance and diagenesis of the evaporite-bearing Burns formation, Meridiani Planum, Mars, *Earth Planet. Sci. Lett.*, *240*, 95-121, doi:10.1016/j.epsl.2005.09.041.

McSween, H. Y., M. B. Wyatt, R. Gellert, J. F. Bell III, R. V. Morris, K. E. Herkenhoff, L. S. Crumpler, K. A. Milam, K. R. Stockstill, L. L. Tornabene, R. E. Arvidson, P. Bartlett, D. Blaney, N. A. Cabrol, P. R. Christensen, B. C. Clark, J. A. Crisp, D. J. Des Marais, T. Economou, J. D. Farmer, W. Farrand, A. Ghosh, M. Golombek, S. Gorevan, R. Greeley, V. E. Hamilton, J. R. Johnson, B. L. Joliff, G. Klingelhoeffer, A. T. Knudson, S. McLennon, D. Ming, J. E. Moersch, R. Rieder, S. W. Ruff, C. Schroeder, J. de Souza, P.A., S. W. Squyres, H. Waenke, A. Wang, A. Yen, and J. Zipfel (2006), Characterization and petrologic interpretation of olivine-rich basalts at Gusev Crater, Mars, *J. Geophys. Res.*, *111*, E02S10, doi:1029/2005JE002477.

McSween, H. Y., Jr. (1994), What have we learned about Mars from SNC meteorites, *Meteoritics*, *29*, 757-779.

Mellon, M. T., B. M. Jakosky, H. H. Kieffer, and P. R. Christensen (2000), High resolution thermal inertia mapping from the Mars Global Surveyor Thermal Emission Spectrometer, *Icarus*, *148*(2), 437-455, doi:10.1006/icar.2000.6503

Michael, G. G., and G. Neukum (2010), Planetary surface dating from crater size-frequency distribution measurements: Partial resurfacing events and statistical age uncertainty, *Earth Planet Sc Lett*, *294*(3-4), 223-229, doi: 10.1016/j.epsl.2009.12.041.

Michalski, J. R., and P. B. Niles (2010), Deep crustal carbonate rocks exposed by meteor impact on Mars, *Nat Geosci*, *3*(11), 751-755 doi:10.1038/ngeo971.

Michalski, J. R., M. D. Kraft, T. Diedrich, T. G. Sharp, and P. R. Christensen (2003), Thermal emission spectroscopy of the silica polymorphs and considerations for remote sensing of Mars, *Geophys. Res. Lett.*, *30*(19), 2008, doi:10.1029/2003GL018354.

Michalski, J. R., M. D. Kraft, T. G. Sharp, L. B. Williams, and P. R. Christensen (2005), Mineralogical constraints on the high-silica Martian surface component observed by TES, *Icarus*, *174*, 161-177, doi: 10.1016/j.icarus.2004.10.022.

Michalski, J. R., M. D. Kraft, T. G. Sharp, L. B. Williams, and P. R. Christensen (2006), Emission spectroscopy of clay minerals and evidence for poorly

crystalline aluminosilicates on Mars from Thermal Emission Spectrometer data, *J. Geophys. Res.*, *111*, E03004, doi:10.1029/2005JE002438.

Mitrofanov, I., D. Anfimov, A. Kozyrev, M. Litvak, A. Sanin, V. Tret'yakov, A. Krylov, V. Shvetsov, W. Boynton, C. Shinohara, D. Hamara, and R. S. Saunders (2002), Maps of Subsurface Hydrogen from the High Energy Neutron Detector, Mars Odyssey, *Science*, *297*, 78-81, doi: 10.1126/science.1084350.

Moersch, J. E., and P. R. Christensen (1995), Thermal emission from particulate surfaces: A comparison of scattering models with measured spectra, *J. Geophys. Res.*, *100*, 7,465-467,477, doi:10.1029/94JE03330.

Monders, A. G., E. Médard, and T. L. Grove (2007), Phase equilibrium investigations of the Adirondack class basalts from the Gusev plains, Gusev crater, Mars, *Meteorit Planet Sci*, *42*(1), 131-148, 10.1111/j.1945-5100.2007.tb00222.x.

Morris, R. V., G.Klingelhöfer, B. Bernhardt, C. Schröder, D. S. Rodionov, J. R.A. de souza, A. Yen, R. Gellert, E. N. Evlanov, J. Foh, E. Kankeleit, P. Gütlich, D. W. Ming, F. Renz, T. Wdowiak, S. W. Squyres, and R. E. Arvidson (2004), Mineralogy at Gusev Crater from the Mössbauer spectrometer on the Spirit Rover, *Science*, *305*(5685), 833-836, doi: 10.1126/science.1100020.

Morschhauser, A., M. Grott, and D. Breuer (2011), Crustal recycling, mantle dehydration, and the thermal evolution of Mars, *Icarus*, *212*(2), 541-558, 10.1016/j.icarus.2010.12.028.

Murchie, S., R. Arvidson, P. Bedini, K. Beisser, J. P. Bibring, J. Bishop, J. Boldt, P. Cavender, T. Choo, and R. T. Clancy (2007), Compact Reconnaissance Imaging Spectrometer for Mars (CRISM) on Mars Reconnaissance Orbiter (MRO), *J. Geophys. Res*, *112*, E05S03, doi:10.1029/2006JE002682.

Mustard, J. F., and J. M. Sunshine (1995), Seeing through the dust: Martian crustal heterogeneity and links to the SNC meteorites, *Science*, *267*, 1623-1626.

Mustard, J. F., and J. E. Hays (1997), Effects of hyperfine particles on reflectance spectra from 0.3 to 25 μm, *Icarus*, *125*(1), 145-163, doi: 10.1006/icar.1996.5583.

Mustard, J. F., B. L. Ehlmann, S. L. Murchie, F. Poulet, N. Mangold, J. W. Head, J. P. Bibring, and L. H. Roach (2009), Composition, Morphology, and

Stratigraphy of Noachian Crust around the Isidis basin, *J. Geophys. Res.*, *114*, E00D12, 10.1029/2009je003349.

Mustard, J. F., F. Poulet, A. Gendrin, J.-P. Bibring, Y. Langevin, B. Gondet, N. Mangold, G. Bellucci, and F. Altieri (2005), Olivine and pyroxene diversity in the crust of Mars, *Science*, *307*(5715), 1594-1597, doi: 1510.1126/science.1109098.

Mustard, J. F., F. Poulet, J. W. Head, N. Mangold, J. P. Bibring, S. M. Pelkey, C. I. Fassett, Y. Langevin, and G. Neukum (2007), Mineralogy of the Nili Fossae region with OMEGA/Mars Express data: 1. Ancient impact melt in the Isidis Basin and implications for the transition from the Noachian to Hesperian, *J. Geophys. Res*, *112*(E8), E08S03, doi: 10.1029/2006JE002834.

Neugebauer, G., G. Munch, H. Kieffer, J. S.C. Chase, and E. Miner (1971), Mariner 1969 infrared radiometer results: Temperatures and thermal properties of the martian surface, *Astron. J.*, *76*, 719-728.

Neukum, G., and D. U. Wise (1976), Mars: A standard crater curve and possible new time scale, *Science*, *194*(4272), 1381-1387, doi: 10.1126/science.194.4272.1381.

Neukum, G., and K. Hiller (1981), Martian Ages, *J. Geophys. Res.*, *86*(B4), 3097-3121, doi:10.1029/JB086iB04p03097

Neukum, G., B. A. Ivanov, and W. K. Hartmann (2001), Cratering records in the inner solar system in relation to the lunar reference system, *Space Sci Rev*, *96*(1), 55-86, doi: 10.1023/A:1011989004263.

Neukum, G., R. Jaumann, and T. H. C.-I. a. E. Team (2004), HRSC: The High Resolution Stereo Camera of Mars Express, *Eur. Space Agency Spec. Publ., ESA*, *1240*, 17-35.

Newsom, H. E., G. E. Brittelle, C. A. Hibbitts, L. J. Crossey, and A. M. Kudo (1996), Impact crater lakes on Mars, *J. Geophys. Res.*, *101*(E6), 14951-14955.

Nowicki, K. J., and P. R. Christensen (in prep), Removal of Line- and Row-Correlated Noise in THEMIS Multi-Spectral Infrared Data, *Mars*.

Nowicki, K. J., C. S. Edwards, and P. R. Christensen (in prep), Removal of white noise from multi-spectral THEMIS data, *Mars*.

Nyquist, L. E., D. D. Bogard, C.-Y. Shih, A. Greshake, D. Stoffler, and O. Eugster (2001), Ages and geologic histories of martian meteorites, *Chronology and Evolution of Mars*, *96*(1-4), 105-164.

Officer, C. B., A. Hallam, C. L. Drake, and J. D. Devine (1987), Late Cretaceous and paroxysmal Cretaceous/Tertiary extinctions, *Nature*, *326*(6109), 143-148.

Osinski, G. R. (2006), Effect of volatiles and target lithology on the generation and emplacement of impact crater fill and ejecta deposits on Mars, *Meteorit Planet Sci*, *41*(10), 1571-1586, doi: 10.1111/j.1945-5100.2006.tb00436.x.

Osinski, G. R., R. A. F. Grieve, G. S. Collins, C. Marion, and P. Sylvester (2008), The effect of target lithology on the products of impact melting, *Meteorit Planet Sci*, *43*(12), 1939-1954, doi: 10.1111/j.1945-5100.2008.tb00654.x.

Osterloo, M. M., V. E. Hamilton, J. L. Bandfield, T. D. Glotch, A. M. Baldridge, P. R. Christensen, L. L. Tornabene, and F. S. Anderson (2008), Chloride-Bearing Materials in the Southern Highlands of Mars, *Science*, *319*(5870), 1651-1654, 10.1126/science.1150690.

Palluconi, F. D., and H. H. Kieffer (1981), Thermal inertia mapping of Mars from 60°S to 60°N, *Icarus*, *45*(2), 415-426, doi: 410.1016/0019-1035(1081)90044-90040.

Pelkey, S. M., J. F. Mustard, S. Murchie, R. T. Clancy, M. Wolff, M. Smith, R. Milliken, J. P. Bibring, A. Gendrin, and F. Poulet (2007), CRISM multispectral summary products: Parameterizing mineral diversity on Mars from reflectance, *J. Geophys. Res*, *112*, E08S14, doi:10.1029/2006JE002831.

Peulvast, J.-P., D. Mége, J. Chiciak, F. Costard, and P. L. Masson (2001), Morphology, evolution and tectonics of Valles Marineris wallslopes (Mars), *Geomorphology*, *37*(3-4), 329-352.

Phillips, R. J., M. T. Zuber, S. C. Solomon, M. P. Golombek, B. M. Jakosky, W. B. Banerdt, D. E. Smith, R. M. E. Williams, B. H. Hynek, O. Aharonson, and S. A. Hauck (2001), Ancient geodynamics and global-scale hydrology of Mars, *Science*, *291*, 2587-2591.

Piqueux, S., and P. R. Christensen (2008), Deposition of CO2 and erosion of the Martian south perennial cap between 1972 and 2004: Implications for current climate change, *J. Geophys. Res.*, *113*(E2), DOI: 10.1029/2007JE002969 doi: 10.1029/2007je002969.

Piqueux, S., and P. R. Christensen (2009), A model of thermal conductivity for planetary soils: 1. Theory for unconsolidated soils, *J. Geophys. Res.*, *114*, E09005, doi:10.1029/2008JE003308.

Piqueux, S., and P. R. Christensen (2011), Temperature-dependent thermal inertia of homogeneous Martian regolith, *J. Geophys. Res.*, *116*, E07004, doi:10.1029/2011JE003805

Piqueux, S., S. Byrne, and M. I. Richardson (2003), Sublimation of Mars's southern seasonal CO2 cap and the formation of spiders, *J. Geophys. Res.*, *108*, 5084, doi:10.1029/2002JE002007.

Piqueux, S., C. S. Edwards, and P. R. Christensen (2008), Distribution of the ices exposed near the south pole of Mars using Thermal Emission Imaging System (THEMIS) temperature measurements, *J. Geophys. Res*, *113*(E8), doi: 10.1029/2007JE003055.

Pollack, J. B., T. Roush, F. Witteborn, J. Bregman, D. Wooden, C. Stoker, O. B. Toon, D. Rank, B. Dalton, and R. Freedman (1990), Thermal emission spectra of Mars (5.4-10.5μm): Evidence for sulfates, carbonates, and hydrates, *J. Geophys. Res.*, *95*, 14,595-514,627, doi:10.1029/JB095iB09p14595

Pondrelli, M., A. Baliva, S. Di Lorenzo, L. Marinangeli, and A. P. Rossi (2005), Complex evolution of paleolacustrine systems on Mars: An example from the Holden crater, *J. Geophys. Res.*, *110*(E4), 10.1029/2004je002335.

Poulet, F., J.-P. Bibring, J. F. Mustard, A. Gendrin, N. Mangold, Y. Langevin, R. E. Arvidson, B. Gondet, C. Gomez, and O. Team (2005), Phyllosilicates on Mars and implications for early martian climate, *Nature*, *438*, 623-627, doi:610.1038/nature04274.

Presley, M. A., and P. R. Christensen (1997a), The effect of bulk density, particle shape, and sorting on the thermal conductivity of particulate materials under martian atmosphere pressures, *J. Geophys. Res.*, *102*(E4), 9221-9229, doi: 10.1029/97JE00271.

Presley, M. A., and P. R. Christensen (1997b), Thermal conductivity measurements of particulate materials, Part I: A review, *J. Geophys. Res.*, *102*(E3), 6535-6549, doi: 10.1029/96JE03302.

Presley, M. A., and P. R. Christensen (1997c), Thermal conductivity measurements of particulate materials, Part II: Results, *J. Geophys. Res.*, *102*(E3), 6551-6566, doi: 10.1029/96JE03303.

Putzig, N. E., and M. T. Mellon (2007), Apparent thermal inertia and the surface heterogeneity of Mars, *Icarus*, *191*(1), 68-94, doi: 10.1016/j.icarus.2007.1005.1013.

Putzig, N. E., M. T. Mellon, K. A. Kretkea, and R. E. Arvidson (2005), Global thermal inertia and surface properties of Mars from the MGS mapping mission, *Icarus*, *173*(2), 325-341, doi: 10.1016/j.icarus.2004.08.017.

Ramsey, M. S., and P. R. Christensen (1998), Mineral abundance determination: Quantitative deconvolution of thermal emission spectra, *J. Geophys. Res.*, *103*, 577-596, doi:10.1029/97JB02784

Ramsey, M. S., P. R. Christensen, N. Lancaster, and D. A. Howard (1999), Identification of sand sources and transport pathways at Kelso Dunes, California using thermal infrared remote sensing, *Geol. Soc. Am. Bull.*, *111*, 636-662, doi: 10.1130/0016-7606(1999)111.

Rewick, R. T., and R. G. Messerschmidt (1991), A Simple Device for Studying FT-IR Emission Spectra of Solid Surfaces, *Applied Spectroscopy*, *45*(2), 297-301, doi: 10.1366/0003702914337687.

Robbins, S. J., G. D. Achille, and B. M. Hynek (2011), The volcanic history of Mars: High-resolution crater-based studies of the calderas of 20 volcanoes, *Icarus*, *211*(2), 1179-1203, doi: 10.1016/j.icarus.2010.11.012.

Rogers, A. D., and P. R. Christensen (2007), Surface mineralogy of martian low-albedo regions from MGS TES data: Implications for crustal evolution and surface alteration, *J. Geophys. Res.*, *112*, E01003, doi:10.1029/2006JE002727.

Rogers, A. D., and O. Aharonson (2008), Mineralogical composition of sands in Meridiani Planum determined from Mars Exploration Rover data and comparison to orbital measurements, *J. Geophys. Res.*, *113*, E06S14, doi:10.1029/2007JE002995.

Rogers, A. D., and R. L. Fergason (2011), Regional-scale stratigraphy of surface units in Tyrrhena and Iapygia Terrae, Mars: Insights into highland crustal evolution and alteration history, *J. Geophys. Res.*, *116*, E08005, doi:10.1029/2010JE003772

Rogers, A. D., P. R. Christensen, and J. L. Bandfield (2005), Compositional heterogeneity of the ancient martian crust: Analysis of Ares Vallis bedrock the THEMIS and TES data, *J. Geophys. Res.*, *110*, E05010, doi:10.1029/2005JE002399.

Rogers, A. D., J. L. Bandfield, and P. R. Christensen (2007), Global spectral classification of martian low-albedo regions with Mars Global Surveyor Thermal Emission Spectrometer (MGS-TES) data, *J. Geophys. Res.*, *112*, E02004, doi:10.1029/2006JE002726.

Rogers, A. D., O. Aharonson, and J. L. Bandfield (2009), Geologic context of bedrock exposures in Mare Serpentis, Mars: Implications for crust and regolith evolution in the cratered highlands, *Icarus*, *200*(2), 446-462, doi:10.1016/j.icarus.2008.11.026.

Rogers, D., and P. R. Christensen (2003), Age relationships of basaltic and andesitic surface compositions on Mars: Analysis of high-resolution TES observations of the northern hemisphere, *J. Geophys. Res.*, *108*(E4), 5030, doi:10.1029/2002JE001913.

Ruff, S. W. (2004), Spectral evidence for zeolite in the dust on Mars, *Icarus*, *168*(1), 131-143, doi: 10.1016/j.icarus.2003.11.003.

Ruff, S. W., and P. R. Christensen (2002), Bright and dark regions on Mars: Particle size and mineralogical characteristics based on Thermal Emission Spectrometer data, *J. Geophys. Res.*, *107*(E12), doi: 10.1029/2001JE001580.

Ruff, S. W., A. S. McEwen, and A. S. Team (2007), An Emerging View of the Stratigraphy of the Columbia Hills in Gusev Crater from HiRISE and Mini-TES Data, *38th Lunar and Planetary Science Conference,(Lunar and Planetary Science XXXVIII), held March 12-16, 2007 in League City, Texas. LPI Contribution No. 1338, p. 2063*.

Ruff, S. W., P. R. Christensen, P. W. Barbera, and D. L. Anderson (1997), Quantitative thermal emission spectroscopy of minerals: A technique for measurement and calibration, *J. Geophys. Res.*, *102*(B7), 14,899-814,913, doi:10.1029/97JB00593

Ruff, S. W., P. R. Christensen, D. L. Blaney, W. H. Farrand, J. R. Johnson, J. R. Michalski, J. E. Moersch, S. P. Wright, and S. W. Squyres (2006), The rocks of Gusev Crater as viewed by the Mini-TES instrument, *J. Geophys. Res.*, *111*, E12S18, doi:10.1029/2006JE002747.

Ruff, S. W., J. D. Farmer, W. M. Calvin, K. E. Herkenhoff, J. R. Johnson, R. V. Morris, M. S. Rice, R. E. Arvidson, J. F. Bell, III, P. R. Christensen, and S. W. Squyres (2011), Characteristics, distribution, origin, and significance of opaline silica observed by the Spirit rover in Gusev crater, Mars, *J. Geophys. Res.*, *116*, E00F23, doi: 10.1029/2010je003767.

Sagan, C., J. Veverka, P. Fox, R. Dubish, R. French, P. Gierasch, L. Quam, J. Lederberg, E. Levinthal, R. Tucker, B. Eross, and J. B. Pollack (1973), Variable features on Mars, 2, Mariner 9, global results, *J. Geophys. Res.*, *78*, 4163-4196.

Salisbury, J. W., and J. W. Eastes (1985), The effect of particle size and porosity on spectral contrast in the mid-infrared, *Icarus*, *64*(3), 586-588, doi:10.1016/0019-1035(85)90078-8.

Salisbury, J. W., L. S. Walter, N. Vergo, and D. M. D'Aria (1992), *Infrared (2.1-25 μm) Spectra of Minerals*, 267 pp., The Johns Hopkins University Press, Baltimore and London.

Salvatore, M. R., J. F. Mustard, M. B. Wyatt, and S. L. Murchie (2010), Definitive evidence of Hesperian basalt in Acidalia and Chryse planitiae, *J. Geophys. Res.*, *115*, E07005, doi:10.1029/2009JE003519.

Schultz, P. H. (1976), Floor-fractured lunar craters, *The Moon*, *15*, 241-273, doi: 10.1007/BF00562240.

Schultz, P. H. (1978), Martian Intrusions: possible sites and implications, *Geophys. Res. Lett.*, *5*(6), 457-460, doi:10.1029/GL005i006p00457

Schultz, P. H., and D. L. Orphal (1978), Floor-fractured craters on the moon and Mars, *Meteoritics*, *13*, 622-625.

Schultz, P. H., and J. F. Mustard (2004), Impact melts and glasses on Mars, *J. Geophys. Res.*, *109*(E1), 10.1029/2002je002025.

Schwenzer, S. P., and D. A. Kring (2009), Impact-generated hydrothermal systems capable of forming phyllosilicates on Noachian Mars, *Geology*, *37*(12), 1091-1094, doi: 10.1130/G30340A.1

Smith, D. E., M. T. Zuber, H. V. Frey, J. B. Garvin, J. W. Head, D. O. Muhleman, G. H. Pettengill, R. J. Phillips, S. C. Solomon, H. J. Zwally, W. B. Banerdt, T. C. Duxbury, M. P. Golombek, F. G. Lemoine, G. A. Neumann, D. D. Rowlands, O. Aharonson, P. G. Ford, A. B. Ivanov, C. L. Johnson, P. J. McGovern, J. B. Abshire, R. S. Afzal, and X. Sun (2001), Mars Orbiter Laser Altimeter: Experiment summary after the first year of global mapping of Mars, *J. Geophys. Res.*, *106*, 23,689-623,722.

Smith, M. D. (2004), Interannual variability in TES atmospheric observations of Mars during 1999-2003, *Icarus*, *167*, 148-165.

Smith, M. D., J. L. Bandfield, and P. R. Christensen (2000), Separation of atmospheric and surface spectral features in Mars Global Surveyor Thermal Emission Spectrometer (TES) spectra: Models and atmospheric properties, *J. Geophys. Res.*, *105*(E4), 9589-9608, doi:10.1029/1999JE001105

Smith, M. D., B. J. Conrath, J. C. Pearl, and P. R. Christensen (2002), Thermal Emission Spectrometer observations of martian planet-encircling dust storm 2001A, *Icarus*, *157*(1), 259-263, doi: 10.1006/icar.2001.6797.

Smith, M. D., M. J. Wolff, M. T. Lemmon, N. Spanovich, D. Banfield, C. J. Budney, R. T. Clancy, A. Ghosh, G. A. Landis, P.Smith, B. Whitney, P. R. Christensen, and S. W. Squyres (2004), First atmospheric results from the Mars Exploration rovers Mini-TES, *Science*, *306*, 1750-1753.

Smith, P. H., L. K. Tamppari, R. E. Arvidson, D. Bass, D. Blaney, W. V. Boynton, A. Carswell, D. C. Catling, B. C. Clark, T. Duck, E. DeJong, D. Fisher, W. Goetz, H. P. Gunnlaugsson, M. H. Hecht, V. Hipkin, J. Hoffman, S. F. Hviid, H. U. Keller, S. P. Kounaves, C. F. Lange, M. T. Lemmon, M. B. Madsen, W. J. Markiewicz, J. Marshall, C. P. McKay, M. T. Mellon, D. W. Ming, R. V. Morris, W. T. Pike, N. Renno, U. Staufer, C. Stoker, P. Taylor, J. A. Whiteway, and A. P. Zent (2009), H2O at the Phoenix Landing Site, *Science*, *325*(5936), 58-56, doi: 10.1126/science.1172339

Smrekar, S., and C. M. Pieters (1985), Near-infrared spectroscopy of probable impact melt from three large lunar highland craters, *Icarus*, *63*(3), 442-452, doi:10.1016/0019-1035(85)90056-9.

Solomon, S. C. (1979), Formation, history and energetics of cores in the terrestrial planets, *Phys Earth Planet In*, *19*(2), 168-182.

Solomon, S. C., O. Aharonson, J. M. Aurnou, W. B. Banerdt, Michael H. Carr, A. J. Dombard, H. V. Frey, M. P. Golombek, S. A. H. II, J. W. H. III, B. M. Jakosky, C. L. Johnson, P. J. McGovern, G. A. Neumann, R. J. Phillips, D. E. Smith, and M. T. Zuber (2005), New Perspectives on Ancient Mars, *Science*, *307*, 1214-1220.

Spohn, T. (1991), Mantle differentiation and thermal evolution of Mars, Mercury, and Venus, *Icarus*, *90*(2), 222-236.

Squyres, S. W., and A. H. Knoll (2005), Sedimentary rocks at Meridiani Planum: Origin, diagenesis, and implications for life on Mars, *Earth Planet. Sci. Lett.*, *240*, 1-10, doi:10.1016/j.epsl.2005.09.038.

Squyres, S. W., R.Arvidson, E. Baumgartner, J. F. Bell, III, P. R. Christensen, S.Gorevan, K.Herkenhoff, G.Klingelhöfer, M.Madsen, R. V. Morris, R.Rieder, and R.Romero (2003), The Athena Mars Rover Science Investigation, *J. Geophys. Res.*, *108*, 8062, doi:1029/2003JE002121.

Squyres, S. W., R. E. Arvidson, S. Ruff, R. Gellert, R. V. Morris, D. W. Ming, L. Crumpler, J. D. Farmer, D. J. D. Marais, A. Yen, S. M. McLennan, W. Calvin, J. F. B. III, B. C. Clark, A. Wang, T. J. McCoy, M. E. Schmidt, and P. A. d. S. Jr (2008), Detection of Silica-Rich Deposits on Mars, *Science*, *320*, 1063-1067, doi:10.1126/science.1155429.

Squyres, S. W., O. Aharonson, R. E. Arvidson, I. J. F. Bell, P. R. Christensen, B. C. Clark, J. A. Crisp, W. Farrand, T. Glotch, M. P. Golombek, J. Grant, J. Grotzinger, K. E. Herkenhoff, J. R. Johnson, B. L. Jolliff, A. H. Knoll, S. M. McLennan, H. Y. McSween, J. M. Moore, J. J. W. Rice, and N. Tosca (2006), Bedrock formation at Meridiani Planum, *Nature*, *443*, doi:10.1038/nature05212.

Squyres, S. W., O. Aharonson, B. C. Clark, B. A. Cohen, L. Crumpler, P. A. de Souza, W. H. Farrand, R. Gellert, J. Grant, J. P. Grotzinger, A. F. C. Haldemann, J. R. Johnson, G. Klingelhofer, K. W. Lewis, R. Li, T. McCoy, A. S. McEwen, H. Y. McSween, D. W. Ming, J. M. Moore, R. V. Morris, T. J. Parker, J. W. Rice, Jr., S. Ruff, M. Schmidt, C. Schroder, L. A. Soderblom, and A. Yen (2007), Pyroclastic Activity at Home Plate in Gusev Crater, Mars, *Science*, *316*(5825), 738-742, doi: 10.1126/science.1139045.

Squyres, S. W., R. E. Arvidson, I. J.F. Bell, J. Bruckner, N. A. Cabrol, W. Calvin, M. H. Carr, P. R. Christensen, B. C. Clark, L. Crumpler, D. J. D. Marais, C. d'Uston, T. Economou, J. Farmer, W. Farrand, W. Folkner, M. Golombek, S. Gorevan, J. A. Grant, R. Greeley, J. Grotzinger, L. Haskin, K. Herkenhoff, S.Hviid, J. Johnson, G. Klingelhofer, A. Knoll, G. Landis, M. Lemmon, R. Li, M. B. Madsen, M. C. Malin, S. M. McLennan, H. Y. McSween, D. W. Ming, J. Moersch, R. V. Morris, T. Parker, J. J.W. Rice, L. Richter, R. Rieder, M. Sims, M. Smith, P. Smith, L. A. Soderblom, R. J. Sullivan, H. Wanke, T. Wdowiak, M. Wolff, and A. Yen (2004a), The Spirit Rover's Athena science investigation at Gusev Crater, Mars, *Science*, *305*, 794-799, doi: 10.1126/science.3050794.

Squyres, S. W., R. E. Arvidson, J. F. B. III, J. Brückner, N. A. Cabrol, W. Calvin, M. H. Carr, P. R. Christensen, B. C. Clark, L. Crumpler, D. J. D. Marais, C. d'Uston, T. Economou, J. Farmer, W. Farrand, W. Folkner, M. Golombek, S. Gorevan, J. A. Grant, R. Greeley, J. Grotzinger, L. Haskin, K. E. Herkenhoff, S. Hviid, J. Johnson, G. Klingelhöfer, A. Knoll, G. Landis, M. Lemmon, R. Li, M. B. Madsen, M. C. Malin, S. M. McLennan,

H. Y. McSween, D. W. Ming, J. Moersch, R. V. Morris, T. Parker, J. W. R. Jr., L. Richter, R. Rieder, M. Sims, M. Smith, P. Smith, L. A. Soderblom, R. Sullivan, H. Wänke, T. Wdowiak, M.Wolff, and A. Yen (2004b), The Opportunity Rover's Athena Science Investigation at Meridiani Planum, Mars, *Science*, *306*(5702), 1698-1703, doi: 10.1126/science.1106171.

Stierwalt, D. L., J. B. Bernstein, and D. D. Kirk (1963), Measurement of the Infrared Spectral Absorptance of Optical Materials, *Applied optics*, *2*(11), 1169-1173, doi: 10.1364/AO.2.001169.

Thomas, P. C., M. C. Malin, P. B. James, B. A. Cantor, R. M. E. Williams, and P. Gierasch (2005), South polar residual cap of Mars: Features, stratigraphy, and changes, *Icarus*, *174*(2), 535-559, doi:510.1016/j.icarus.2004.1007.1028.

Thorpe, T. E. (1978), Viking orbiter observations of the Mars opposition effect, *Icarus*, *36*(2), 204-215.

Thorpe, T. E. (1979), The Mars opposition effect at 20° N latitude and 20° W longitude, *Icarus*, *37*, 389-398.

Tornabene, L. L., J. E. Moersch, H. Y. McSween, V. E. Hamilton, J. L. Piatek, and P. R. Christensen (2008), Surface and crater-exposed lithologic units of the Isidis Basin as mapped by coanalysis of THEMIS and TES derived data products, *J. Geophys. Res.*, *113*, E10001, doi:10.1029/2007JE002988

Torson, J. M., and K. J. Becker (1997), ISIS- A software architecture for processing planetary images, *Lunar and planetary science XXVIII*, 1997.

Triggs, B., A. Zisserman, R. Szeliski, P. McLauchlan, R. Hartley, and A. Fitzgibbon (2000), Bundle Adjustment — A Modern Synthesis, in *Vision algorithms: theory and practice*, edited, pp. 153-177, Springer Berlin / Heidelberg.

Vasavada, A. R., J. L. Bandfield, B. T. Greenhagen, P. O. Hayne, M. A. Siegler, J.-P. Williams, and D. A. Paige (2012), Lunar equatorial surface temperatures and regolith properties from the Diviner Lunar Radiometer Experiment, *J. Geophys. Res.*, *117*, E00H18, doi: 10.1029/2011je003987.

Widdowson, M., J. N. Walsh, and K. V. Subbarao (1997), The geochemistry of Indian bole horizons: palaeoenvironmental implications of Deccan intravolcanic palaeosurfaces, *Palaeosurfaces: Recognition, Reconstruction and Palaeoenvironmental Interpretation. Geological Society, London, Special Publications*, *120*, 269ñ281.

Wilhelms, D. E., and S. W. Squyres (1984), The martian hemispheric dichotomy may be due to a giant impact, *Nature*, *309*, 138-140.

Wilhelms, D. E., J. F. McCauley, and N. J. Trask (1987), The geologic history of the moon, *Washington: USGPO; Denver, CO (Federal Center, Box 25425, Denver 80225): For sale by the Books and Open-file Reports Section, US Geological Survey, 1987.*

Wilson, E. B., Jr., J. C. Decius, and P. C. Cross (1955), *Molecular Vibrations: The Theory of Infrared and Raman Vibrational Spectra*, McGraw-Hill.

Wilson, L., and J. W. Head (1994), Mars: Review and analysis of volcanic eruption theory and relationships to observed landforms, *Rev Geophys*, *32*(3), 221-263, doi:10.1029/94RG01113

Wilson, L., and J. W. Head (2007), Explosive volcanic eruptions on Mars: Tephra and accretionary lapilli formation, dispersal and recognition in the geologic record, *Journal of Volcanology and Geothermal Research*, *163*(1-4), 83-97.

Wray, J. J., R. E. Milliken, C. M. Dundas, G. A. Swayze, J. C. Andrews-Hanna, A. M. Baldridge, M. Chojnacki, J. L. Bishop, B. L. Ehlmann, S. L. Murchie, R. N. Clark, F. P. Seelos, L. L. Tornabene, and S. W. Squyres (2011), Columbus crater and other possible groundwater-fed paleolakes of Terra Sirenum, Mars, *J. Geophys. Res.*, *116*(E1), E01001, doi: 10.1029/2010je003694.

Wyatt, M. B., and H. Y. McSween, Jr. (2002), Spectral evidence for weathered basalt as an alternative to andesite in the northern lowlands of Mars, *Nature*, *417*(6886), 263-266, doi: 210.1038/417263a.

Wyatt, M. B., V. E. Hamilton, H. Y. McSween, Jr., P. R. Christensen, and L. A. Taylor (2001), Analysis of terrestrial and martian volcanic compositions using thermal emission spectroscopy: I. Determination of mineralogy, chemistry, and classification strategies, *J. Geophys. Res.*, *106*(E7), 14,711-714,732, doi:10.1029/2000JE001356

Yamaguchi, Y., A. B. Kahle, H. Tsu, T. Kawakami, and M. Pniel (1998), Overview of Advanced Spaceborne Thermal Emission and Reflection Radiometer (ASTER), *Ieee T Geosci Remote*, *36*(4), 1062-1071, doi: 10.1109/36.700991.

Zhong, S., and M. T. Zuber (2001), Degree-1 mantle convection and the crustal dichotomy on Mars, *Earth Plan. Sci. Lett.*, *189*(1-2), 75-84.

Zuber, M. T. (2001), The crust and mantle of Mars, *Nature*, *412*, 220-227, doi:10.1038/35084163.

Zuber, M. T., S. C. Solomon, R. J. Phillips, D. E. Smith, G. L. Tyler, O. Aharonson, G. Balmino, W. B. Banerdt, J. W. Head, C. L. Johnson, F. G. Lemoine, P. J. McGovern, G. A. Neumann, D. D. Rowlands, and S. Zhong1 (2000), Internal Structure and Early Thermal Evolution of Mars from Mars Global Surveyor Topography and Gravity, *Science*, *287*, 1788-1793, doi: 10.1126/science.287.5459.1788.

APPENDIX A

AUTHOR PERMISSION FOR USE OF PUBLISHED MATERIAL

Philip R. Christensen, Victoria E. Hamilton, Keith J. Nowicki, Noel Gorelick, Jonathan Hill, and Kimberly Murray, and have all granted permission for the use of co-authored materials in this dissertation.

BIOGRAPHICAL SKETCH

Christopher S. Edwards was a Ph.D. Candidate at Arizona State University until August 2012. He completed his M.S. in Geological Sciences from ASU in 2010. After defending his Ph.D. in early August 2012, he will undertake a Postdoctoral Fellowship in Planetary Science at the California Institute of Technology. Edwards has collaborated extensively with the 2001 Mars Odyssey Thermal Emission Imaging System (THEMIS), Mars Global Surveyor Thermal Emission Spectrometer (TES) and Mars Exploration Rovers Mini-Thermal Emission Spectrometer (Mini-TES) science teams during his tenure at Arizona State University. His research interests focus on the composition, physical properties and processes, and morphology of planetary surfaces, with an emphasis on Mars and the Earth. A major element of his research has been the design and development of infrared remote sensing instruments for use in the laboratory and for fieldwork. His research uses infrared spectroscopy, radiometry, laboratory spectroscopic measurements, field observations, and numerical modeling, and has taken him to field sites in the western U.S., Yellowstone, Hawaii, and Spain, as well as the Himalayan mountains of Bhutan. He was recently awarded the School of Earth and Space Exploration's Outstanding Geology Student for 2012 and the ASU Graduate and Professional Student Association/Graduate College Outstanding Mentor Award for 2012.